



Provided by the author(s) and University of Galway in accordance with publisher policies. Please cite the published version when available.

Title	Size and compositional dependent effects of marine aerosol on cloud condensation nuclei
Author(s)	Fossum, Kirsten
Publication Date	2018-12-06
Publisher	NUI Galway
Item record	http://hdl.handle.net/10379/14795

Downloaded 2024-04-26T14:46:43Z

Some rights reserved. For more information, please see the item record link above.





OÉ Gaillimh
NUI Galway

Size and Compositional Dependent Effects of Marine Aerosol on Cloud Condensation Nuclei

A Thesis

Submitted by

Kirsten Nicole Fossum

for the degree of

Doctor of Philosophy

School of Physics, College of Science,
Ryan Institute's Centre for Climate & Air Pollution Studies
and Marine Renewable Energy Ireland,
National University of Ireland Galway.

Academic Supervisor: Professor Colin O'Dowd
Co-supervisors: Dr Jurgita Ovadnevaite & Dr Darius Ceburnis

December, 2018.

Table of Contents

Table of Contents	i
Declaration	iv
Abstract	v
Acknowledgements.....	vi
1. Motivation and study objectives	1
2. Review of the current state of knowledge	3
2.1 Aerosol definitions, sources, and composition.....	3
2.2 Aerosol cloud formation and interactions.....	6
2.3 Marine aerosol and climate	13
2.3.1 Marine aerosol composition.....	15
2.3.2 Pollution in the marine environment	22
2.3.3 Marine cloud condensation nuclei	24
2.4 Ice nucleating particles	26
3. Methods and measurements.....	29
3.1 Sampling locations	29
3.1.1 PEGASO Cruise, Southern Ocean (Jan 2 nd - Feb 12 th , 2015)	29
3.1.2 Mace Head Atmospheric Research Station, North East Atlantic.....	31
3.2 Supporting instrumentation	32
3.2.1 Condensation particle counter	32
3.2.2 Particle sizing by electrical mobility diameter	34
3.2.3 Aerosol Mass Spectrometer	36
3.3 Cloud condensation nuclei counter	37
3.3.1 Calibration.....	39
3.3.2 Polydispersed set-up.....	43
3.3.3 Monodispersed set-up.....	44
3.4 Black carbon instrumentation	44
3.5 Interpreting data.....	45
3.5.1 Air Mass Analysis	46
3.5.2 Köhler theory	47
3.5.3 κ -Köhler theory and aerosol hygroscopicity.....	49
3.5.4 Degree of neutralisation	50

Table of Contents

3.5.5	Monodispersed CCN total concentration calculation, and percent contributions	50
4.	Results 1—black carbon measurements in marine environments suggest the persistence of clean conditions	53
4.1	The clean Southern Ocean confirmed by SP2 measurements	53
4.2	OM is not correlated to BC in clean conditions	57
4.3	The clean North East Atlantic confirmed by SP2 measurements and MAAP comparison	60
4.4	How prevalent is BC in the remote marine environment?	69
5.	Results 2—summertime aerosol physico-chemical properties and links to cloud activation in the Southern Ocean	71
5.1	CCN in regional air masses.....	72
5.1.1	Physico-chemical aerosol properties in cAA air masses.....	72
5.1.2	Physico-chemical aerosol properties in mP air masses.....	85
5.1.3	Physico-chemical aerosol properties mT air masses.....	88
5.1.4	Sea-salt events.....	88
5.2	Antarctic ice samples	92
5.3	What do summertime Southern Ocean CCN reveal?	92
5.4	Comparing Southern Ocean CCN to the North East Atlantic	93
6.	Results 3—sea-salt suppression of sulphate nuclei activation.....	99
6.1	Can the ambient sulphate accumulation mode be explained by heterogeneous in cloud sulphate production (<i>via</i> SO ₂ oxidation)?	100
6.2	Suppression analysis of ambient Southern Ocean data trends.....	101
6.3	Simulating ambient data via parcel model(s).....	105
6.4	Modelling suppression with sea-salt distributions extending into the Aitken mode	109
6.5	Model sensitivity to environmental parameters and sea-salt number concentration.....	113
6.6	Suppression analysis conclusions	121
7.	Conclusions	123
7.1	Summary of main results	124
7.2	Discussion on Main Findings.....	126
7.3	Future work for elucidating marine cloud nucleating processes	130
APPENDIX A.....		132
A.1	Calibration data for cloud condensation nuclei counters	132

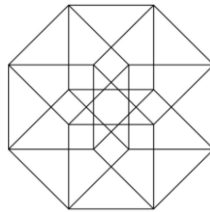
Table of Contents

A.2	Inter-comparison of two CCN chambers	132
APPENDIX B	135
B.1	AIOMFAC model.....	135
B.2	Bubble-Tank Antarctic ice experimentation	139
B.3	LINAM experimental technique.....	143
References	145
Table of Abbreviations and Symbols	166
List of Figures	168
List of Tables	174
Dissemination of Research	176

Declaration

I hereby declare that none of the work described in this thesis has been presented to this or any other university in support of an application for a higher degree.

Kirsten N. Fossum



Abstract

This work investigates marine aerosol physico-chemical properties (e.g. size and chemistry) and its Cloud Condensation Nuclei (CCN) properties under natural background conditions. Black carbon (BC), a tracer for anthropogenic pollution, was used to classify Southern Ocean air mass cleanliness, where the study focussed on anthropogenic influences and was compared to the North East Atlantic, which is closer to pollution sources. Despite this, the lowest prevailing BC mass concentration levels were similar for either ocean ($\sim 0.1 \text{ ng m}^{-3}$) with extreme pollution levels above 80 ng m^{-3} for about 0.3 % of the time over both observation periods.

In order to elucidate the relative contribution of 'primary' wind-produced sea spray and 'secondary' gas-to-particle aerosols to marine cloud droplet formation, a novel detailed analysis of droplet activation critical supersaturation *versus* critical diameter was conducted in remote environmental marine air (i.e. maritime polar and modified continental Antarctic air masses) in parallel to modelled chemically-homogenous aerosols. The analysis revealed that, for realistic marine boundary layer cloud supersaturations, primary CCN contributed 8–51 % to the estimated cloud droplet concentration (as determined by the Hoppel intermodal-minimum) at wind speeds $< 16 \text{ m s}^{-1}$. At higher wind speeds, primary marine aerosol could contribute up to 100 % of estimated cloud droplet concentration.

It was observed that within air masses enriched with sea spray CCN, the contribution of secondary (mainly non-sea-salt-sulphate) particles to cloud droplet concentration was significantly reduced despite a higher availability of sulphate CCN. Further analysis revealed a highly correlated inverse linear trend between activated sea spray particles and the percentage of activated sulphate particles. In practice, the addition of sea-salt CCN appeared to suppress the activation of sulphate CCN. An ensemble of three 1-D microphysical droplet growth and activation parcel models corroborated this suppression effect and found that under favourable conditions, as much as a ~ 100 % enhancement in cloud droplet concentration were predicted as the availability of sea-salt nuclei decreased and vertical updraft increased.

Acknowledgements

To begin, I would like to extend my thanks to my supervisor, Professor Colin O'Dowd. While it has been a metaphorically long road, your patience and expertise has always made it appear walkable. I sincerely appreciate the work that you have done to create funding for my project and a space for me within your research group. To my co-supervisors, Dr Jurgita Ovadnevaite and Dr Darius Ceburnis, I would also express my thanks and my gratitude for their guidance, shared knowledge, and captivating discussions.

This work was supported by funding from the European Union's Seventh Framework Programme (FP7/2007-2013) project BACCHUS under grant agreement n_ 603445; and SFI under MaREI.

I would also like to thank H. Coe and J. Allan from the Centre for Atmospheric Sciences, School of Earth and Environmental Sciences, University of Manchester, Manchester M13 9PL, UK who provided the SP2 instrument used throughout this work. I would also like to thank R. Simo and M. Dall'Osto from the Institut de Ciències del Mar (CSIC), Barcelona, Catalonia, Spain, for organising the Antarctic cruise that led to the large marine dataset used in this work. The Antarctic cruise was supported by funding from Spanish Ministry of Economy and Competitiveness (MINECO) as part of the PEGASO (Ref.: CTM2012-37615) and BIO-NUC (Ref:CGL2013-49020-R) projects; HEA-PRTL14.

Other immeasurable support came from various people and other nouns, a few to name:

Dr Jana Preißler for her collaboration and patience, Dr Derek Coburn without whom my head may have come loose, my extended research group including Gerry Spain who can be found at Mace Head research facility and always up for an ocean swim, the entire NUIG School of Physics including the staff, technicians, and PhD students therein (for it takes a village to raise a PhD student), the window beside my desk, caffeine, my *confidante* Ali Connolly who has struggled to the end with me, all the strange pictures my sister Ryanna Fossum sent me that made me smile, John Samuel Rafael Keady and his never-ending hugs, and my family.

A special acknowledgement belongs to my parents, Dr Sabrina Kemeny and Prof. Eric R. Fossum, whose innovation never ceases to amaze me and whose love followed me across the Atlantic Ocean and I'm sure would even follow me to the restaurant at the end of the universe.

To anyone I am fond of or has helped me but that I have erroneously forgotten to mention here, thank you.

This work is dedicated to those who seek answers, ask questions, or are otherwise reading this thesis, and to my many parents who always lit the way.

1. Motivation and study objectives

You can know the name of a bird in all the languages of the world, but when you're finished, you'll know absolutely nothing whatever about the bird... So let's look at the bird and see what it's doing -- that's what counts.

Richard P. Feynman

Rapid climate change, recognised to be mainly caused by human pollution (Stocker, 2013), poses a large threat to human security, disproportionately affecting indigenous and impoverished communities world-wide. In order to develop efficient policies to mitigate climate change, accurate knowledge of the causes and effects of climate change are needed. Climate forecast accuracy is only as precise as our understanding of Earth's climate system, which is strongly regulated by the cycling of water vapour through the atmosphere. Aerosol effects on cloud formation cause large uncertainties in predicting the balance of reflected and absorbed solar radiation through Earth's atmosphere (Stocker, 2013). To understand the role of air pollution (or anthropogenic aerosol) in changing Earth's climate, more information is needed about the natural state of the aerosol involved in Earth's climate-feedback system when unperturbed by pollution. Because the marine environment is the largest surface source of Earth's climate-feedback systems, special attention should be given to marine aerosol. Marine aerosol can have varying physio-chemical effects on cloud condensation nuclei (CCN) and ice nuclei (IN) which ultimately impact aerosol-cloud interactions.

Overall, this project aims to investigate marine aerosol influences on the chemical and physical nature of cloud condensation nuclei activation and thereby further our understanding of the complicated nature of aerosol-cloud interactions in the marine environment. The aim is achieved by advancing our understanding on cloud condensation nuclei (CCN) through the analysis of data collected during the PEGASO campaign in the Southern Ocean (austral summer, January-February 2015) *via* a cloud condensation nuclei chamber (CCNC) and a suite of other *in-situ* instrumentation measuring physical and chemical particle characteristics. Other marine datasets were also used in this research, including measurements collected during the BACCHUS campaign on the coast of the North East Atlantic (August-September 2015).

Motivation and study objectives

The objectives of this research are:

- ❖ To elucidate the nature of marine aerosol over remote oceans and its perturbation by air pollution.
- ❖ To characterise the cloud nucleating properties of remote natural marine aerosols and determine the relative contribution of different natural sources and processes to the actual cloud condensation nuclei (CCN) population.
- ❖ To evaluate the coupling, competition and sensitivity between primary and secondary CCN activation.

2. Review of the current state of knowledge

2.1 Aerosol definitions, sources, and composition

Aerosols are a combination of gases and airborne particles, the particles may be liquid or solid, of varying size with size dependence often associated with their chemical composition or source, see Figure 2.1. This research principally focusses on the physico-chemical properties of cloud nucleating particles (namely liquid nucleation) with a dry (relative humidity < 40 %) particle diameter on the order of 1 μm or less. Larger sized particles are also important cloud droplet nuclei, given a high enough buoyancy (or low enough settling velocity) to get mixed up to cloud base. However, larger particles are far less numerous than particles of 0.01 – 1 μm size, have a huge surface area, and are highly effective cloud nuclei based on size alone, so chemical composition does not often affect nucleating ability. Cloud droplet seed particles are referred to as cloud condensation nuclei (CCN) where liquid water activation occurs, which is when water vapour condenses onto the CCN rapidly forming a water droplet more than ten times its original size. Ice nuclei particles (INP) refers to the same process except solid-phase ice formation on particles occurs. Particle sizes are described in four main mode categories: the nucleation mode, the Aitken mode, the accumulation mode, and the coarse mode. No single mode has a clear size cut-off although ranges are often used. In this work the mode ranges are approximately a diameter < 0.03 μm for the nucleation mode, 0.03 μm < diameter < 0.09 μm for the Aitken (Aitken, 1880, 1918) mode, 0.09 μm < diameter < 1 μm for the accumulation mode, and a diameter > 1 μm for the coarse mode (Figure 2.1). In the natural marine environment, large particles are often sea-salt and are hygroscopic so will readily absorb water even in subsaturated conditions (Lewis and Schwartz, 2004; O'Dowd and de Leeuw, 2007). Other large or supermicron aerosol includes airborne water droplets, bacteria, fungal spores, pollen, and dust particles. Dust has been detected in the marine environment from long range transport (Jennings et al., 1997; Duce and Tindale, 1991), and speculations have been made that dust can even be settled out onto the marine surface and re-suspended through wave crashing and bubble-bursting (Gavin Cornwell et al., 2017). Large particles leave the atmosphere relatively quickly, often when undergoing atmospheric settling before cloud droplet nucleation, or are precipitated out after nucleation.

Review of the current state of knowledge

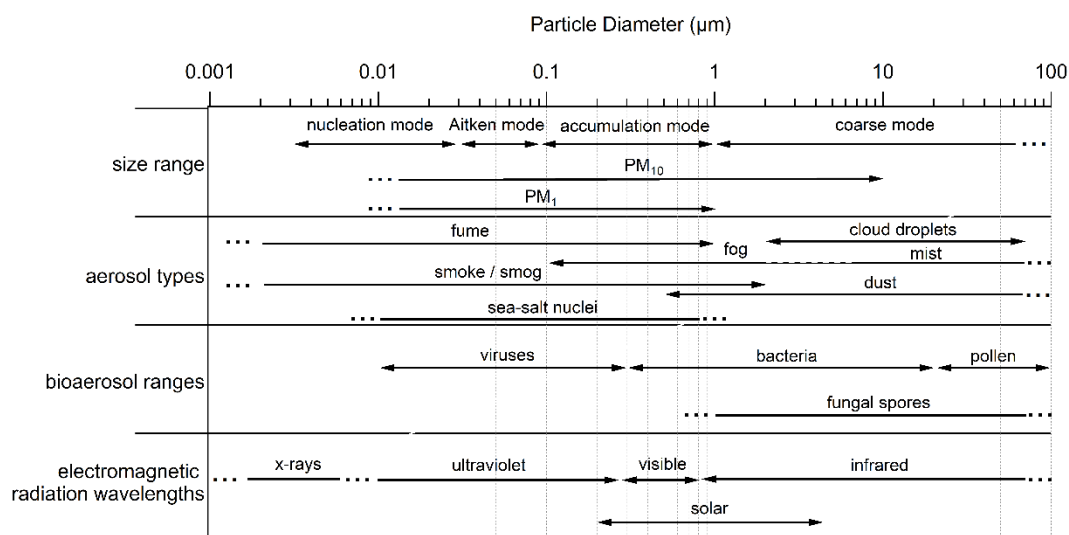


Figure 2.1. The general breakdown of aerosol particle type by size ranges and nomenclature. This graph is adapted from a similar graph in Hinds (1982).

Aerosol generation

Particles entering the atmosphere directly as fragments of a bulk parent primary material are called primary aerosol. In the marine environment this is from wave crashing or bubble-bursting at the marine surface, which is mostly due to shear stress of wind over the marine layer (Woodcock et al., 1953; Blanchard, 1963; Monahan, 1968) or to cavitation from artificial wave breaking from human industry (i.e. ship traffic), but there are also benthic sources of bubbles from the gaseous releases at the sea floor (Woolf, 2001). Bubble-bursting results in two major primary aerosol size ranges and chemistry. The first, which is associated with smaller particles, happens when the bubble film bursts into many tiny droplets containing scavenged surfactants and particulate matter that would have been suspended on the bubble surface (Woolf, 1997) forming primary particles. The second is through the formation of a jet-drop which occurs when a bubble bursts and allows water to rush into the freed space producing a large drop of similar chemistry to bulk seawater. The jet-drop is associated with larger sized primary particles, and was originally thought to represent a small number fraction of aerosol (Lewis and Schwartz, 2004; Blanchard and Woodcock, 1957). A recent study (Wang et al., 2017) has shown that jet drops produced from the bursting of ultrafine bubbles could produce a substantial number of submicrometre primary particles (~20-43 % of the submicrometre fraction, depending on seawater chemistry) which is more than originally estimated (Lewis and Schwartz, 2004; Blanchard and Woodcock, 1957). All primary marine aerosol (PMA) are also referred to as sea spray aerosol (SSA), and usually comprise a combination of

Review of the current state of knowledge

sea-salt, particulate organic matter (POM), and organic matter (OM) surfactants present in the seawater.

Aerosol particles formed *via* gas-to-particle conversion are called secondary. The mechanisms for secondary particle formation include new particle formation (NPF), condensation of vapours, and aqueous-phase oxidation in cloud or out. Cloud processing, in which aqueous solution chemistry occurs, is considered the most rapid mechanism for the formation of secondary aerosol in the marine environment (O'Dowd et al., 2000b). The secondary product of aqueous phase heterogeneous oxidation of atmospheric SO₂ is sulphate (SO₄), which is found in high abundance in atmospheric aerosol. When organic vapour concentrations are high, such as in the Arctic, the condensation of vapours has been shown to be an important mechanism for secondary aerosol formation (Burkart et al., 2017). NPF, a secondary formation process in which gaseous precursors form molecular clusters, usually requires a low condensation sink, or else the newly coalesced particles will evaporate before becoming stable. If a newly formed particle can reach a diameter ~6 nm, then its rate of loss is reduced to such a degree that particles of this size often remain a particle and continue to grow in size (O'Dowd et al., 2002b). NPF has been shown to be a large source of particle formation globally, with reaction pathways ranging widely based on the environment in which it is occurring. Attention has turned to the changing polar scenery induced by global warming offering more opportunities for NPF (Kyrö et al., 2013) in permafrost melt zones. On the whole, low-volatility molecules are necessary to create stable particle clusters, usually through ternary reactions as binary reaction rates are too slow to overcome losses from stronger condensation sinks (Kulmala et al., 2000). Coastal environments have been identified as strong sources for NPF through the formation of iodine-oxide compounds (Sellegrri et al., 2016; Allan et al., 2015; O'Dowd et al., 2002b; O'Dowd et al., 2002a). Further particle growth can occur through Brownian scavenging (coagulation) and cloud droplet coalescence, which can often lead to a combination of primary and secondary composite particles.

Particle Chemistry

The general compositional fractions of aerosol are well studied globally, and source apportionment is quickly identifying which local sources are contributing fractionally to measured aerosol in smaller regional scales. Large scale natural emissions of aerosol can be tracked using satellite retrievals. Figure 2.2 shows a momentary capture of the modelled wind dispersal of both primary (i.e. dust, sea-salt, and black carbon) and secondary aerosol (i.e. sulphate), while organic carbon can be primary or secondary. The marine environment produces SSA and sulphate-based secondary marine aerosol (SMA) and is one of the largest natural contributors to global aerosol.

Review of the current state of knowledge

The marine environment itself covers major swaths of the surface area of the earth, estimated at 71 %. In terms of aerosol generation, it contributes heavily to global natural primary and secondary aerosol emissions. Where natural sources are estimated to produce a few thousand Teragrams (Tg) per year (yr) of aerosol, anthropogenic emissions are only estimated in the hundreds of Tg per yr (G. de Leeuw et al., 2011; Klimont et al., 2017). The marine environment alone puts out 3.5×10^3 Tg yr⁻¹ of sea spray aerosol (SSA), where there is $\sim 10 \text{ g m}^{-2} \text{ yr}^{-1}$ of SSA (G. de Leeuw et al., 2011) and $\sim 3 \text{ mmol m}^{-2} \text{ yr}^{-1}$ of sulphur volatiles (Charlson et al., 1987).

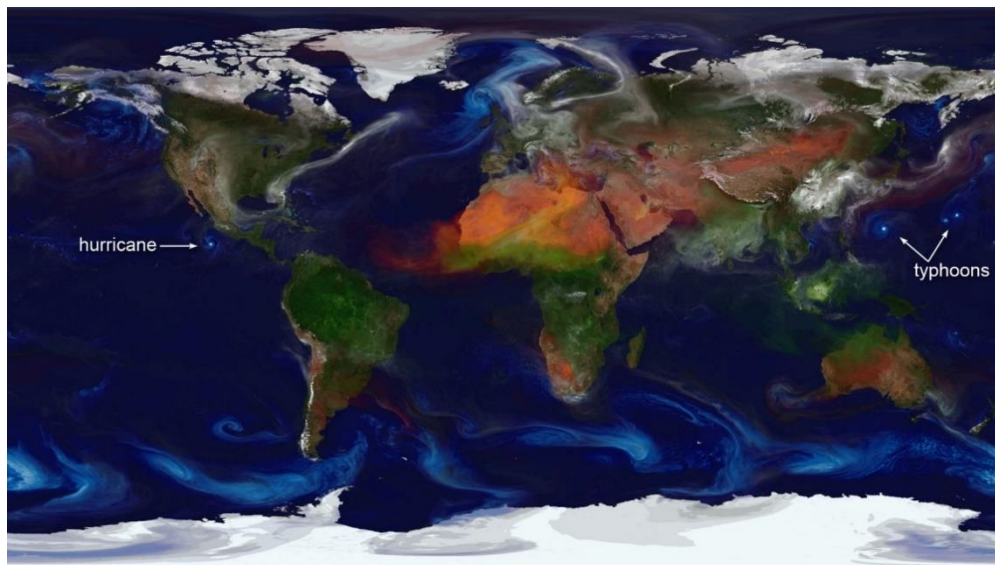


Figure 2.2. Modelled wind dispersal of vast quantities of dust (red), sea-salt (blue), sulphate (white) and black and organic carbon (green) around the world. Reproduced from NASA (<http://gallagher-photo.com/2013/09/12/a-portrait-global-aerosols-nasa/>).

2.2 Aerosol cloud formation and interactions

While water vapour is the largest climate forcer in the atmosphere, aerosol particles play an important role in water vapour cycling within the atmosphere, indirectly and directly modifying the climate. Particles interact with incoming short-wave solar radiation and can also affect outward long-wave global radiation. This dissertation research is focussed on possible particle effects to the short-wave radiation rather than long-wave. The aerosol direct effect occurs through the radiation interaction with the particles as they exist in the atmosphere at relative humidity. Relative humidity (RH), expressed as a percentage, is a measure of the amount of water vapour that air can hold at a given temperature and pressure. When relative humidity is $< 100 \%$ we refer to the air as subsaturated, conversely when it is $> 100 \%$ we refer to it as supersaturated. For many particles such as SSA, the ambient subsaturated RH

Review of the current state of knowledge

is often great enough for the formation of haze aerosol through some water uptake, increasing a particle's size and sphericity. A particle's direct scattering effect is dependent on its refractive index, shape, and diameter, although the scattering properties of an aerosol population are also dependent on the number-size distribution of its particles. The larger the scattering impact the larger the aerosol optical depth (AOD). The number contribution flux of SSA, which is related to wind speed, significantly affects the direct scattering properties of marine aerosol, due to the power-law relationship between AOD and wind speed (Mulcahy et al., 2008). In the North East Atlantic, scattering properties are proportional to the square of the wind speed independent of season. However, seasonal high biological activity often leads to half of the scattering of low biological activity periods (Vaishya et al., 2012). Vaishya et al. (2012) attributed this scattering difference to the presence of a high fraction of submicrometre organic matter. The organic matter particles reduced the refractive index of the particles, explaining 70 % of the reduction in scattering alone. Another 22 % of the reduction in scattering could be explained when considering the changed size distribution during high biological activity coupled with the lowered refractive index of the organic matter particles.

The aerosol indirect effect occurs through radiation interaction with cloud droplet particles, which exist in the atmosphere in supersaturated regimes. Once aerosols meet supersaturated conditions, which force the condensation of water onto available surfaces such as aerosols, they become "activated" and continue to grow by condensation. Grown particles are now considered cloud droplets and affect optical properties of a cloud through their cloud droplet number concentration (CDNC) and effective radius (R_e). The indirect effects (first and second, respectively) are described by these properties. The first indirect effect, also called the "Twomey effect" (Twomey, 1974), refers to cloud optical depth (the density of cloud droplets within the cloud) which is directly proportional to the reflecting surface area of the droplets. The second indirect effect refers to the clouds' atmospheric lifetime, which is a measure of how long the clouds' reflectance will last. The cloud lifetime is sensitive to both synoptic meteorological conditions and dynamical cloud microphysical interactions but is also determined by cloud droplet radius or surface area. The cloud droplet radius is sensitive to water vapour availability which is controlled through CDNC, i.e. by the first indirect effect. Increasing CDNC should reduce the overall droplet radii, increasing net cloud droplet surface area and leading to more reflectance of incoming short-wave radiation. Both indirect effects are important components of determining Earth's net radiative budget, as low-level clouds modulate solar reflection. The marine surface is a dark absorbing layer, so the added albedo of low-level clouds has a particularly profound effect on the marine radiative budget. The Intergovernmental Panel on Climate Change (IPCC) estimates for 2013 reveal that aerosol effects on clouds could have a profound negative forcing impact, however the estimation still has a high uncertainty (see Figure 2.3), in part due to the

Review of the current state of knowledge

complicated nature of aerosol-cloud interactions, and also due to the uncertainty in the field of in-cloud aerosol production (Stocker, 2013). Cloud adjustments due to aerosols (combined with aerosol direct forcing) could be the largest negative forcing feedback in the Earth's radiative budget. If cloud adjustments due to aerosol results in stronger negative forcing, this could balance some of the positive radiative forcing from anthropogenic emissions and result in a lower net atmospheric warming effect. However, the negative forcing could also be quite small, which would result in more rapid atmospheric warming. The indication from the Fifth IPCC report is that information is lacking about aerosol-cloud interactions resulting in low levels of confidence (Figure 2.3), making the study of these interactions of utmost importance for accurate climate forcing predictions.

In terms of aerosol-cloud interactions, many physical principles and chemically-mediated reactions come together to regulate the formation of clouds through dynamical processes. First, you have the single-particle dynamics and then secondly the aerosol population as a larger system, although neither are mutually exclusive. The single-particle cloud interaction can be described as cloud droplet activation which is the free and rapid addition of water vapour onto the existing particle, also known as condensation, increasing the particle size 100-fold and becoming 'activated'. This is mediated when the equilibrium vapour pressure, at a certain temperature, is larger than the saturation vapour pressure after which condensation occurs more readily than evaporation.

Review of the current state of knowledge

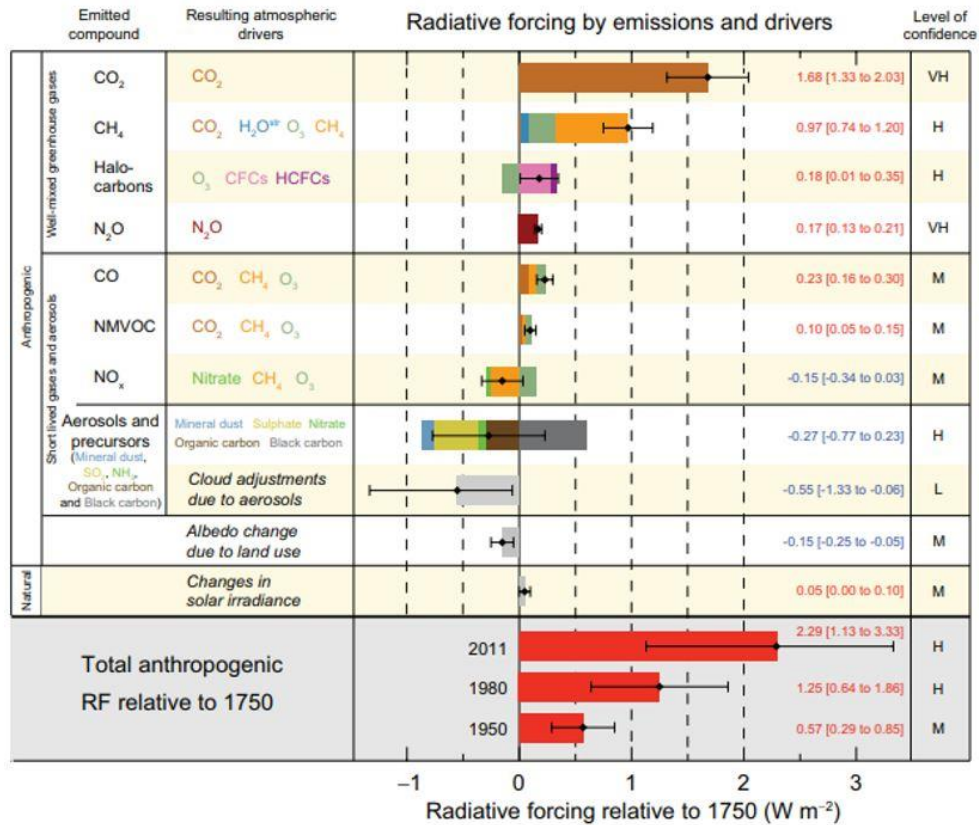


Figure 2.3. Radiative forcing breakdown of the Earth (in 2011 relative to 1750) reproduced from Stocker (2013). Best estimates are shown in black diamonds with uncertainty intervals and level of confidence on the right (VH-very high, H-high, M-medium, L-low, and VL-very low).

The process of cloud droplet formation is described by Köhler theory through equilibrium thermodynamics (Köhler, 1936). The theory brings together the Kelvin effect which describes the change in saturation vapour pressure over a curved surface and Raoult's law which describes the effects of water activity (i.e. solute effects) on the saturation vapour pressure of the droplet (see Section 3.5.2 for equations and further explanation). The hygroscopicity of chemically homogenous aerosol will follow theoretical curves of activation (see Köhler Theory in Section 3.5.2) based on surface tension effects and the water activity of the solute. Theoretical models such as AIM (Wexler and Clegg, 2002; Clegg et al., 1998a, b) or the AIOMFAC (Zuend et al., 2011; Zuend et al., 2008) use initial parameters to calculate the solute and solvent activities of aqueous phase solutions, which are then used to find critical supersaturation of activation by dry particle size. Cloud droplet formation is dependent on the environmental temperature, chemical composition and size of the seed particle. Most particles which activate will form cloud droplets, however smaller sized particles will only form cloud droplets if kinetic limitations are overcome when appropriately long supersaturations are sustained, or else these activated particles can evaporate (McFiggans et al., 2006). These kinetic limitations are shown to be

Review of the current state of knowledge

more important for larger populations of hydrophobic CCN particles, and are often negligible in clean marine conditions. Nenes et al. (2002) have shown that chemical effects during this activation process change droplet number enough to rival the changes in droplet number from increased ambient particle concentrations alone. In variable updrafts water soluble organic carbon (WSOC) can lead to increased activation through the lowering of surface tension (σ), and film forming compounds were found to either lower or raise CDNC depending on the distribution of the film among particle sizes. In the previously mentioned study, due to low CCN concentrations found in marine environments, film forming compounds were not seen to have a large impact on marine aerosol. Later, Ovadnevaite et al. (2011a) showed that primary marine organics in the North East Atlantic, which has been earlier shown through tank experimentation to be mostly water-insoluble organic matter (WIOM) (Facchini et al., 2008), can be associated with high CCN activation efficiency.

Cloud droplet formation on a single particle is contingent on environmental supersaturation, which has more to do with larger scale dynamical processes. Meteorological conditions, such as pressure (P), temperature (T), wind speed (U), and vertical updraft (w), are often the most deciding factors in cloud peak supersaturation (the largest supersaturation reached during cloud formation). However, given measurements over a short timescale, with relatively constant meteorological conditions (P , T , and U), w becomes the deciding factor in cloud peak supersaturation and is often the largest controlling factor in regional systems with invariant meteorology. Within a cloud, w is not constant, small eddy variances near cloud base can result in aerosol exposure to a range of peak supersaturations. The regional scale is often more important for parameterisations, modelling or forecasting, so the average cloud peak updrafts are used for analysis of the aerosol population. In the marine environment, supersaturations are usually observed at a median value of 0.3 % or less in tropical regions (Hoppel et al., 1986; Roberts et al., 2006; Leaitch et al., 1996), which is expected from the prevalence of shallow convection over most oceans. Higher supersaturations can frequently occur during cyclonic activity or frontal passages. While meteorological factors set the range of possible cloud peak supersaturations other factors further determine the maximum reached supersaturation; CCN number concentration, size, and chemistry play an important role (McFiggans et al., 2006; O'Dowd et al., 2000b; O'Dowd et al., 1997b; O'Dowd and Smith, 1993; Hoppel et al., 1996).

Higher supersaturations can be reached when CCN concentrations are lower (Hudson et al., 2010), reducing the water scavenging by particle activation and keeping the partial pressure of the water vapour higher. In the Southern Ocean, ambient vertical updrafts have been measured directly in a wide range, $-0.34 - 0.79 \text{ m s}^{-1}$ averaging $0.06 \pm 0.39 \text{ m s}^{-1}$ (Snider et al., 2017). It should be noted that when positive vertical

Review of the current state of knowledge

updrafts occur they do so within a positive standard deviation. Snider et al. (2017) found mean marine updrafts to be $\sim 0.4 \text{ m s}^{-1}$, corresponding to a range of effective supersaturations with an upward limit estimated at 0.57 % and an average of ~ 0.09 %. The low mean supersaturations found in the southern latitudes compared to the tropical regions may be due to differences in meteorological conditions. Changes in supersaturation could have huge repercussions in the cloud reflectance and lifetime, altering the climate forcing effects of marine stratocumulus clouds for submicron marine aerosol, with concentrated particle counts highly sensitive to supersaturation fluxes.

Aerosol chemistry and size can also have an effect on particle activation which in turn can alter cloud peak supersaturation. Since Köhler theory involves both chemical and physical terms for activation, CCN and INP hygroscopicity are related to both particle composition and relative size. Particle hygroscopicity is complicated and while particle activation can be largely determined by size (Dusek et al., 2006), activation of smaller Aitken and accumulation mode particles are mainly determined by chemical composition. As smaller particles are most numerous in the atmosphere, the fraction of particles which act as CCN compared with INP may have more to do with chemical composition. Chemical properties that make effective CCN are not consistent with boundary layer (warm cloud) INP. For example, dust, mainly feldspar type dust, is one of the most activation efficient INP types (Atkinson and Whale, 2013), but it does not contribute to CCN populations. Sea-salt, rather than dust, particles are one of the most active CCN. Although it is an ineffectual INP at relatively warm temperatures ($> -20^\circ\text{C}$), it can be as effective as mineral dust at $< -53^\circ\text{C}$ (Wagner et al., 2018). Both dust and sea-salt particles are known to exist at a varied range of sizes, but which have a proclivity to be found dominating the mass (volume) at large sizes. This often gives them competitive advantages at scavenging available water vapour during early activation stages. The addition of aerosols to the atmosphere means less liquid water vapour per droplet nucleus, which may lead to increased detection of long-range-transported giant particles as well as increased detection of source-dependent particles (Sorooshian et al., 2015).

The climate effects of crystalline versus liquid droplets differ, and as such both CCN and INP concentrations are important to contextualise. CCN and INP activation characteristics are presented in different ways owing to the independent and dependent factors which are of most importance to possible climate effects. CCN characteristics are often presented as a function of dry particle diameter (classically radius, although diameter has recently begun to dominate the field) and critical supersaturation allowing for the distinction of size-dependent activation efficiencies. A size and chemistry dependent parameter, κ (Petters and Kreidenweis, 2007), has been used to describe CCN hygroscopicity (see κ -Köhler theory in Methods). INP are often represented through ice-surface active area or number concentration as a

function of temperature (Figure 2.4), as cloud temperature is often the most deciding factor in INP concentration.

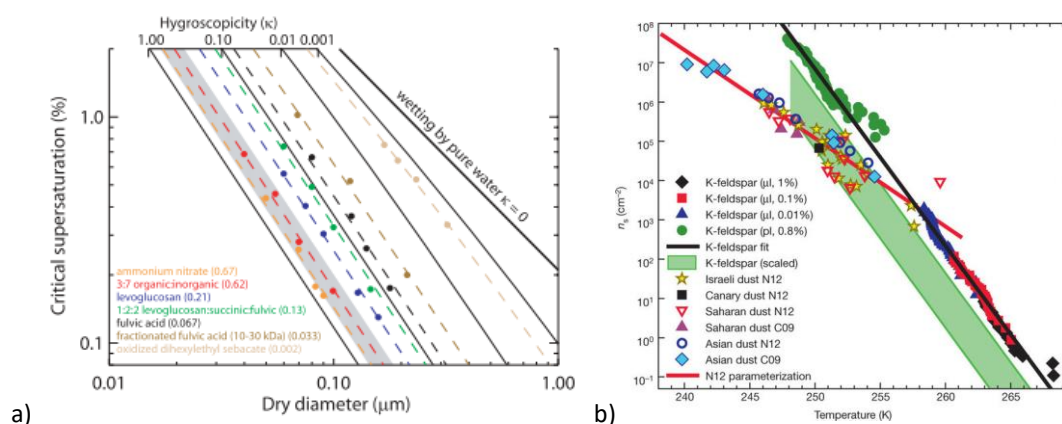


Figure 2.4. CCN (a) and INP (b) representations of activation efficiency by chemical composition. Graph a) is reproduced from Petters and Kreidenweis (2007) and shows s_c - D_d data for pure compounds, organic mixtures and organic-inorganic mixtures. Data for (a) are taken from Svenningsson et al. (2006), Dinar et al. (2006), and Petters et al. (2006). The 3:7 organic:inorganic mixture is the “polluted” mixture from Svenningsson et al. (2006). Dashed lines indicate best-fit κ values for each particle type, as shown in the legend. Shaded area indicates reported range of values for ammonium sulphate (Table 1 in Petters and Kreidenweis (2007)). Kappa values were computed for $\sigma_{s/a}=0.072 \text{ Jm}^{-2}$ and $T=298.15 \text{ K}$. Graph b) is reproduced from Atkinson and Whale (2013) showing the nucleation site density for K-feldspar and natural dusts. Data for (b) is from picolitre experiments extended to higher temperatures by use of microliter-sized droplets, with a fit provided ($\ln(n_s)=-1.038T+275.26$, valid between 248 and 268 K). Experimental K-feldspar concentrations in weight percent are provided in the key. Temperature uncertainties for microlitre experiments (not shown) were estimated at $\pm 0.4\text{K}$ and uncertainty in n_s (not shown) is estimated at $\pm 25\%$. Several natural dust samples (N12 and C09) are compared. The mineralogical compositions of the dusts used in those samples are unknown, but feldspar mass content in natural soils typically varies between 1 % and 25 %. Hence, n_s values are scaled assuming K-feldspar is present at between 1 % and 25 % of the natural dust particles’ surface.

Importantly, cloud processing in marine non-precipitating clouds is thought to be responsible for the transfer of material from the gas-to-particle phase and the growth of particles from the Aitken ($0.08 \mu\text{m}$ dry particle diameter) to accumulation mode ($0.15 \mu\text{m}$ dry particle diameter) (Hoppel et al., 1986). Marine aerosol number-size-distributions are often bimodal with one dominant peak in both the Aitken and accumulation mode. Marine aerosol that have been exposed to non-precipitating clouds show increased mass associated with CCN particles consistent with the aqueous-phase processing of SO_2 to SO_4 (Hoppel et al., 1994), which confirm cloud droplet activation as a mechanism of particle growth. As illustrated in Figure 2.5, Hoppel Theory (Hoppel et al., 1986) proposes that in a well-mixed marine boundary layer (MBL) an initial (monomodal) number-size distribution will be exposed to a MBL cloud supersaturation which will activate all particles with critical diameters

(chemistry dependent) greater than that associated with the cloud supersaturation. These particles then grow in mass with the addition of SO_4 through aqueous-phase processing, and once evaporated appear as a secondary mode of larger sized particles. Meanwhile, the non-activated droplets remain as interstitial aerosol in cloud and do not change drastically in mass (and therefore size) and remain at the same size and number concentration after exposure to the non-precipitating cloud environment as before exposure (Figure 2.5). Hoppel Theory proposes that the bimodal marine distribution formed after processing in non-precipitating clouds (often in multiple cycles) can be used to predict the effective (well-mixed) marine boundary layer cloud supersaturation using the modal minima (Hoppel minimum) found between the Aitken and accumulation mode. The supersaturation can be inferred from particle composition, and was found to be $\sim 0.15\% - 0.25\%$ in the tropical marine boundary layer (Hoppel et al., 1996).

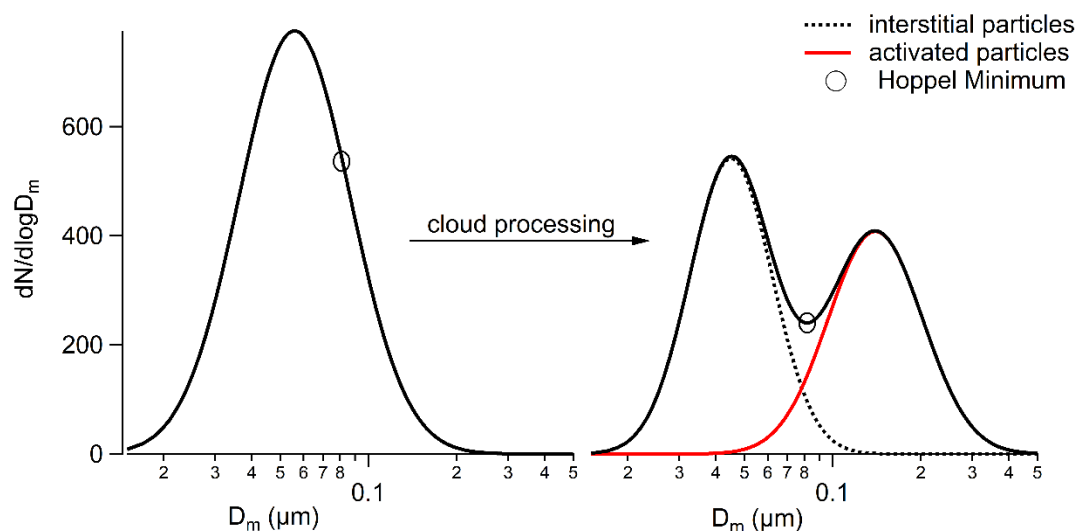


Figure 2.5. Hoppel Theory overview of the formation of a bimodal size-distribution from an initial distribution after being exposed to non-precipitating cloud(s) (both full distributions are shown in black as a function of mobility diameter in log-scale). In the bimodal distribution the number of particles is conserved, but the particles at diameters $>$ Hoppel minimum (shown as a circle) are grown large upon activation (red mode) and the particles at diameters $<$ Hoppel minimum remained of the same size (dotted black mode).

2.3 Marine aerosol and climate

As discussed in Section 2.2, aerosols can directly and indirectly interact with incoming solar radiation. Over a dark absorbing marine surface, even optically thin layers of low-level cloud coverage can have a significant impact on the overall albedo of the ocean surface. Haze layers, directly scattering incoming shortwave solar radiation, have a similarly significant impact. The degree to which primary marine aerosol (PMA) or secondary marine aerosol (SMA) serve as good haze or cloud particles

Review of the current state of knowledge

depend on their hygroscopic properties which are ultimately controlled by their physio-chemical characteristics.

SMA has been suggested to be the major component in a marine aerosol atmospheric negative feedback loop, counteracting greenhouse-gas climate forcers (Lovelock, 1972). The original proposed negative feedback system (i.e. the CLAW hypothesis, named after its authors (Charlson et al., 1987)) centred on the marine sulphur cycle, in which dimethylsulphide (DMS), a degraded form of the phytoplankton osmolyte (whose presence only exists in certain species of phytoplankton (Keller, 1989; Liss et al., 1993; Nightingale and Liss, 2003)), and whose production is hypothetically regulated by light and temperature, is oxidised (the conversion yield of DMS is 15 % into methanesulphonic acid (MSA) and 75 % into SO_2 (Chen et al., 2018)) to eventually form non-sea-salt sulphate (nss- SO_4), an important secondary CCN (Charlson et al., 1987; Lovelock and Watson, 1982). The increase in CCN leads to an increase in cloud droplet concentrations and related reflectivity of low-level clouds (a net radiative cooling effect), thus cooling the climate down and completing the negative feedback loop. However, it is still unknown whether environmental changes from increased cooling (or from other environmental factors such as increasing atmospheric CO_2 concentrations) will incur positive or negative responses in DMS production, due to the complexity of its generation in nature (Ayers and Cainey, 2007). Aqueous DMSP concentrations are directly related to (aqueous) DMS concentrations which are subsequently ventilated into the atmosphere through air-sea exchange (Liss et al., 1997). The associated phytoplankton bloom DMSP concentrations are species dependent (Liss et al., 1993) as well as bloom phase dependent (with more DMSP produced during demise phases) (Liss et al., 1997), creating variation in the DMS contribution of any given bloom at any time. Some autotrophic species which would be high in Chl-*a*, such as dinoflagellates and coccolithophores, produce more DMSP than other bloom species, such as diatoms (Lizotte et al., 2017; Liss et al., 1993). Studies have further shown a connection between water depth and DMSP concentration (Lizotte et al., 2012) seemingly supporting evidence for a solar radiation relationship to DMSP (and therefore DMS production). Evidence has also been provided that oceanic DMS concentrations correlate to climate forcing in terms of solar radiation dose, (Vallina and Simó, 2007), leading to an increase in CCN in warmer climates (Hegg et al., 1991; Ayers and Gras, 1991). Despite this, the existence of the originally proposed feedback has been challenged as the contributions to marine CCN are more complex than originally believed (Quinn and Bates, 2011).

The involvement of sea-salt, a PMA component, was originally ruled out of any feedback loop due to assumed insufficient particle concentrations and inability to reach the cloud base due to large sizes (Charlson et al., 1987). Later, an alternative feedback system based on increasing wind speeds driving the production of sea-salt CCN was proposed (Latham and Smith, 1990). Initial studies of sea-salt aerosol found

Review of the current state of knowledge

that it dominated mass concentrations, rather than number, and were correlated to wind speed (Monahan, 1968; Blanchard, 1963). However, recent studies have proved that sea spray is also contributing to the number of small particle sizes, going down to even 15 nm in diameter (Cravigan et al., 2015; Ovadnevaite et al., 2014b).

2.3.1 Marine aerosol composition

Due to the nature of cloud droplet activation and the cloud-climate effect, size-dependent particle chemistry is important in cloud activation, therefore, differentiating the number-size distributions of different chemical constituents within the aerosol population is important for understanding their influence on clouds. It is widely accepted that the Aitken mode is dominated by SMA, namely nss-SO₄ (Quinn et al., 2000; Quinn et al., 1998; O'Dowd et al., 1997a). The accumulation mode number dominance can swing between SMA and PMA depending in most cases on wave-state dependent sea-salt contributions, which can be seen in the sea-salt mass concentration. For oceanic regions experiencing prolonged wind speeds exceeding 15 m s⁻¹, it is very likely that an accumulation mode would be fractionally dominated by PMA. Sea-salt is responsible for the majority of cloud nucleating particles and light scattering in the Southern Ocean (Murphy et al., 1998).

Experiments have attempted to isolate the SSA (namely sea-salt) modes from ambient number-size distributions, both using methods which assume a monomodal SSA size-distribution (Quinn et al., 2017; Modini et al., 2015) and also assuming a multi-modal size distribution (Fossum et al., 2018). Sea-salt itself is extremely wave-state dependent, and multiple versions of wind-speed related flux parameterisation exist for ambient fitted sea-salt aerosol and also lab generated sea-salt aerosol (Ovadnevaite et al., 2014b; G. de Leeuw et al., 2011; Clarke et al., 2006; Mårtensson et al., 2003; Salter et al., 2015). While lab generation often results in poor overlap between lab and ambient observations, lab measurements can test the theoretical sensitivity of certain parameters, such as temperature dependency. Many lab studies have found that increasing sea-surface temperature reduces SSA particle production, which is mainly accounted for by decreases in production of smaller sized particles, although larger sized particles are often seen to slightly increase in production (Mårtensson et al., 2003; Bowyer et al., 1990; Zábory et al., 2012; Sellegri et al., 2006). The order of magnitude of these changes differs widely, as well as the particle diameter which marks this change, which can be attributed to differences in methodology, the sea-salt production mechanism, and also dynamic or static sea-surface temperature change. For example, using sea-salt (Sigma Aldrich, S9883) water Salter et al. (2014) showed that increasing (static) temperatures result in large decreases in concentration of plunging-jet produced SSA particles with dry diameter

Review of the current state of knowledge

< 1 μm (from -1.3°C to 9°C) These lab studies (Mårtensson et al., 2003; Bowyer et al., 1990; Zábory et al., 2012; Sellegri et al., 2006; Salter et al., 2014) produce results which conflict with ambient measurements and resultant parameterisations which show the opposite temperature dependence of increasing number concentrations with increasing sea-surface temperature (Ovadnevaite et al., 2014b; Jaeglé et al., 2011). A recent lab investigation (Forestieri et al., 2018) into sea-salt number concentration dependence agrees with the monotonic dependence on sea-surface temperature (moderate increases in number concentration with temperature) observed in ambient studies. The same study also noted that seawater composition may play an equally large role in determining sea-salt number-concentration, which may be a partial cause of the discrepancies in the other laboratory studies as different seawater types were used. The composition of the seawater in terms of salinity and organic surfactant composition can affect the physical properties of bubble formation and bursting specifically as surfactants affect bubble stability (Garrett, 1967). Forestieri et al. (2018) experimented with four seawater compositions: NaCl water, reef seawater, filtered seawater, and filtered and autoclaved reef seawater. The study found that temperature trends were observed in the artificial seawater but that the real seawater had more complex and random temperature dependence, likely due to the some physical or chemical evolution or change in the surface-active organic compounds with time.

It has been shown in multiple studies that the distribution of SSA (or sea-salt) is not monomodal but having upwards of five modes (Salter et al., 2015; Ovadnevaite et al., 2014b; Fuentes et al., 2010b), and that this distribution can change depending on sea-surface temperature, surface turbulence, and seawater composition although the latter has the strongest effect on the number and distribution of the modes (Forestieri et al., 2018). Sea-surface temperature sensitivity increases with increasing size, and may have a larger impact on the fraction of SSA particles acting as CDNC than on the total SSA number (Forestieri et al., 2018). Changes to sea-salt number concentration and number-size distributions (accumulation mode) have been shown to affect modelled CDNC through the use of a cloud parcel model (O'Dowd et al., 1999a). Seawater salinity can also affect SSA generation, but as salinity does not vary greatly over the world's oceans this effect is lessened, except in areas of sea-ice melt or heavy rainfall, where an unmixed layer of fresh water could occur. Ocean circulation can also affect the composition of the surface water through upwelling and downwelling both caused by directional surface winds. Upwelling will result in rising deeper water leading to increased concentrations and production of organics while down-welling will result in sinking of the surface water, decreasing the concentration of organics (Smith and Konferenzen, 1995; Karp-Boss et al., 2004). Different SSA (or sea-salt) flux parameterisation take different dependencies into account, and a comparison of the major parameterisations can be seen in Figure 2.6. Do to the differing measurement conditions and possible changes in seawater

Review of the current state of knowledge

composition, it is difficult to determine which of any parametrisation is better. However, parameterisations which result in multiple SSA modes better represent ambient marine measurements.

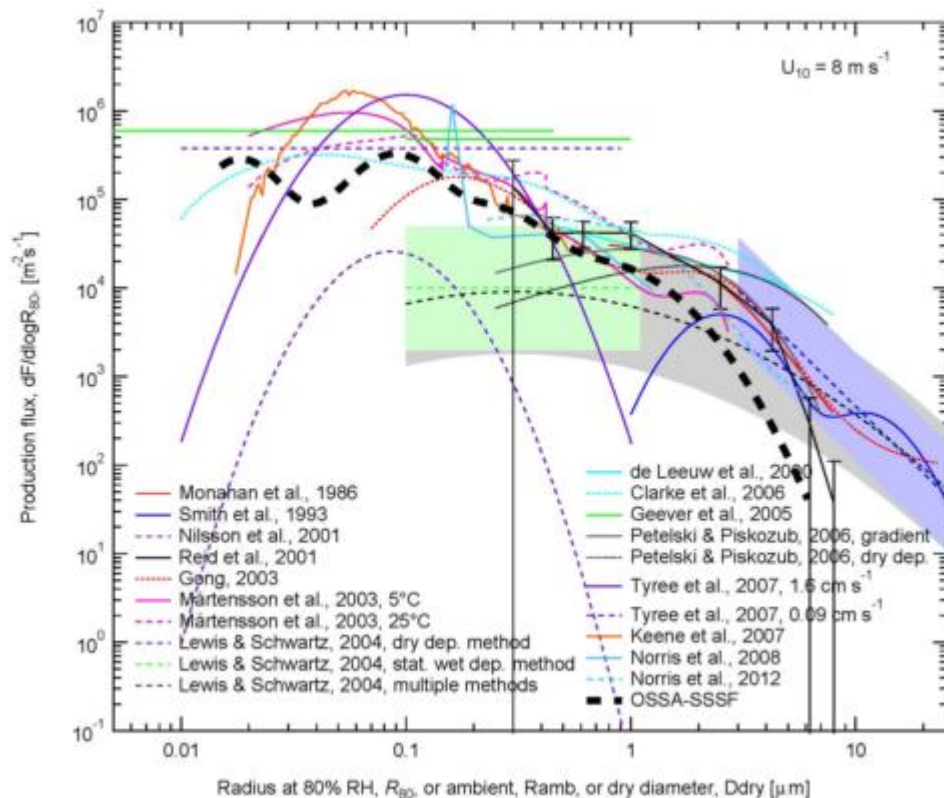


Figure 2.6. Reproduced from Ovadnevaite et al. (2014b), the graph shows a comparison of the sea spray aerosol source function derived in Ovadnevaite et al. (2014b) (OSSA-SSSF) with other SSSF (Mårtensson et al., 2003; Lewis and Schwartz, 2004; Clarke et al., 2006; Monahan et al., 1986; Smith et al., 1993; Nilsson et al., 2001; Gong, 2003; Leeuw et al., 2000; Reid et al., 2001; Geever et al., 2005; Tyree et al., 2007; Norris et al., 2008; Norris et al., 2012; Petelski and Piskozub, 2006; Keene et al., 2007), evaluated for wind speed $U_{10} = 8 \text{ m s}^{-1}$ (or $U_{22} = 8 \text{ m s}^{-1}$ for Geever et al. (2005)). Also shown are central values (curves) and associated uncertainty ranges (bands) from review of Lewis and Schwartz (2004), which denote subjective estimates by those investigators based on the statistical wet deposition method (green), the steady state deposition method (blue), and taking into account all available methods (grey); no estimate was provided for $R_{80} < 0.1 \text{ } \mu\text{m}$. Lower axis denotes radius at 80 % relative humidity, R_{80} , except for formulations of Nilsson et al. (2001), Mårtensson et al. (2003), and Clarke et al. (2006) which are in terms of dry particle diameter, D_{dry} , approximately equal to R_{80} and those of Geever et al. (2005), Petelski and Piskozub (2006) (dry deposition method), and Norris et al. (2008), which are in terms of ambient radius, R_{amb} . Formulations of Tyree et al. (2007) are for artificial seawater of salinity at the two specified bubble volume fluxes. Formulations of Nilsson et al. (2001) and Geever et al. (2005) of particle number production flux without size resolution are plotted arbitrarily as if the flux is independent of R_{amb} over the size ranges indicated to yield the measured number flux as an integral over that range. (Figure and caption modified from de Leeuw et al. (2011)).

Review of the current state of knowledge

Aerosol number concentrations and chemical fractions change with altitude, having hugely different concentrations and fractions above and below cloud. Typical sub-cloud concentrations range from 50-2,000 particles cm^{-3} and are affected both by meteorology and season. Aerosol surface fluxes and chemistry are also subject to seasonal sensitivity, where spring and summer generally bring higher concentrations of organo-sulphate and organic species, whereas winter brings more storms and higher concentrations of sea-salt (Figure 2.7). These seasonal trends can have large impacts on aerosol chemistry, ultimately impacting how the marine aerosol affects the regional and global climate.

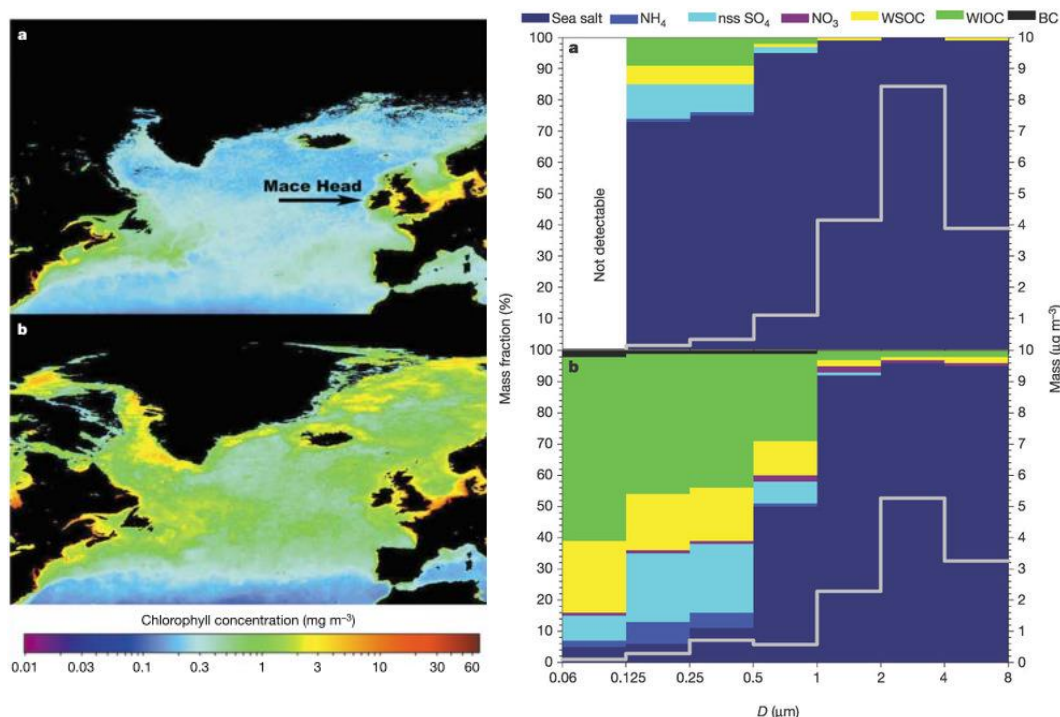


Figure 2.7. Chemical size breakdown and chlorophyll-a maps in winter (a) and summer (b), reproduced from O'Dowd et al. (2004). Organic matter at the sea-surface. SeaWiFS-derived seasonal average (5-year) sea-surface chlorophyll concentrations in winter (a) and spring (b), illustrating low biological activity in North Atlantic waters during winter and high activity in spring (courtesy of SeaWiFS Project, NASA/Goddard Space Flight Center and ORBIMAGE). The location of Mace Head is shown in a. Marine air masses arrive at Mace Head after at least 96 h transit over the ocean from the Arctic and northwest Atlantic. Chemical composition of marine aerosols. Shown are average size-segregated chemical compositions and absolute mass concentrations for North Atlantic marine aerosols sampled with a Berner Impactor, for low biological activity (a) and high biological activity (b) periods. The concentrations of WSOC, WIOC and BC are reported as mass of organic matter (see Cavalli et al. (2004) for a full discussion).

The relative reflectance or absorbance of incoming shortwave solar radiation by secondary marine aerosol (SMA) often relates to the fraction and distribution of OM

within the aerosol population. The regional and seasonal variations of organics in marine aerosol continues to be investigated. During high biological activity, sea spray particles are enriched in organic matter with the sea-salt fraction being significant at larger size, but OM dominating smaller particle mass (O'Dowd et al., 2004; O'Dowd and Smith, 1993; Murphy et al., 1998). O'Dowd et al. (2004) showed that organic fractions in marine aerosol are seasonally linked to marine biological blooms, often changing from a 15 % bloom contribution in winter to a 63 % contribution in summer. In the North East Atlantic, chlorophyll-*a* (Chl-*a*) has been positively correlated with OM (Rinaldi et al., 2013) given a sufficient time-lag is introduced. O'Dowd et al. (2015) later demonstrated that sea spray OM fraction (OM_{ss}) is variable and also dependent on biological activity. The same study showed that monthly Chl-*a* mean concentrations are significantly correlated to OM_{ss} ($r > 0.9$), which contrasts to a previous study (Quinn et al., 2014) where a simultaneous correlation between sea spray OM and Chl-*a* was not observed. A low correlation between simultaneous measurements was elucidated by O'Dowd et al. (2015) explaining that the high correlation coincides with the demise of the bloom, rather than the growth phase.

Further quantification of the relationship between plankton blooms and OM fractions in sea spray has been shown in the South Indian Ocean through direct measurement (Ceburnis et al., 2016), and also through the measured enhancement of the indirect effect by marine OM (McCoy et al., 2015). Ceburnis et al. (2016) showed that primary production yields particulate organic carbon (POM— carbon isotope ($\delta^{13}C$) light), which is distinct from dissolved organic carbon (carbon isotope heavy) in that the latter has undergone atmospheric aging and lacks oceanic variance. The study also concluded that the OM fraction in sea spray increases given turbulent surface water conditions in areas where primary production is high (e.g. Chl-*a* concentrations are high). McCoy et al. (2015) reported that modelled biogenic primary and secondary sources correlated well over time with changes in satellite derived CDNC in the Southern Ocean, estimating that biogenic sources increase the mean reflected solar radiation in summer (10 W m^{-2}). While the addition of CCN is reported as correlated to biological activity (Ovadnevaite et al., 2011a) and clearly impacts regional cloud coverage (Krüger et al., 2014; McCoy et al., 2015), the aerosol-cloud system remains extremely complex.

Marine aerosol is rarely chemically homogenous over all sizes, although some homogeneity can exist over the Aitken and accumulation mode size range. Ambient aerosol can be externally mixed, meaning that at a given size particles are chemically distinct from each other, or internally mixed, meaning that through secondary processing an aerosol of a given size is a mixture of chemical species (often a mixture of primary and secondary aerosol). A completely internally mixed aerosol population would have particles with the same composition (or agglomerate composition) regardless of size, such that every chemical species comprising the particles would be

Review of the current state of knowledge

found in equal proportions in every particle. A completely externally mixed population would have particles at similar size with completely different chemical constituents. In reality, sampled aerosol is a combination of internal or external mixtures (due to an abundance of primary and secondary aerosol sources) which varies with size dependence. Determining whether ambient aerosol is externally or internally mixed has been difficult to resolve. Lab studies (Prather et al., 2013) have shown that particles in clean marine conditions can be internally mixed (Figure 2.8), and measurements taken in the Arctic (Kirpes et al., 2017) and Southern Oceans (Gaston et al., 2018) have shown that internal mixtures are prominent when secondary aerosol concentrations are high. Both studies include measurements of polluted aerosol, which seems to react heterogeneously with SSA, reducing κ values. The mixing state of marine aerosol in pristine field conditions has been harder to ascertain, although it has been suggested that cloud-processed marine aerosol would always have some degree of internally mixed species (Murphy et al., 1998). Other laboratory studies have stipulated that different aerosol formation pathways (i.e. large and ultrafine bubble-bursting producing jet drop and film drop aerosol) of sub-micrometre SSA would result in externally mixed particles of different chemical composition (Wang et al., 2017). The mixing state of the aerosol matters because it affects how aerosols react as a population to activate into cloud droplets or be effective haze particles. As discussed previously, homogenous, low- κ aerosol populations will have similar critical supersaturations. As such, depression of the maximum cloud peak supersaturation through competitive activation over the same dry particle size will not occur, as is the case with non-homogenous sulphate sea-salt particle populations (O'Dowd et al., 1999b). The more aerosols available for condensation, the less water vapour available per particle. Scavenging of available water vapour occurs over time, starting in sub-saturated conditions. Larger and more hygroscopic particles (in accordance with their S_c dependent D_c) will absorb water vapour. Sea-salt, large highly hygroscopic marine primary particles, effectively reduce the peak cloud supersaturation as it selectively scavenges available water vapour prior to and during CCN activation. If, however, sea-salt is internally mixed with other chemical species homogeneously across the sizes, then the critical diameter of activation can be decreased, reducing the effects of the selective early activation.

One method of determining the mixing state of the aerosols is through single particle analysis, which has been deployed both in the lab and in the field (e.g. Kirpes et al. (2017); Prather et al. (2013)). The disadvantage of this method is that not every particle is sampled, and the analysis may not be representative of the air sample. Polluted marine systems in the Arctic have been shown to have internally mixed aerosols from persistent anthropogenic transported haze and may therefore suffer from reduced CCN activation efficiency compared with nascent SSA. Other methods to estimate the mixing state of aerosols have used size-resolved mass-spectrometry

Review of the current state of knowledge

to estimate the mixing, or CCN size-resolved analysis to determine the hygroscopicity of different aerosol sizes (Fossum et al., 2018).

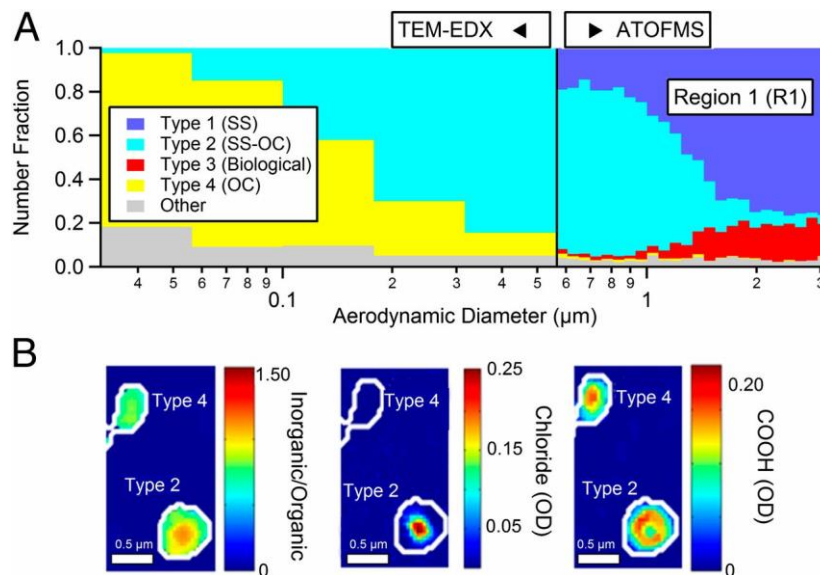


Figure 2.8. This graph shows external and internal mixture types of lab generated marine particles by size and mass fraction, reproduced from Prather et al. (2013). (A) Size-resolved chemical mixing state for R1 (see Prather et al. (2013) Fig. 2). Integration of two single particle analysis methods [TEM with energy-dispersive X-ray (EDX) analysis < 562 nm and ATOFMS > 562 nm] shows the existence of four major particle types. (B) STXM chemical spatial maps of the two most dominant submicrometre particle types (types 2 and 4) highlight the differences in the inorganic-to-organic ratios (Left), abundance of chloride (Centre), and carboxylates (Right).

Another large area of uncertainty within the field is the fraction of marine boundary layer (MBL) CCN which are produced from atmospheric entrainment, which usually refers to large scale movements of air from the free troposphere (FT) into the marine boundary layer. The composition of cloud droplets (especially at cloud top nearest the FT) alters the evaporation of droplets at cloud top, which is important for accurately representing cloud radiative properties. Sanchez et al. (2017) showed that disregarding the evaporation cycling processes of droplets around the edge of clouds can result in an overestimation of the short wave radiative flux at cloud top. Primary marine aerosol is usually within the MBL although transfer higher into the atmosphere can occur, with SSA being reasonably transported (by simulation) into the troposphere (Wise et al., 2012). Conversely, smaller sized particles from the FT can subside down into the boundary layer and mix with surface generated particles. In this way the FT is both a source and sink for MBL aerosol. Clarke et al. (1998), proposed that a significant source of MBL aerosol was from the subsidence of particles formed aloft by NPF processes in FT cloud outflow regions. Katoshevski et al. (1999) calculated that the contribution of particles from the FT to marine boundary layer were between 69-89 %, but that the MBL aerosol mass was

Review of the current state of knowledge

dominated by sea-salt particles (62-98 %). A study (Dadashazar et al., 2017) looking at the interface between the FT (above cloud) and boundary layer (below cloud) off the Californian coast showed that NPF was highest at the entrainment interface layer, consistent with findings from Clarke et al. (1998). The same study also showed that sub-cloud aerosol had overall lower particle concentrations when compared to the FT or the entrainment interface layer, but higher fractions of larger particle diameters. Additionally, thicker clouds coincided with the lowest concentrations of sub-cloud aerosol with particle diameters < 110 nm. During the Ace-2 Lagrangian studies, Hoell et al. (2000), studied the evolution of air masses in relation to boundary layer height. This study suggested that when gradients between the boundary-layer and FT form, on certain occasions with changes in boundary layer height, the FT can become a source or sink for MBL aerosol.

As the composition of FT aerosol can differ drastically from the marine boundary layer, with larger incidences of pollution aerosol, the results of processes in the entrainment layer has the potential to change aerosol-cloud interactions and affect interstitial aerosol populations within cloud through gradient concentration movements. However, the mixing of clean FT air into the boundary layer does not necessarily impact strongly on MBL cloud properties. While the contribution of small particles from the FT cannot be neglected in the MBL, the contribution to CDNC populations may be much lower. CDNC are not directly proportional to CCN concentrations and tend to be more related to accumulation mode CCN. FT particles are usually smaller and would impact less on CDNC. Evidence presented in O'Dowd et al. (2014) suggest that entrainment does not influence the concentration-based fluxes of marine aerosol. Through the use of chemical fingerprinting and isotope analysis, the non-marine aerosol components were isolated out and were not found to impact heavily on mass concentrations. The analysis of coupled cloud layer measurements *via* ground based sensing show correlation exists between number concentration fluxes of sub-cloud polluted CCN and cloud optical thickness (Preißler et al., 2016). The good agreement between marine boundary layer particle and remote-sensing measurements strengthens the idea that the larger submicron CCN in the sub-cloud layer have more to do with cloud droplet activation than mixing *via* entrainment of FT aerosol.

2.3.2 Pollution in the marine environment

The main tropospheric pollutants in the marine environment are ship related combustion (or other industrial activity related combustion), human related activity on islands, and long-range transport of continental pollutants. Black carbon (BC), a resultant particle of incomplete combustion, is ubiquitous to anthropogenic pollution

Review of the current state of knowledge

and can be used as a tracer for anthropogenic contamination (Wolff and Cachier, 1998; O'Dowd et al., 1993), and is also responsible for major direct solar radiation absorption (Ramanathan and Carmichael, 2008). In 2015, ship emissions were estimated to contribute a total of $5.3 \times 10^{10} - 8.0 \times 10^{10}$ g of BC (Comer et al., 2017) (which can be averaged over the Ocean's surface and 1 km marine boundary height to be $\sim 6 \times 10^{-3}$ ng m⁻³ s⁻¹). Aerosol mass spectrometry and photometry instrumentation is used to measure the tracers of this human activity in natural marine emissions.

In the context of climate-feedback systems and aerosol-cloud-interactions, the origin of aerosols must be highly constrained to differentiate between natural and polluted aerosol population properties. Due to the linear relationship found in the S. Pacific Ocean during the VAMOS Ocean Cloud Atmosphere Land Study (VOCALS) regional experiment between BC and organic matter (OM), Shank et al. (2012), proposed that BC concentrations are not effective in distinguishing natural marine aerosol from polluted aerosol. Therefore, the study proposed that OM measured in the North East Atlantic may also be anthropogenic in origin. This would have large implications for studies previously reporting on clean marine OM, such as Ovadnevaite et al. (2011a); Ovadnevaite et al. (2011b), and Cavalli et al. (2004) which used BC limits (in part) to distinguish clean marine from re-circulated polluted or continentally influenced air masses. However, O'Dowd et al. (2014), showed through a multi-component analysis, OM and BC measurements were not correlated when employing the established clean sector technique. The O'Dowd et al. (2014) study demonstrates that Mace Head research station (MHD) can be considered a reliable station for studying natural marine aerosol from the North East Atlantic.

Marine biological production is related to nutrient availability, and therefore somewhat dependent on the deposition of trace elements onto the sea surface. Continental transport of dust (iron) and anthropogenic aerosol (nitrogen) provides trace element deposition which can be used as nutrients fuelling phytoplankton blooms (Duce and Tindale, 1991). The transport of anthropogenic aerosol is associated to marine production of organics because it has been shown to increase the solubility of iron leading to easier uptake by biota (Baker et al., 2016; Baker and Croot, 2010), and also because many low latitude oceanic regions are nitrogen poor and the addition of this trace element has been shown to stimulate biological production (Duce et al., 2008; Jickells and Moore, 2015). Therefore, the influence of anthropogenic aerosol may influence the oceanic system and cause changes to measured marine aerosol by increasing or changing marine biological production in surface seawater, so accidental correlations between OM and BC (a tracer for anthropogenic transport) should not be discarded without consideration of regional air transport patterns.

While pollution itself is wide-spread and subject to global transport, the frequency of occurrence of high incident atmospheric pollution can be different depending on the ocean in question. The North Atlantic has been shown to be heavily influenced by anthropogenic sources during early winter (O'Dowd et al., 1993). When it comes to the high latitude marine regions, the Arctic marine region can be more heavily polluted than the Antarctic marine region. The Arctic region is affected by BC from short and long-range transport (Dorothy and James, 2005) due to the effects of strong late winter—early summer northward transport (Barrie, 1986) which results in a natural level of BC around 20 ng m^{-3} in the summer (Gogoi et al., 2016). However, median measurements of the North East Atlantic show $< 10 \text{ ng m}^{-3}$ for the summer months (unpublished data from Mace Head MAAP instrument measurements from the summer of 2017) which may indicate a severe change in BC mass concentrations in the North East Atlantic compared with the Arctic regions. The Antarctic marine region appears to be less influenced by pollution, somewhat owing to the lack of industrial activity in the Southern Hemisphere compared with the Northern Hemisphere and the Antarctic circulation. Marine BC measurements in the S. Ocean report BC mass concentration measurements (using a mixture of BC instruments) on the order of $\sim 1 \text{ ng m}^{-3}$ (Shank et al., 2012; Weller et al., 2013; Chylek et al., 2015; Wolff and Cachier, 1998).

As mentioned above, the anthropogenic influence differs for every Ocean, therefore, BC values typical of 'clean' or 'pristine' air masses must be established for every instrument and location. For example, Grigas et al. (2017) employed the use of frequency distributions for BC mass concentrations and looked at the lognormal modes to statistically assign pollution classifications. This method has also been implemented in this research.

2.3.3 Marine cloud condensation nuclei

Marine cloud condensation nuclei are a sub-group of marine aerosols, contextualised by the likelihood that they will nucleate into cloud droplets at varying supersaturations. Marine CCN are studied, in large part, to better predict marine CDNC. CDNC size distribution and chemistry is difficult to directly measure from the ground, whereas CCN are easily measured at the ground. CDNC measurements can be derived *via* satellite imagery or ground based laser optical measurements, but the source of the CDNC is hard to ascertain. Current studies are looking to elucidate the formation of cloud droplets from potential nuclei using top-down (satellite) and bottom-up (ground-based) measurements using modern experimental methods. However, many limitations, including the coupling state of the marine cloud layer, make these studies difficult to reconcile. The lack of closure between top-down and

Review of the current state of knowledge

bottom-up studies, emphasises the need for continued *in-situ* measurements of CCN.

Marine inorganics such as sea-salt and sulphate, being highly hygroscopic have relatively unchanging growth kinetics between the sub and supersaturated regimes. Marine CCN is often comprised of non-sea-salt sulphate (nss-SO₄), sea-salt, or some other combination of SMA potentially internally mixed with sea-salt. Generally, sea-salt CCN have the highest activation efficiency, with a CCN derived hygroscopicity parameter κ value of ~ 1.28 (calculated for $T = 298.15$ K, and a constant surface tension of pure water $\sigma = 72.75$ mJ m⁻²), although lower κ values are often used in models (e.g. 1.12 in Snider et al. (2017) and 1.16 in Burrows et al. (2018)). Sulfuric acid (H₂SO₄) also has a large activation efficiency, with κ values ranging from 0.7 calculated from the AIOMFAC model (see supplementary material from Ovadnevaite et al. (2017) to 0.9 from AIM (see Petters and Kreidenweis (2007)). Ammonium sulphate (AS, or (NH₄)₂SO₄) κ values also range between each model with values of 0.58 and 0.61 respectively (calculated for $T = 298.15$ K, and a constant surface tension of pure water $\sigma = 72.75$ mJ m⁻²). Various κ values are used in models to simulate nss-SO₄ aerosol, with recent model studies using 0.507 (Burrows et al., 2018), suggesting a suppression of activation efficiency from what is theoretically calculated for fully neutralised sulphate species. This may be effective for slightly polluted marine conditions where organic vapours may condense onto existing particles lowering hygroscopicity of already highly hygroscopic particles but is not ideal for clean conditions.

Summer biological activity means increased DMS-correlated CCN (Sanchez et al., 2018) and increased primary organic matter enrichment in sea spray aerosol (O'Dowd et al., 2015). Organic matter (OM) can have widely varying properties, often showing reduced hygroscopicity. Marine organics come in two major types, often referred to as water soluble or water insoluble organic carbon/matter (WSOC and WIOC respectively). WSOC has fairly hygroscopic properties, however, WIOC being more numerous in PMA than the latter (Facchini et al., 2008) (see also, Figure 2.7) is generally hydrophobic, but may have dichotomous effects in water uptake. It has been shown that OM in PMA in the North East Atlantic can have low growth factors in subsaturated conditions but show increased CCN activation efficiency in supersaturated conditions. The increased activation leads to an increase in CDNC of ~ 500 cm⁻³ in marine stratocumulus (Ovadnevaite et al., 2011a). These highly CCN active particles, thought to be marine hydrogels, seem to be biogenic species dependent. Laboratory studies (Dawson et al., 2016) observed a hydrogel proxy leading to little enhancement of sea-salt activation but found that the salt significantly increased the activation potential of the OM. Other mesocosm experiments found negligible change in CCN concentration with bloom activity (Schwier et al., 2017; Collins et al., 2016).

Review of the current state of knowledge

There is evidence to suggest that when small secondary marine particles (40 nm in dry mobility diameter) are ~ 55 % OM (or 20 % depending on the type of OM) their CCN activation efficiency will significantly increase (Ovadnevaite et al., 2017). It is unclear whether all species of OM might also display some of these properties when coating other particles. Other studies not restricted to clean marine conditions have shown that aerosol influenced by coastal pollution (anthropogenic OM) can have decreased CCN κ values (Gaston et al., 2018). While there are chemical differences between anthropogenic and biogenic OM, these studies differ widely in their BC mass concentrations with the former containing aerosol with $< 5 \text{ ng m}^{-3}$ and the latter having upwards of 300 ng m^{-3} for oceanic air masses, suggesting that increased activation efficiency from OM may only be effective when BC concentrations are significantly low enough to suggest similarly low values of anthropogenic OM. Conversely, high concentrations of anthropogenic pollution leads to increased particle concentrations which should result in increases in CDNC (Ramanathan et al., 2005; Seinfeld, 2008; Twomey, 1974). Additionally, a study off of the North Pacific coast seems to suggest that cloud processing of carbonaceous material increases their hygroscopicity (Asa-Awuku et al., 2015), so the age of the anthropogenic OM must also be considered.

2.4 Ice nucleating particles

Thus far, the activation potential of liquid phase cloud droplets (CCN activation potential) in the marine environment has been discussed, however isolating effective INP in warm ($> -30^\circ\text{C}$) solid phase activation is incredibly important for accurately predicting the albedo effect of clouds. Cloud glaciation can alter the radiative scattering effects of clouds, and also the lifetime of clouds. Low-level liquid cloud scattering reflects incoming shortwave radiation while allowing outgoing long-wave radiation. However, low-level clouds can also be mixed-phase (composed of supercooled liquid and ice) when temperatures are sufficiently low ($< 0^\circ\text{C}$). The scattering effect of ice crystals differs from that of spherical droplets (described by the Mie solution to Maxwell's equations) and are incredibly dependent on crystal morphology making them hard to model as many meteorological-dependent morphologies exist (Figure 2.9). If models assume low-level mixed-phase clouds are composed of liquid droplets over ice crystals the results show a serious misprediction of cloud albedo (Sun and Shine, 1994). The cloud lifetime can also be affected through a "glaciation indirect effect" for which glaciation induces precipitation through the ice phase, offsetting the indirect effect of liquid clouds (Lohmann, 2002). It should be noted that INP concentrations can be extremely low and still cause a cloud to transition from liquid to ice phase, given the correct temperature regime, due to large crystal fracturing and the process of riming

Review of the current state of knowledge

(Hallett and Mossop, 1974; Sun et al., 2010). Observed precipitation rates can be explained by a concentration of 1 INP particle cm^{-3} at -10°C (Zeng et al., 2009). It should be noted that pollution aerosol does not contribute significantly to INP concentrations (published data from the *BACCHUS* collaborative project, summarised in deliverable D5.9 (Lohmann et al., 2018)) .

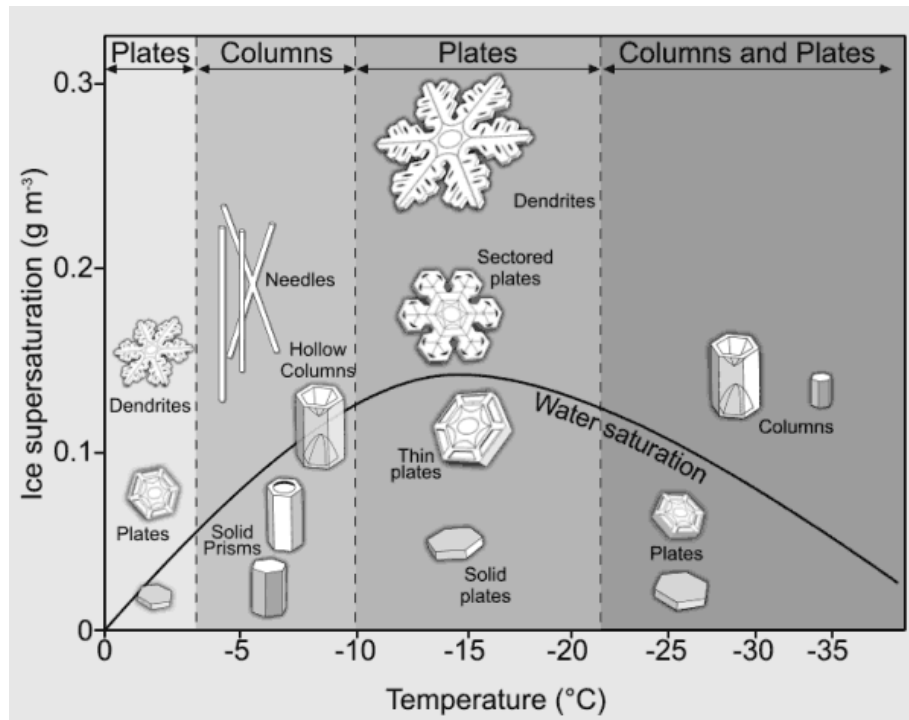


Figure 2.9. Ice crystal morphology as a function of ice supersaturation and ambient temperature, reproduced from the University of Manchester, Centre for Atmospheric Science, Website (Emersic).

A review study on INP in 2012 (Murray et al., 2012), concluded that mineral dust sources made up the majority of INP at temperatures below -15°C , and that above this temperature threshold, only biological material could serve as effective INP. A satellite observation study (Choi et al., 2010), found an inverse relationship with the fraction of supercooled droplets (at -20°C) to lofted dust concentrations, indicating that dust may be an effective glaciation inducer. Atkinson and Whale (2013), showed that feldspar minerals were the most important component of dust particles in warm temperature ($< -15^\circ\text{C}$) ice nucleation. Another study showed that atmospheric ageing (exposure to O_3) could also effectively increase the INP activation potential of mineral particles while reducing the ice nucleation of dust in the deposition mode (Kanji et al., 2013), suggesting more complicated ice nucleation patterns for atmospherically aged ambient particles.

Review of the current state of knowledge

Marine INP are less numerous than continental INP. McCluskey et al. (2018a) showed that SSA has a factor of 1,000 less ice nucleating sites by surface area than mineral dust. However, marine phytoplankton exudates and other OM are likely sources of warm-temperature INP (Wilson et al., 2015), occurring in the lower stratosphere, and with a relative lack of dust in the environment, may be a likely catalyst for INP formation in mixed phase and ice phase clouds. INP exist in the marine environment on the order $< 1 \times 10^{-4} \text{ cm}^{-3}$ ($< 0.1 \text{ L}^{-1}$) at $-15 \text{ }^\circ\text{C}$ (DeMott et al., 2016), so detection can be an issue. Yet low-level mixed phase clouds persist over the N. Atlantic where boundary layer temperatures can be anywhere from -20°C to slightly above freezing. Studies also show that biological production can increase the number concentration of INPs by up to a factor of 10 at warmer temperatures ($-15 < T < -10 \text{ }^\circ\text{C}$). INP concentrations show sensitivity to a range of sub-freezing temperatures ($-10 \text{ }^\circ\text{C}$) and seawater composition which suggests multiple temperature-dependent INP element types naturally occur (DeMott et al., 2016).

INP OM can be found as dissolved organic carbon (DOC) or particulate (POC) (McCluskey et al., 2018a), but determining which is responsible for warm ice nucleation has been hard to isolate. POC is linked seasonally with primary production and the decay cycle of phytoplankton blooms, comprising of heat labile molecules and microbes. Long term marine INP measurement studies are lacking in the literature, providing little information on INP seasonality in the marine environment. Long-term marine sampling measurements (and subsequent heat treatment analysis) would be a possible way to isolate the seasonal DOC (molecules that are not heat labile) and POC ice-nucleating fraction. Also lacking, are size dependent INP measurements for the marine environment, although studies of continental INP with size resolution have shown that $63 \pm 21 \%$ of particles, active at $-25 \text{ }^\circ\text{C}$, are $> 1 \text{ } \mu\text{m}$ in aerodynamic diameter, with $42 \pm 17 \%$ active at $> 2.5 \text{ } \mu\text{m}$ (Mason et al., 2016), demonstrating a proclivity of larger sized continental INP to be more active. This would be consistent with known continental activation regimes and does not necessarily reflect the marine INP properties, especially since it has been shown that fragments of, rather than whole bacteria (a likely marine INP), are more practical INP in chamber experiments (Suski et al., 2018).

3. Methods and measurements

The focus of this section is to outline the aerosol measurement system and data analysis methods employed in acquiring and characterising the sample data studied in this dissertation. It also details several other systems which were run in parallel providing further data to aid in a comprehensive analysis. Current state of the art aerosol measurements can be performed a few ways and with a number of techniques thanks to an array of systems. The following sub-sections describe the specific instrumentation, acquisitions settings, and techniques used to gather the main physical parameters of interest, including aerosol particle density, size distribution, and chemical composition.

3.1 Sampling locations

Data used in the main findings of this study come from field measurements from two sampling sites, the Southern Ocean (PEGASO Cruise) and the North East Atlantic (Mace Head Research Station). Both sites are described in detail in the following sections. Common instrumentation and analysis techniques from each campaign or site location can be found in Section 3.2-3.5. Specific instrumentation or changes in techniques may be found in the respective results chapter.

3.1.1 PEGASO Cruise, Southern Ocean (Jan 2nd - Feb 12th, 2015)

The first measurement location, the Southern Ocean, was a ship cruise path. The PEGASO (Plankton-derived Emissions of trace Gases and Aerosols in the Southern Ocean) cruise took place on-board the research vessel, *Hesperides*, which traversed the Scotia Sea and Drake Passage region of the S. Ocean, between the tip of S. America and the Antarctic Peninsula (Figure 3.1). The cruise was organised by the Barcelona Institute of Marine Sciences, and joined by the National University of Ireland Galway, in an effort to elucidate regional aerosol processes through the investigation of biological, physical, and chemical components of the Antarctic marine environment. The main findings of the campaign are reported by Dall'Osto et al. (2017). The portion of the cruise used in this research, whose path can be seen in Figure 3.1, took place between Jan 2nd and Feb 12th, 2015, departing from Ushuaia and returning to the same city. During the cruise standard meteorological parameters were monitored and recorded and aerosol sampling of nascent aerosol was run continuously with brief bubble-tank experimentation interrupting ambient sampling throughout. Ambient aerosol measurements were taken from a laminar

Methods and measurements

flow aerosol-dedicated sampling duct, 9 m in length and 1" outer diameter, with a $PM_{2.5}$ cut-off at a flow rate of 5 L min^{-1} , where overall residence time of particles in the main duct was 40 seconds prior to sampling by instruments. Instrumentation included a high-resolution time-of-flight aerosol mass spectrometer (HR-ToF-AMS) from Aerodyne Research Inc., a TSI model 3080 scanning-mobility particle sizer (SMPS) with TSI model 3010 condensation particle counter (CPC, flow 1 L min^{-1} , range $0.01\text{--}0.5 \mu\text{m}$), a single particle soot photometer (SP2) commercially available from Droplet Measurement Technologies, Inc. (DMT), and the continuous-flow streamwise thermal-gradient CCN counter (CCNC) commercially available from DMT (Roberts and Nenes, 2005; Rose et al., 2008). During tank experimentation, the same instrumentation set-up was employed, however, the main duct was replaced by a duct connected to the tank chamber. The chamber itself held sea-ice samples (melted) mixed with ocean sampled water, which was aerosolised via waterfall/plunging jet. The same experimental tank set-up can be found described in Schwier et al. (2015). The tank was run with zero air for 60 minutes prior to starting the jet. Ocean water collected for the experiments was taken with a Conductivity, Temperature, and pressure of seawater (Depth) instrument (CTD) from beside the cruise ship at four metres depth.

The cruise encountered three major air mass types, maritime polar (*mP*), continental AntArctic (*cAA*), and maritime tropical (*mT*). Graphical depictions and descriptions of the encountered air masses can be found in Chapter 5.

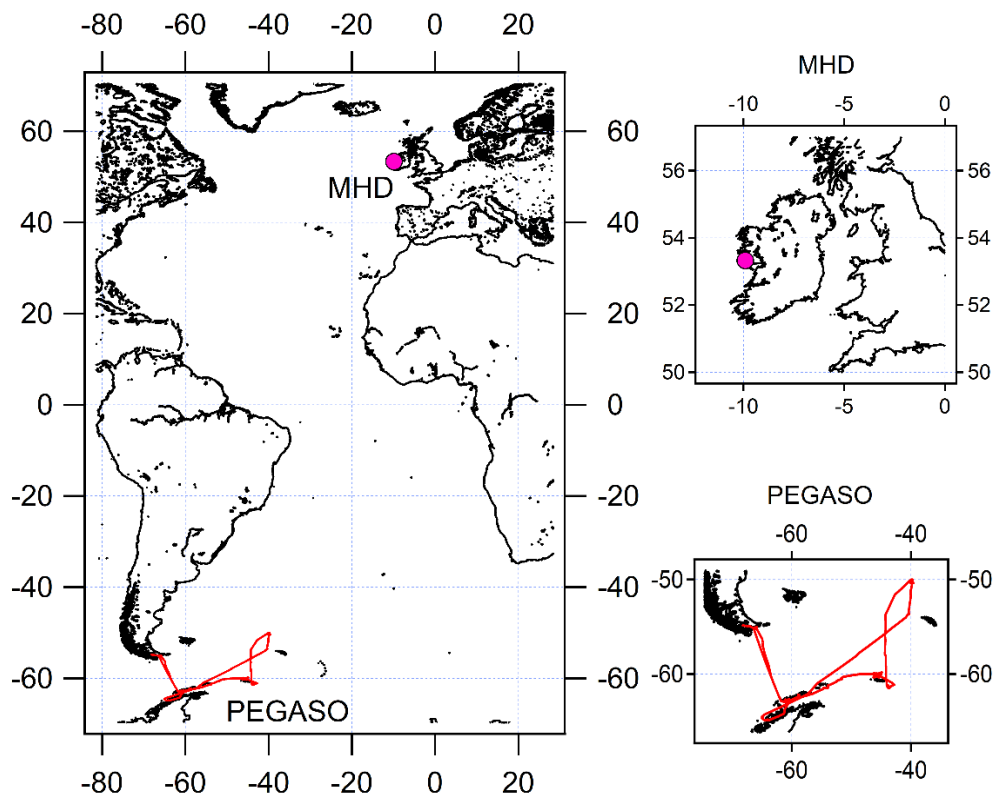


Figure 3.1. Sampling locations overlaid on a partial world map. The PEGASO cruise path is marked with the red line, and MHD is marked on the map with a pink circle. Both sites are shown in higher resolution on the right side of the graph.

3.1.2 Mace Head Atmospheric Research Station, North East Atlantic

The second measurement location, the Mace Head atmospheric research station (MHD), is located at 53.3253° N, 9.9044° W, on the west coast of Ireland. The MHD facility, shown in Figure 3.1, is a continual monitoring aerosol lab exposed to marine aerosol flow from the North Atlantic and continental aerosol flow from Ireland and Europe. Further discussion of air masses encountered at MHD can be found in Chapter 4. Samples are taken from two main community ducts which pull air from a 10 m tower (~ 20 m above mean sea level). One duct is strictly for non-coarse mode (NCM duct) measurements and is 10 cm in diameter made of stainless steel with a nominal flow of ~ 150 L min^{-1} , allowing for isokinetic sampling to several instruments simultaneously *via* feeds off the NCM duct. The flow in this NCM duct is provided by a blower and maintained using a control valve during regular flow checks. The other duct, suitable for coarse measurements (CM duct), is similar in diameter but made from aluminium and hooked up to a vacuum rather than blower pump.

Methods and measurements

Aerosol sampling at MHD is classified by sector criteria. Sampled aerosol is considered marine when 'clean' sector criteria are met. Sampled aerosol not meeting these criteria fall into the 'all' or 'polluted' sector category. The criteria for clean sector includes a wind direction (WD) between 190°-300° relative to magnetic North, wind speeds (WS) $> 0.5 \text{ m s}^{-1}$, and black carbon (BC) mass concentrations $< 15 \text{ ng m}^{-3}$ as measured by a model 5012 multi-angle absorption photometer (MAAP, Thermo Fisher Scientific Inc., Waltham, MA) described in more detail in Section 3.4. Previous studies at MHD have clean sector criterion which rely on total particle concentrations $< 700 \text{ cm}^{-3}$ in conjunction with BC mass concentrations $< 50 \text{ ng m}^{-3}$ (Rinaldi et al., 2010; Rinaldi et al., 2009). Other studies have relied on a three step process of (1) checking that BC mass concentrations remained at marine ambient levels, (2) air mass trajectories were marine in origin, and (3) carbon monoxide concentrations remained consistent with the ambient marine background and showed no influence of biomass burning (O'Dowd et al., 2004; Cavalli et al., 2004). However, later analysis of MHD data confirmed that the criteria of WD, WS, and BC mass concentration were enough to ensure marine conditions (Grigas et al., 2017; O'Dowd et al., 2014). This criterion in conjunction with the use of air mass trajectory analysis, discussed in Section 3.5, is used in this study to determine clean marine conditions at MHD. Additionally, clean sector aerosol sampled at MHD does not experience major coastal effects, outside of an enhancement of the number concentration of nucleation mode particles, such that clean sector marine air can be taken as representative of the remote North East Atlantic (O'Dowd et al., 2014; Rinaldi et al., 2009).

Samples meeting 'all' and 'polluted' sector criteria have also been collected from MHD. The all sector category is a blanket statement for when no criteria was used and aerosol was sampled indiscriminately. The polluted criterion is met when BC mass concentrations are $> 50 \text{ ng m}^{-3}$, however an additional continental criterion can be added limiting the WD to between 45°-135°. Filter sampling of the sectors can be set-up by sector-controlled pump systems. The MHD Clean Sector Sampler (described in Rinaldi et al. (2010)) uses a 0 and 5V logic signal to control the power to a pump when preprogrammed sector criteria are met dictating when aerosol should be sampled.

3.2 Supporting instrumentation

3.2.1 Condensation particle counter

Aerosol particle counting can be realised in the micron range quite effectively using optical probe techniques. Aerosol particle sizes in the sub-micron range, however, lie below the detection limit of most optical measurement systems and in these

Methods and measurements

instances condensation particle counter (CPC) techniques are commonly employed. A CPC operates by condensing vapours onto the particles passing through the instrument. The condensation process grows these particles to droplets of large enough size to be detected by an optical particle counter. Condensation activation must happen on all particles of sizes within its operating limits. The laser-based optical counter relies on the scatter of light from the focussed beam as particles pass through it to count the density of particles per volume of air. Butanol based CPCs are employed for the data presented here, although primarily a TSI model 3010 and 3772 were used in conjunction with other instrumentation. These CPCs operate at a flow rate of 1.0 L min^{-1} and have a lower detection limit of 10 nm (particle diameters), and have an upper count limit of $10^4 \text{ particles cm}^{-3}$ (model 3010) or slightly higher (model 3772). The 50 % cut-off diameter is 10 nm, however, referring to Figure 3.2 (the counting efficiency curve for the 3772 system as provided by TSI (TSI, 2014)), counting losses can occur up to 30 nm particle diameter that can be corrected for. Butanol is ideal for condensation because of its high volatility but is relatively benign from a toxicity standpoint, relative to other volatiles. During periods of the study, inter-comparisons were regularly performed between units at MHD, where each unit must be within 10 % of the average measurements to pass. The aerosol distribution for smaller particles (2 – 20 nm) are counted *via* an ultrafine CPC (model 3025 or 3776) in conjunction with a mobility sizer, however as Nano-SMPS data was not widely used in this dissertation, these CPCs will not be described in detail.

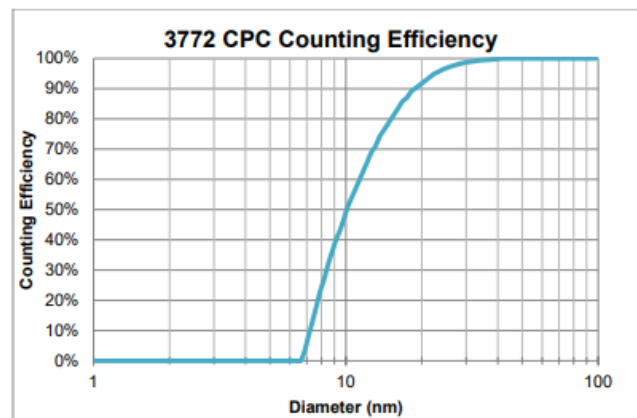


Figure 3.2. Counting efficiency curve of 3772 TSI CPC, reproduced from the *FUNDAMENTALS OF CONDENSATION PARTICLE COUNTERS (CPC) AND SCANNING MOBILITY PARTICLE SIZER™ (SMPS™) SPECTROMETERS* literature provided by TSI on their website http://www.tsi.com/uploadedFiles/Site_Root/Products/Literature/Application_Notes/Review_on_CPC_and_SMPS_CPC-003-US-web.pdf?id=32305 (TSI, 2014).

3.2.2 Particle sizing by electrical mobility diameter

In this dissertation, aerosol number density measured from the CPCs are used in conjunction with differential mobility analysers (DMA) to measure the size-resolved aerosol concentration. The DMA operates by employing a user controlled electrostatic field applied to the charged aerosol sample as it is injected into a laminar flow along the length of the DMA column, as shown in Figure 3.3. A high voltage central rod in the middle of the flow creates an electric field and certain particles of a distinct electrical-mobility move through an inlet opening. Particles of smaller electrical-mobility are not curved fast enough into the inlet and particles which have excessively large electrical-mobility move too quickly towards the rod (Figure 3.3). Particle sizing is dictated by the DMA transfer function which predicts the range of dry particle sizes (by electrical-mobility) allowed to pass through the DMA by each set voltage. This is based on the ratio between the sample and sheath air flow. The transfer function is triangular, centred at mobility

$$Z_p^* = \frac{Q_{sh} \ln\left(\frac{r_o}{r_i}\right)}{2\pi LV} \quad (1)$$

With full width at half max height, such that,

$$\Delta Z_p = Z_p^* \frac{Q_a}{Q_{sh}} \quad (2)$$

Where Q_{sh} is the sheath flow rate, Q_a is the sample flow rate, r_o , r_i , and L is the outer and inner radius and length of the DMA classifier aerosol chamber, and V is the applied rod voltage (Knutson and Whitby, 1975). In general operation, the ratio of flows used to control the full width of the transfer function is typically set at $Q_a/Q_{sh} \approx 0.1$, for the DMA system at MHD. This transfer function applies for fixed voltage DMA use, like that used in conjunction with the cloud condensation nuclei counters described in Section 3.3.3. Scanning voltage DMA uses, such as for a scanning mobility particle sizer (SMPS), need some correction because the scanning DMA transfer function for the SMPS does not have a nicely fixed shape like that of the static voltage transfer function (which is used to size segregate CCN measurements discussed in Section 3.3.3). This results in retrieved particle size and concentration errors which are less pronounced for ambient aerosol with a wide particle size distribution, although the errors can be reduced with increased time per scan (Collins et al., 2004). The DMA transfer function produces a spread of particles sizes about the target size for a given DMA high-voltage-drive value, as dictated by the ratio of air flows. Increasing the sheath to sample flow ratio of the DMA can decrease the spread of the particles which enter the so called monodisperse sample outlet.

Methods and measurements

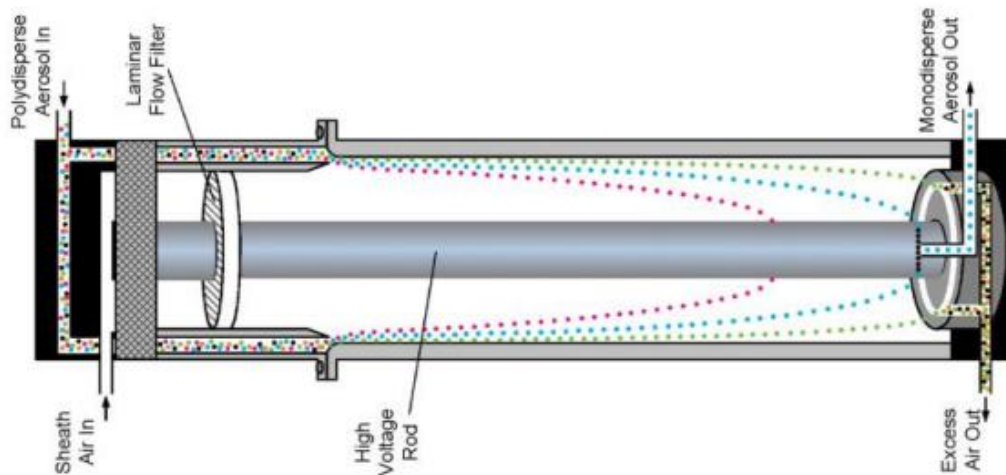


Figure 3.3. Schematic of aerosol flow through a DMA, reproduced from the *FUNDAMENTALS OF CONDENSATION PARTICLE COUNTERS (CPC) AND SCANNING MOBILITY PARTICLE SIZER™ (SMPS™) SPECTROMETERS* literature provided by TSI on their website http://www.tsi.com/uploadedFiles/Site_Root/Products/Literature/Application_Notes/Review_on_CPC_and_SMPS_CPC-003-US-web.pdf?id=32305 (TSI, 2014).

Mobility diameter is based on a particle's aerodynamic movement and the charge of the particle. A neutraliser, also known as a bipolar charger (Kr-89, TSI model 3077A, with radioactivity of 370 MBq which reduces with age, rated for a flow up to 5 L min⁻¹) is placed before the sample inlet to the DMA. The radioactive (beta) source emits ionisation radiation which changes the charges of the aerosol passing through the charger and results in an assortment of both negative and positive ions with differing charge magnitudes. The residence time through the charger (and associated plumbing) is sufficient for an equilibrium charge state of the particles to be reached. The equilibrium charge state is effectively grouped around a charge neutral state, although singly, doubly and triply charged particles persist in significant fractions. The fraction of equilibrium multiply charged particles (positive and negative) are well described by the Fuchs stationary-state-charge distribution (Fuchs, 1963). Due to both the fraction of multiply charged particles and the retrieved particle size errors from the transfer function, particles with a range of electrical-mobility may pass through the DMA. This results in concentration errors, in which more particles are counted than exist at that electrical-mobility size, or conversely fewer, where particles of that electrical-mobility size did not get through due to multiple charging. Therefore, charge corrections are automatically applied in certain instrument programming (e.g. SMPS systems) or are made during data processing (e.g. for the systems described in Section 3.3.1 & 3.3.3) for particles sampled through the DMA, and are described in Wiedensohler (1988); Fuchs (1963). The Fuchs stationary-state-charge distribution (Fuchs, 1963) shows only ~ 1-20 % of particles being singly charged, where decreasing particle size goes along with decreasing fractions of singly

Methods and measurements

charged particles. Additionally, lower concentrations (C) result in higher counting uncertainty (σ_c), with the relationship,

$$\sigma_c = 100 \% * \frac{1}{\sqrt{C}} \quad (3)$$

The charge corrections must be considered for nebulised particles or ambient particles with critical or ambient modal diameters $d_m > 0.1 \mu\text{m}$ (Rose et al., 2008; Petters et al., 2007). Ambient samples that are not exposed to bipolar chargers, having longer atmospheric lifetimes, often have less diverse charging states than newly generated aerosol, so these corrections often make little difference to the counted aerosol.

The number-size distributions of submicrometre aerosol (dry mobility diameters (d_m) >20 nm) are ultimately found using a scanning mobility particle sizer (SMPS). This combines the DMA and CPC systems to electrically size and count the sampled particles. The custom built SMPS used in this study used a TSI model 3081 DMA, and model 3010 CPC. The SMPS has an aerosol flow rate of 1 L min^{-1} . The number size distributions of aerosol with $d_m < 20$ nm are measured with a TSI Nano-SMPS with a model 3085 DMA and model 3025 ultrafine-CPC, using an aerosol sample flow of 1.5 L min^{-1} . The SMPS instruments utilise DMA voltage up and down scanning to establish the particle size concentration of the aerosol. The SMPS uses equally log-spaced bins ($\log\Delta d_m \approx 0.0156$) to filter the relative concentration of the aerosol from d_m of 19.7 – 502 nm. The Nano-SMPS employs a similar technique, but for a smaller d_m of 3 – 20 nm.

3.2.3 Aerosol Mass Spectrometer

The chemical composition of measured (non-refractory) aerosol was determined using the Aerodyne High Resolution Time of Flight Aerosol Mass Spectrometer (HR-ToF-AMS, or AMS, Aerodyne Research Inc., Billerica, MA). The instrument which is described in DeCarlo et al.(2006), is capable of retrieving size-resolved chemical composition. The AMS has a $1 \mu\text{m}$ aerodynamic vacuum diameter (d_{va}) 50 % cut-off which can be converted to an equivalent mobility diameter (DeCarlo et al., 2004) of 577 nm, as $d_m = d_{va} / (X_{AMS} \cdot \rho_{ss})$, where X_{AMS} is an AMS related shape factor = 0.8, and ρ_{ss} is the density of NaCl (a proxy for sea-salt) = 2.165 g cm^{-3} . HR-ToF-AMS ammonium nitrate calibrations were performed routinely following the methods described by Jimenez et al.(2003) and Allan et al.(2003). All measurements mentioned here were performed with a time resolution of 5 minutes, unless otherwise specified, with a vaporizer temperature of about $600 \text{ }^\circ\text{C}$. The composition-dependent collection efficiency, which refers to the fraction of dry particles bouncing

Methods and measurements

off of the AMS vaporiser relative to wet particles sticking to and being vaporised by it (Middlebrook et al., 2012), was applied for the measurement periods discussed in this study. Sea-salt concentrations were measured following the method described in Ovadnevaite et al. (2012). Briefly, sea-salt mass concentrations were determined by using the $^{23}\text{Na}^{35}\text{Cl}^+$ ion fragment as a signature for sea-salt and scaling by a factor of 51. To prevent excess thermal ionisation of Na^+ , which could disrupt the accuracy of the measurement, tuning of the instruments voltage bias (increase of 0.1-0.2 V) is necessary. This method, is yet the most robust for AMS sea-salt measurements, although it maintains a 20 % sea-salt measurement uncertainty, however, care should be taken in polluted environments where Cl displacement by nitric or sulfuric acid is likely. The scaling factor applied to the $^{23}\text{Na}^{35}\text{Cl}^+$ would underestimate the total sea-salt mass as it would not extend to this pollution processed sea-salt. However, off-line measurements using standard ion chromatography methods, confirmed that the AMS correlated to off-line measurements (correlation coefficient, r , = 0.93 and r^2 = 0.87) perhaps in part because Cl replacement does not seem to occur heavily in the North East Atlantic.

3.3 Cloud condensation nuclei counter

CCN are measured using the Continuous-Flow Streamwise Thermal-Gradient Cloud Condensation Nuclei Chamber (CCNC). The design was proposed by Roberts and Nenes (2005) to enhance cloud condensation nuclei (CCN) measurements by taking a direct count of the CCN number concentration in sampled air at a given supersaturation, by passing sample aerosol through a column chamber. The chamber, through temperature control, keeps a constant supersaturation through its centreline promoting activation of any CCN which have a critical supersaturation (S_c) equal to or lower than the set chamber supersaturation as they pass along the length of the column, these are then detected by an optical particle counter (OPC) (Figure 3.4). Without condensation, particles do not grow to a sufficient size to be detected by the OPC, and these particles pass through the CCN uncounted. The OPC uses a diode laser with a wavelength of 660 nm as the light source, counting a sizing range for activated particles of 0.75 to 10 μm (Droplet-Measurement-Technologies, 2012). The OPC uses 20 sizing bins supposedly to allow for more information about particle growth, although recent MHD experiments indicate that the sensitivity of the OPC is not sufficient to use as a measure of relative droplet growth between different chemical species of equal d_m . The theory of operation is discussed in detail by Roberts and Nenes (2005) and relies on the concept that the diffusion of water vapour is faster than the diffusion of heat. As sample aerosol passes through the centreline of the column, a supersaturated condition is met, as controlled by the temperature difference between the top and bottom of the column. Since the

Methods and measurements

column temperature is controlled so that $T3 > T2 > T1$ (see Figure 3.4), at a point C in the centreline, the actual partial pressure of water vapour is equal to the actual partial pressure at point B on the column wall. However, point C is at a lower temperature corresponding closer to point A on the column wall (see Figure 3.4). This is essentially allowing water vapour to travel from warmer conditions to colder ones and become supersaturated and condense onto the sample aerosol. This principle of operation includes the necessity for all points on the wetted inner column wall to be fully saturated. In operation, proper use of distilled or deionised water is needed to avoid possible mineral or surfactant deposition on the column wall. Improper storage of the instrument through incomplete drying, or exposure to air, can result in the crumbling of the inner column paper. Regular calibration is required to make sure that the instrument is operating to reach the expected supersaturation.

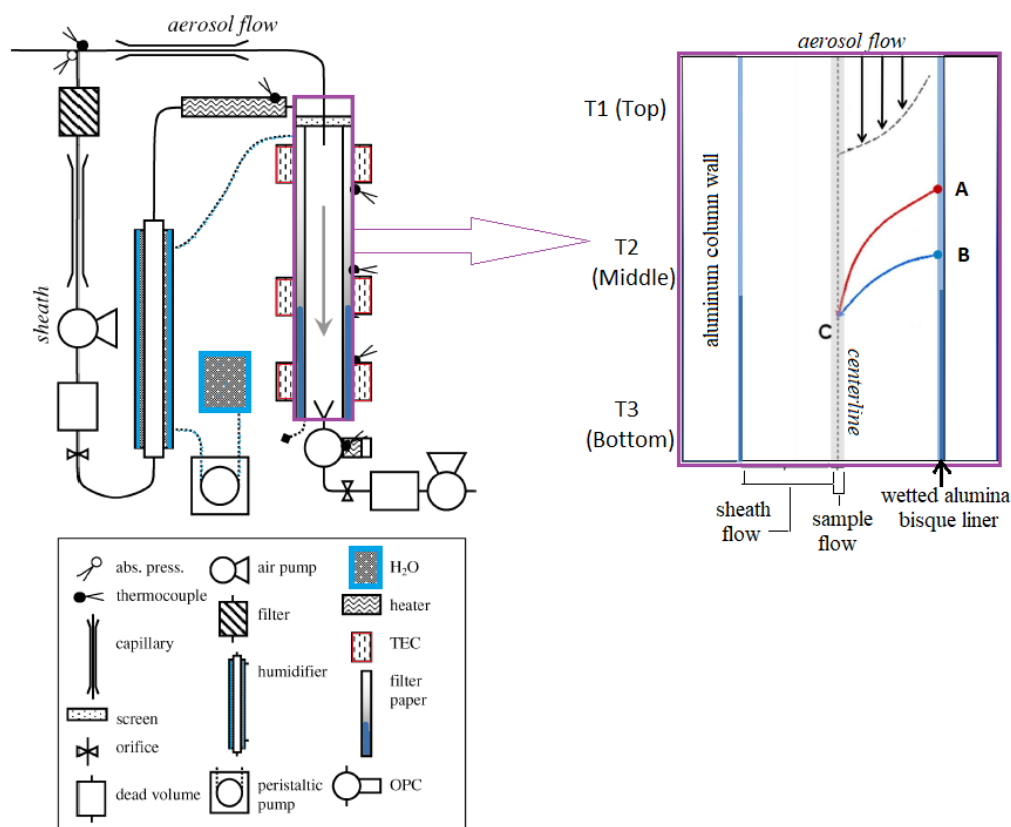


Figure 3.4. A diagram of airflow through the CCNC instrument adapted from Roberts and Nenes (2005) and the basic theory of column centreline supersaturation adapted from the DMT Inc. Cloud Condensation Nuclei (CCN) Counter Manual for Single-Column CCNs; DOC-0086 Revision I-2.

Studies have addressed CCNC experimental accuracy through the use of post-collection corrections (Rose et al., 2008; Lance et al., 2006) limiting error in the CCN

Methods and measurements

instrument measurement accuracy to only ± 1 % between different lab runs and ± 5 % between field-runs. Attempts to universalize the theoretical values and parameterisations (Lance et al., 2006; Petters and Kreidenweis, 2007), of critical supersaturation per particle type, used in calibration, have also been studied. However, different approaches in activation modelling and thermodynamic parameterisations have been shown to incur deviations in results as high as 25 % for $(\text{NH}_4)_2\text{SO}_4$, and 12 % for NaCl condensation nuclei, (which are two of the most commonly used calibration solutions) (Rose et al., 2008). These deviations are thought to be due to differences in the representation of the water activity of the aqueous salt solutions. Therefore, all relevant parameters relating to water activity modelling used for calibration or comparison, along with the relevant methods must be cited clearly.

3.3.1 Calibration

In this work, calibrations were performed regularly during intensive month-long campaigns, once at the beginning and end of the campaign. The calibration was performed using the set-up described in Rose et al. (2008) and shown in Figure 3.5. Size-segregated supersaturation scans were performed for 11 different log-normally spaced particle dry mobility diameter (d_m) sizes (20, 26, 33, 42, 54, 70, 90, 115, 148, 190, and 244 nm). For each d_m , the CCNC then ran through approximately nine supersaturations between 1 % and 0.1 %, with a dwell time at any one of these supersaturations of ~ 120 seconds. During any run the first supersaturation cycle was a duplicate to allow time for column temperature stabilisation and the data from this initial supersaturation was discarded. The first 60 seconds of each d_m scan was also discarded so that column temperature stabilisation and plumbing time lags between CPC counting and CCNC counting could be corrected for. Ammonium sulphate (MERCK, Darmstadt, Germany) was used in conjunction with deionised water in a TSI atomizer (model 3076) to generate the calibration aerosol. The relative humidity of the resulting aerosol was kept below 25 %, using a 50 strand TSI nafion tube (model PD-06060T-24MSS) with filtered dry sheath air flow which had passed through silica gel. Overall concentrations were held between 1300-1700 particle cm^{-3} using a dilution arrangement to minimise the impact of quantum effects of splitting small quantities of aerosol, and to remain below particle counts which would effectively be hydration limited by the maximum water vapour available through the CCNCs wetted columns.

Methods and measurements

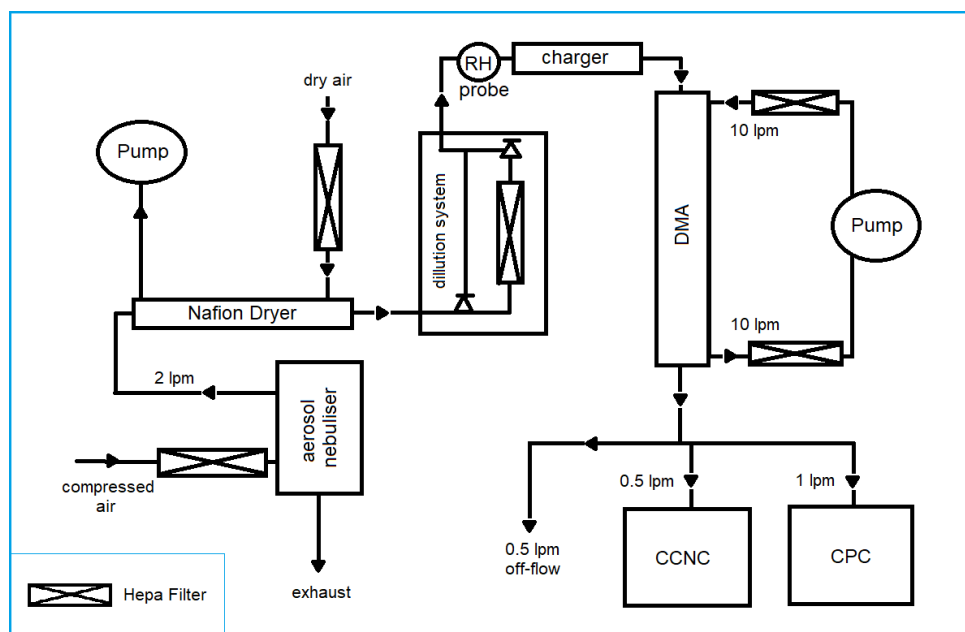


Figure 3.5. CCNC calibration instrument set-up.

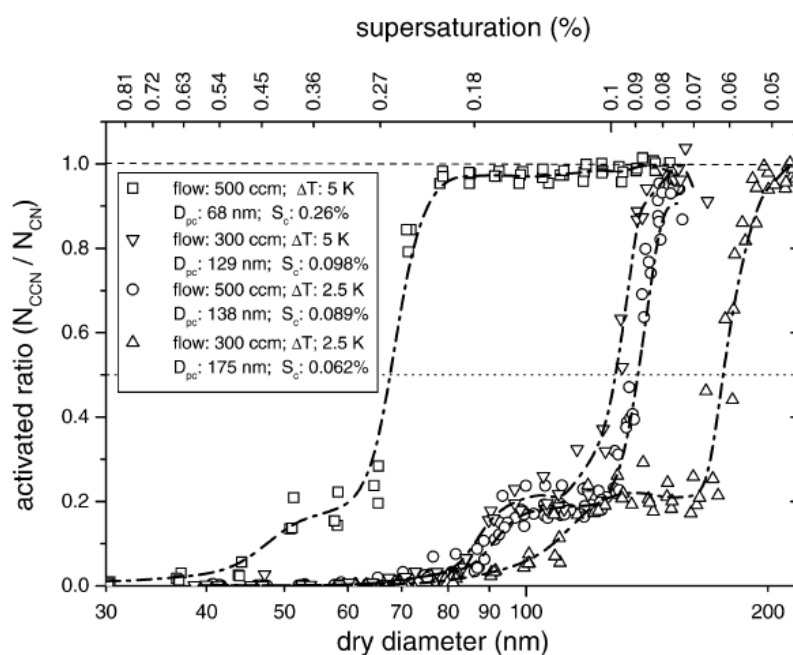


Figure 3.6. Activation curves for different CCNC operating conditions reproduced from (Roberts and Nenes, 2005). Aerosol at a particular dry diameter is considered activated when the ratio of CCN (i.e., droplets greater than $1 \mu\text{m}$) to total aerosol is greater than 0.5. The shoulders result from multiple charge particles from the DMA classification.

Methods and measurements

Calibration data is then analysed. Quality control flags are placed on any data which is outside of the ideal operating limits of the CCNC and CPC (e.g. abnormal flow, temperature stabilisation issues of the column, etc.). Data of the ratio between the measured CCN concentrations (N_{CCN}) and total aerosol concentrations (N_{CN}) are plotted against the d_m range for each supersaturation scan (see Figure 3.6). This data is corrected for possible counting discrepancies between the CPC and CCN in each case. First sigmoid fits,

$$\frac{N_{CCN}}{N_{CN}} = \frac{1}{(1+\exp(-(d_m-c)*(a)))} \quad (4)$$

described by a half maximum value (a) and rate (c), are fitted to scans of 0.4 – 1 % supersaturations and allowed to reach a height (H_1) holding the absolute minimum at zero. Each sigmoid fit should ideally be reaching unity (H_0), however if the either the CPC or CCNC was over- or under-counting then some shift from unity is expected. The mean of H_1 values (H_2) for the sigmoid fits for supersaturations > 0.4 %, and all data is then normalised to this shift (H_0/H_2), such that unity is reached for higher supersaturations of ammonium sulphate. Lower supersaturations are not used because counting discrepancies may be exacerbated for particles of large size due to a proclivity for more multiply charged particles, leading to non-monotonic N_{CCN}/N_{CN} activation curves (Petters et al., 2007). The need for charge corrections is determined using the graphical methods presented in Rose et al. (2008). After neutral charges, which will not make it through the DMA system, doubly charged particles are the most numerous. This can be viewed in the N_{CCN}/N_{CN} spectrum by a double plateau before the critical diameter, referred to as a shoulder in Figure 3.6. If this shoulder is greater than 0.1, a correction must be applied. The fraction of doubly charged particles, $(N_{CCN}/N_{CN})_2$, is approximately equal to the height of the shoulder. The fraction of singly charged particles, $(N_{CCN}/N_{CN})_1$, can be found by,

$$(N_{CCN}/N_{CN})_1 = \frac{N_{CCN} - N_{CN} * (N_{CCN}/N_{CN})_2}{N_{CN} - N_{CN} * (N_{CCN}/N_{CN})_2} \quad (5)$$

Sigmoid fittings are then created for all supersaturations scans. The half max points of the sigmoid curves are the critical diameters of activation (D_c) found for the ammonium sulphate calibration relative to the supersaturation scan, which is the associated critical supersaturation (S_c). The supersaturation linked D_c points are graphed against each other in \log_{10} - \log_{10} space. For a chemically homogenous solution such as ammonium sulphate, the curve should appear linear in this graphical space (Petters and Kreidenweis, 2007).

The range of supersaturations plotted against critical diameters are fit in linear space with a regression line. This line becomes the resultant slope created by the CCN column during calibration. Comparison between theoretical values for ammonium

Methods and measurements

sulphate S_c - D_c curves are compared to the calibration results, although d_m must be converted to an equivalent volume diameter (d_{eq}). A combination of theoretical values from the AP3 Köhler model (Rose et al., 2008) and AIOMFAC (Zuend et al., 2008) model have been used. Theoretical models used for calibration should be calculated at the temperature of the sampled aerosol during lab calibration (although the change in S_c from 298.15 K to 293.15 K was only $< 0.01\%$). The AIOMFAC model assumed a constant surface tension of pure water, $\sigma_w = 0.072 \text{ N m}^{-1}$ for the calculation. The AP3 model takes its water activity from the Aerosol Inorganics Model (AIM) (Clegg et al., 1998a, b), and surface tension coefficients for aqueous salt solutions from Seinfeld and Pandis (1998) and solution density parameterisations from Tang and Munkelwitz (1994). Deviations in critical supersaturation and diameter between the two models are relatively small (see Figure 3.7) so the difference to the calibration of CCNC critical diameter makes a small difference, on the order of a 100th of a supersaturation. For each D_c , corresponding supersaturation values on the resultant slope from the CCNC calibration are compared with the corresponding theoretical S_c value found at the same D_c . This S_c is the “real” supersaturation reached by the CCNC for the set change in temperature (T3-T1) in the CCNC column. The resultant real S_c values are applied to sample data as the actual supersaturation experienced by the CCN as they traverse the CCNC column. Unless explicitly stated otherwise, calibrated data were compared against the AP3 model and are shown with the 298.15 K theoretical values as comparison when plotting monodispersed CCN data.

MHD is a continuous monitoring station, such that at least one of the CCNCs are in operation at any time. Calibrations of the instruments are performed regularly, although the MHD aerosol lab remains mostly in controlled laboratory conditions (T $\sim 20^\circ\text{C}$). Long-term data is processed using a combination of relevant calibrations. Data gathered after modifications to the instrument necessitate new calibration supersaturation values. Relevant calibrated supersaturations and associated uncertainties for this dissertation can be found in Appendix A.1. The activation curves (such as in Figure 3.6) are used to find the uncertainty for each supersaturation by taking the average of the deviations from unity for each individual data point along the upper plateau of the curve.

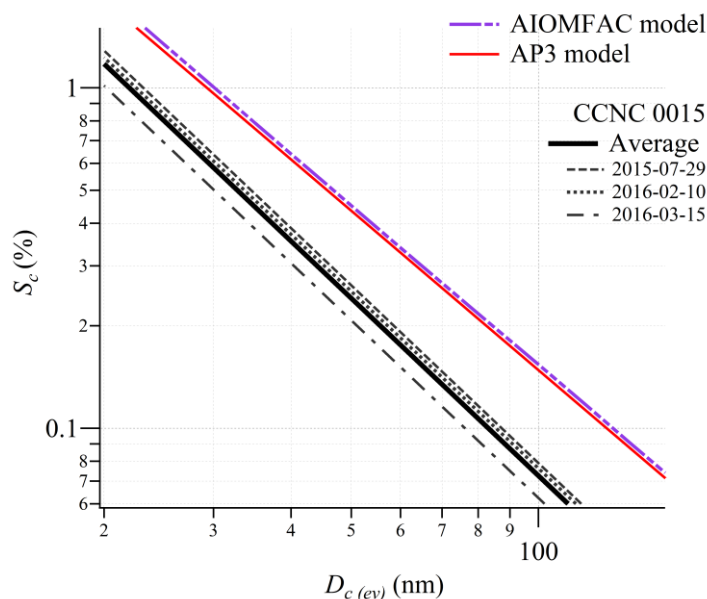


Figure 3.7. Typical CCNC instrument column supersaturation drift shown as calibration slopes from one CCNC instrument as a function of critical supersaturation (S_c) and equivalent volume diameter ($D_{c(eq)}$) derived from d_m . Three calibrations between July 2015 and March 2016 for the CCNC 0015 is shown in black, differentiated by line dash type, with the average shown as a thick solid black line. The graph also shows the AP3 (solid red line) and AIOMFAC (dashed maroon line) models referred to in the main text.

3.3.2 Polydispersed set-up

The CCNC can be run in two modes. The first, referred to as polydispersed mode, is the default mode and measures total CCN concentration at a range of set supersaturation (Note: this is different from the calibrated supersaturations). The second, discussed in the following section, is referred to as the monodispersed mode and requires the addition of further instrumentation and programming. The polydispersed mode is convenient for tracking trends in the number of CCN as a function of time and supersaturation. Polydispersed mode is the primary MHD operation mode for long-term monitoring. In this mode the inlet of the CCNC pulls 0.5 L min^{-1} of sample air through into the inlet manifold where it is divided into 0.050 L min^{-1} of sample air, and 0.45 L min^{-1} of filtered and humidified sheath flow air. The CCNC cycles through five supersaturations (0.75, 0.5, 0.35, 0.25, and 0.1 %) for a duration of 5 minutes per supersaturation, making the time resolution for a full N_{CCN} supersaturation spectrum 25 minutes.

3.3.3 Monodispersed set-up

The second mode is monodispersed (referring to particle size) which measures the total CCN concentration at a certain supersaturation for a fixed size aerosol as controlled by a DMA. The monodispersed mode is used to resolve the ambient activation potential of CCN. In much of the same way as is done in the calibration, aerosol critical activation diameters can be calculated to resolve both size-resolved and overall aerosol hygroscopicity. The physical set-up for measuring CCN in monodispersed mode is physically the same as the calibration except for the following:

CCN are sampled (from the NCM duct at MHD) from the environment rather than generated in lab (although lab generation can be sampled for experimentation). There is no dilution system (see Figure 3.5), so overall number is controlled by the environment you are sampling. Relative humidity is kept as low as possible but allowed up to 30 %, due to physical restrictions in long-term off-site monitoring. Lastly, supersaturation and size spectra are generated by first fixing a supersaturation and then cycling through 12 different lognormally spaced sizes (20, 20, 26, 33, 42, 54, 70, 90, 115, 148, 190, and 244 nm). As with the calibration runs, the first 20 nm size scan is not used for longer scan resolution, but when measured, is scrapped in data analysis but serves to allow CCNC column temperature stabilisation between supersaturation switches. The supersaturation spectra contain the same five distinct supersaturations as with the polydispersed mode (0.75, 0.5, 0.35, 0.25, and 0.1 %). Depending on different campaigns, higher time resolution may be necessary, so the duration for the scan of one size could be in the range of 80-300 seconds, making total time resolution for the monodispersed mode in the range of 80 – 300 minutes. Monodispersed set-up and calibration set-up both employ a DMA TSI model 3081 with a sample to sheath flow ratio of 2:10, which must be kept constant for the transfer function embedded in the software.

3.4 Black carbon instrumentation

The single particle soot photometer (SP2) and a Thermo scientific model 5012 multiangle absorption photometer (MAAP) were both deployed as atmospheric BC monitoring instruments. The instruments measure different mass concentrations, however have been shown to be reliable, following the same time trends with low time-resolution (~ 1 hour) (Weller et al., 2013). The SP2 operates as single particle analyser, effectively capable of counting every particle. The MAAP, collects a sample on a filter spot and measures the light absorption which is subsequently converted into BC concentration by applying an attenuation cross-section.

Methods and measurements

The MAAP normally operates at a flow rate of 10 L min^{-1} at a time resolution of 5 min. The instrument measures transmittance and reflectance at two angles to calculate absorbance (using a mass attenuation cross-section of $6.6 \text{ m}^2 \text{ g}^{-1}$ at 670 nm), the method is described further in Petzold and Schönlinner (2004). Black carbon concentration is calculated by taking into account the forward and backward emitted radiation fields using a data inversion algorithm. The algorithm, using a radiation transfer method, accounts for multiple scattering processes within the deposited aerosol, between the particles and the filter itself. The instrument integrates in real-time resulting in negative values at five minute resolution, depending on the overall aerosol loading of the tape before reaching its threshold saturation and being replaced by new tape section. For accuracy, 15-60 min averages of the data may be necessary at low loadings.

The SP2, manufactured by *Droplet Measurement Technologies, Inc.*, was provided by the Centre for Atmospheric Science, School of Earth and Environmental Sciences, at the University of Manchester. The SP2 samples at a flow rate of 0.12 L min^{-1} and employs a technique (Stephens et al., 2003) to induce incandescence *via* focused laser beam on every refractory particle which passes through it. The SP2 operates by detecting the incandescence of absorbing material as it passes through the focussed laser beam (1060 nm). Most absorbing material is black carbon (BC), although other metals are also absorbing. Non-absorbing material is vaporised before incandescence of the absorbing material occurs (sometimes delaying incandescence if the non-absorbing material is coating the absorbing core). When incandescence occurs, absorbing material emits light at a colour indicative of its boiling point temperatures. As metals and BC have easily discernible boiling point temperatures the four detectors (some detecting 350-800 nm and some detecting 630-800 nm) allow the instrument to distinguish between them during measurements. Using the intensity of the signal, this allows measuring of the refractory BC mass, number concentrations and BC core size. Calibrations and data quality checks were performed according to the technique outlined by McMeeking et al. (2010). Of the two methods, the SP2 gives superior information both in particle number, size, and BC type. Reconciling measurements from either must be done with parallel observations and operates on the assumption that the SP2 delivers unbiased BC concentration. Such an analysis is performed in Chapter 4.

3.5 Interpreting data

Methods and measurements

3.5.1 Air Mass Analysis

Tracking air mass movements

Overall, air mass movements were tracked backwards in time using the HYSPLIT trajectory database, in NOAA archives (Stein et al., 2015; Rolph, 2016). Most trajectories were calculated as air mass back trajectories reaching back 120 hours before the arrival of the sampling point. Trajectories were calculated for 50 – 100 meters above sea level, and both the air mass trajectory height and estimations of the height of the marine boundary layer were pulled from the HYSPLIT model. These can be found overlaid on various maps in this thesis. Air mass back trajectories were used to determine air mass type by origin and source influence.

Estimation of aerosol exposure to biological activity

As an indicator of biological activity, Chl-*a* is an important proxy for marine productivity and biomass abundance. To represent the relative exposure of the sampled aerosol to biologically rich waters, HYSPLIT trajectory model outputs were overlaid onto satellite retrieved Chl-*a* concentrations to estimate the mean ocean Chl-*a* concentration traversed by the air mass back-trajectory path. A detailed description of the retrieval of these Chl-*a* maps can be found in Fossum et al. (2018) and appendix A of Rinaldi et al. (2013). Briefly described here, multiple sensors from satellite imaging (SeaWiFS, MERIS, MODIS-Aqua, and VIIRS time-series) were used to retrieve daily mean satellite sea-surface Chl-*a* concentrations (mg m^{-3}). Gaps in the data, due to environmental factors such as clouds or sea-ice, were resolved by employing multi-channel singular spectral analysis (M-SSA) (Kondrashov and Ghil, 2006) in the Chl-*a* mean concentrations. Chl-*a* maps used were at 0.1° resolution, and air mass trajectories at hourly resolution. Weighted (when applicable) aerosol exposure to biologically productive waters can be calculated. The mean Chl-*a* concentration was calculated by first taking the accumulated concentration within pixels under the air mass back-trajectory path for the 72 hours prior to arriving at the ship, less the last three hours, and then taking the mean of all back-trajectory accumulated mean concentrations over the period (trajectories showed minimal vertical variation of the air mass over the periods selected). The last three hours are neglected to avoid introducing a bias into the dataset since significant secondary particle formation could not be expected to have occurred over that timescale before reaching the measurement location. Additionally, for the PEGASO cruise, the ship was likely to be in the immediate vicinity of a bloom, making it especially relevant to discard the last three hours of trajectory overlay. No additional diurnal consideration was used in assessing Chl-*a* exposure as the cruise experienced 18-22 hours of daylight (depending on the latitude of the ship and day of the month).

Methods and measurements

Definition of steady state conditions for analysis

Air masses are associated with synoptic-scale meteorological systems and exhibit conserved meteorological parameters (e.g. equivalent potential temperature and total water mixing ratio) which are typically invariant within the air mass. Notable changes in the meteorological parameters at a particular location are normally more associated with large scale dynamics (e.g. frontal passage), representing a change in air mass, rather than small scale dynamical processes (e.g. entrainment and surface fluxes) that eventually transform the air mass with time. Similar to pseudo-steady-state meteorological parameters being characteristics of air mass origin, atmospheric composition variables (e.g. gases and aerosols) are also expected to possess pseudo-steady-state characteristics. Aerosol spectral properties associated with air masses in this dissertation were selected and analysed on the basis of periods of relatively stable or invariant meteorological and atmospheric composition characteristics. Stability in duration, meteorological parameters, size distribution parameters (e.g. modal size and number concentration), and chemical composition were required for pseudo-steady state consideration.

Data gathered during the PEGASO cruise, and during other measurement periods, were analysed through air mass classification based on pseudo-steady state stability. An arbitrary target of relative stability over durations of eight hours was sought as the minimum requirement for selection and inclusion into the air mass characterisation database, although some inclusion of periods with stability over four hours occurred. In addition to relatively invariant meteorological parameters, size distribution parameters (e.g. modal size and number concentration) were required not to vary more than 20 % from the mean. A similar requirement was afforded to aerosol chemical composition, particularly non-sea-salt sulphate (nss-SO₄). Finally, a further selection criterion was that the back-trajectories had to indicate advection of the air over the same source region from the start to the end of the period.

3.5.2 Köhler theory

The process by which water vapour molecules condense to form cloud droplets is described by Köhler theory. This theory involves the Kelvin effect, by which changes in the saturation vapour pressure are related to the radius of the curvature of the droplet, and Raoult's law which relates the solute to the saturation vapour pressure (Fuentes et al., 2010a; Pruppacher, 1997; Hinds, 1982). A cloud droplet is an aerosol particle surrounded by water molecules. Once the CCN has activated it is a cloud droplet and has both a physical component associated with its shape and size, and a chemical component associated with the chemical makeup of the solute. If the CCN was soluble, the solute is a homogenous mixture, if it was insoluble the solute

Methods and measurements

would be heterogeneous. The droplet itself must maintain a partial vapour pressure greater than the saturation vapour pressure (equilibrium partial pressure of a flat surface, P_s) in order to prevent molecules from leaving the droplet surface; the smaller the droplet the smaller the partial vapour pressure (Hinds, 1982).

The Kelvin effect, describes the change in saturation vapour pressure due to the curvature of a surface.

$$\ln\left(\frac{P}{P^0}\right) = \frac{2\sigma V_m}{rRT} \quad (6)$$

Or

$$\frac{P}{P^s} = e^{\frac{4\sigma M}{RT\rho d^*}} \quad (7)$$

Where, P is actual vapour pressure, P^0 is the saturated vapour pressure, σ is the surface tension, V_m is the molar volume, r is the radius of the droplet, R is the ideal gas constant, T is the temperature at equilibrium vapour pressure (Hinds, 1982).

Raoult's Law describes the partial vapour pressure of a component (i), in solution. Where the equilibrium vapour pressure of any component is proportional to its mole fraction in the solution such that,

$$P_i = (P_i^*)(x_i) \quad (8)$$

Or

$$e_{sat,s}/e_{sat,w} = a_w(T) \quad (9)$$

Where P_i^* is the vapour pressure of pure component i , x_i is the mole fraction of component i in mixture of solution, and P_i is the vapour pressure of component i in a gaseous mixture above the solution. Also, $e_{sat,s}$ is the equilibrium vapour pressure over an aqueous salt solution, $e_{sat,w}$, is the equilibrium vapour pressure over pure water, and a_w is the water activity at a given temperature, T (Pruppacher, 1997).

Such that, the two can be combined into what is known as Köhler Theory. Which describes the properties of an activated droplet due to its chemical make-up and diameter.

$$\ln\left(\frac{P_w D_p}{P^0}\right) = \frac{4M_w\sigma_s}{RT\rho_w D_p} - \frac{6n_s M_w}{\pi\rho_w(D_p^3)} \quad (10)$$

Where P_w is the droplet water vapour pressure, P^0 is the corresponding saturation vapour pressure over a flat surface, M_w is the molecular weight of pure water, ρ_w is

Methods and measurements

the density of pure water, σ_s is the droplet surface tension, n_s is the moles of solute, and D_p is the droplet diameter.

Or to get the saturation ratio (s) for subsaturated and supersaturated conditions as,

$$s = a_w * \exp\left(\frac{4\sigma_w M_w}{\rho_w R T D}\right) \quad (11)$$

Where the subscript, w, denotes water specific components and D is the droplet diameter (Fuentes et al., 2010a). The theory predicts the behaviour of CCN activation based on external and internal conditions.

3.5.3 κ -Köhler theory and aerosol hygroscopicity

As mentioned numerous times, there is a need for consistent tools for theoretical analysis of data and for inter-comparison. κ -Köhler theory allows for the comparative study of aerosol hygroscopicity. It utilises a single parameter, κ , to describe the relative activation potential of particles. The approximation for κ can be described as (Eq. 10 in Petters and Kreidenweis (2007)),

$$\kappa = \frac{4A^3}{27D_d^3 \ln^2 s_c} \quad (12)$$

$$A = \frac{4\sigma_{s/a} M_w}{RT\rho_w} \quad (13)$$

Where D_d is the dry diameter, s_c is the critical supersaturation or the (critical) saturation ratio (s_c) which is often expressed as a percentage (S_c) given by $S_c = s_c - 1$), and $\sigma_{s/a}$ is the surface tension of the solution/air interface which is held fixed at 0.072 Jm^{-2} . This approximation is only valid when $S_c < 1.0 \%$ and $\kappa > 0.2$. Outside these bounds, the approximation begins to fail, as the slope of particles at low hygroscopicity begin to curve. In these instances, Eq. 14 can be used to determine κ . For inter-comparison unless otherwise specified, $T = 298.15 \text{ K}$. Monodispersed CCNC data can easily be found using the above κ calculation using S_c and D_c in place of D_d . However, the κ approximation can be found in forms more readily available to growth factor (GF) related data.

$$\frac{RH}{\exp\left(\frac{A}{D_d g f}\right)} = \frac{g f^3 - 1}{g f^3 - (1 - \kappa)} \quad (14)$$

Where the GF is represented as gf and RH is expressed as a fraction (Eq. 11 in Petters and Kreidenweis (2007)). The κ approximation for the saturation ratio (s) over an aqueous solution droplet of diameter, D , can also be extended down to the subsaturated regime ($s < 1$) for which

$$s(D) = \frac{D^3 - D_d^3}{D^3 - D_d^3(1-\kappa)} \exp\left(\frac{4\sigma_s/aM_w}{RT\rho_w D}\right) \quad (15)$$

The critical supersaturation can be calculated as the maximum of the above curve for a given kappa and dry particle diameter. Here D is the wet droplet diameter which must be expressed as a range to solve for the maximum of the curve (Eq. 6 in Petters and Kreidenweis (2007)).

Marine inorganics are more easily predicted using the κ approximation, however due to the different nature of marine organics in the subsaturated and supersaturated regimes, their behaviour can be hard to describe with a single parameter.

3.5.4 Degree of neutralisation

The degree of neutralization (DON_{mol}), defined as the molar ratio of measured NH_4^+ to the quantity of NH_4^+ needed to fully neutralize the observed major inorganic anions in the aerosol, was calculated when applicable using the HR-ToF-AMS composition data. DON_{mol} ranges from 0 to 1 where $\text{DON}_{\text{mol}} = 0$ means no neutralization (i.e., sulphate and nitrate in dissolved acidic form) whereas a $\text{DON}_{\text{mol}} = 1$ means all measured SO_4 and NO_3 exists as ammonium sulphate and ammonium nitrate components, respectively. The DON_{mol} value is calculated by ionic balance as

$$\text{DON}_{\text{mol}} = \frac{n_{\text{NH}_4^+}}{2 \times n_{\text{SO}_4^{2-}} + n_{\text{NO}_3^-}}, \quad (16)$$

where $n_{\text{NH}_4^+}$, $n_{\text{SO}_4^{2-}}$ and $n_{\text{NO}_3^-}$ denote the molar amounts of the indicated ionic species determined for a specific sample. The measured nitrate amounts were small compared to both the sulphate and ammonium molar amounts. The DON_{mol} determined from field data can then be used in conjunction with predictions from the AIOMFAC model (see Appendix B.1) for aqueous particles consisting of ammonium sulphate mixed with sulphuric acid, providing a comparison of the CCN properties at the same DON_{mol} as well as over the full range of DON_{mol} possible.

3.5.5 Monodispersed CCN total concentration calculation, and percent contributions

When CCN are measured for monodispersed particle mobility diameters (without another CCNC instrument running in polydispersed mode), time trends of total ambient CCN numbers as a function of supersaturation are not measured. To resolve total N_{CCN} , hourly CCN critical dry diameters were applied to SMPS size-distribution

Methods and measurements

data. It was assumed that, for pseudo-steady periods, critical dry diameters derived from the CCNC measurements would represent the run-away activation dry diameter. Particles greater than this diameter would readily activate under a certain peak supersaturation level. Total N_{CCN} were derived from summing SMPS data collected for particle diameters greater than D_c as a function of supersaturation percentage (S). For the PEGASO cruise dataset, N_{CCN} determined at 0.8 % supersaturation can be considered a maximum value of marine CCN, (i) since derived marine N_{CCN} start reaching a maximum limit at supersaturations as low as 0.5 % (see Figure 5.7) and (ii) because the ambient marine cloud base will not typically exceed 0.8 % supersaturation (Twomey, 1959; Twomey and Wojciechowski, 1969).

Following Hoppel Theory (Hoppel et al., 1986), the inter-modal minimum is the critical diameter of free activation experienced by an aerosol population at cloud base. The inter-modal minimum is caused by a cloud peak supersaturation (S_{peak}) which can be quantified by finding the corresponding S_c for the inter-modal, D_c , on the CCN ambient aerosol curves. As the ambient CCN curve is based on the average size-dependent physico-chemical aerosol population properties, the D_c for different chemical species at S_{peak} may be different from the ambient.

For the PEGASO cruise dataset, PMA is considered here to be chemically represented by the theoretically derived S_c - D_c curve of NaCl, and SMA is represented by the DON_{mol} determined partially neutralised sulphate. This simplification is reasonable based on the small fractions of OM (excluding MSA) in either merged air mass case (described in Chapter 5) compared with the inorganic components, which may otherwise affect the hygroscopic properties of the aerosol. Using the number-size distributions of the aerosol, and the D_c of SMA and PMA respectively, the number contribution of the different aerosol types which would be considered activated into cloud droplets can be calculated. First, the SMPS data is constrained by fitting a sea-salt distribution. In this dissertation sea-salt distributions from the North East Atlantic (Ovadnevaite et al., 2014b) are used for the Southern Ocean dataset in the absence of an ambient multi-modal sea-salt distribution from the Southern Ocean. Using one spectral shape from a wind speed of 6.3 m s^{-1} , which is similar to the average wind speed recorded throughout the PEGASO cruise ($\sim 7.5 \text{ m s}^{-1}$), the distribution is scaled based on mass calculations from the HR-ToF-AMS. However, the HR-ToF-AMS has a PM_{10} aerodynamic vacuum cut-off which must be converted to an equivalent mobility diameter (DeCarlo et al., 2004) for mass based scaling. Spherical particle volume equivalent is derived using the density of sea-salt (2.17 g cm^{-3}). The aerodynamic vacuum cut-off diameter of $1 \text{ }\mu\text{m}$ then equates to a mobility equivalent diameter of $0.0544 \text{ }\mu\text{m}$. The scaled sea-salt distributions are subtracted from the overall number size distributions with the remainder being assumed as the SMA number contribution. Using the D_c for either, the normalised number-size distributions of sea-salt (PMA) and SMA, respectively, are converted to absolute number and summed

Methods and measurements

up for mobility diameters $> D_c$. The total activated number is similarly the sum of the number-size distribution for sizes $>$ inter-modal minimum. The percent contribution of PMA is determined as the fraction of activated PMA particles to the total activated number. Values derived for this calculation and the percent contributions from the PEGASO cruise dataset can be found in Table 5.4 (*mP* 1 is omitted for lack of CCN data, and *mP* 4 is omitted due to large inter-modal minimum errors from number size distribution data instability). The inter-modal minimum calculation has an inherent uncertainty of $\pm 5\%$, which owes to the combination of a $\pm 10\%$ uncertainty in the SMPS size-binning which is somewhat reduced in the later fitting of the ambient data. The uncertainty of the CCN counter is $\pm 0.02\%$ for S_{peak} values. Due to the nature of the contribution calculation and the relatively steady nature of the PMA distribution, the maximum deviation in D_c or S_{peak} from either uncertainty would only result in a $\pm 8\%$ contribution change.

Results 1—black carbon measurements in marine environments suggest the persistence of clean conditions

4. Results 1—black carbon measurements in marine environments suggest the persistence of clean conditions

In this chapter BC measurements taken from a single particle soot photometer (SP2) are used to assess the permeation of air pollution over remote oceans. Black carbon (BC) as a tracer for anthropogenic pollution is measured by the SP2, throughout the PEGASO cruise of the Scotia Sea region. The remote oceanic region has been reported to have a high fraction of pristine days during the austral summer months (Hamilton et al., 2014), making it an ideal marine environment to observe what should be clean marine conditions. Other SP2 measurements from the Southern Ocean reported that clean marine conditions only persist when BC mass concentrations are $< 1.8 \text{ ng m}^{-3}$, and with CO at $< 56 \text{ ppb}$ (Shank et al. 2012). By way of comparison, SP2 measurements from continental sources in the Northern Hemisphere measure 300 – 50 ng m^{-3} on average for urban and remote sites respectively (McMeeking et al., 2010). To assess the marine background BC mass concentrations of remote marine environments, the BC mass concentrations are analysed as frequency distributions. In this way, the permeation of pollution (using the tracer BC) can be evaluated both as a function of persistence and overall mass contribution.

BC mass concentrations from the Southern Ocean PEGASO cruise are found to have a persistent mode of very low concentrations ($< 0.4 \text{ ng m}^{-3}$) of BC mass in pristine marine conditions. A second available SP2 dataset, from a short campaign at Mace Head research station (MHD), over April 2nd-24th 2015, is also analysed (see Methods for details about MHD) and found to have a similarly persistent but low BC concentrations. These results are reported in the following section with more detail.

4.1 The clean Southern Ocean confirmed by SP2 measurements

The PEGASO campaign allowed for measurements to be taken from typical Southern Ocean source regions and included aerosol from maritime tropical, maritime polar, and continental Antarctic air masses. The air mass back trajectories which crossed the path of the research vessel are shown in Figure 4.1. The trajectories were

Results 1—black carbon measurements in marine environments suggest the persistence of clean conditions

calculated in relation to the movement of the ship, with a starting height of 50 m above sea level, every 12 hours for a backwards run time of 72 hours. Typically, maritime tropical air masses that advected over the ship during the cruise experienced some modification from the South American continent evidenced by increased BC mass concentrations.

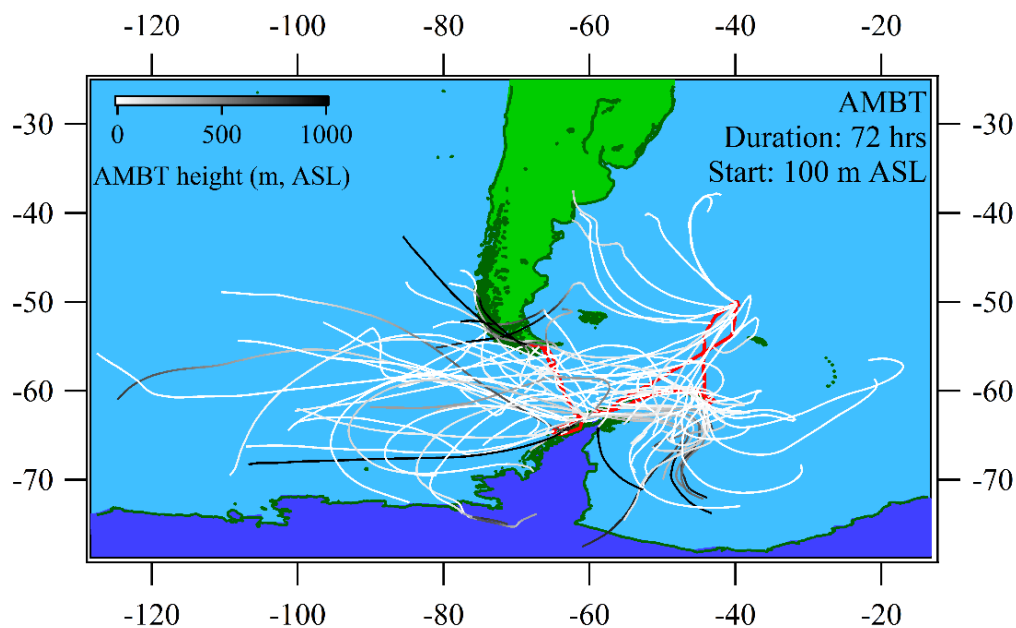


Figure 4.1. Overlain air mass back trajectories (AMBT) on cruise region. Each trajectory shows the relative air mass path (white-black lines) 72 hours prior to crossing the ship's path (red) at 100 m above sea level (ASL). The height of the trajectory relative to sea level is shown in greyscale, and for the most part reflects that most of the trajectories stayed well below 500 m ASL.

During the cruise, 5711 minutes (952 hours or 39.66 days) of SP2 data were recorded, of which 40931 minutes (682 hours or 28.4 days) were not obviously contaminated by local pollution from the research vessel nor involved in lab generated sampling. These 28.4 days are used as the ambient Southern Ocean measurements. The mass concentration of BC (ng m^{-3}) measured in Antarctica by location can be seen in Figure 4.2. For most of the traversed path, BC levels remained below 1 ng m^{-3} . Times when larger concentrations occurred have been attributed to either local (Island human activity), transported pollution (from the South American continent), or possible ship pollution. The period of mid-high BC concentration ($\sim 80 \text{ ng m}^{-3}$ average with sustained concentrations above 4 ng m^{-3} lasting 1 – 3 hours) between the Shetland and S. Orkney Islands had air mass back trajectories which revealed the air movements advecting across the Shetland Islands before arriving at the research vessel. The periods of high BC ($25 - 400 \text{ ng m}^{-3}$ average lasting 6 - 12 hours), which occurred within 10° latitude and longitude of the Sandwich Islands, can be largely

Results 1—black carbon measurements in marine environments suggest the persistence of clean conditions

attributed to long range transport (30 to +72 hours prior) of aerosol advecting over Argentina to meet the ship. However, local pollution from other unknown vessels has not been ruled out. Additionally, measurements taken around King George Island were considered polluted ($\sim 50 \text{ ng m}^{-3}$), in line with results from Weller et al. (2013) which suggest BC annual mass concentrations are higher here than at other coastal stations.

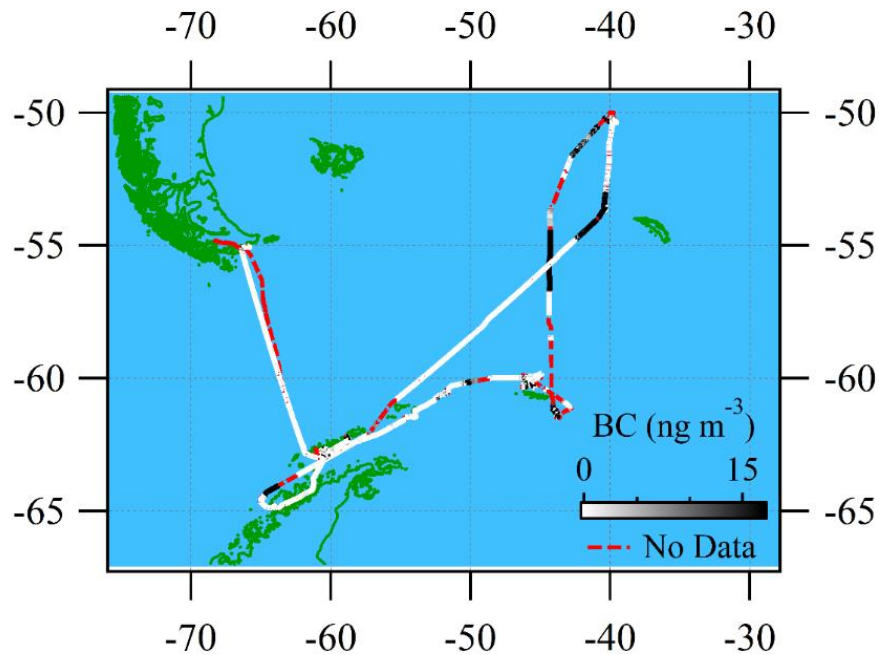


Figure 4.2. The ship's cruise path is shown on a latitude-longitude map, with continental borders shown in green. The BC concentration is shown in a linear greyscale, where white represents a BC mass concentration of 0 ng m^{-3} and black represents $+17 \text{ ng m}^{-3}$. It should be noted that BC was sometimes measured in excess of 1000 ng m^{-3} , however the scale is used to demonstrate the frequency and location for which the measurements were less than 1 ng m^{-3} . The red dotted line indicates parts of the cruise in which no ambient data was available, or for which ambient data was exposed to the research vessel's own ship exhaust plumes and deleted for analysis.

The 28.4 days of ambient Southern Ocean BC data from the Scotia Sea region can be used to assess the persistence of BC pollution in this remote oceanic region. The BC mass concentration data is plotted as a frequency distribution (Figure 4.3) and lognormally fitted using the IGOR Pro (Version 6.37, WaveMetrics, Lake Oswego, OR, USA) *multipeakfitting2* package (WaveMetrics, 2015). The frequency distributions were calculated in 1000 equally stepped bins in logspace, as concentrations were measured from zero to over 1000 ng m^{-3} . Each bin was normalised to its bin width in linear space, then using a baseline of 0, lognormal modes were fitted to the distribution iteratively to minimise residuals. The parameters of these modes were

Results 1—black carbon measurements in marine environments suggest the persistence of clean conditions

then used to describe the 95th percentile of the modal BC. For a lognormal distribution ($\ln(\sigma_g)$), the difference between the BC concentration of the 95th percentile ($C_{95\%}$) and the modal concentration ($C_{50\%}$) is considered $2\sigma_g$ (Hinds, 1982).

$$2\sigma_g = \frac{C_{95\%}}{C_{50\%}} \quad (17)$$

The resulting fitted frequency distribution and modes are presented in Figure 4.3, with lognormal modes described numerically in Table 4.1, with the most frequent occurrences of BC mass often below 1 ng m^{-3} . The fitted ambient measurements reveal that aerosol in the Southern Ocean during austral summer is most frequently (93 % of the time) permeated by BC mass concentration $< 0.39 \text{ ng m}^{-3}$. To a lesser extent, three modes were detected with varying degrees of pollution. The first, occurring for approximately 7 % of the time, showed BC concentrations between 0.4 ng m^{-3} and 5 ng m^{-3} (Table 4.1) and will be considered 'clean' (as it is not pristine nor is it polluted). The second mode contained BC mass concentrations of $5 - 81 \text{ ng m}^{-3}$, and the last contained $81 - 612 \text{ ng m}^{-3}$. The latter two modes occurred $\sim 0.3 \%$ of the time with negligible measurements of BC mass concentrations in excess of 612 ng m^{-3} . Since, populated islands were found to cause an increase in BC concentrations of a $\sim 50 \text{ ng m}^{-3}$, contamination from islands should be accounted for in the Southern Ocean region. The frequency of detection of this contamination was $< 0.3 \%$ for the cruise, which traversed close to the Islands. Therefore, this frequency occurrence may be biased high for measurements in the remote Southern Ocean. However, for coastal research stations in and around Antarctica this may be a constant source of pollution which may artificially increase background BC observations. Ship pollution can also be a major source of contamination, not just to the environment but to measurements aboard research vessels. This pollution must be considered in post-measurement analysis. Such contamination was identified and discarded in this study, but some small fraction of local or re-circulated ship contamination may have missed detection. Additionally, the Southern Ocean was observed to have very low ambient concentrations of BC, with BC concentrations above 612 ng m^{-3} occurring less than 0.001 % of the cruise duration.

Results 1—black carbon measurements in marine environments suggest the persistence of clean conditions

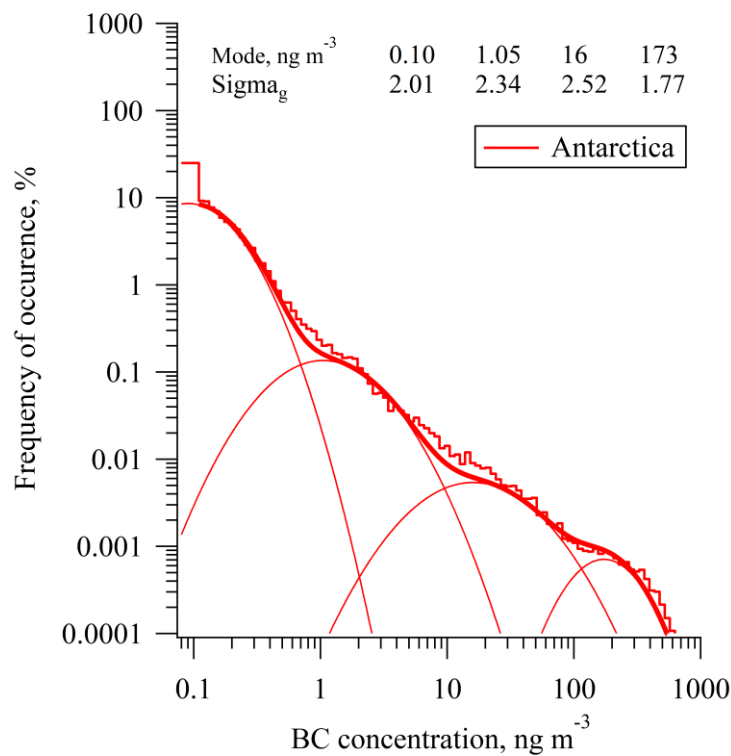


Figure 4.3. Frequency distribution plot of AD dataset from the SP2 instrument. Normalised frequency of occurrence (%) are shown against BC mass concentrations for bins equally spaced in logspace. Fitted lognormal modes are shown. Top of the graph shows the lognormal mode position with geometric standard deviation (σ_g) underneath.

4.2 OM is not correlated to BC in clean conditions

Evaluating the prevalence of BC mass concentrations in marine air enables the separation of air into that affected by pollution and not affected. This is important for organic material, which can be marine or anthropogenic in origin, and which has source dependent aerosol properties. Studies have also shown that anthropogenic transport of trace elements (such as nitrogen and iron) and subsequent deposition onto the ocean surface can lead to increased marine biological production (Baker and Croot, 2010; Duce et al., 2008). With the right environmental conditions, such as oceanic upwelling (Smith and Konferenzen, 1995), an area such as the Western Coast of South America may experience frequent continental transport and upwelling which could result in a correlation between anthropogenic pollution and subsequent marine OM concentrations which are in fact related but not simultaneously correlated in time. However, simultaneous high time-resolution measurements of BC (a tracer of anthropogenic aerosol) and OM after long-term prevailing clean conditions or oceanic downwelling should not be correlated. The extent to which submicron organic mass (OM), exclusive of methanesulphonic acid, should be

Results 1—black carbon measurements in marine environments suggest the persistence of clean conditions

considered marine in origin in the Southern Ocean has been questioned (Shank et al., 2012) on the basis of high correlations between OM and BC mass concentrations. The somewhat polluted and pristine observations periods of the Southern Ocean dataset are evaluated to test the degree to which OM (as a function of BC) can be considered marine in origin.

OM mass concentration ($\mu\text{g m}^{-3}$) from the Southern Ocean is compared against BC mass concentrations (SP2 measurements), and the ratio of OM:BC is also compared against BC (Figure 4.4). The data is capped at a moderately clean limit of $< 5 \text{ ng m}^{-3}$ (Table 4.1), and also a pristine limit of 0.4 ng m^{-3} . Parallel OM measurements from and HR-ToF-AMS for the clean and pristine periods were used for comparison. The comparison of OM to BC for the Southern Ocean data yields no correlation ($R^2 = 0.002$, for OM and OM/BC alike), supporting the idea that measured OM in pristine—moderately clean conditions is, in fact, marine in origin.

Three years of MAAP (see Section 3.4) equivalent BC (EBC) data and high resolution time-of-flight aerosol mass spectrometer data gathered at MHD (2009 – 2011) (O'Dowd et al., 2014) is used as a basis for comparison against Southern Ocean data. The MHD data is defined as being clean and pristine at levels of $< 50 \text{ ng m}^{-3}$ and $< 15 \text{ ng m}^{-3}$, respectively (Grigas et al., 2017). The Southern Ocean has not been categorised similarly with multi-year data, although Shank et al. (2012) has reported that clean-conditions are met only when SP2 measured BC mass concentrations are $< 1.8 \text{ ng m}^{-3}$. Therefore, pristine and clean limits are set according to the cleanest (approximately $< 0.4 \text{ ng m}^{-3}$) and second cleanest (approximately $< 5 \text{ ng m}^{-3}$) modes presented in Table 4.1 from the PEGASO cruise SP2 dataset. The differences in the limits between each ocean are owed to a combination of factors including different instrumentation (discussed further in the Section 4.3), ocean environments, and sampling duration. As can be seen in Figure 4.4, the Southern Ocean data is similar to data from the North East Atlantic under clean conditions. The Southern Ocean data contained lower BC mass concentrations which can be explained by the differences in BC instrumentation, where the Southern Ocean measurements were taken by an SP2 which measures incandescent mass vs. the MAAP used in the North East Atlantic which measures optically absorbing mass. The MAAP measuring higher BC mass concentrations has also been reported in inter-comparison studies (Slowik et al., 2007; Raatikainen et al., 2015). OM measurements in the Southern Ocean were much lower overall than those reported from the North East Atlantic by almost an order of magnitude. This was then propagated into the OM/BC ratios which were higher overall in the Southern Ocean. Large OM plumes were not observed during the cruise in the Southern Ocean during clean conditions, which is in opposition to observations in the North East Atlantic where relatively large plumes of OM occur in clean conditions (Figure 4.4). Observations of large OM plumes in the Southern

Results 1—black carbon measurements in marine environments suggest the persistence of clean conditions

Ocean were concurrent with BC plumes, which may be why correlations between OM and BC in the Southern ocean have been erroneously extended to the North East Atlantic (Shank et al., 2012).

Table 4.1. Parameters from the lognormal mode fittings of the frequency distribution by peak (pk). Mode positions (C_0) and σ_g are in terms of the BC mass concentration in ng m^{-3} , while the amplitude of the mode (Amp) is in % occurrence and is not the height of the mode but rather the amplitude as described in Hinds (1982). The BC concentration for which 95 % of the mode is accounted for ($C_{95\%}$, see Methods) is in ng m^{-3} .

Mode	C_0	σ_g	Amp	$C_{95\%}$
<i>Antarctica pk 1</i>	9.56E-02	2.01	6.54+00	0.39
<i>Antarctica pk 2</i>	1.05	2.34	1.25E-01	4.91
<i>Antarctica pk 3</i>	16	2.52	5.43E-03	80.6
<i>Antarctica pk 4</i>	173	1.77	4.42E-04	612
<i>MHD pk 1</i>	9.86E-02	1.45	1.30E+00	0.29
<i>MHD pk 2</i>	0.66	3.44	3.24E+00	4.53
<i>MHD pk 3</i>	7.5	1.40	2.33E-01	21.1
<i>MHD pk 4</i>	28	1.53	3.09E-02	85.3
<i>MHD pk 5</i>	170	1.66	1.32E-02	566

Results 1—black carbon measurements in marine environments suggest the persistence of clean conditions

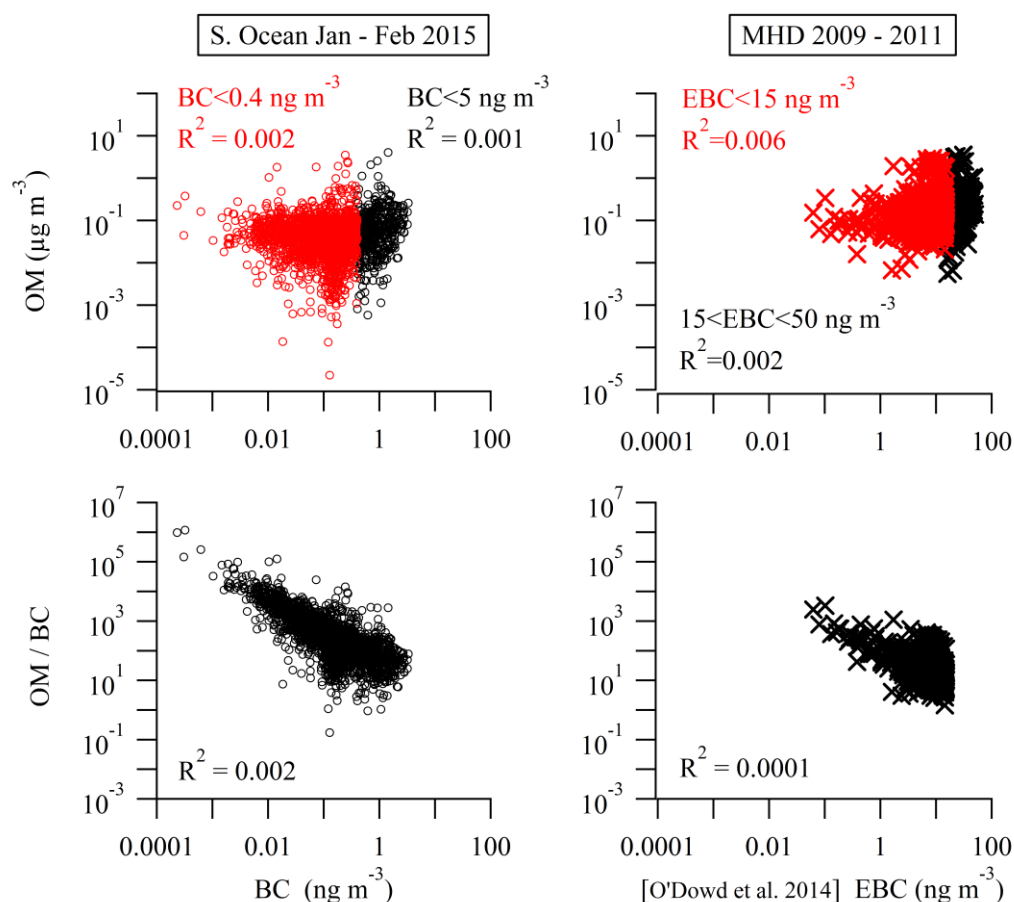


Figure 4.4. Comparison between the OM ($\mu\text{g m}^{-3}$) concentration and OM:BC ($\text{ng m}^{-3}/\text{ng m}^{-3}$) ratios of Southern Ocean (left panels) which were taken as clean levels for $\text{BC} < 5 \text{ ng m}^{-3}$ (black circles) and pristine for $\text{BC} < 0.4 \text{ ng m}^{-3}$ (red circles), and MH from O'Dowd et al. (2014) reproduced (right panels). Southern Ocean data points are shown in open black circles. Crosses represent the O'Dowd et al. (2014) data, where the red crosses denote $\text{BC} < 15 \text{ ng m}^{-3}$. The MH data shows equivalent BC (EBC) from an MAAP, so likely BC concentrations are biased high as compared with the Southern Ocean SP2 data.

4.3 The clean North East Atlantic confirmed by SP2 measurements and MAAP comparison

While it might be expected that marine BC mass concentrations in the North Atlantic, being in the Northern Hemisphere, would be higher than that of the Southern Hemisphere, no comparison of parallel SP2 instrument measurements of background BC levels have been reported. At Mace Head (MHD) research station, a coastal North Atlantic Station, 51 % of measured air masses adhere to the clean sector wind direction (Jennings et al., 2003), and of those, the vast majority adheres to ‘pristine’

Results 1—black carbon measurements in marine environments suggest the persistence of clean conditions

criteria ($BC < 15 \text{ ng m}^{-3}$ *via* MAAP) (Grigas et al., 2017). It should be noted that these BC mass concentrations limits were calculated by a MAAP through the conversion of optically absorption, and these concentrations should be larger than concentrations measured with an SP2, as the latter measures BC particles *via* laser incandescence. O'Dowd et al. (2014) showed that when applying both wind direction and BC criteria, maritime measurements from the North East Atlantic exhibit marine aerosol properties unperturbed by anthropogenic influences, seemingly supporting an idea that the North Atlantic often has a relatively low background level of BC. To the authors' knowledge, this is the first published SP2 dataset from Mace Head research station, and for the greater sub-polar North East Atlantic region.

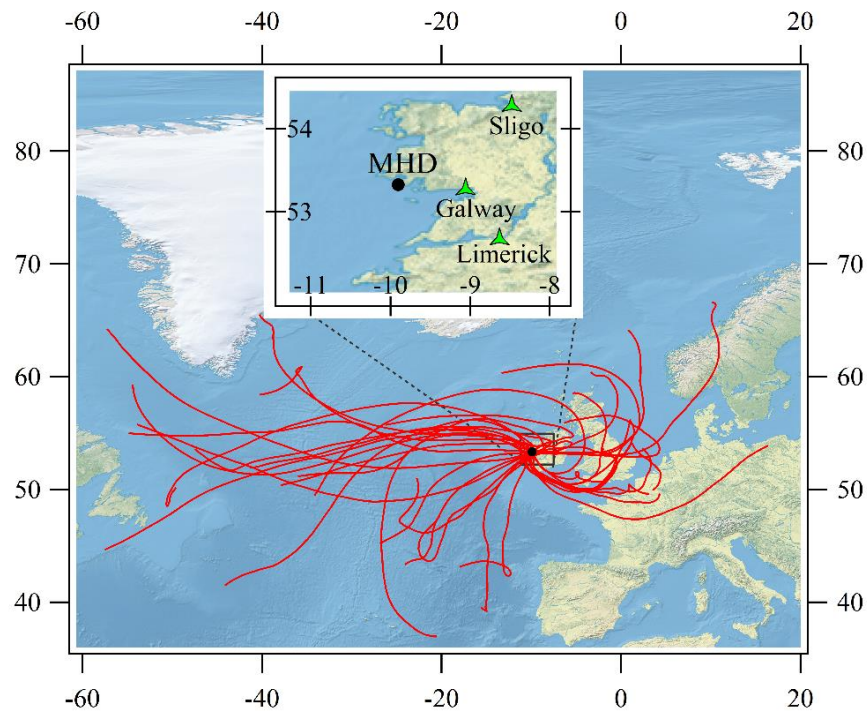


Figure 4.5. Air mass back trajectories shown for April 2– 20 at 12-hour intervals (red lines). Each trajectory is projected 72 hours from 15 m above sea level from Mace Head research station (MHD). Top right of the graph shows detailed overlay of the MHD geographic location relative to other Irish cities.

The MHD campaign was impacted by several different air masses and include both a maritime polar (*mP*) and maritime tropical (*mT*) air mass, as well as a maritime Arctic (*mA*) and continental polar (*cP*) air mass. Some of the marine air masses were modified by continental Europe, such as with *mT* air masses passing over Southern

Results 1—black carbon measurements in marine environments suggest the persistence of clean conditions

Ireland. Air mass back-trajectories calculated from MHD at a starting height of 50 m above sea level, every 12 hours for a backwards run time of 72 hours, are shown in Figure 4.5.

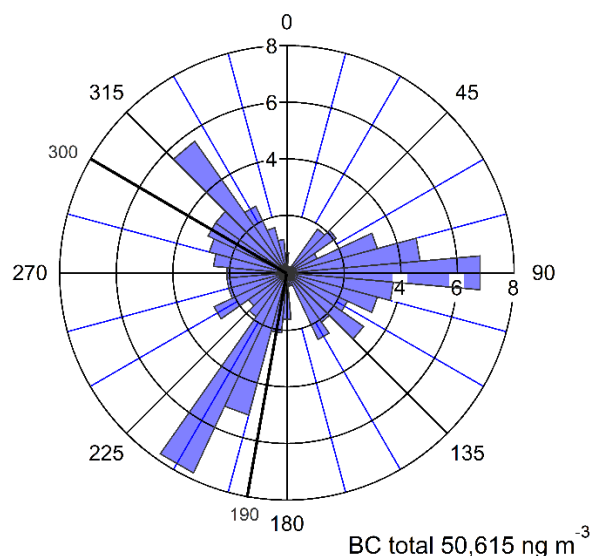


Figure 4.6. Percentage of total BC mass loading (concentration) by wind direction (0°-360°) for the month of April 2015 at Mace Head atmospheric research station (MHD). Total black carbon mass concentration measured over the entire measurement period is shown at the bottom. The percent of the total BC mass loading measured (radial lines in %) by each 10° WD increment is shown in blue as a function of WD. The MHD “clean sector” is considered between 190–300°, which is indicated in thicker black lines.

The full (SP2) BC dataset for the month of April 2015, is shown in Figure 4.6 as a total BC mass concentration loading wind rose, and also as a time series in Figure 4.7. The wind rose shows the percentage total measured BC from a certain wind direction as a function of the gross total BC concentration measured over the whole period. From the wind rose it is apparent that a large percentage (~28 %) of the total black carbon mass came from the marine sector direction with 15 % coming from between 195 - 215°. Approximately 36 % of the total BC (18,220 ng m⁻³) came from directly inland (Figure 4.6). Over the observation period, about 50,614.5 ng m⁻³ of BC was cumulatively measured, with the 0.1 ng m⁻³ (WD ~ 290°) and 680 ng m⁻³ (WD ~ 124°) being the lowest and highest hourly averaged concentration over the period (Figure 4.7). The wind rose only indicates the total mass BC loading by wind direction, but does not relay the duration or magnitude of high BC concentration measurements measured by the SP2, meaning a long period of low BC concentrations from one wind direction can appear similar to a very short period of high BC concentration. However, this information is relayed in the time series (Figure 4.7) which shows both wind direction and BC concentration. Based on the air mass trajectories a portion of

Results 1—black carbon measurements in marine environments suggest the persistence of clean conditions

the BC mass from the marine sector can be attributed to recirculation from the Irish coast. This is a commonly encountered air trajectory movement in Ireland due to the normal track of Atlantic depressions which causes cyclonic activity (Lamb, 1972). The cyclonic activity, centred over Ireland or the North East Atlantic, leads to the recirculation of continentally modified air out into the ocean, where it then approaches MHD from the marine wind direction sector. The time trends of BC and wind direction (Figure 4.7) confirm periods of frequent South Westerly winds which were within the marine sector but coincided with concentrations on the order of $10 - 1000 \text{ ng m}^{-3}$. The larger concentrations mostly coincides with cyclonic activity which circulates air down from the north over the United Kingdom and (or) mainland Western Europe out over the Atlantic again where it approaches MHD from the south west. This cyclonic activity is growing more common with increasing vigour of global circulation yearly (Sweeney, 1985).

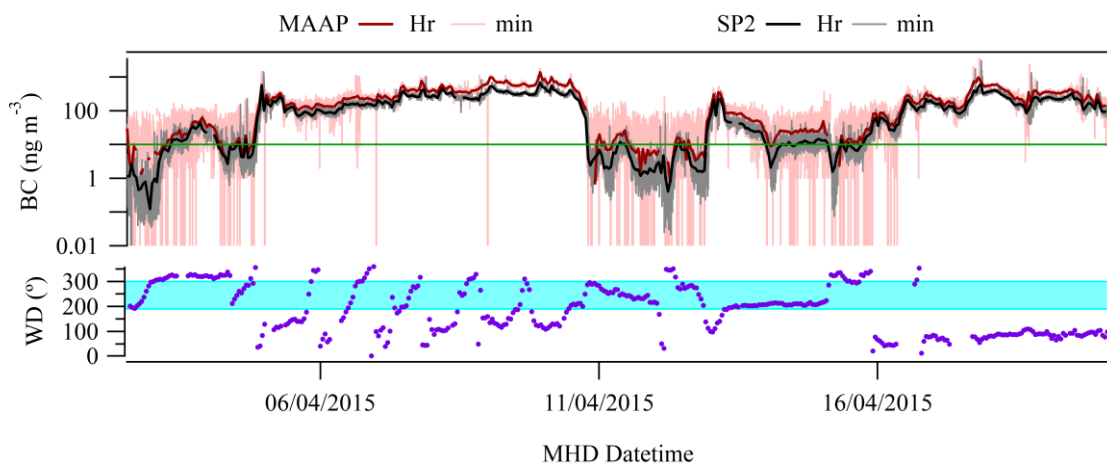


Figure 4.7. Time series of MHD BC data and wind direction (WD) data for April 2 – 20, 2015 during the MHD campaign. On top, BC data from the SP2 (black – hourly averaged, grey—1-minute resolution) and MAAP (red – hourly averaged, pink—1-minute resolution) are shown. The green line straight across indicates 7 ng m^{-3} . On the bottom, WD data is shown in degrees ($^{\circ}$), with the blue shaded area denoting clean sector WD.

Clean sector analysis at MHD follows stringent criteria which ensure the sampling of clean marine air. These criteria include wind direction ($190^{\circ} - 300^{\circ}$), a total particle concentration ($d_m > 20 \text{ nm}$) below 700 cm^{-3} , post-analysis assessment of trajectories to ensure no advection over land within 4-5 days previous, and BC mass concentrations below 15 ng m^{-3} as measured by and MAAP (or 50 ng m^{-3} as measured by an aethalometer)(Ceburnis et al., 2011). This analysis has already established that wind direction alone is not an effective filter for pollution (Figure 4.6). However, the SP2 MHD dataset, presented here as marine, is only filtered for WD on the assumption that what can reach MHD through the oceanic sector WD could be

Results 1—black carbon measurements in marine environments suggest the persistence of clean conditions

measured from a remote the remote North East Atlantic. These data, plotted as a frequency distribution (Figure 4.8) and fitted with lognormal distributions, show four concentration modes. Each mode relates to a grouped range of BC concentrations which occur, or are measured, at MHD and can each be considered here to represent different sources of BC. The lowest measured BC mode described to be within the 95th percentile (see Eq. 17) included concentrations $< 0.29 \text{ ng m}^{-3}$, which occurred 34 % of the time. The highest occurrence at 55 %, within the WD criteria, came from the second lognormal mode between 0.29 ng m^{-3} and 5 ng m^{-3} . The next mode, $5 - 21 \text{ ng m}^{-3}$, occurred for just over 10 % of time. The last two modes occurred for a combined 1.1 % of the time extending up to 85 ng m^{-3} and then up to 566 ng m^{-3} , for 0.8 % and 0.3 % of the time respectively (Table 4.1). Unlike the data presented in Grigas et al. (2017), which took all sector data from five years of MAAP measurements at MHD, the frequency distributions of the clean sector analysis used just over 150 hours of high time-resolution data. Thus, while the four modes are recorded in Table 4.1, the efficacy of a frequency distribution analysis on this length of data may be somewhat lessened, and therefore, the Grigas et al. (2017) pollution categorisation is used over the modal frequencies presented here for comparison discussed later in this analysis. Since the Grigas et al. (2017) pollution categorisation is for MAAP based mass concentrations which likely overestimate the mass concentrations measured by the SP2, a correction between the MAAP and SP2 instruments should be made and is calculated from the inter-comparison of the two instruments running simultaneously at MHD (Figure 4.7) discussed further on.

Similar to the Southern Ocean results, the lowest BC mass concentration mode in the North East Atlantic is centred on a mode peak of 0.10 ng m^{-3} . While this mode was observed nearly 3x more often in the Southern Ocean than the North East Atlantic, this is to be expected. The month of April in the Atlantic may be considered one of the most polluted months in the Atlantic, having some of the lowest occurrences of pristine days at ~ 1 day per month (Hamilton et al., 2014). The model study, Hamilton et al. (2014), reports that the North East Atlantic in another month, such as August, could have anywhere from 2-10 days of pristine weather. Since April compared with August could reasonably have a third of the pristine days, it would stand to reason that the frequency occurrence of pristine air in North East Atlantic during August would have thrice the frequency. This implies that the North East Atlantic summer would experience a similar occurrence of the BC mass concentration mode peak of 0.10 ng m^{-3} as the Southern Ocean in austral summer. The evidence of both oceans having similarly low modal concentrations (and likely BC sources) supports the assumption that the low BC mass concentration mode centred at $\sim 0.1 \text{ ng m}^{-3}$ may be considered a baseline for global clean marine conditions. A comparison of the Southern Ocean and MHD fitted frequency distributions of the SP2 BC measurements can be seen in Figure 4.9.

Results 1—black carbon measurements in marine environments suggest the persistence of clean conditions

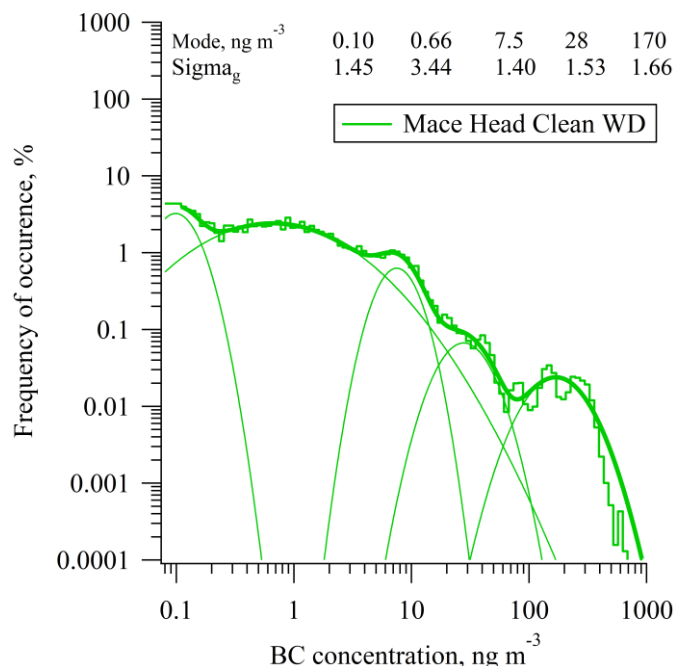


Figure 4.8. Frequency distribution plot of MHD BC mass concentration measurements from the SP2 instrument. The graph shows BC mass concentrations for bins lognormally spaced ($d\log BC \approx 0.06 \text{ ng m}^{-3}$ in depth). Lognormal modes are shown separate from the combine frequency distribution with the lognormal mode position and geometric standard deviation (σ_g) shown at top.

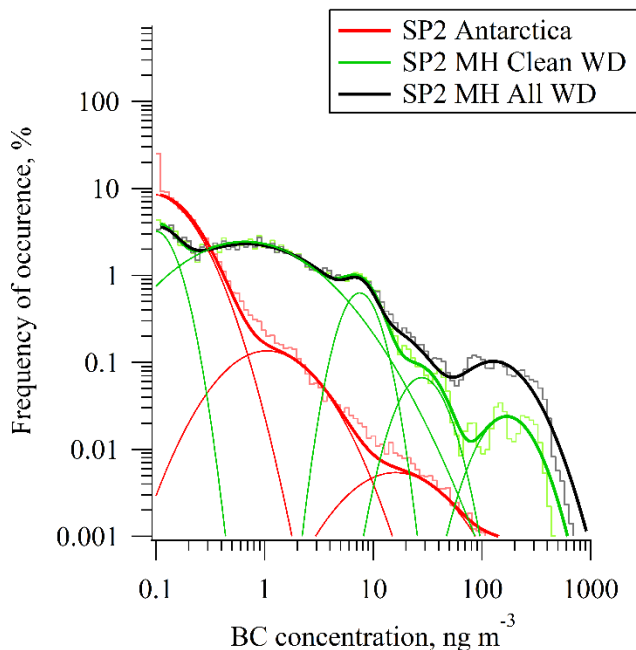


Figure 4.9. Comparison between the fitted frequency distributions of three sets of BC data. The distribution for Antarctica is represented in red. The MHD data is represented by two distributions of the SP2 data, filtered for clean WD (green) and unfiltered (black). The actual frequency distribution data which was fitted is shown in lighter shades of the aforementioned colours. Fitted distributions for Antarctica and MHD clean WD data are shown with peak modes.

Results 1—black carbon measurements in marine environments suggest the persistence of clean conditions

Comparing SP2 and MAAP parallel measurements

While only 36 % of the MHD SP2 observation period was compliant with wind directions clean sector criteria, the full month of data was also analysed as a frequency distribution (Figure 4.9). The full month differs from the oceanic sector WD data in that there is increased frequency of more polluted modes. Additionally, a comparison can be made between simultaneous MAAP measurements during that time. The BC datasets from Mace Head (SP2 and MAAP) were averaged hourly to reduce noise from the MAAP time series (time series raw and averaged can be seen in Figure 4.7). The hourly datasets of the SP2 and MAAP were then correlated using a linear regression method, which resolves Pearson correlation coefficients (r) and fit equations.

The trend of SP2 data against MAAP data (Figure 4.10) shows decreasing agreement with increasing mass concentrations. The MAAP measures black carbon optically through the absorption of radiation. When non-BC absorbing particles are present the MAAP overestimates BC concentration due to interference with the other absorbing matter (Cappa et al., 2008). Due to the interference overestimation could be the result of calibration conversion for absorption to mass in the MAAP if it is calibrated preferentially for clean conditions (Slowik et al., 2007). Therefore, the trend between SP2 and MAAP data must be fit with separate linear regressions to accurately compare BC concentration regimes between the two instruments. In cleaner conditions ($<30 \text{ ng m}^{-3}$), the MAAP overestimates by a smaller fraction, but is offset by about $+2.3 \text{ ng m}^{-3}$ from measurements made by the SP2 (blue line in Figure 4.10). Conversely, in more pollution ($>30 \text{ ng m}^{-3}$) the MAAP tends to overestimate BC more but without a significant offset (red and black lines Figure 4.10). To accommodate this in the analysis presented here, linear regressions were fit from $0 - 30 \text{ ng m}^{-3}$ (to represent clean conditions), $0 - 150 \text{ ng m}^{-3}$ and $150 - 13071 \text{ ng m}^{-3}$ (maximum data point) detection on the MAAP scale. The results show relatively good agreement in each case with $r = 0.990$, $r = 0.987$, and $r = 0.985$ for the lower to higher concentration regressions, respectively. From these it is seen that the MAAP overestimated BC differently for each BC concentration regime. At the two lower concentration regimes the MAAP overestimates by a little less than a third, while at the highest concentration regime (red line in Figure 4.10) it overestimates BC by a little less than half. It is important to note that at BC concentrations associated with pristine conditions (MAAP measuring $< 15 \text{ ng m}^{-3}$) the small offset in the linear regression trend represents a significant change in BC concentration measured by the SP2. For this reason the pristine and clean limits must be treated separately for comparison.

The (approximately) 44 % overestimation of the BC mass concentration by the MAAP appears extreme but another comparison of an MAAP to SP2 in Raatikainen et al.

Results 1—black carbon measurements in marine environments suggest the persistence of clean conditions

(2015), reported an even more extreme over-estimation of the MAAP measurements (from 0 – 700 ng m⁻³) by 500 % of the SP2 measurements. That study could only justify the overestimation with the assumption that some large fraction of the absorbent material (possibly brown carbon) being optically measured by the SP2 had high volatility or low absorption at the wavelength used by the SP2. However, a 50 % overestimation of mass by the MAAP as compared with the SP2 has also been reported in Slowik et al. (2007), and this overestimation is proposed to be the result of calibration conversion for absorption to mass in the MAAP. The calibration standard used for the SP2 may also not be ideal for BC found in the North East Atlantic and may combine with the MAAP calibration to reasonably explain a portion of the overestimation, although no more than about a 30 % difference, as an instrumental calibration issue would be consistent over all the linear fits.

According to Grigas et al. (2017), pristine air occurs at MHD when BC concentrations < 15 ng m⁻³ as measured by the MAAP. It is estimated that on average this corresponds to an SP2 reading of 7.4 or ~ 7 ng m⁻³, implying that the first two frequency SP2 BC modes (see Table 4.1) in the North Atlantic clean wind sector dataset can be considered pristine. More conversions from MAAP sector classifications to SP2 can be seen in Table 4.2. Applying this further to the SP2 BC frequency modes measured at MHD the third mode would straddle the pristine (BC < 7 ng m⁻³) and clean classification (7 ng m⁻³ < BC < 34 ng m⁻³). The fourth peak falls into the moderately polluted category, with the final peak falls into the polluted category. The statistical grouping of BC mass concentrations (from a clean sector wind direction of 190° – 300°) based upon this categorisation is shown in Figure 4.11a, which also shows the frequency of occurrence of the classification. Based on clean sector wind direction alone, this study finds that springtime aerosol is either within the pristine or clean marine air category 65 % of the time at MHD, and in general (without clean sector wind direction criteria) springtime aerosol is within those classifications 2.5 % of the time (see Figure 4.11b).

Results 1—black carbon measurements in marine environments suggest the persistence of clean conditions

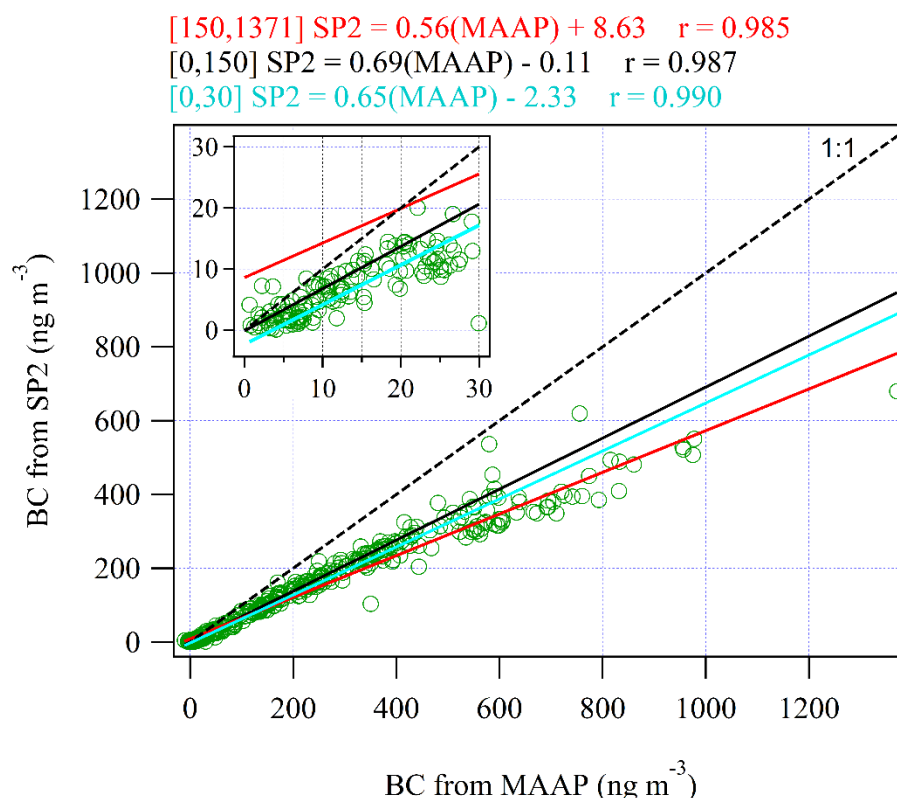


Figure 4.10. Comparison of the SP2 and MAAP measurements running simultaneously at Mace Head for the month of April 2015. Green points are for averaged hour resolution data. A 1:1 fit line is shown in back dashes. Red line is a least square fit linear regression for data on the range of MAAP BC concentrations of 150 – 1371 ng m^{-3} , where the black line is the same but for concentrations below 150 ng m^{-3} , and the blue line for concentrations of 0 – 30 ng m^{-3} . Comparison is not linear over all concentrations, so this is used to derive relative BC concentration over different regimes. If MAAP concentration is 15 ng m^{-3} , then SP2 concentration $\sim 7 \text{ ng m}^{-3}$, and where the MAAP concentration would read 50 ng m^{-3} , the SP2 would read $\sim 34 \text{ ng m}^{-3}$.

Table 4.2. The classification of air masses arriving at MHD from BC mass concentration data. The classifications were derived by Grigas et al. (2017) based upon five years of MAAP data from MHD. Using SP2 and MAAP comparisons the equivalent mass concentrations as measured by an SP2 instrument are reported.

BC sector classification	Pristine	Clean	moderately polluted	polluted	extremely polluted
Grigas et al. (2017) MAAP	< 15	15 - 50	50 - 300	300 - 1000	> 1000
SP2 equivalent	< 7	7 - 34	34 - 177	177 - 570	> 570

Results 1—black carbon measurements in marine environments suggest the persistence of clean conditions

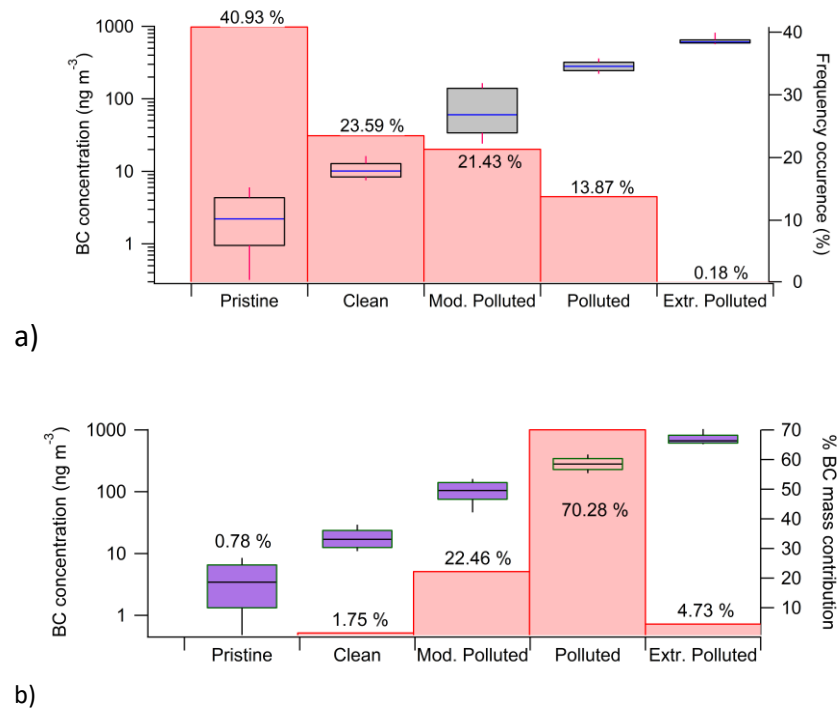


Figure 4.11. a) Black carbon concentrations are shown with statistical grouping by box plot (left axis) and by frequency of occurrence (right axis) for WD clean data. b) Black carbon mass concentrations are shown with statistical grouping by box plot (left axis) and the percent contribution to total BC mass measured (right axis) for all MHD SP2 data. Both plots are as a function of BC sector classification (see Table 6.2) defined in Grigas et al. (2017) and adapted to SP2 concentrations.

4.4 How prevalent is BC in the remote marine environment?

Overall, the Southern Ocean proved reasonably devoid of persistent intense pollution, with 93 % of a two-month campaign showing less than 0.4 ng m⁻³ of BC mass (this would translate to about 4.2 ng m⁻³ reading on the MAAP). Island activity was shown to influence the ambient aerosol with ~ 50 ng m⁻³ of BC measured by the SP2 (~73 ng m⁻³ MAAP), making local sources responsible for enhancing BC concentration up to levels which exceed clean air criteria even by North East Atlantic (MHD) standards.

MHD is also clean for large periods in spring with an average exposure of the marine North East Atlantic environment to 35 % of the time of moderately – extremely polluted periods. The rest of the time can be considered clean, being pristine (<7 ng m⁻³) about 41 % of the time. When inter-comparing the simultaneous MAAP and SP2 measurements at MHD, different linear fits were used for different BC mass

Results 1—black carbon measurements in marine environments suggest the persistence of clean conditions

concentration regimes. The clean concentrations ($<30 \text{ ng m}^{-3}$) have a slightly different y-intercept to the moderately clean concentrations ($<150 \text{ ng m}^{-3}$) and this alters concentrations on the order of 1 ng m^{-3} or less, such as with 0.4 ng m^{-3} . Each relationship is described by a different linear fit: $[BC_{SP2}] = 0.65 \cdot [BC_{MAAP}] - 2.33$ for $BC_{MAAP} < 30 \text{ ng m}^{-3}$, $[BC_{SP2}] = 0.69 \cdot [BC_{MAAP}] - 0.11$ for $BC_{MAAP} < 150 \text{ ng m}^{-3}$, and $[BC_{SP2}] = 0.56 \cdot [BC_{MAAP}] + 8.63$ for $150 \text{ ng m}^{-3} < BC_{MAAP}$. In pristine conditions an SP2 measurement of zero BC would be equivalent to a MAAP measurement of 3.6 ng m^{-3} .

The Southern Ocean SP2 measurements are of the same magnitude as those reported by other studies. Shank et al. (2012), reported a maximum clean-condition BC concentration of 1.8 ng m^{-3} in the Southern Pacific area where our study found a clean-condition BC concentration of 0.4 ng m^{-3} for the Scotia Sea, implying that BC mass concentrations may range within the Southern Ocean region. The Neumayer station reported nearly constant long-term yearly BC measurements of $\sim 2 \text{ ng m}^{-3}$ (MAAP) (Weller et al., 2013) and would be equivalent to an SP2 reading of nominally zero. This would suggest that coastal stations like these experience similar levels of pollution as compared with the open ocean around Antarctica.

The Northern and Southern Hemispheres experience different levels of pollution due, perhaps, to a combination of seasonal differences and the increased industrial activity and population of the Northern Hemisphere. However, this study shows that remote Oceans, such as the North East Atlantic and Southern Ocean experience similarly low levels of BC pollution ($\sim 0.1 \text{ ng m}^{-3}$). Discrepancies in frequency of occurrence should be ignored as the different seasonal measurement periods create inequity in the comparison between the two remote oceanic systems. Each BC concentration mode in the frequency of occurrence graphs (e.g. Figure 4.9) represents a different source of BC. The overlapping position of the modes in the two oceans is suggestive of similar BC sources, having equally small concentration modal positions regardless of hemisphere. This implies that the North East Atlantic can be as pristine as the Southern Ocean. Additionally, during periods of pristine BC mass concentration conditions ($<0.4 \text{ ng m}^{-3}$), no correlation was found between OM and BC ($r^2 = 0.002$) in the Southern Ocean, matching similar results of non-correlation ($r^2 = 0.006$) for pristine periods observed over the North East Atlantic. This suggests that while limits of clean marine conditions may vary, once applied correctly, marine aerosol can be considered to be free of anthropogenic influence.

5. Results 2—summertime aerosol physico-chemical properties and links to cloud activation in the Southern Ocean

This chapter focuses on aerosol properties in the Southern Ocean, around Antarctica, through the Drake Passage and Scotia Sea region. The Southern Ocean is an ideal natural laboratory to study marine aerosol production and sources as demonstrated by the previous chapter. This chapter seeks to characterise physio-chemical properties of the summertime aerosol in the Scotia Sea region of the Southern Ocean. This location was originally chosen for its proximity to the Weddell Sea, which experiences intensive below/in-ice algal blooms where increased production of secondary marine aerosol has been measured (O'Dowd et al., 1997a; Zemelink et al., 2008; Zemelink et al., 2005). Increased concentrations of DMSP, the precursor form of aqueous DMS, have been reported for phytoplankton species in colder temperatures (likely acting as a cryoprotectant) (Karsten et al., 1996) and in ice-covered waters (Galindo et al., 2015). As the Weddell Sea is one of the coldest seas in the world, temperature related increases in DMSP production are extremely relevant. In summer, some of the sheet ice breaks up and becomes pack ice and a water-air interface is established. DMSP also has a strong dependence on bloom species type, where multiple species of dinoflagellates and coccolithophores are associated with greater DMSP production and diatom blooms are often associated with negligible concentrations of DMSP (Lizotte et al., 2012). A study (Lizotte et al., 2017) conducted in the Southern Ocean region during the austral summer reported that sampled blooms dominated by dinoflagellates and coccolithophores had DMSP concentrations which significantly correlated to Chl-*a* measurements, suggesting that in these seasonal blooms, DMSP production may be tracked using autotrophic biomass. Due to both the absence of continental contamination and also the abundance of blooms in the Scotia Sea and Weddell Sea region, the Southern Ocean offers unique measurement opportunities to study the effects of biological activity on CCN properties.

This chapter presents data gathered from a suite of in-situ instrumentation on a sea expedition around the Drake Passage of the Southern Ocean from January 2nd to February 12th, 2015. A detailed description of the instrumentation set-up can be found in Section 3.1.1. The following is an investigation of the aerosol physio-chemical traits of both on-site lab-generated sea spray and ambient aerosol. Physical and chemical properties of PM₁ sub-cloud ambient particles are characterised for steady-state air masses encountered during the cruise.

5.1 CCN in regional air masses

This section characterises steady-state aerosol properties associated with different air masses in the oceanic region. Analysis of the data revealed 12 pseudo-steady state periods, shown in Figure 5.1 (and further described in Table 5.1), from which 2 main prominent air masses were identified and one less prominent ('pseudo-steady-state' defined in Section 3.5.1). The two predominant air masses were continental Antarctica (*cAA*) and maritime polar (*mP*), while the less frequent air mass was maritime tropical (*mT*) which was generally associated with polluted incursions from South American outflow, as shown in Figure 5.2.

The CCNC used during the cruise was calibrated as described in Section 3.3.1. Following arguments made in Rose et al.(2008), charge corrections were not deemed necessary since no sigmoidal shoulder appeared in the data. The CCNC cycled through five water supersaturations which after calibration were found to be 0.08, 0.29, 0.47, 0.82, and 1.48 %. Critical dry diameters for this supersaturation range were obtained at a minimum time resolution of one hour.

5.1.1 Physico-chemical aerosol properties in *cAA* air masses

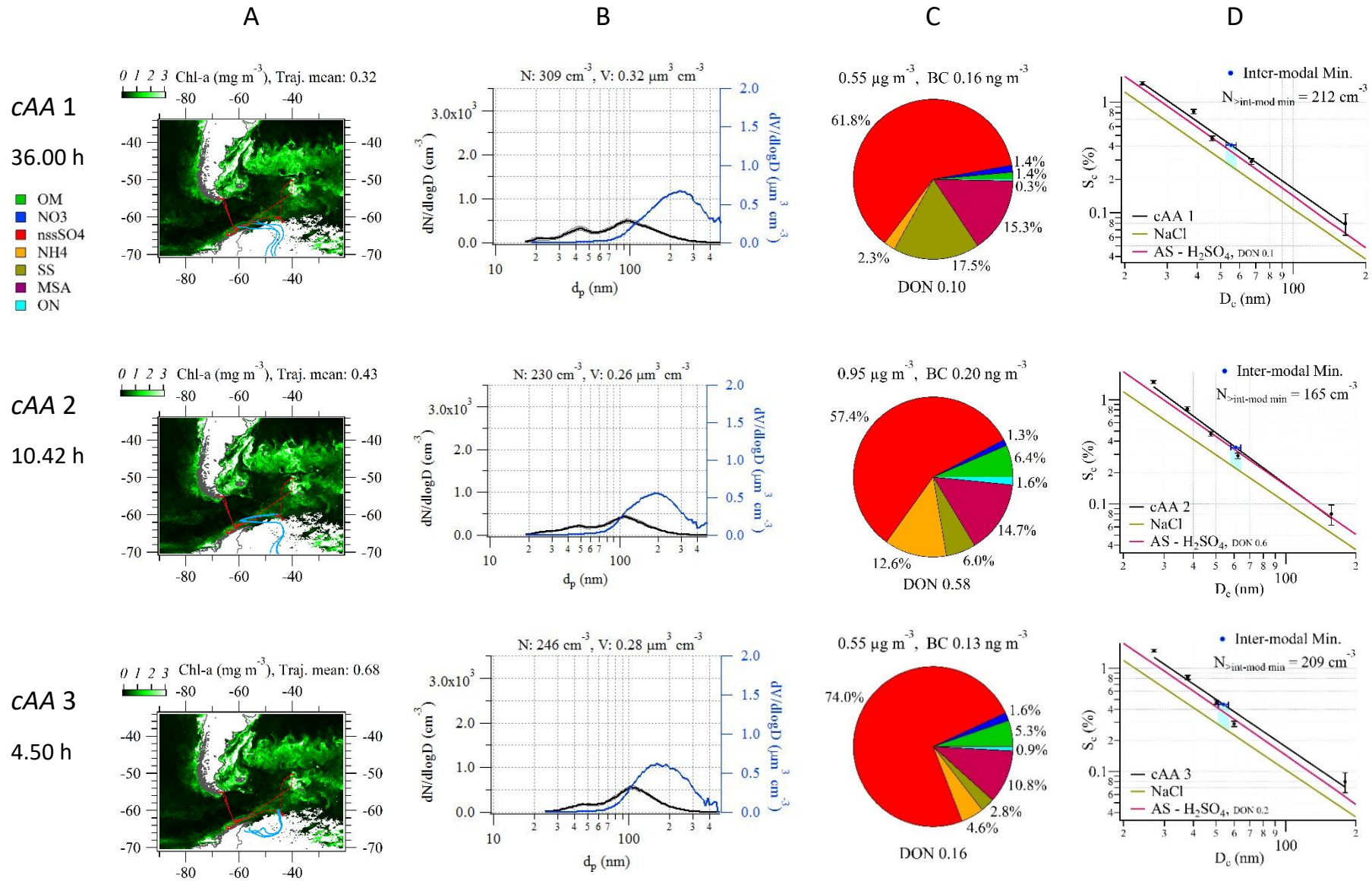
The *cAA* air masses formed over Antarctica are amongst the coldest and driest in the world. During this cruise, *cAA* air masses encountered were sourced from the Antarctic plateaux flowing Northward in the katabatic outflowing wind driven by the subsiding free troposphere (FT) air in the high-pressure polar region above the plateaux. The *cAA* outflow traverses initially ice surfaces which evolve into broken pack ice as the air advects out over the Weddell Sea, *en route* to the open oceanic waters. In summer, as the pack ice replaces the winter sheet ice, the biologically-rich waters are exposed, presumably enabling the sea-air flux of particles and gases. HYSPLIT (Stein et al., 2015) trajectories reveal that the air flow over the Weddell Sea was generally associated with stagnant high-pressure systems taking, at times, up to 90-120 hours to penetrate through to the open waters. All the *cAA* periods discussed here were affected by the passage over the Weddell Sea before reaching the ship, so they are, strictly speaking, modified *cAA*. These periods show the highest Chl-*a* mean concentration along the trajectory paths (see Section 3.5.1) and are likely influenced by biologically productive waters in the Weddell Sea.

Each air mass hosted aerosol with distinctive characteristics associated with that particular air mass, therefore both the *cAA* cases and *mP* cases were each consolidated, respectively, into a representative air mass type 'average' for ease of comparison, shown in Figure 5.3. The individual periods included in the consolidated

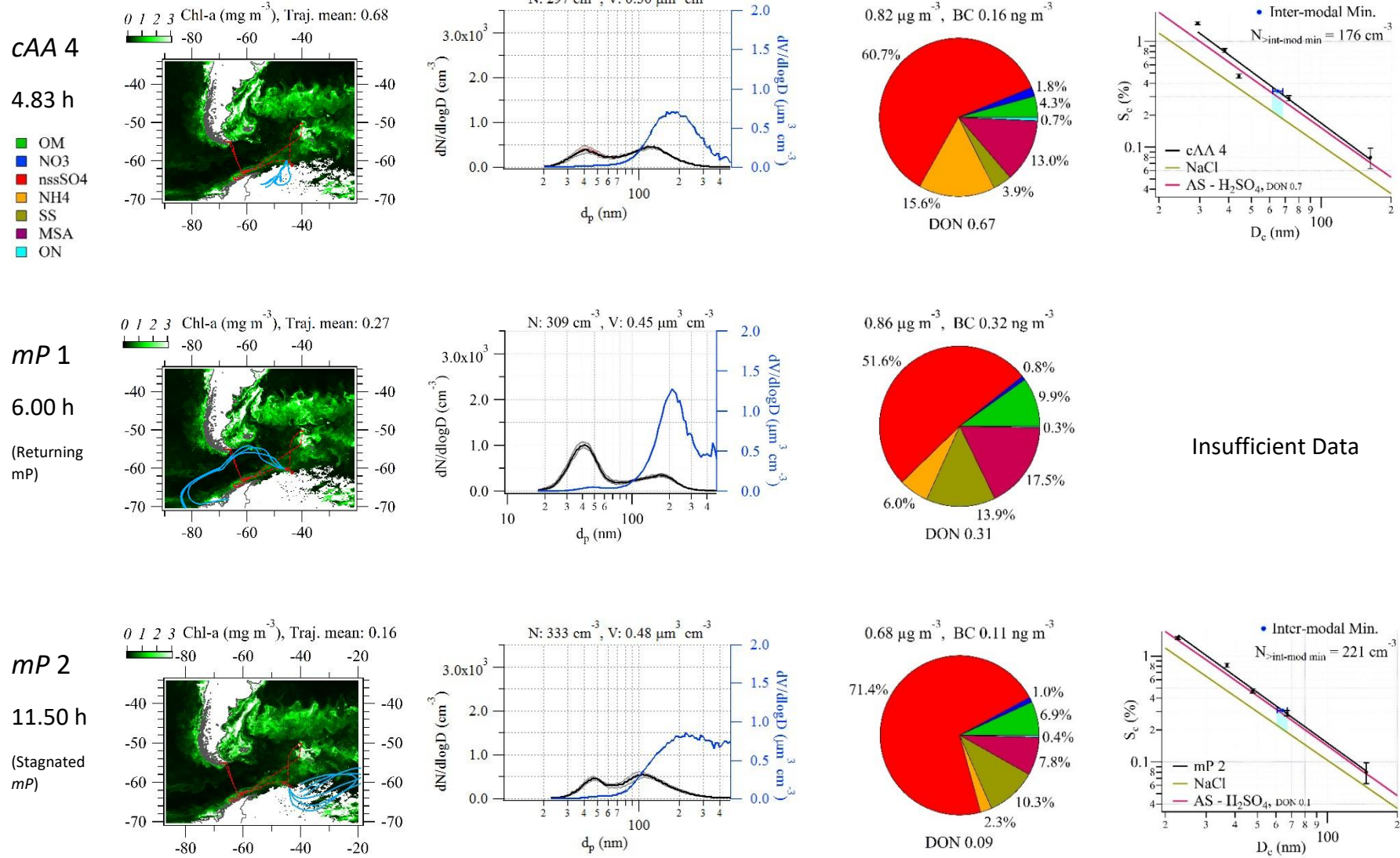
Results 2—summertime aerosol physico-chemical properties and links to cloud activation in the Southern Ocean

dataset are displayed in Figure 5.1, where the *cAA* case is combined *cAA* periods 1, 2, 3, and 4, and where the *mP* case is combined *mP* periods 1, 3, 4, and 5).

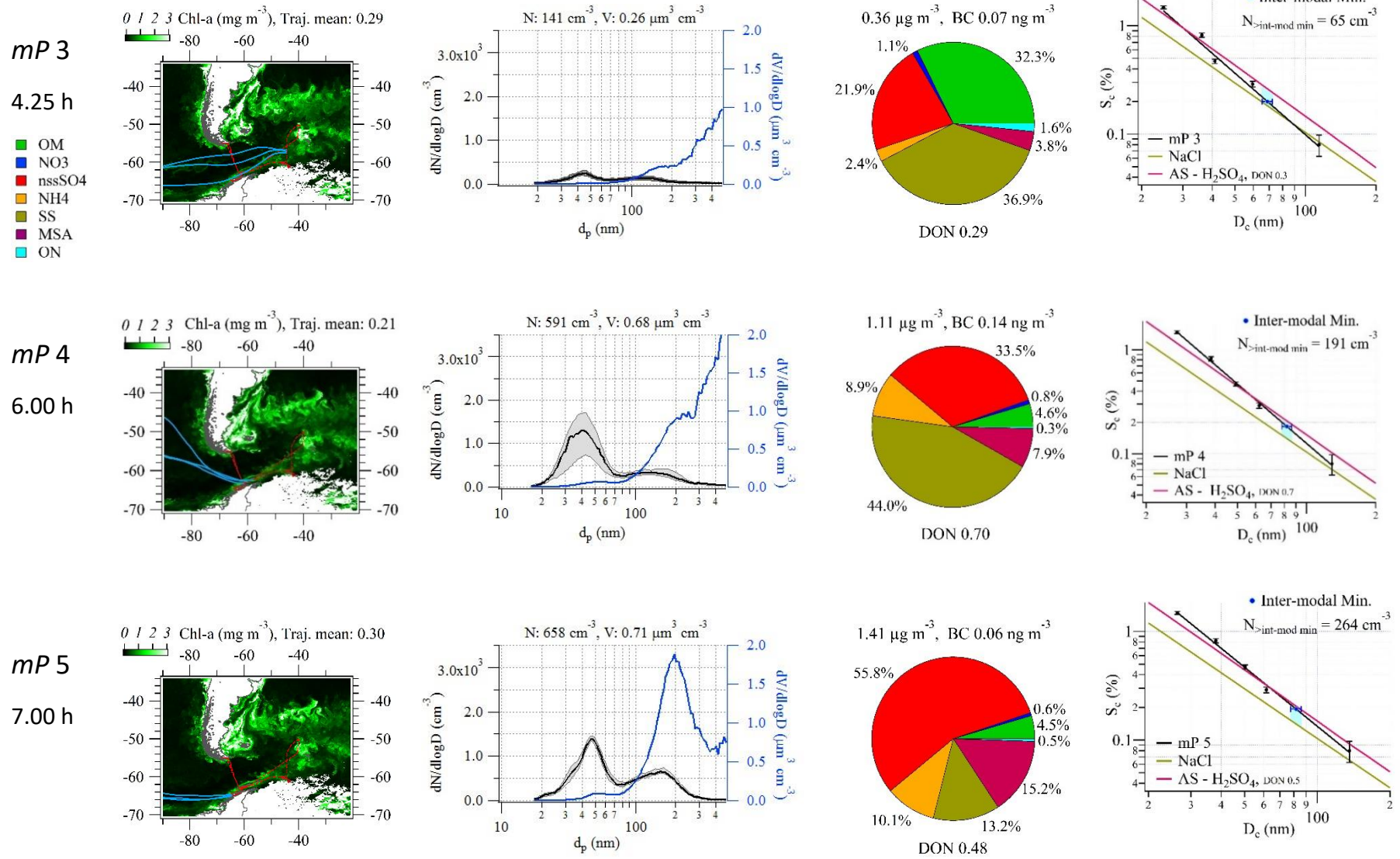
Results 2—summertime aerosol physico-chemical properties and links to cloud activation in the Southern Ocean



Results 2—summertime aerosol physico-chemical properties and links to cloud activation in the Southern Ocean



Results 2—summertime aerosol physico-chemical properties and links to cloud activation in the Southern Ocean

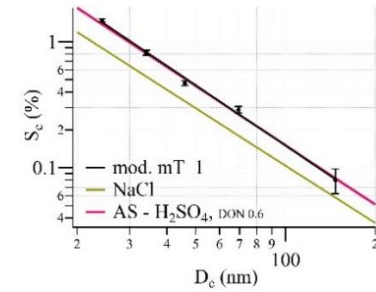
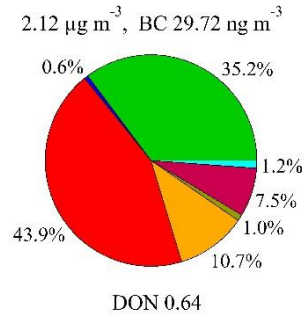
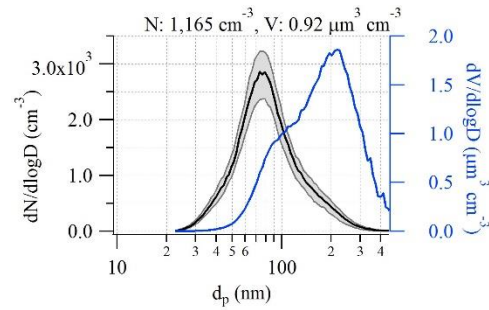
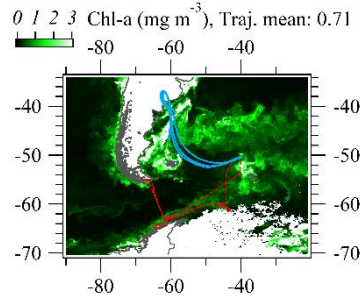


Results 2—summertime aerosol physico-chemical properties and links to cloud activation in the Southern Ocean

mT 1

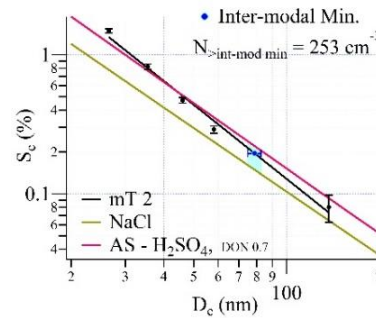
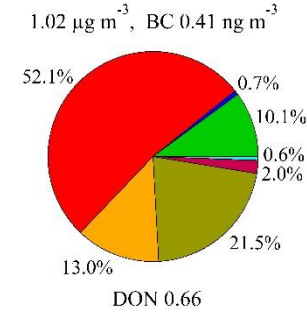
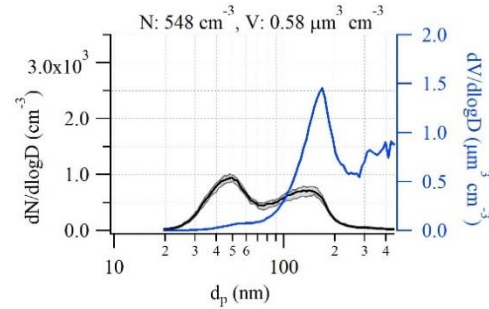
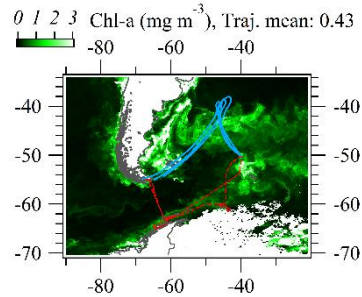
8.50 h
(Modified mT)

- OM
- NO3
- nssSO4
- NH4
- SS
- MSA
- ON



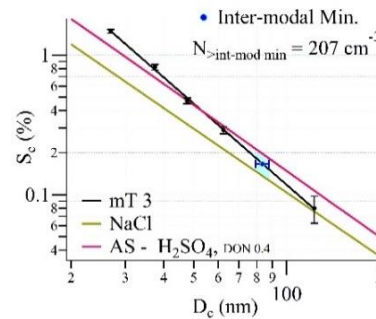
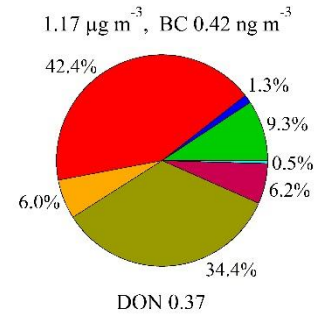
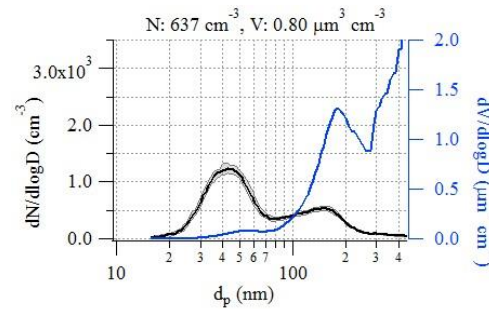
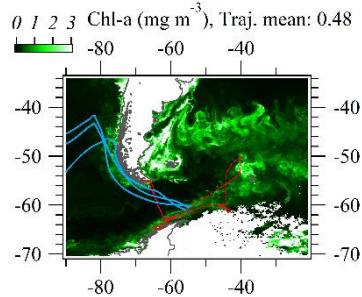
mT 2

5.92 h



mT 3

6.00 h



Results 2—summertime aerosol physico-chemical properties and links to cloud activation in the Southern Ocean

Figure 5.1. Aerosol chemical and physical characterization, each presented period listed in chronological order by air mass. Each period has 5 columns, descriptor, A, B, C, and D. The descriptor lists period number followed by any air mass modification then the steady-state duration of the period. [A] Chl-*a* satellite daily retrievals with overlaid air mass back-trajectories extracted from HYSPLIT (Rolph, 2016; Stein et al., 2015). In dotted red, PEGASO cruise ship path. In blue, 120 hr back trajectory ending 100m AGL directly above the ship location. There are three trajectories, representing the air mass origin at the start, middle, and end of the period. Chl-*a* satellite retrievals are at $0.1^\circ \times 0.1^\circ$ resolution, where the darkest green represents close to 0 mg m^{-3} , and nearly white represents 3 mg m^{-3} average Chl-*a* in that pixel. Chl-*a* scale on the top left and the average Chl-*a* concentration during the period under the trajectories on the top right corner. [B] Particle number (black) and volume (blue) size distributions: number distribution variance during the period is shown in grey. On top are the total average number of particles [cm^{-3}] (N), and total average particulate volume [$\mu\text{m}^3 \text{ cm}^{-3}$] (V). [C] Pie chart of chemical mass fractions (OM: organic matter, SS: sea-salt, ON: organic nitrogen). On top, submicron particle mass [$\mu\text{g m}^{-3}$] followed by black carbon mass [ng m^{-3}] (BC). On bottom, degree of neutralization (DON) where 1 means that all sulphate and nitrate exist as ammonium sulphate and ammonium nitrate (Adams et al., 1999). [D] CCN activation efficiency curves. Graph shows critical supersaturation against critical dry diameter; the slope derived from the measurements during the period is shown in black (supersaturation uncertainty presented by vertical error bars), and the predicted slopes of partially neutralized (based on DON) sulphuric acid from the AIOMFAC model shown in red while the NaCl line shown in olive brown predicted by AP3 model (Rose et al., 2008). The inter-modal minimum point, extracted from the log-normal fit of number-size-distributions, shown in blue with $\pm 5\%$ size error. At top, the number of particles larger than the inter-modal minimum.

Results 2—summertime aerosol physico-chemical properties and links to cloud activation in the Southern Ocean

Table 5.1. Log-normal parameter fits for number and volume size distributions. Particle size, modal spread (δ), and hygroscopicity parameter (κ) for fitted number—size distribution peaks shown on left. Fitted particle volume and spread peaks shown on right. Dashed lines represent the lack of more peaks in the volumetric distributions. Missing κ -values indicate that lognormally fitted peak diameters were outside of sizes resolved by CCNC.

	N			V	
	Peak, nm	δ	κ	Peak, nm	δ
<i>cAA 1</i>	24.4	1.3	0.48	-	-
	40.8	1.2	0.48	-	-
	101.5	1.5	0.50	130	1.4
	-	-	-	230	1.4
<i>cAA 2</i>	28.7	1.2	0.40	-	-
	46.2	1.2	0.46	-	-
	111.1	1.4	0.59	186	1.6
	-	-	-	480	1.1
<i>cAA 3</i>	44.1	1.2	0.43	-	-
	109.1	1.4	0.47	129.3	1.3
	-	-	-	214.2	1.4
<i>cAA 4</i>	40.6	1.3	0.38	46.7	1.2
	118.6	1.5	0.48	184.5	1.5
<i>mP 1</i>	40.5	1.3	0.34	49.6	1.3
	147	1.4	0.53	212	1.4
	-	-	-	455	1.2
<i>mP 2</i>	45.4	1.2	0.52	-	-
	109.5	1.5	0.61	211.4	1.7
	-	-	-	562.7	1.4
<i>mP 3</i>	27.1	1.2	0.51	-	-
	43.2	1.2	0.73	-	-
	114	1.5	1.43	160.4	1.4
	322.8	1.2	-	534.8	1.6
<i>mP 4</i>	39.5	1.3	0.42	49.8	1.3
	126.1	1.5	1.06	231.5	1.6
	304.2	1.5	-	589.3	1.4
<i>mP 5</i>	22.5	1.2	-	-	-
	45.9	1.3	0.47	53.3	1.5
	139.6	1.4	-	198	1.4
	-	-	-	456.6	1.2
<i>mT mod.</i> 1	43.2	1.3	0.52	-	-
	74	1.3	0.58	94.1	1.3
	118	1.6	0.57	208.7	1.4
<i>mT 2</i>	46.8	1.3	0.55	57.3	1.3
	127.2	1.4	1.03	159.3	1.3
	343.7	1.2	-	391.6	1.4
<i>mT 3</i>	42.5	1.4	0.48	57	1.4
	136.3	1.4	-	177.6	1.3
	371	1.2	-	465.2	1.4

Results 2—summertime aerosol physico-chemical properties and links to cloud activation in the Southern Ocean

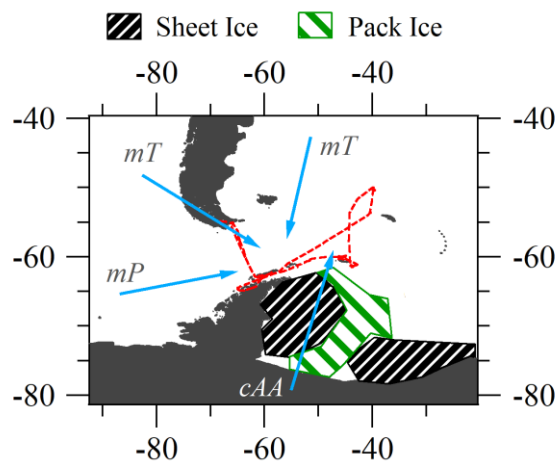


Figure 5.2. Map of Southern Ocean region, ship course marked in red. Movement of air masses from three principal source regions shown in blue arrows; continental Antarctic (*cAA*), maritime Polar (*mP*) from the West, and maritime tropical (*mT*) or modified-*mT*, both from north and northwest of -60° latitude. Approximate summer regions of pack ice (green striped) and lasting sheet ice (black striped) in the Weddell Sea are shown.

For the *cAA* case average, the total aerosol and CCN concentrations (at the highest measured supersaturation of 0.8 %) were $270 \pm 40 \text{ cm}^{-3}$ and $217 \pm 31 \text{ cm}^{-3}$, respectively. The submicron size distribution was bimodal, exhibiting a log-normal Aitken mode distribution with modal diameter peaking at 42 nm and a log-normal accumulation mode distribution with modal diameter peaking slightly larger than 100 nm (see Table 5.2). The latter mode contributed 70 % of the submicron number concentration. When the bimodal distribution is fitted with log-normal modes, the inter-modal minimum can be accurately calculated to be 56 nm (see Table 5.3). The *cAA* air mass average mass concentration was $0.60 \pm 0.16 \mu\text{g m}^{-3}$, with black carbon concentrations of 0.17 ng m^{-3} confirming the pristine nature of the air, and DON_{mol} of 0.17 pointing to a quite acidic aerosol. Sea-salt mass fraction derived from the AMS reveals a very modest 16 % contribution ($0.095 \mu\text{g m}^{-3}$) to the total PM_{10} mass, and even smaller contribution from OM (2 %). Most of the chemical composition is comprised of nss-SO_4 (61 % by mass), ammonium (4 %), and methanesulphonic acid (MSA, 15 %).

The associated critical diameter curve (i.e. S_c v D_c), or activation lines, for *cAA* aerosol indicates a chemically homogeneous aerosol as a function of size but with activation efficiency slightly less than ammonium sulphate (i.e. there is a ~ 12 % deviation in the S_c for the environmental sample compared to that theoretically calculated for partially neutralised sulphuric acid at 27 nm, and a ~ 7 % deviation at 105 nm). The activation lines depend on the hygroscopicity parameter κ , which in our case is derived from CCN activation measurements; however, CCN-derived κ -values display a variance, dependent on particle size (the Kelvin effect) whereby smaller Aitken

Results 2—summertime aerosol physico-chemical properties and links to cloud activation in the Southern Ocean

mode particle sizes show the largest κ variance. This variance arises in κ -Köhler theory, as κ is associated with the water activity of a droplet rather than its size. This section of the Southern Ocean study uses sophisticated water activity vs. composition resolved values based on the Aerosol Inorganic-Organic Mixtures Functional groups Activity Coefficients (AIOMFAC) model (Appendix B.1). This can be seen for a species like ammonium sulphate for which κ -values differ from the accepted value of 0.61 (Petters and Kreidenweis, 2007) with size-dependence (Ovadnevaite et al., 2017). For the *cAA* activation efficiency curve, small differences between D_c show variations in κ ($\sim 7\%$ difference in κ at 27 nm up to $\sim 14\%$ difference of κ at 104 nm, see Table 5.2) which are not within the bounds of the expected variations and point to some slight chemical inhomogeneity in the measured size range. As deviations may arise in κ -values when the chemical composition of the aerosol is size dependent, κ -values are listed with respect to the particle diameter (D_p) for modal number-size distribution peaks (Table 5.1 and 5.2).

On the S_c - D_c plot (Figure 5.3), the inter-modal minimum (taken from the aerosol size-distribution and thought to represent the average critical activation diameter for the activation of the size distribution into ambient clouds) occurs at a critical supersaturation of $\sim 0.40\%$. Using the theoretically derived activation curves of partially neutralised sulphate as a comparison, the inter-modal minimum occurs at a D_c on the measured environmental activation curve well above the corresponding D_c on the theoretically derived curve. This means that the S_c at the inter-modal minimum of the measured aerosol is larger than the S_c of aerosol composed entirely of partially or completely neutralised sulphate at that same size.

This is a reduction of activation potential from that of ammonium sulphate particles. As this is in opposition to the increase in activation potentials that would be affected by sea-salt and/or $(\text{NH}_4)_2\text{SO}_4$ - H_2SO_4 aerosol, the reduction is instead likely due to a mixture of (water-soluble) organics and NH_4 neutralising MSA (see Figure 5.4). This analysis (see Section 3.5.5) suggests little contribution of primary sea spray aerosol to ambient *cAA* CCN abundance.

Results 2—summertime aerosol physico-chemical properties and links to cloud activation in the Southern Ocean

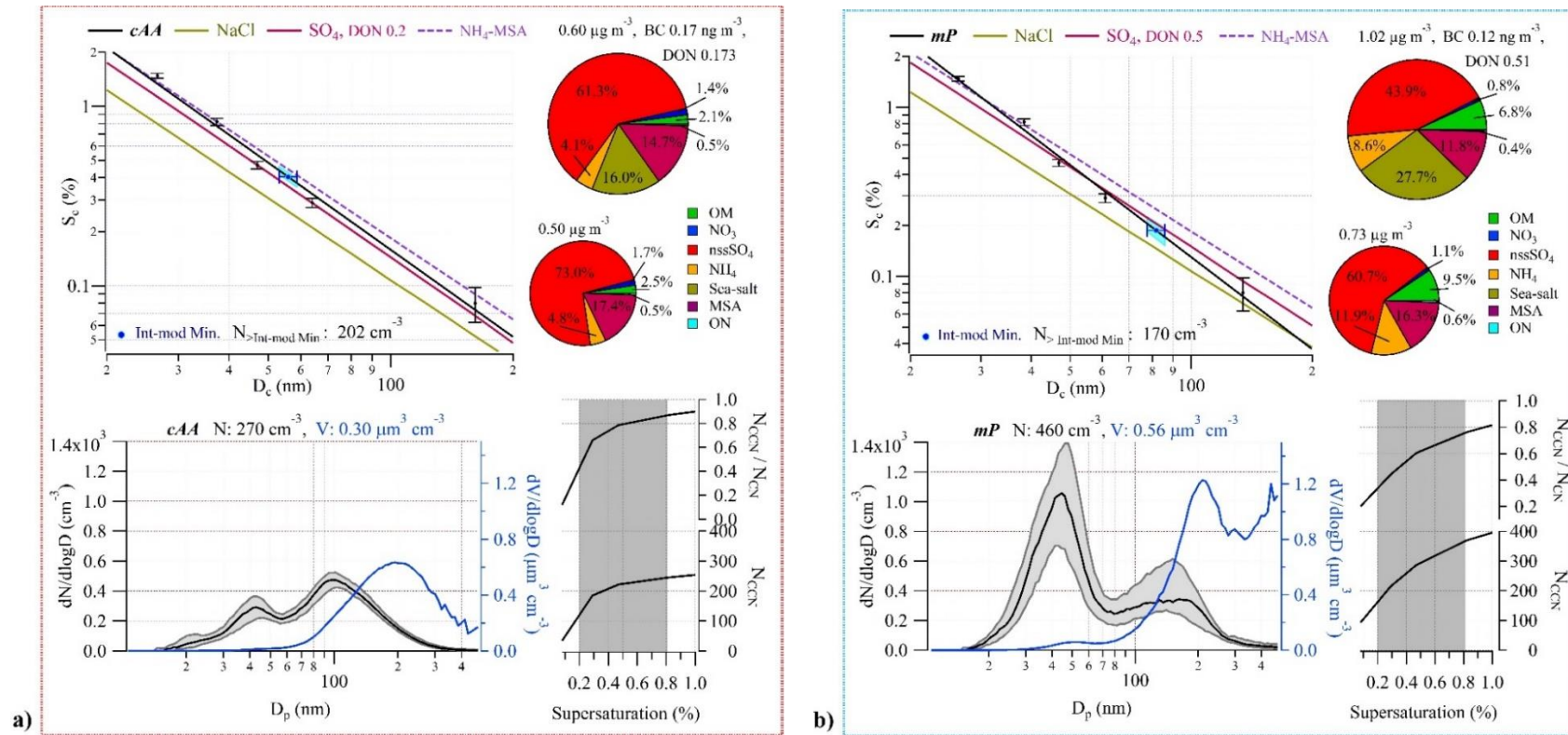


Figure 5.3. Physical and chemical properties of *cAA* (Weddell Sea influenced) air masses (a) and *mP* air masses (b). All data from each steady-state case are lumped together into an air mass average. Bottom left: Median number-size distribution (black) and volumetric size distribution (blue), with D_p the SMPS-derived dry particle diameter. Shaded grey area represents 25th -75th percentile range with the total particle number and corresponding volume concentrations noted at the top. Bottom right: On top, the ratio of CCN to all particles greater than 20 nm, on bottom, the total number of CCN for varying supersaturation. Shaded range of supersaturations represent typical values for marine stratocumulus clouds. Top left: CCN activation efficiency as a function of critical supersaturation and particle diameter, on top, the Inter-modal minima indicated in blue, with 10 % SMPS sizing error (the blue shaded region corresponds to the spread of S_c values considering SMPS sizing errors) and the total number concentration of particles at sizes greater than the inter-modal minima. In black, fitted CCN activation curve obtained from the measurements with corresponding error bars. The red line represents partially neutralized sulphate according to the DON indicated (using mixture of $\text{H}_2\text{SO}_4 + (\text{NH}_4)_2\text{SO}_4$), the olive brown line represents NaCl, and the purple dashed line represents ammonia-neutralised MSA (i.e. $\text{NH}_4\text{-MSA}$ salt) where all lines are based on predictions by the AIOMFAC model. Top right: Pie chart of chemical mass fractions, with the total mass concentration, average black carbon concentration, and DON_{mol} noted on top. The smaller pie chart is the breakdown of the non-sea-salt aerosol species.

Results 2—summertime aerosol physico-chemical properties and links to cloud activation in the Southern Ocean

When a cloud forms on an initial monomodal distribution (or an existing bimodal distribution), the activated droplets selectively grow in (dry) size as the droplets act as dilute aqueous chemical reactors converting SO_2 into sulphate (Hoppel et al., 1994). In a bimodal number-size distribution where this process has occurred, the inter-modal minimum can be regarded as the average aerosol sample- D_c . Other growth processes leading to bimodality, such as coalescence and Brownian scavenging, are not considered here following arguments made by O'Dowd et al. (2000b). Namely, due to the cloudiness of the region (Figure 5.5 and 5.6), low particle concentration, and the large sized diameter of the modes. Essentially, during cloud droplet formation, a 'bite' is taken out of the large-diameter side of the monomodal aerosol distribution and these are activated nuclei that grow in nuclei mass *via* aqueous phase sulphate production in the cloud. On exit from the cloud, the emerging aerosol is bimodal, with the activated nuclei forming a larger-diameter (accumulation) mode. Hence all particles larger than D_c are regarded as having been activated into cloud droplets previously and all particles smaller than D_c are non-activated interstitial aerosol and remain as an Aitken mode. Using this approach, we can evaluate that, for the average of *cAA* aerosol forming a cloud, the D_c is 56 nm, resulting from a peak supersaturation of $S_c \approx 0.4\%$, leading to the activation of 202 droplets cm^{-3} from a total aerosol population of 270 cm^{-3} . Combining this approach with the activation curve analysis (see Section 3.5.5), we calculate that for the range of peak supersaturations (0.34% - 0.45%) observed in the *cAA* cases, 2-13% of the activated CCN are PMA (see Table 5.4).

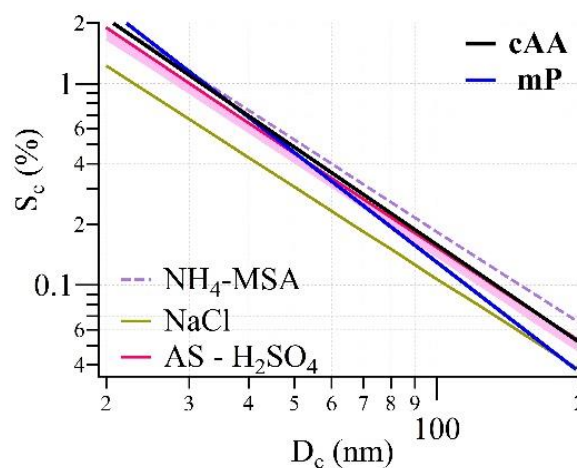


Figure 5.4. CCN activation efficiency as a function of critical supersaturation and diameter. Two merged cases, *cAA* and *mP*, shown in black and blue respectively. AIOMFAC model-predicted values of NaCl in olive brown, sulphate varying degree of neutralization in pink covering the DON_{mol} range

Results 2—summertime aerosol physico-chemical properties and links to cloud activation in the Southern Ocean

from H_2SO_4 to $(\text{NH}_4)_2\text{SO}_4$ (dark pink), and ammonia-neutralised MSA (i.e. $\text{NH}_4\text{-MSA}$ salt) in dashed purple.

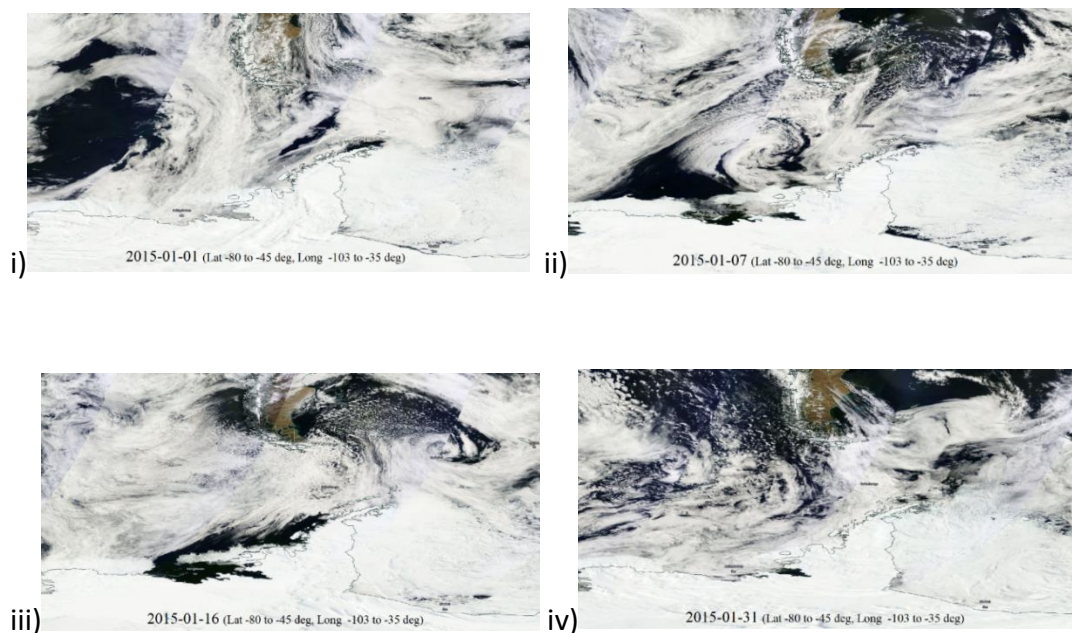


Figure 5.5. Satellite images taken from NASA Worldview(NASA, 2018) (<https://worldview.earthdata.nasa.gov/>) for four separate days in January 2015; (i) Jan 1st, (ii) Jan 7th, (iii) Jan 16th, and (iv) Jan 31st. Images show daily resolution of the cloudiness in the region and are representative of the cloud cover occurring for the extent of the PEGASO cruise. Each image is at ~5 km resolution and shows a composite of each day at latitudes from -80 to -45 degrees and longitudes from -103 to -35 degrees.

Results 2—summertime aerosol physico-chemical properties and links to cloud activation in the Southern Ocean

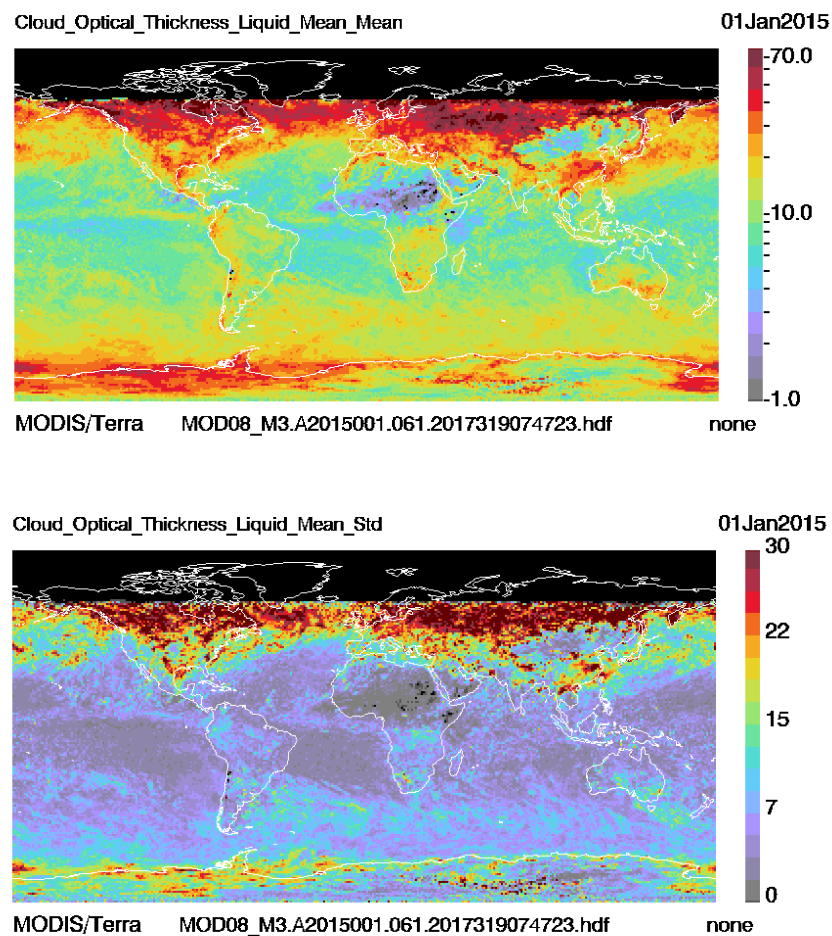


Figure 5.6. Satellite monthly mean composites of liquid cloud optical thickness (top) and the monthly standard deviation (bottom) globally. Images taken of January 2015 from MODIS L3 monthly collection 6.1, [<https://modis-atmos.gsfc.nasa.gov/images/l3-monthly-browse>](NASA, 2017).

5.1.2 Physico-chemical aerosol properties in *mP* air masses

The *mP* air masses formed over cold unfrozen polar marine waters, around 60 °S latitude. These air masses are moist but constrained in terms of total water content by the cold environment. During Antarctic summer, the polar regions above ~65 °S latitude are characterised by prevailing easterlies near the ocean/land surface, while at mid-latitudes (30 °S – 60 °S) westerlies prevail (see, e.g., observational data and model predictions by Broeke et al. (1997)) The *mP* air masses during the cruise typically advected with the westerly prevailing winds as part of the Circumpolar Antarctic Circulation. The *mP* air masses sometimes return south as returning-*mP* air masses following short excursions to the north. From the selected periods in this

Results 2—summertime aerosol physico-chemical properties and links to cloud activation in the Southern Ocean

study, all *mP* trajectories are consistently open ocean trajectories even though some may have advected relatively close to, or over, coastal waters.

By way of contrast to the *cAA* aerosol, the *mP* aerosol had an average total number concentration of $460 \pm 223 \text{ cm}^{-3}$ (i.e. double that in the continental air) while activated CCN at the highest measured supersaturation (0.8 %) was $420 \pm 168 \text{ cm}^{-3}$. The marine aerosol possessed a dominant Aitken mode at about 42 nm dry mobility diameter, but in contrast to the *cAA* aerosol had an amplitude four times that of the accumulation mode, which peaked at 140 nm. The inter-modal minimum was found at 82 nm, corresponding to critical supersaturation of 0.19 % on the $S_c\text{-}D_c$ CCN activation curve (Figure 5.3b). It is important to note that the Aitken mode at approximately 42 nm was remarkably stable regardless of variation in modal amplitude or accumulation mode peak diameter. Also, in sharp contrast to the *cAA* aerosol, total mass was $1.02 \pm 0.45 \mu\text{g m}^{-3}$ (compared to $\sim 0.60 \mu\text{g m}^{-3}$ in the *cAA* case) and the volumetric size distribution peaked at 210 nm and 480 nm, although the larger peak was fit with available data and may in fact peak at a larger diameter. The *mP* air mass had an average black carbon mass concentration of 0.12 ng m^{-3} , also indicating pristine air, however DON_{mol} was 0.51 suggesting more neutralised aerosol. More sea-salt, not surprisingly, was evident in the marine aerosol with the AMS-derived mass concentrations showing a total mass concentration of $0.282 \mu\text{g m}^{-3}$, of which 28 % was sea-salt. Chemical contributions in the *mP* aerosol were otherwise dominated by *nss-SO*₄ (44 %), MSA (12 %), ammonium (7 %), and OM (7 %). The *mP* air masses at 0.3 % supersaturation activated $\sim 200 \text{ CCN cm}^{-3}$ and at 0.8 % supersaturation approximately 400 CCN cm^{-3} were activated, changing the $N_{\text{CCN}}/N_{\text{CN}}$ ratio from 0.4 to 0.7. The ratios are lower than the equivalent *cAA* aerosol, pointing to a lower fraction of the aerosol activating in the *mP* air.

Table 5.2. Log-normal fit parameters for number and volume size distributions. Particle dry diameter (peak diameter, nm), spread (δ), κ , and equivalent κ -value for pure ammonium sulphate at that particle size ($AS_{\text{eq}} \kappa$) for fitted number peaks shown on left. Particle volume-size distribution (peak diameter, nm) and spread (δ) of the fitted peaks shown on right. Empty spaces indicate that corresponding peaks have an amplitude too small to be fitted reliably. All κ computed assuming a constant surface tension of 0.072 N m^{-1} .

	N			$AS_{\text{eq}} \kappa$	V	
	Peak, nm	δ	κ		Peak, nm	δ
<i>cAA</i>	26.8	1.28	0.41	0.44	-	-
	41.5	1.20	0.45	0.57	-	-
	104.2	1.53	0.55	0.63	193.0	1.60
<i>mP</i>	42.2	1.32	0.47	0.57	-	-
	138.7	1.52	0.99	0.64	212.1	1.38
	-	-	-	-	483.3	1.29

Results 2—summertime aerosol physico-chemical properties and links to cloud activation in the Southern Ocean

In the critical activation curve (Figure 5.3b), the slope is characteristic of a size-varying chemical composition for the CCN, suggesting different CCN species activating at different supersaturations and critical diameters. This is seen as the activation line of the environmental sample deviates from a parallel slope associated with any of the different homogeneous chemical species or fixed compositions and diverges from the sulphate species line, with a DON_{mol} of 0.5, towards the NaCl activation line. The measured ambient critical CCN activation curve shows an inferred 23 % contribution of primary sources at the inter-modal minimum. For the larger nuclei around $55 \text{ nm} < D_c < 200 \text{ nm}$, S_c lies between that of standard values for sea-salt and ammonium sulphate, with a corresponding hygroscopicity parameter at CCN activation of $\kappa = 0.99$ at 140 nm , while the activation of particles below 50 nm require a higher S_c , $\kappa = 0.47$ at 42 nm (assuming a constant surface tension of 0.072 N m^{-1}). For the average of *mP* aerosol, the D_c is 82 nm , corresponding to a peak supersaturation of $S_c \sim 0.19 \%$, leading to the probable activation of 170 cm^{-3} droplets from a total aerosol population of 460 cm^{-3} . For the suite of *mP* cases, the relevant range of S_c was calculated as 0.19% to 0.31% , with an $8 - 51 \%$ PMA contribution to the activated CCN or cloud droplet population in *mP* air (see Table 5.4). The 51% case, *mP* 3, corresponds to a wind speed of 16 m s^{-1} which was the highest wind speed during any steady-state case sampled.

Table 5.3. Inter-modal minima points and corresponding parameters listed according to their occurrence: inter-modal diameter, number of particles at the inter-modal diameter, critical supersaturation corresponding to inter-modal minimum and number of particles above inter-modal minimum diameter.

	$D_{\text{int-mod min}}$, nm	N at $D_{\text{int-mod min}}$, cm^{-3}	S_c , %	$N_{>\text{int-mod min}}$ cm^{-3}
<i>cAA</i> 1	55.3	3.8	0.41	212.3
<i>cAA</i> 2	61.0	2.7	0.35	165.4
<i>cAA</i> 3	54.0	2.5	0.45	208.5
<i>cAA</i> 4	65.0	3.0	0.34	175.9
re. <i>mP</i> 1	78.2	2.2	-	142.0
<i>mP</i> 2	63.9	4.4	0.31	221.3
<i>mP</i> 3	68.8	1.5	0.20	65.3
<i>mP</i> 4	82.1	3.7	0.18	191.0
<i>mP</i> 5	81.7	5.0	0.19	263.6
<i>mT</i> mod. 1	-	-	-	-
<i>mT</i> 2	78.7	6.3	0.20	253.1
<i>mT</i> 3	83.4	4.8	0.17	207.0
Case <i>cAA</i>	55.9	3.2	0.40	201.9
Case <i>mP</i>	81.8	3.4	0.19	169.8

5.1.3 Physico-chemical aerosol properties *mT* air masses

Maritime tropical (*mT*) air masses were least frequently observed, typically emerging from the South Atlantic (or Pacific) sub-tropical high-pressure region and at times, these air masses could briefly traverse South America leading to a modified (tropical) marine air mass which invariably, becomes polluted from South American outflow. The observed *mT* incursions exhibited characteristics very like *mP* air masses, as both represent maritime conditions, except one period (*mT* 1) that showed a very low percentage of primary aerosol loading, with an elevated black carbon concentration (30 ng m^{-3}) and the largest overall particle concentration ($1,165 \text{ cm}^{-3}$). *mT* 1 can be classified as an *mT* anthropogenically modified air mass. The *mT* air mass total number concentrations varied from $550\text{--}640 \text{ cm}^{-3}$, with little variation of CCN number concentrations at 0.8 % supersaturation, excluding pollution-modified *mT* air masses (Figure 5.7). The two un-modified *mT* periods show number and volume size-distributions very similar to *mP* aerosol, with a dominant Aitken mode compared to the accumulation mode. However, the difference in the number concentration between Aitken and accumulation modes was less, being almost double as opposed to quadruple in *mP* periods. The only fully modified *mT* period also appeared as the only monomodal pseudo-steady state period observed. The *mT* air mass chemical composition was similar to *mP* periods, except with a smaller fraction of MSA and increased fraction of OM. Generally, the BC concentration is higher than what is considered pristine for the *mP* air masses in the Scotia Sea region ($< 0.2 \text{ ng m}^{-3}$) but still clean ($< 0.5 \text{ ng m}^{-3}$) for marine aerosol. The N_{CCN}/N_{CN} revealed distinct fractions for 0.3 % supersaturation ranging from 0.3 to 0.6, but reached 1 at 0.8 % supersaturation (Figure 5.7). The *mT* air masses show similar log-scale slopes on the $S_c\text{-}D_c$ curves to *mP* air masses in terms of activation efficiency (Figure 5.1), but *mT* 1 followed an activation efficiency like neutralised sulphate and had increased activated fractions like *cAA* aerosol (Figure 5.7), which is a typical behaviour for such low concentrations of sea-salt ($\sim 0.02 \text{ } \mu\text{g m}^{-3}$).

5.1.4 Sea-salt events

Selecting steady state scenarios, for the reasons described above, results in an exclusion of a notable component of the dataset that do not meet these steady state conditions. Consequently, only one period with wind speed over 10 m s^{-1} , *mP* 3 with 16 m s^{-1} wind, is included in the analysis, yet wind speeds up to 25 m s^{-1} were not uncommon. Unsurprisingly, high wind speed periods were not steady-state due to high wind energy and rapid movements, but of interest to this study, due to high sea-salt concentrations. The cruise average, and median, was $\sim 10 \text{ m s}^{-1}$ with a standard deviation of 4 m s^{-1} , whereas the median for the steady state cases was 7.5 m s^{-1} with similar standard deviation (Figure 5.8).

Results 2—summertime aerosol physico-chemical properties and links to cloud activation in the Southern Ocean

Overall during the study, the maximum observed ambient sea-salt submicron mass peaked at a concentration of $2.09 \mu\text{g m}^{-3}$, whereas nss-SO₄ mass concentration reached only $1.12 \mu\text{g m}^{-3}$. Additionally, observations of 4 periods (Figure 5.9) that just missed the criteria for steady-state classification show major sea-salt mass events (Event 1-4), where the sea-salt PM₁ mass concentration exceeded $1.0 \mu\text{g m}^{-3}$. We acknowledge the nonlinearity between submicron particle mass and number concentration and studied the most stable cases (Event 1 and 4) in detail to resolve sea-salt and nss-SO₄ number-size distribution particle concentrations and activated droplet concentrations. We observed 420 particles cm⁻³ in Event 1, which had a mean sea-salt mass concentration of $1.5 \mu\text{g m}^{-3}$ (~ 170 particles cm⁻³) with a nss-SO₄ mean mass concentration of $0.13 \mu\text{g m}^{-3}$ (~ 250 cm⁻³), the highest sea-salt to nss-SO₄ ratio. Event 2 had 460 particles cm⁻³ with a relative mean sea-salt and nss-SO₄ mass concentration of $0.61 \mu\text{g m}^{-3}$ and $0.41 \mu\text{g m}^{-3}$, respectively. Event 3 had the largest particle concentration at 540 cm⁻³, with $0.9 \mu\text{g m}^{-3}$ of sea-salt and $0.3 \mu\text{g m}^{-3}$ of nss-SO₄. Event 4 had the lowest number concentration at 140 particles cm⁻³, but a relatively high ratio of mean sea-salt mass to nss-SO₄ with absolute concentrations of $0.92 \mu\text{g m}^{-3}$ (~ 110 cm⁻³) and $0.12 \mu\text{g m}^{-3}$ (~ 30 cm⁻³). We calculate that, in these high sea-salt:nss-SO₄ mass events, sea-salt contributes 60 – 100 % of the activated droplet concentration at a peak supersaturation < 0.32 % (Table 5.4), exemplifying PMA, namely sea-salt, as a serious contributor to overall mass and CDNC.

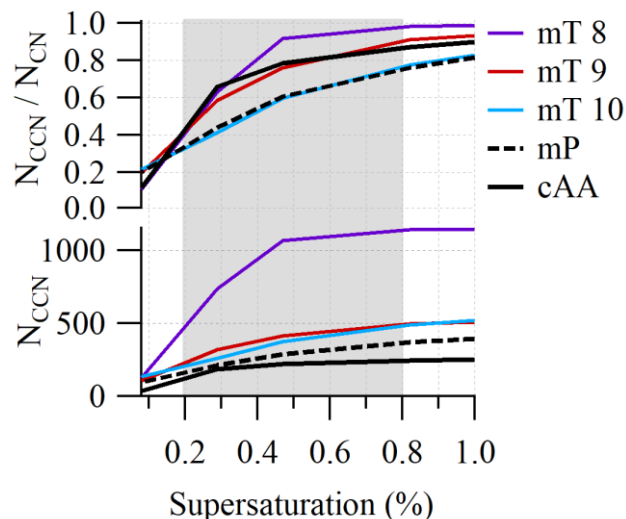


Figure 5.7. On top, the ratio of CCN to all particles greater than 20 nm, listed by air mass source region. On bottom, the total number of CCN for varying supersaturation. Shaded range of supersaturations represent typical values for marine stratocumulus clouds.

Results 2—summertime aerosol physico-chemical properties and links to cloud activation in the Southern Ocean

Table 5.4. Values used for PMA number contribution calculation. Inter-modal minimum (D_c) values gave corresponding cloud peak supersaturation (S_{peak}) based on ambient S_c - D_c curves. The same curves resolved the critical diameters of SMA (D_{SMA}) and PMA (D_{PMA}) which were used in conjunction with number-size distribution data to find the number of activated SMA and PMA particles and find the percent contribution of PMA (% PMA) to the cloud droplet number. The number concentration of PMA and SMA has an associated $\pm 5 \text{ cm}^{-3}$.

	S_{peak} , %	D_{SMA} , nm	D_{PMA} , nm	act SMA, cm^{-3}	act PMA, cm^{-3}	% PMA
cAA 1	0.41	50.7	41.3	185	27	12.7
cAA 2	0.35	58.6	45	150	15	9.1
cAA 3	0.45	48.4	38.2	205	4	1.9
cAA 4	0.34	59.9	45.9	170	6	3.4
mP 1	-	-	-	-	-	-
mP 2	0.31	61	48.9	203	18	8.1
mP 3	0.2	81.8	64.8	32	33	50.5
mP 4	-	-	-	-	-	-
mP 5	0.19	85	66.3	216	47	17.8
Case cAA	0.40	51.8	41.7	175	25	12.4
Case mP	0.19	86.8	69.3	130	39	23.0
E1	0.30	63.8	50.4	63	102	61.8
E4	0.32	61.8	48.8	0	62	100.0

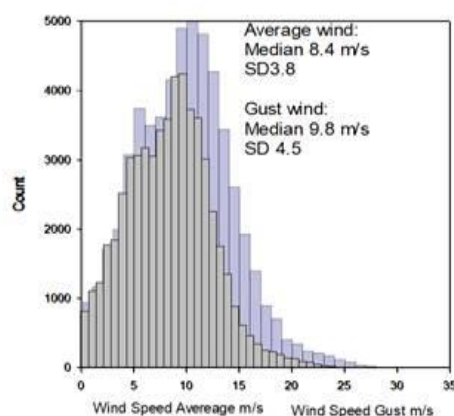


Figure 5.8. Frequency distributions of wind (grey) and gust (blue-grey) measurements taken on the research ship during ambient sampling periods used in this analysis.

Results 2—summertime aerosol physico-chemical properties and links to cloud activation in the Southern Ocean

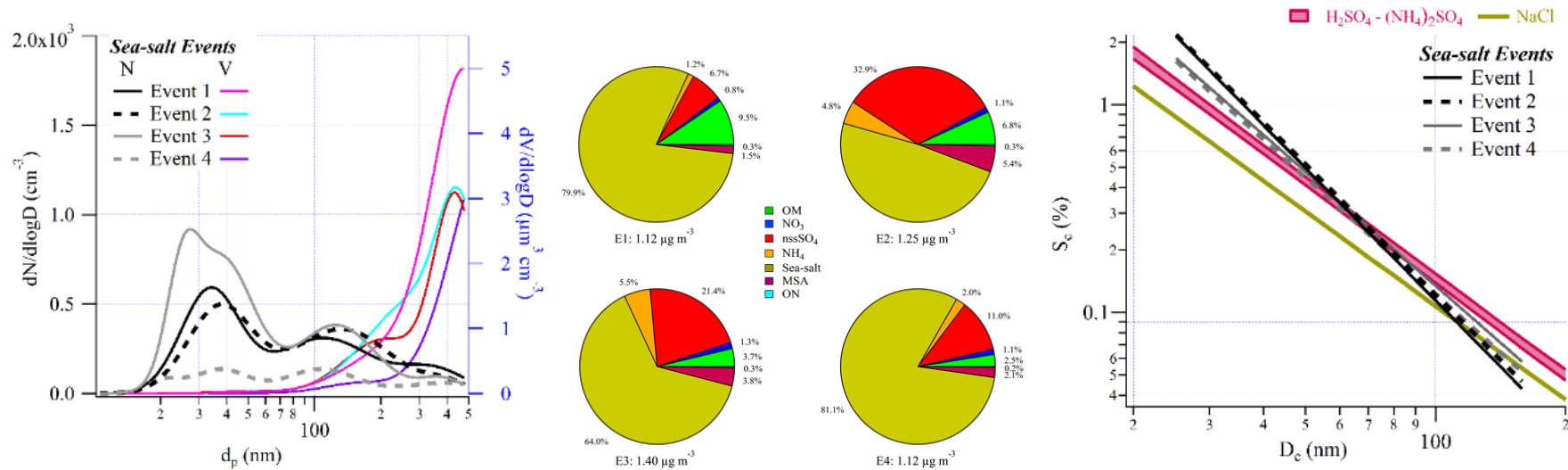


Figure 5.9. Sea-salt Event analysis shown for SMPS, HR-ToF AMS, and CCNC data shown. The left panel showing number (N) and volume (V) size distributions of Event 1 -4 (E1-4), Black and grey solid and dashed lines represent the number-size distributions while the coloured solid lines represent the volume distributions. The middle panel shows AMS chemical fractions of all four events with total mass concentration at the bottom of each pie-chart, respectively. The right panel shows CCN activation efficiency curves of sea-salt events with critical supersaturation plotted against critical dry diameter; the slopes derived from the measurements during the periods are shown. The AIOMFAC model predicted NaCl line, in olive brown, and the sulphuric acid to neutralized sulphate ($\text{H}_2\text{SO}_4 - (\text{NH}_4)_2\text{SO}_4$) range are shown.

5.2 Antarctic ice samples

Additionally, ice samples from the Antarctic sea-ice zone were aerosolised in bubble-tank experiments (see Methods) in order to evaluate the sea-ice influence on CCN properties. Detailed analysis can be found in Appendix B.2. The results of these experiments showed that some highly CCN activation efficient particles were generated in the submicrometre size-range from the sea-ice (Figure B2). However, these CCN particles had no regional impact as they did not affect the ambient CCN spectra for the *cAA* air masses which advected over the Weddell Sea region (Figure B3).

5.3 What do summertime Southern Ocean CCN reveal?

In contrast to other oceanic waters (e.g. the North Atlantic), the continental air comprised quite a low-complexity aerosol population. Despite advecting over the Weddell Sea pack-ice region, the *cAA* air comprised almost exclusively of biogenic sulphate products (*nss-SO₄* and MSA, and their neutralised variants) and close to insignificant values of organic aerosol. Similarly, the *mP* air carrying the most ‘maritime’ aerosol comprises simply of similar sulphur species plus sea-salt. Other species (e.g. organic nitrogen, primary organic matter) were present in such minute quantities that their ability to influence atmospheric processes of note seems to be limited, if anything, to potential involvement in nucleation and cluster growth processes.

On average, the CCN number concentration in *mP* air masses was effectively double the concentrations found in *cAA* air masses at a supersaturation of 0.8 %. However, at a lower supersaturation of ~ 0.3 %, *mP* air masses exhibited similar CCN abundance as *cAA* air masses, of approximately 200 CCN cm⁻³. In *mP* and *mT* aerosol, about 75 % of the aerosol number population resided in the Aitken mode (which can be considered un-activated CCN) in contrast to *cAA* aerosol where 70 % resided in the accumulation mode (which can be considered activated CCN) (Hoppel et al., 1994).

As reported previously (Dall’Osto et al., 2017), overall, the largest observed SMA component in all air masses was *nss-SO₄*, and sea-salt dominated the PMA component. At low supersaturations of the order of 0.1-0.2 %, sea-salt tended to dominate the activated fraction particularly under high winds. In *mP* air masses, the CCN activation efficiency closely followed that of pure sea-salt for most particles with

Results 2—summertime aerosol physico-chemical properties and links to cloud activation in the Southern Ocean

$D_p > 200$ nm, confirming that CCN particles at low supersaturation were principally PMA in origin. The fraction of CCN that were PMA decreased with increasing S_c and gradually reduced to about 20 % or less at the inter-modal minima below which CCN were almost entirely SMA; however, due to the size-differentiated composition of marine aerosols, this is to be expected. The concentration of CCN is typically reported over a wide supersaturation typically ranging from 0.1 % to 1 % (Twomey, 1959; Twomey and Wojciechowski, 1969; Hudson et al., 2010; Hudson et al., 2015). Nevertheless, our results suggest that average supersaturations larger than 0.45 % were not relevant in this region, based on the estimations of critical supersaturation from the inter-modal minima of the number-size distributions (Table 5.3).

These results illustrate that when realistic marine boundary layer cloud supersaturations are considered (e.g. ~0.2-0.45 %, rather than 1 %), SMA dominates the number fraction of activated cloud droplets at the higher end of realistic supersaturations. However, sea-salt can also contribute significantly to the activated droplet concentration, challenging the conclusions from Quinn et al. (2017) stating that nss-sulphate is the only major contributor to marine CCN in most oceanic regions. More effort needs to be made to deconvolve the number fraction of sea-salt particles contributing to (relevant) CCN in the marine environment. This becomes especially important when considering that the susceptibility of the global cloud-radiation system is such that a 15-20 % change in cloud properties (e.g. cloud extent and albedo) would be sufficient to counteract the radiative perturbation awarded by a doubling of CO₂ (Slingo, 1990) and we contend that, while SMA is often the controlling force for CDNC, at relevant supersaturation, sea-salt can have a profound effect on activated droplets, susceptibility and thus, global albedo.

5.4 Comparing Southern Ocean CCN to the North East Atlantic

This section compares the Southern Ocean monodispersed CCN data, presented above, with that of a case study of North East (NE) Atlantic CCN, measured from Mace Head research station (MHD), located on the West coast of Ireland (see Methods, 3.1.2). Size-segregated (or monodispersed) CCN data is not run operationally at MHD, due to attention and manual interaction required, therefore, these data are only available for brief periods supporting some intensive measurement campaigns. Due to instrument failures, further maintenance, and pollution periods, parallel measurements of monodispersed CCN data with size and chemical data is further limited. The data from a summer case study in August (2015) during a research

Results 2—summertime aerosol physico-chemical properties and links to cloud activation in the Southern Ocean

campaign (BACCHUS campaign) is compared against those from the Southern Ocean presented for the austral summer in the previous chapter. The case studies of the NE Atlantic presented here represent typical conditions of their air mass type for the summer season based on the aerosol chemistry (Ovadnevaite et al., 2014a). Therefore, the case studies provide some good examples of NE Atlantic CCN behaviour in the summer month of August.

The MHD facility is described in full in Section 3.1.2, the data presented here is from the MHD facility and follows the procedures and conditions previously outlined. Campaign specific calibration results were used for the August 2015 CCN data, with supersaturations and uncertainties reported in Table A1. Every case analysed for this section had a BC mass concentration that remained less than 15 ng m^{-3} for the duration of the period. All BC measurements came from the MAAP (averaged over 30 minutes) and all chemical measurements were from the HR-ToF AMS, both described in Section 3.4. All data presented here are in UTC local time. This chapter has calculated κ -values, all of which were calculated from Eq. 12 and 13 in Section 3.5.3, using $T = 293.15$, which was the sampling temperature and assuming a surface tension of pure water = 0.072 N m^{-1} . CCN data is presented using D_c , which is the critical (dry mobility) diameter. Theoretical (NaCl, and $(\text{NH}_4)_2\text{SO}_4$) values of D_c were converted from volume equivalent diameter to mobility diameter for graphical comparison following DeCarlo et al. (2004) for κ calculations using shape factor correction ($\chi_{\text{NaCl}} = 1.08$, $\chi_{(\text{NH}_4)_2\text{SO}_4} = 1.04$) from Hinds (1982).

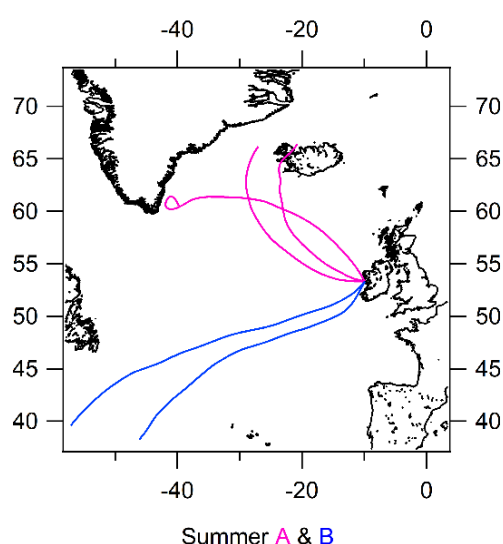


Figure 5.10. Air mass back trajectories from HYSPLIT calculated for 120 hrs at a starting height of 50 m AMSL are shown for the summer periods A (in pink) and B (in blue). Each period shows a new trajectory every 6 hour.

Results 2—summertime aerosol physico-chemical properties and links to cloud activation in the Southern Ocean

Two cases were analysed from the BACCHUS campaign which took place at MHD in August 2015. One of these periods (Summer B) over-laps with a period discussed in McCluskey et al. (2018b), therein called M1. However, the bulk of that published work is concerned with ice nucleating particles and does not discuss CCN. The first period (Summer A) occurred from August 5th 22:55 – 6th 14:15 and is a *mP* air mass (Figure 5.10) with a median wind speed of $\sim 7 \text{ m s}^{-1}$, the second period (Summer B) occurred from August 9th 11:43 – 19:10, 2015 and is a *mT* air mass (Figure 5.10) with a median wind speed of $\sim 8 \text{ m s}^{-1}$. Period number-size distribution (lognormally fitted modes described in Table 5.5), chemical, and BC data can be found in Figure 5.11. The summer NE Atlantic periods comprise of a much larger concentration of OM (Figure 5.11) in comparison to the Southern Ocean. Comparing the NE Atlantic periods to the merged *mP* Southern Ocean case (Figure 5.3) a higher mass fraction of OM is found (14 – 44 % more), corresponding to higher approximate absolute mass concentrations of OM (0.25 - 0.84 $\mu\text{g m}^{-3}$ respectively). MSA (a specific type of OM) has a large mass fraction presence in the Southern Ocean. Taking this into account as part of the OM fraction, the Southern Ocean displayed about 18.6 % equalling 0.19 $\mu\text{g m}^{-3}$ of OM (including MSA) and the NE Atlantic showed a range of 26 - 52 % (equalling 0.37 – 0.95 $\mu\text{g m}^{-3}$).

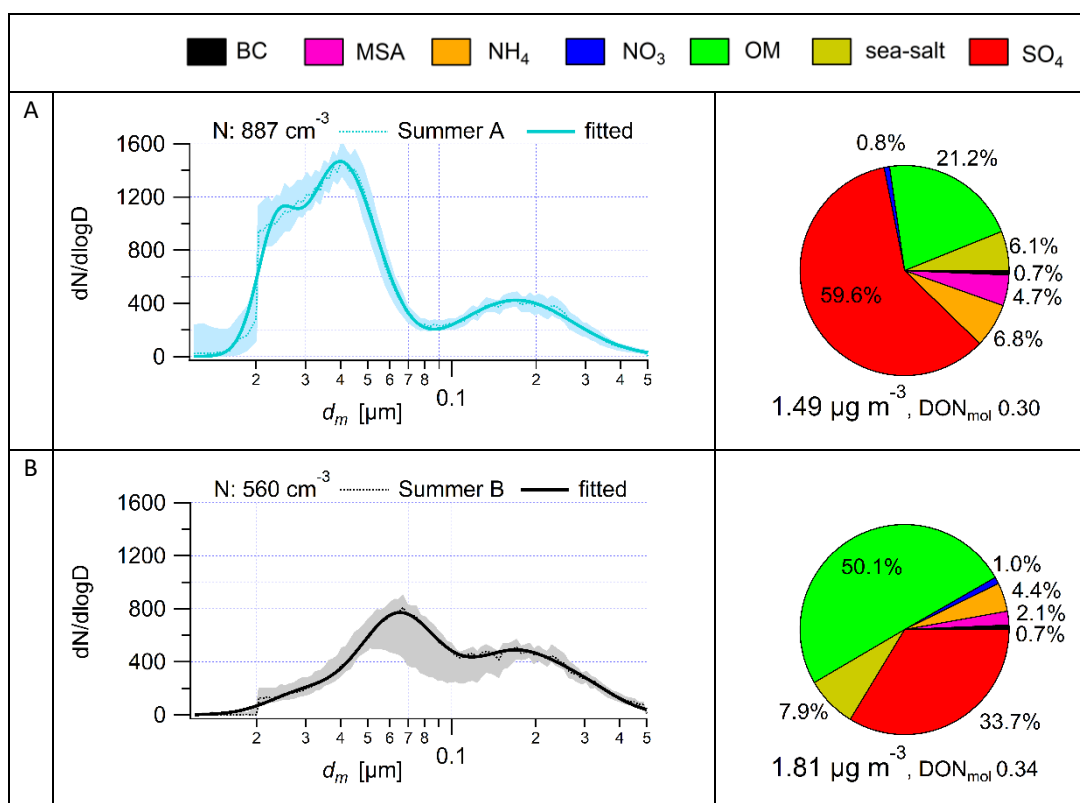


Figure 5.11. Number-size distribution data and chemical mass fractions for the summer North East Atlantic cases sampled at Mace Head research station in 2015 and 2017. The left column shows the median SMPS data for each case in dotted lines, with the fitted data shown in a thick solid line.

Results 2—summertime aerosol physico-chemical properties and links to cloud activation in the Southern Ocean

Shaded areas between the lighter lines represent the 75th-25th percentiles, with total mean number concentration written at the top. The right column shows the HR-ToF-AMS non-refractory chemical data and MAAP BC mass concentrations as pie charts of the mass fractions. The absolute mass concentrations and DON_{mol} are written at the bottom, with a colour key on the rightmost of the figure.

The monodispersed CCN data for the summer periods are shown in Figure 5.12. Summer A and B both show activation efficiency between that of ammonium sulphate and sea-salt at $d_m < 30$ nm. For particles larger than 30 nm the CCN activation behaviour follows that of sulphate, lessening in activation efficiency around 50 nm, before returning to slightly better activation. Both cases appear to be chemically inhomogeneous at different particle size modes. When both cases are fitted into one CCN slope, the data shows an activation efficiency curve that slightly decreases in efficiency with increasing size. However, overall the CCN curve suggest that particles are activating like ammonium sulphate. Around the nucleation mode there is a slight enhancement of CCN activation efficiency, and in the Aitken-accumulation mode there is a slight suppression of CCN activation efficiency from that of ammonium sulphate (Figure 5.12). The κ -values for the fit line at 40 nm and 100 nm (extrapolated) dry critical diameters (D_c) were 0.55 and 0.54 respectively (at $T = 293.15$ K). The inter-modal minimum for Summer A was at 86 nm (d_m) and for Summer B was at 118 nm (d_m). Using the fitted ambient summer NE Atlantic S_c - D_c CCN curve this suggest a relevant cloud peak supersaturation < 0.3 %.

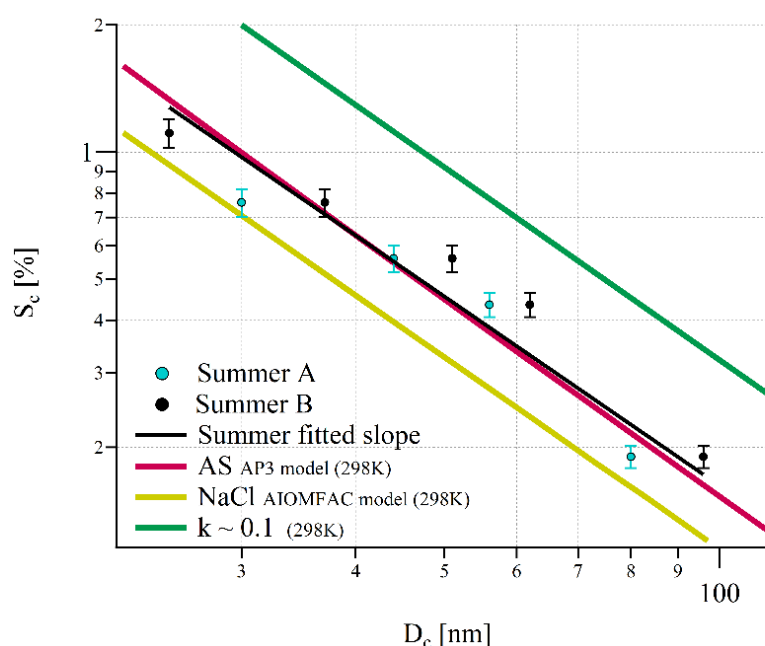


Figure 5.12. CCN activation curves for MHD summer marine data. Individual data points are plotted as markers with error bars representing the uncertainties in the supersaturations. The black line is the fitted slope of the plotted data. The predicted slopes of ammonium sulphate (AS) from the AP3

Results 2—summertime aerosol physico-chemical properties and links to cloud activation in the Southern Ocean

model (Rose et al., 2008) and NaCl from the AIOMFAC model (Zuend et al., 2008) are shown in red and olive brown, respectively.

A comparison of the CCN properties between Southern Ocean austral summer marine aerosol and NE Atlantic summer case study aerosol are shown in Figure 5.13. It is important to note that this comparison uses the average of two case studies of the NE Atlantic summer which lacks periods with larger fractions of sea-salt which reached a maximum of $0.85 \mu\text{g m}^{-3}$ during the BACCHUS campaign, and reached mass fractions of $\sim 55\%$ (during a period of instability). The Southern Ocean fitted CN trends reflect a particle population which increases in CCN activation efficiency with increasing diameter. Conversely, the summer NE Atlantic case shows CCN activation that is almost like a homogenous nss-SO₄ population, with a very slight decrease in activation efficiency with increasing diameter (Figure 5.13). Smaller particles in the *mP* Southern Ocean case appear to activate similarly to particle composed of an NH₄-MSA combination, gradually activating more and more like sea-salt. Smaller particles in the NE Atlantic marine case, activate at a higher activation efficiency than ammonium sulphate, gradually decreasing in activation efficiency.

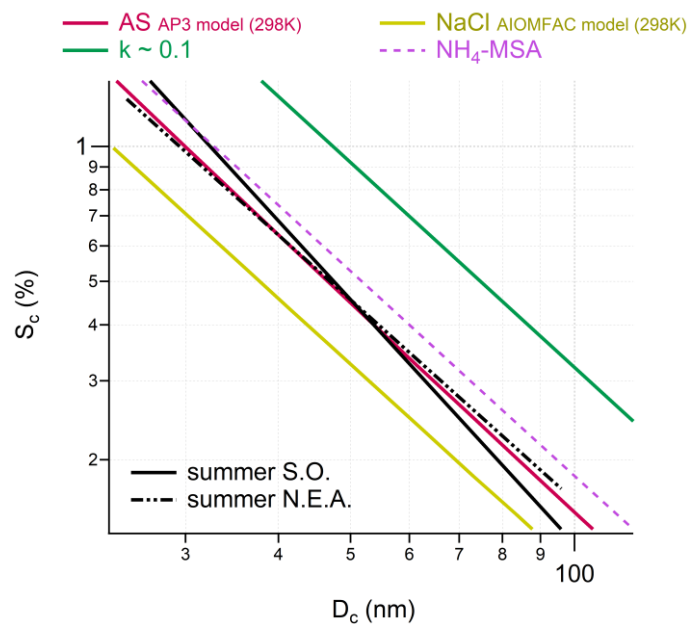


Figure 5.13. A comparison of CCN S_c - D_c curves between Southern Ocean (S.O.) and North East Atlantic (N.E.A.) submicrometre summer CCN populations. CCN S_c - D_c curves of the overall trend the North East Atlantic marine summer case study (solid black line) and the *mP* merged summer Southern Ocean case (dot-dashed black line) are shown. Theoretical curves (all for 298.15 K, and a constant surface tension of 0.072 N m^{-1}) of ammonium sulphate (AS) (maroon line) from the AP3 model (Rose et al., 2008), NaCl (olive brown line) and NH₄-MSA (dashed purple line) calculated from the AIOMFAC model (Zuend et al., 2011; Zuend et al., 2008), and a theoretical line for a $\kappa \sim 0.1$ (green line) calculated from κ -Köhler theory (Petters and Kreidenweis, 2007).

Results 2—summertime aerosol physico-chemical properties and links to cloud activation in the Southern Ocean

In the Southern Ocean, secondary aerosols contribute the most to overall particle concentrations when wind speeds are below $\sim 10 \text{ m s}^{-1}$, but it is the varying interaction of primary and secondary aerosol which changes the cloud nucleating ability of the aerosol population over different environments. However, PMA number concentration fractions do not have to be larger or even half that of SMA number concentration fractions to effectively reduce the indirect effect, especially if updraft velocity is small.

A major difference between the North Atlantic and the Southern Ocean *mP* cases is the OM contribution, which was greater in the North Atlantic cases even with similar wind speeds to the Southern Ocean. The larger presence of OM may be related to the different bloom dynamics between the two oceans, with the North East Atlantic having clearly defined phases of blooms over the summer months and the Southern Ocean having relatively constant blooms all austral summer. Different blooms will have variable impacts on seawater composition (e.g. on DMSP concentrations (Lizotte et al., 2017) and other trace elements) and different phases will affect the organic components in the seawater (e.g. viruses, bacteria, cell structures, etc.). It has also been demonstrated that DOM is subducted quickly in the Southern Ocean but is ubiquitous in North Atlantic surface seawater (Hansell and Carlson, 2001). The short study presented here suggest that the North East Atlantic aerosol population is more complex than the Southern Ocean.

6. Results 3—sea-salt suppression of sulphate nuclei activation

The results of the previous chapter suggested that the propensity of total cloud droplet number concentration (CDNC) was to decrease with higher number contributions of sea-salt in the Southern Ocean. The result was pointing to the sea-salt as being a controlling factor in determining the fraction of particles activating into droplets, which also resulted in noticeable differences in number-size distributions of the ambient *mP* and *cAA* aerosol in the Southern Ocean. The cloud parcel model(s) is, therefore, deployed in this chapter to assess and quantify this effect.

In the analysis presented in Chapter 5, sea-salt contributed significantly to the *mP* aerosol mass (~28 %, representing $0.283 \mu\text{g m}^{-3}$), compared with the mass fractions in the *cAA* cases (~16 %, representing $0.096 \mu\text{g m}^{-3}$). The reduction in critical cloud peak supersaturation (S_c) also shown in the results of Chapter 5 (Table 5.4) is suspected to be linked to the higher fraction of sea-salt particles present in the marine cases. E.g. the coarse mode sea-salt (or PMA in general) activation scavenges available water vapour and, thus, suppresses the S_c . As air is reaching peak supersaturation, sea-salt particle activation competes with SMA particle activation in the accumulation and Aitken mode. As these larger sea-salt particles activate they scavenge available water vapour effectively reducing the vapour pressure and suppressing cloud peak supersaturation as a function of the number concentration of activated particles.

The concept of competitive activation between PMA and SMA is well established (O'Dowd et al., 1999b; O'Dowd et al., 1997b; O'Dowd et al., 1999a). Liquid water availability for activation is limited by the environmental conditions of the air mass. During cloud dynamical processes similarly-sized particles exposed to the cloud peak supersaturation may not freely activate, due to the uptake of water vapour by more hygroscopic particles (Nenes et al., 2001). O'Dowd et al. (1999b) hypothesized that, in the marine environment, sea-salt and sulphate particles often compete for activation, with pure sea-salt or internally mixed sea-salt winning the battle. This is based on its low critical supersaturation and more efficient growth in subsaturated regimes prior to activation. Additionally, sea-salt extends from the ultra-fine to supermicron size mode, meaning that (if sea-salt is present) some sea-salt particles will activate at almost any realistic supersaturation. The ultrafine sea-salt mode ($d_m < 0.1 \mu\text{m}$), when considered in models, leads to a 50 % increase of CCN at 0.2 % supersaturation in marine air compared to modelled CCN without the ultrafine sea-salt mode (Pierce and Adams, 2006). Mårtensson et al. (2010), modelled the effects of sea-salt in the formation of the Aitken and accumulation modes, finding,

among other things, that sea-salt simulated in the Aitken mode from an ultrafine flux is important for accurately simulating the ambient number-size distributions and CDNC measured in the marine environment.

6.1 Can the ambient sulphate accumulation mode be explained by heterogeneous in cloud sulphate production (*via* SO₂ oxidation)?

Before continuing with the extended analysis, the inter-modal minimum, or Hoppel minimum, analysis technique from Chapter 5 must be confirmed as a viable approach not just using the theory of activation dynamics but also by the sulphate production chemistry. Hoppel et al. 1986, proposes that the minimum in the size distribution between the Aitken mode and the accumulation mode is produced by chemical cloud processing in which predominantly nss-SO₄ nuclei, at sizes down to the aforementioned inter-modal minimum are activated into cloud droplets. The resulting aqueous droplet solutions provide excellent chemical reactors for hosting aqueous-phase oxidation of SO₂ into sulphate, thereby increasing the dissolved mass in the cloud droplet and, on evaporation, leaving residual particles whose dry size has increased by about a factor of 2-3 (O'Dowd et al., 2000a). This process is thought to be the only way to form a distinct SMA accumulation mode particle in the absence of high fraction of condensing OM vapours or extraordinarily high SO₂/H₂SO₄ concentrations. Consequently, we can conceptualise the source of potential CCN (being near the Aitken mode size range) as a monomodal distribution. The activation process splits the SMA Aitken mode into two components, one which grows into the accumulation mode and the other which is essentially a cropped Aitken mode with a smaller number concentration (N) and modal diameter. So, when modelling the effect, the original Aitken mode must be constructed. The accumulation mode represents the activated nuclei. The total number of particles is conserved (within 15 % of ambient measurement uncertainty) during the transformation into separate modes.

The ambient Southern Ocean data had a recurrent Aitken mode at $d_m = 43$ nm, taking this as the approximate positioning of the monomodal reservoir of potential CCN, the growth of these particles is considered. The data shows that a significant portion of SMA particles are found in the accumulation mode, with the total SMA number concentration for the *mP* cases on the order of 100-400 cm⁻³, and for the *cAA* cases on the order of 200-300 cm⁻³. Total sulphate concentrations were on the order of ~ 0.4 µg m⁻³ for both air mass types. Studies of MBL chemistry and subsequent sulphate production are available in the literature. A relevant study (O'Dowd et al., 2000a) modelled cases of varying sulphate and sea-salt number-size distributions to evaluate

the heterogeneous sulphate production. One case with a high SO_4 particle concentration of 158 cm^{-3} (which is near to the Southern Ocean calculated SMA concentrations) was modelled using various SO_2 atmospheric concentrations. The modelled output gave the mass of produced SO_4 from the heterogeneous aqueous phase oxidation of SO_2 (a process which occurs on the order of seconds and in some cases milliseconds). It is estimated that in the Southern Ocean, as with other remote oceanic regions, SO_2 mixing ratios would be about 20-30 parts per trillion (ppt). Linearly extrapolating the results from the high SO_4 particle concentration case to this atmospheric concentration of SO_2 , it is found that approximately $0.2 \mu\text{g m}^{-3}$ of sulphate would be produced in the aqueous droplets of the cloud residual mode. This equates to most of the particles at least doubling in dry diameter size upon evaporation of the droplet. This is consistent with the resultant accumulation mode found in the Southern Ocean ambient cases, where there would be 2-3-fold increase in particle diameter. In O'Dowd et al. (2000a), it is also shown that sulphate production in the aqueous phase of activated droplets is 3-4 orders of magnitude greater than sulphate production in wet un-activated sulphate or sea-salt aerosol. Additionally, growth scale for sulfuric acid condensation can be estimated using equations found in O'Dowd et al. (2000b). A conservative estimate of condensation growth is made using the upper limit of the Aitken mode size range of $d_m \sim 63 \text{ nm}$, and assuming that all available SO_2 vapour has been converted to equivalent amounts of equilibrium state H_2SO_4 vapour. It is estimated that it would take about 75-80 days for a 63 nm dry diameter particle to grow by condensation of H_2SO_4 vapours to 100 nm in size. If you extend this estimate to the peak mode Aitken diameter of 43 nm, the time scale would lengthen further. Therefore, the Hoppel minimum analysis approach appears viable for the presented environmental conditions, and thus can be extended for further analysis.

6.2 Suppression analysis of ambient Southern Ocean data trends

In the extended analysis of the PEGASO cruise dataset, the same principal assumption is made: that the Hoppel mechanism of activation and subsequent production of sulphate leading to dry particle diameter growth (Hoppel et al., 1986) applies to the bimodal distributions from the pseudo-steady-state cases (see arguments made in Section 6.1). Thus, in the marine environment the inter-modal minimum between the Aitken and accumulation mode is representative of the critical diameter of activation (D_c) of the aerosol population as a whole. The SMPS size-distribution spectra represents the result of a possible range of iterative cloud processing (1-10 cloud events considering a single marine source (Pruppacher and Klett, 1978)) of a population of particles. In terms of the particle population, the Aitken mode can be

Results 3—sea-salt suppression of sulphate nuclei activation

conceptualised as the source of potential CCN, and the accumulation mode as the actual activated nuclei.

As the system we are observing (the Southern Ocean) is relatively simple being made up of mostly sea-salt, and sulphate with other secondary particles, and without strong influence of primary OM (see Chapter 5), PMA can be considered to be sea-salt for differentiation of the particle size-distribution modes. For the extended analysis of the pseudo-steady state periods identified in Chapter 5 (Figure 5.1), some cases were altered or eliminated when more stringent steady-state criteria were adhered to. Cases belonging to *mT* incursion periods were cut from analysis due to their anthropogenic influence. Case *cAA* 1 was also separated into two equal duration periods *cAA* 1a and 1b, where the former had significantly higher fractions of sea-salt possibly due to more exposure time along the open ocean rather than just the Weddell Sea. Each case was then analysed following the concept of Modini et al. (2015), seeking to differentiate PMA from SMA in the case size distributions. Contrary to assumptions made by Modini et al. (2015) and Quinn et al. (2017) a multimodal distribution for PMA was assumed rather than a monomodal. As *mP* 4 had a less stable particle size-distribution, it was not analysed. Due to the brevity of the cruise it was assumed that all cases were equally possible to be encountered in the same fraction of time during the summer months in the region. Thus, the averages of all cases were analysed as *cAA* and *mP* typical distributions, as well. The fraction of both SMA or PMA particles which were assumed as to be activated (following methods in Section 3.5.5) are shown in Table 6.1 for each case. The trends between sea-salt activation and CDNC of the ambient cases are plotted in Figure 6.1.

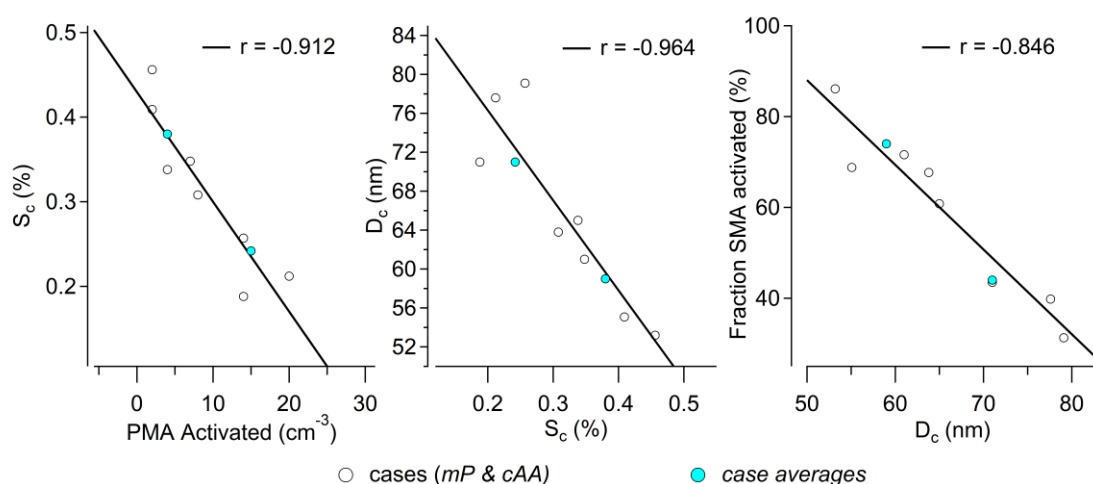


Figure 6.1. Linear representation of the link between the critical supersaturation (S_c , %) and number of PMA which activate into cloud droplets (PMA Activated) (Left); critical diameters (D_c) and S_c (Middle); and the fraction of SMA which then activate into cloud droplets (Fraction SMA activated) and D_c (Right). The three linear representation give Pearson's R-values at the top of the graph (all are significant for $p < 0.01$) and show each *mP* and *cAA* cases as open circles, with the blue closed circles showing the results of the average case examples.

Results 3—sea-salt suppression of sulphate nuclei activation

The order of the panels in Figure 6.1 simulates the independent and dependent variables which are affected by the activation of PMA particles. Cloud peak supersaturation is plotted as a function of PMA activation (Figure 6.1 left panel), as it should be affected by the PMA particle activation. This is seen as a linearly decreasing trend (Figure 6.1) with a Pearson’s correlation coefficient of $r = -0.91$ (significant at $p < 0.01$). It illustrates that for the eight cases presented here, four *mP* and four *cAA*, a modest increase in PMA activation, from 2 cm^{-3} droplets to 20 cm^{-3} droplets reduces the peak supersaturation from 0.4 % to 0.2 %. This reduction in S_c is compared against the derived cloud critical diameter from the inter-modal minima (D_c) of the cases considered, as the S_c should be a controlling factor in what sized particles freely activate, triggering the Hoppel Mechanism. Figure 6.1 (middle panel) shows that a reduction in S_c from 0.4 % to 0.2 % increases D_c from 55 nm to 78 nm ($r = -0.964$, $p < 0.01$). The final plot in Figure 6.1 (right panel) shows a comparison of the cloud peak critical diameter with the derived fraction of SMA. If the reservoir of SMA particles is relatively constant, then the number of particles which can activate should be directly linked to the critical diameter of activation. The reduced critical diameter (from 55 nm to 78 nm), in turn, reduces the percentage of SMA activated from ~ 80 % to ~ 40 % ($r = -0.846$, $p < 0.01$).

Table 6.1. Calculated values from ambient measurements are listed by case. Number concentrations listed should be taken with a standard deviation of 2 cm^{-3} . The critical diameter of activation or the inter-modal minimum (D_c), was compared to ambient CCN S_c - D_c slopes to find the cloud peak supersaturation (S_c). This was then used in conjunction with AIOMFAC (Zuend et al., 2011) theoretically derived NaCl CCN S_c - D_c curves to find the corresponding PMA activation diameter (D_c sea- salt). Total number (N), activated number (CDNC), and total and activated numbers of SMA and PMA respectively are also listed.

Case	D_c	S_c	D_c sea-salt	N cm^{-3}	CDNC cm^{-3}	N_{SMA} cm^{-3}	CDNC_{SMA} cm^{-3}	N_{PMA} cm^{-3}	CDNC_{PMA} cm^{-3}
<i>cAA</i> 1b	55.1	0.409	41.4	291	200	288	197	3	2
<i>cAA</i> 2	61.0	0.348	45.0	224	161	215	154	11	7
<i>cAA</i> 3	53.2	0.456	37.7	239	206	237	204	3	2
<i>cAA</i> 4	65.0	0.338	45.9	284	173	283	173	6	4
<i>mP</i> 1	79.1	0.257	55.0	434	142	416	132	22	14
<i>mP</i> 2	63.8	0.308	48.8	319	218	310	210	13	8
<i>mP</i> 3	71.0	0.188	67.4	129	60	108	47	25	14
<i>mP</i> 5	77.6	0.212	62.4	644	263	611	247	35	20
<i>cAA</i> avg.	59	0.38	43.4	263	187	256	190	6	4
<i>mP</i> avg.	71	0.242	58.6	387	176	362	159	25	15

Results 3—sea-salt suppression of sulphate nuclei activation

This is the first experimental evidence showing monotonically-decreasing SMA cloud droplet concentrations with higher PMA activated fraction. These results are more extensive than those presented in O'Dowd et al. (1999b) showing the effects of sea-salt on nss-SO₄ at varying updrafts using one case study. These trends show multiple ambient cases where this effect is being enacted in the marine environment. In fact, on average, there is a 2.5 % suppression of SMA number activation per PMA particle activated. The average activated PMA concentration in *mP* air was $14 \pm 4.7 \text{ cm}^{-3}$. Comparing this to when there was effectively no sea-salt, using the relationships in Figure 6.1 it can be estimated that the activation of PMA particles will suppress 4 times as many SMA CCN from activating. On average, the presence of 14 activated PMA nuclei cm^{-3} will reduce the cloud droplet concentration from 198 cm^{-3} to 142 cm^{-3} droplets.

To look for a suppression of (SMA) cloud droplet concentrations with increasing sea-salt concentration, satellite measurements over the Southern Ocean were retrieved. These image products reveal that cloud effective radius for January 2015, is (of the order of 5-10 microns) over and immediately north of the Weddell Sea ice region than the lower latitude open ocean, while cloud optical depth shows a 5-fold decrease as you move from the Weddell Sea region to North of the pack ice region (Figure 6.2). These trends are inverted in the aerosol sea-salt extinction maps of the region where sea-salt aerosol optical depth increases 6-fold as you move away from the higher latitudes and out towards the open Ocean. This implies that over the Weddell Sea region, where sea-salt is present in lower concentration than the open ocean directly north of it, more cloud droplets are formed, in turn, reducing the available water vapour per droplet resulting in smaller droplets. This corroborates the ambient trends in Figure 6.1 whereby increases in sea-salt number concentration (PMA concentration) leads to decreases in S_c , effectively reducing the amount of liquid water and leading to a lower concentration of larger cloud droplets. This relationship is investigated further with the use of a cloud parcel model in the next section.

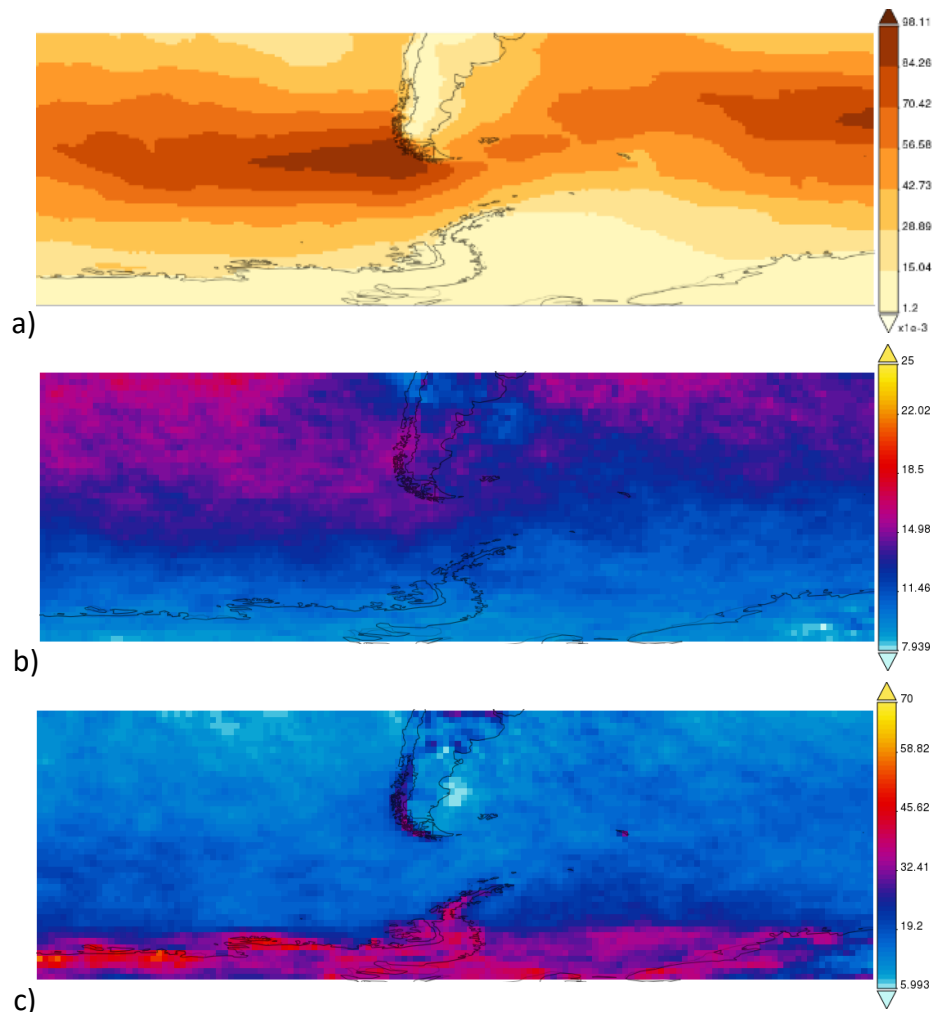


Figure 6.2. MODIS retrievals of the PEGASO cruise region from December – February 2015. (a) MODIS product sea-salt optical depth. (b) Cloud (liquid water) droplet effective radius. Larger effective radii are encountered over the open ocean irrespective of marine productivity while lower effective radii are seen nearer the coast and over the Peninsula and Weddell Sea area where PMA is at a minimum. (c) Liquid water cloud optical depth. Both cloud products are from MODIS at a 1° resolution and averaged over the month of January 2015. The high optical depth values correspond to the regions where effective radius is low, and the fraction of activated nuclei is high (i.e. the absence of sea-salt).

6.3 Simulating ambient data via parcel model(s)

To investigate the Hoppel mechanism of droplet nucleation, the process of activation *via* monomodal SMA and multimodal PMA initiators is simulated using a 1-D microphysical droplet activation model for natural marine conditions. Rather than use one model to test the activation, three 1-D cloud microphysical models are used for comparison. Two of the models use a numerical approach to calculations, and one uses an analytical approach. The Analytical-Parcel Model (κ A-PM), is described in Snider et al. (2017), with an earlier version described in Snider et al. (2003), there referred to as the *UWyo parcel model*. The κ A-PM uses κ -Köhler theory

Results 3—sea-salt suppression of sulphate nuclei activation

(see Section 3.5.3) to describe water activity of the aqueous droplet. One cloud microphysical Numerical-Parcel Model (iN-PM), written in Fortran, uses ionic balance to estimate water activity and was run for all steady-state PEGASO cases and a description can be found in O’Dowd et al. (1999). The model uses a combination of lagrangian microphysical equations for the formulation of droplet growth in a rising adiabatic parcel (Pruppacher and Klett, 1978), which accounts for the equilibrium activation of particles. Water activity is based on ionic disassociation and associated coefficients are determined by built in formulations (Pitzer, 1991) while other coefficients follow the methods of Abdul-Razzak and Ghan (2000). The other numerical model employs similar formulations, however in place of water activity parametrisation by ionic balance, it uses the κ -Köhler approximation of water activity as a function of droplet size. This model is written in Python (κ N-PM), and is open source code called *Pyrcel* (<http://github.com/darothén/pyrcel>) (Rothenberg and Wang, 2015). The κ A-PM was run as a control test for accuracy between the numerical models, as an exercise in model inter-comparison. All models were run for the same initial parameters ($P = 920$ hPa, $T = 278.15$ K, $RH = 98.5$ %, accommodation (condensation) coefficient of 0.96 (1.0)), and the assumption of either bisulphate or sulfuric acid as the main SMA constituent depending on the DON_{mol} of each pseudo-steady-state case.

In the models multimodal PMA distributions were used as input, derived from the source function found in Ovadnevaite et al. (2014b). The sea-salt aerosol population comprises five modes (Table 6.2) over the sub-micron size range (Ovadnevaite et al., 2014b). One mode at 230 nm (and another more minor at 830 nm), although not so evident in number space, dominates the mass of the sea-salt population as can be seen when plotted in mass or volume space. The peak of the number size distributions for sea-salt occurs around 90 nm dry mobility diameter with two further smaller diameter modes evident. The smallest mode, at ~ 18 nm, is almost equal in magnitude to the 90 nm peak at surface-level wind speeds < 20 m s⁻¹.

The cloud parcel microphysical models used in this study all required initial input parameters including T , P , updraft velocity (w), RH , α_T , α_c , aerosol particle modes, and either particle ionic composition or κ -values. For the iN-PM, this was in the form of mixing ratio and v_s (number of disassociating ions; 3 for SO_4 and 2 for NaCl), while for the κ N-PM and κ A-PM it was in the form of κ -values (from κ -Köhler theory). The input parameters outside of the particle number-size distributions are listed in Table 6.3, while the inputs of the SMA initiator (lognormal) mode is listed in Table 6.4 for the model comparison to the κ A-PM. Table 6.4 lists the starting case SMA based number concentration and amplitude, but these values were varied for the model comparison.

Results 3—sea-salt suppression of sulphate nuclei activation

Table 6.2. Sea-salt modal parameters used for scaling for sea-salt initiator for parcel models. The modes are based on a 6.3 m s^{-1} wind speed parametrisation in Ovadnevaite et al. (2014b). Peak location (x_0), peak geometric spread (σ_g), and peak amplitude (A) are shown.

Cases	Mode 1	Mode 2	Mode 3	Mode 4	Mode 5
x_0	0.018	0.041	0.09	0.23	0.83
σ_g	1.42	1.28	1.42	1.54	1.87
A	27.6	11.5	31.5	8.8	2.5

Table 6.3. The iN-PM input variables and example of input used for comparison to κ N-PM. The parameters were slightly changed when comparing to the κ A-PM.

Parameter	Used value (κ A-PM comparison)
relative humidity, %	98.5 (98.5)
activity coefficient	5.0
osmotic coefficient	1.0 (1.0)
accommodation coefficient, α_T	0.96 (0.96)
condensation coefficient, α_c	1.0 (1.0)
Temperature, K	258.15-273.15 (283.15)
Pressure, hPa	920.0 (900)
updraft velocity, m/s	0.1-0.5 (0.07-0.3)
mixing ratio, used to calculate molecular weight of sulphate	0.8 (0.8)
number of size distribution points (SS = sea-salt)	100 (200)
number of size distribution points (S = sulphate)	300 (200)
κ -value of sulphate (ammonium sulphate – H_2SO_4)	0.6-0.9 (0.6)
κ -value of sea-salt	1.12 (1.12)

Table 6.4. SMA monomodal input parameters of the case used to compare the cloud parcel models. Lognormal Peak location (x_0), peak geometric spread (σ_g), peak amplitude (A), and final number concentration yield of the peak (N). The last columns show the scaling used on the sea-salt number distribution and resultant sea-salt particle number (cm^{-3}). The sea-salt distributions had 5 modes (see Table 6.2). These lognormal distributions were generated using Eq. 18.

Case	x_0	σ_g	A	N SO_4	Sea-salt scaling	N sea-salt
<i>mP X</i>	0.051	1.46	290	385	$\times 0.961$	67

Results 3—sea-salt suppression of sulphate nuclei activation

To test the sensitivity of each model (and associated differences between them), a base case was used for an *mP*-like aerosol population, described in Table 6.4. The test was run using the same initial parameters and the results are shown in Figure 6.3. The model calculated resultant cloud peak supersaturation (S_c , %) and cloud droplet number concentration (CDNC) are shown. All models calculate CDNC based on the number of activated droplets or droplets of size $> 3 \mu\text{m}$ in diameter. It was found that the difference between the models could be quite large ($\sim 40\%$), with the iN-PM showing the largest difference from either of the other two, by achieving higher maximum supersaturations and therefore CDNC per updraft. For example, at a SO_4 based particle number concentration of $200 \text{ particles cm}^{-3}$, the calculated S_c of the $\kappa\text{N-PM}$ showed a 32-37 % difference from the iN-PM and only a 2-4 % difference from the $\kappa\text{A-PM}$. The difference between the iN-PM and the two κ -value based models is not surprising, as the ion-based approach will likely yield different results to the κ -based approach. Differences in the output are smaller between the κ based analytical and numerical model. However, the analytical model ($\kappa\text{A-PM}$) activated less particles per S_c than the numerical model. These results illustrate that the type of model being used can lead to notable differences in absolute cloud droplet number concentrations or supersaturation, however, they all maintain similar activation kinetic trends.

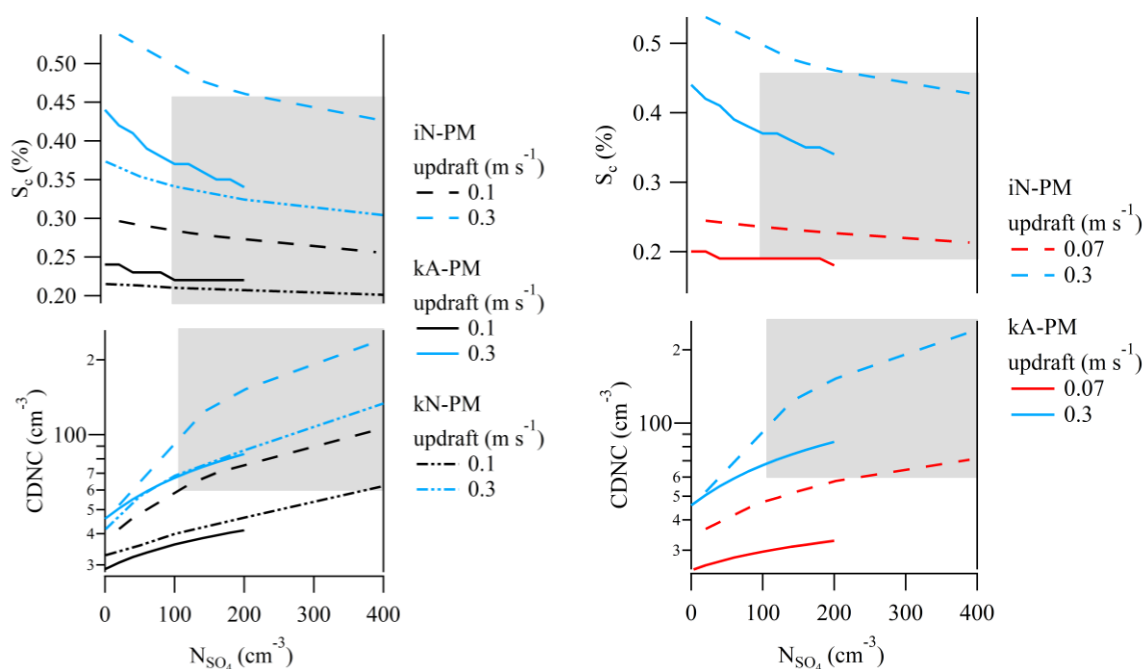


Figure 6.3. (Left) Inter-comparison of model results of cloud peak supersaturation (S_c %) and cloud droplet number concentration (CDNC cm^{-3}) for three parcel model types is shown. The iN-PM, $\kappa\text{A-PM}$, and $\kappa\text{N-PM}$ are compared at 0.1 m s^{-1} and 0.3 m s^{-1} updraft and varying SO_4 number concentrations (N_{SO_4}). (Right) Inter-comparison of two model types, the iN-PM and $\kappa\text{A-PM}$, at 0.07 m s^{-1} and 0.3 m s^{-1} and varying SO_4 number concentrations (N_{SO_4}). The different updrafts are represented by different colours and the different models are represented by differing line format. The grey shaded area marks measured ambient N_{SO_4} , CDNC, and S_c values.

Results 3—sea-salt suppression of sulphate nuclei activation

The difference between the κ activity and ion activity models has not been extensively studied in this research, however, it should be considered that the use of two simple 1-D cloud parcel models can neither accurately describe the ambient aerosol nor show results with < 40% difference to each other. The question must be asked, why? The aerosol described in this system is less complicated than that of aerosol in other systems (such as the North East Atlantic). The models, while using different solvers embedded in their programming, only truly differ by the theoretical representation of water activity (κ -values, versus ionic composition and dissociation of ions). The differences likely arise during simulation of the subsaturated regime. Specifically, the different water activity parameterisations may behave differently in the subsaturated regime. Theoretically, κ -Köhler theory can be extended down to subsaturated conditions (Petters and Kreidenweis, 2007), however a study comparing calculated κ -values from experimental measurements in the supersaturated regime (from CCN measurements) and the subsaturated regime (from hygroscopicity measurements of GF) could not reach closure (Irwin et al., 2010). This may imply that during the initiation of the model, when the initial droplet radii are approximated by Köhler or κ -Köhler theory in the subsaturated regime, the latter may be approximated incorrectly. This would cause the off-set seen in the trends, while maintaining model accuracy in activation kinetics in the supersaturated regimes. These 1-D models are often used in the creation and testing of parameterisations (Mårtensson et al., 2010; Conant et al., 2004; Fountoukis et al., 2007; O'Dowd et al., 1999a) so a 40 % difference between is less than ideal for CDNC when considering cloud radiative properties in the natural environment.

6.4 Modelling suppression with sea-salt distributions extending into the Aitken mode

All three tested models show similar trends but dissimilar absolute values for the same basic input. As the two κ -based models were very similar in modelled output, the next section focusses on comparing the iN-PM and κ N-PM output using the steady-state cases (Section 6.2) as input. This is to minimise differences that may arise between the numerical and analytical approach while highlighting the differences between an ionic and κ -based activity model. To assess which of the two numerical models better represented the actual absolute values, the models were tested against ambient data for validation.

A reverse-engineering of the SMA Aitken monomodal distributions which would theoretically be produced in the marine environment from a single source, was performed. First, an assumption is made that upon cloud formation, un-activated particles ($d_m < D_c$) will experience very little aqueous phase chemistry and no

Results 3—sea-salt suppression of sulphate nuclei activation

significant increase in the dry particle size. Then, the changes in number-size distribution spectrum as a function of cloud droplet nucleation and subsequent growth can be considered (Figure 6.4). As the particles grow in wet droplet diameter (D), the production rate of sulphate increases by orders of magnitude, thereby increasing mass significantly in the activated droplets (regime (ii) to (iii) in Figure 6.4). After subsequent evaporation out of cloud, the activated Aitken mode droplets will have increased in mass and thereby dry particle size. However, those particles which did not activate, did not experience similar amounts of sulphate addition and have not significantly changed in mass. Upon evaporation these particles should return to a similar dry size. Therefore, when considering a dry particle distribution, the smaller diameter particles should remain unchanged in slope, amplitude, and position (within uncertainty bounds) if these particles have critical activation supersaturation larger than those experienced in cloud. For the ambient cases considered here, this refers to the left side of the Aitken mode for the bimodal marine distributions. Then it follows that for fitting the SMA monomodal distributions for model input, the monomodal distribution should reasonably match the left of the Aitken mode shoulder of the ambient distribution while conserving total SMA particle number (N_{SMA}). Holding N_{SMA} fixed, lognormal fittings can be adjusted to fit the aforementioned criteria using the distribution function (Hinds, 1982),

$$\frac{dN}{d\log D} = \frac{Amp}{\sqrt{2\pi}(\ln(\sigma_g))} \exp\left(-\frac{(\ln(D)-\ln(x_0))^2}{2(\ln(\sigma_g))^2}\right) \quad (2.303) \quad (18)$$

where the normalised distribution ($\frac{dN}{d\log D}$) at a given dry mobility particle diameter, D , was fit using σ_g , the geometric spread x_0 , the peak position, and Amp , the amplitude of the peak. If the fitting should not match the Aitken shoulder than there will either be a surplus or deficiency of un-activated particles. A surplus could possibly be explained by NPF events; however, a deficiency cannot be accounted for in the post-activation and subsequent growth number-size distribution spectrum.

To find out which of the two numerical models (iN-PM and κN-PM) is better at capturing the relationship between PMA activation, critical supersaturation, and SMA activation observed in the ambient data, each model was run for the same initiators relevant to the ambient case (Table 6.5). No inter-modal minimum (D_c) value exists for the output of the models, as different chemical species are represented separately. To show the same trends depicted for suppression in the ambient cases, critical diameter of activation of the SMA mode (D_c , SMA) was used to compare against critical supersaturation and the fraction of activated SMA particles. Neither model accurately represents the measured trends seen in the ambient dataset fully. The iN-PM better predicts CDNC (Figure 6.5), yet shows little change in S_c despite large changes in CDNC nor reproduces the ambient fraction of

Results 3—sea-salt suppression of sulphate nuclei activation

SMA CDNC trends (Figure 6.6). The κ N-PM better reproduces S_c (Figure 6.6) but fails to show good agreement with the ambient CDNC calculated (Figure 6.5). Both CDNC and S_c are important to the idea of supersaturation suppression, however, while CDNC may vary, S_c is a direct measure of changes in cloud dynamical parameters rather than CDNC which is an indirect measure. Therefore, the κ N-PM is the more robust of the two at being able to describe suppression of the cloud peak supersaturation, while CDNC accuracy is less ideal.

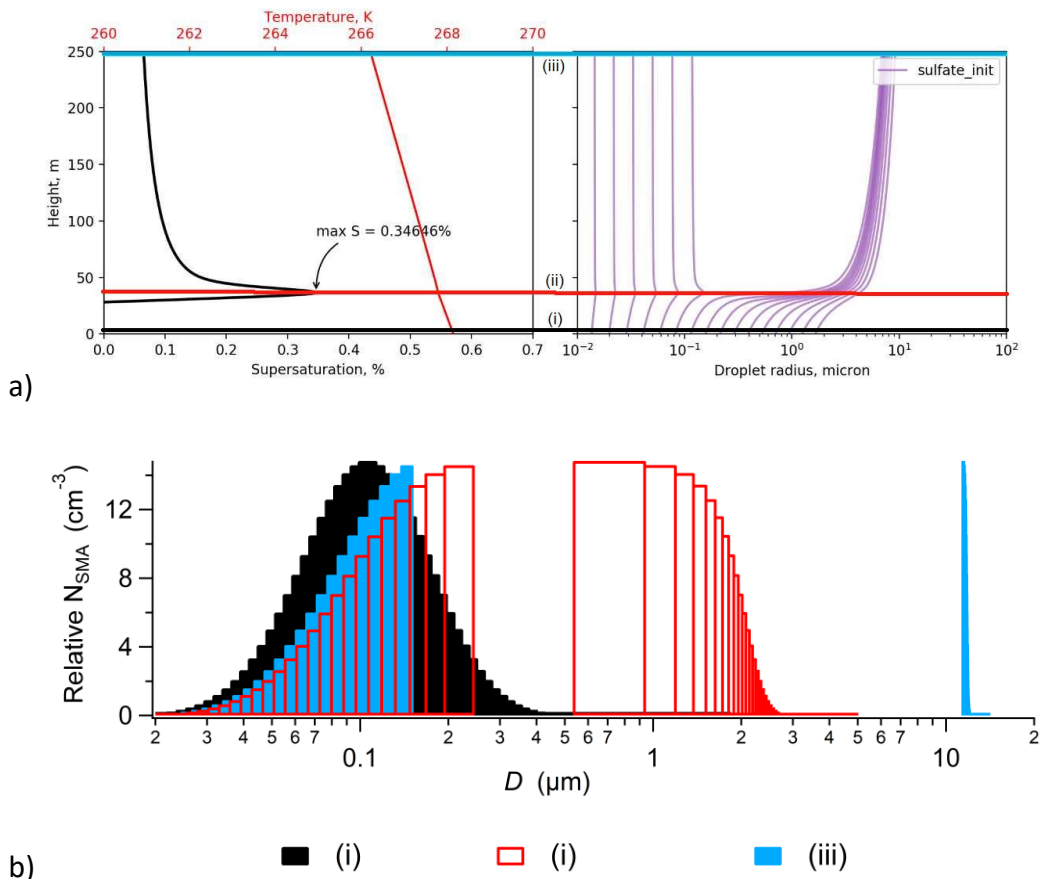


Figure 6.4. Activation spectrum of an adiabatic lifting parcel in a 1-D model (*Pyrce1*), using 20 bin sections, with starting temperature of 268.15 K, at 0.3 m s^{-1} vertical velocity. (a) (Left) the temperature and supersaturation vertical profiles. (Right) Droplet radius as a function of parcel height. The activation of droplets can be seen in particles which are at larger diameters at maximum height. Three regimes are highlighted by colour coded horizontal lines, with black (i) referring to the time at cloud base before droplet activation, red (ii) at droplet activation, and blue (iii) at cloud top after droplet activation, respectively. (b) The relative wet droplet diameter (D) for the three regimes are shown as a function of SMA number concentration (N_{SMA}).

Results 3—sea-salt suppression of sulphate nuclei activation

Table 6.5. SMA monomodal input parameters of the PEGASO ambient cases for the cloud parcel models. Lognormal Peak location (x_0), peak geometric spread (σ_g), peak amplitude, (Amp), and final number concentration yield of the peak (N). The last columns show the scaling used on the sea-salt number distribution for wind speed 6.3 m s^{-1} from Ovadnevaite et al. (2014b) and resultant sea-salt particle number concentration (cm^{-3}). The sea-salt distributions had five modes (see Table 6.2). These lognormal distributions were generated using the Eq. 18 (Hinds, 1982).

Cases	x_0	σ_g	A	N	Sea-salt scaling	N sea-salt
<i>cAA</i> 1b	0.063	1.53	291	288	X0.005	3
<i>cAA</i> 2	0.076	1.6	217	215	X0.021	11
<i>cAA</i> 3	0.071	1.44	240	234	X0.005	3
<i>cAA</i> 4	0.056	1.45	287	284	X0.012	6
<i>mP</i> 1	0.046	1.41	422	416	X0.043	22
<i>mP</i> 2	0.063	1.4	314	311	X0.025	13
<i>mP</i> 3	0.052	1.38	110	109	X0.048	25
<i>mP</i> 5	0.056	1.46	618	611	X0.067	35

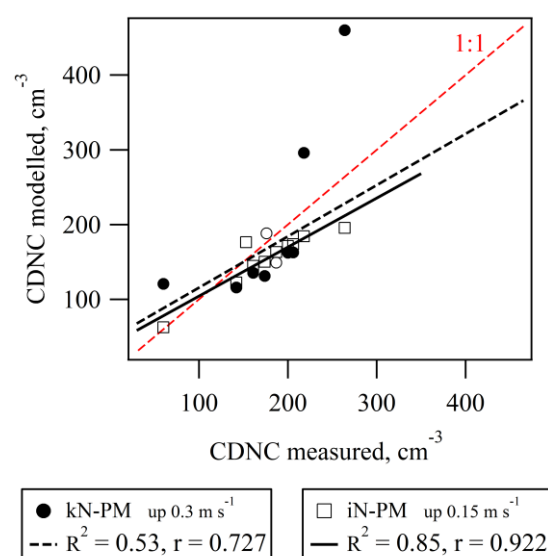


Figure 6.5. CDNC relationship between calculated (measured) and modelled from ambient Southern Ocean cases. The iN-PM is shown as square markers, and the kN-PM are shown as closed circles with averages of each air mass (*mP* and *cAA*) case shown in open circles. A 1:1 line is shown in red, with the fitted relationship between measures and modelled of each model also shown. The linear relationship of the PN-PM is shown as a solid line while the kN-PM is shown as a dashed line.

Results 3—sea-salt suppression of sulphate nuclei activation

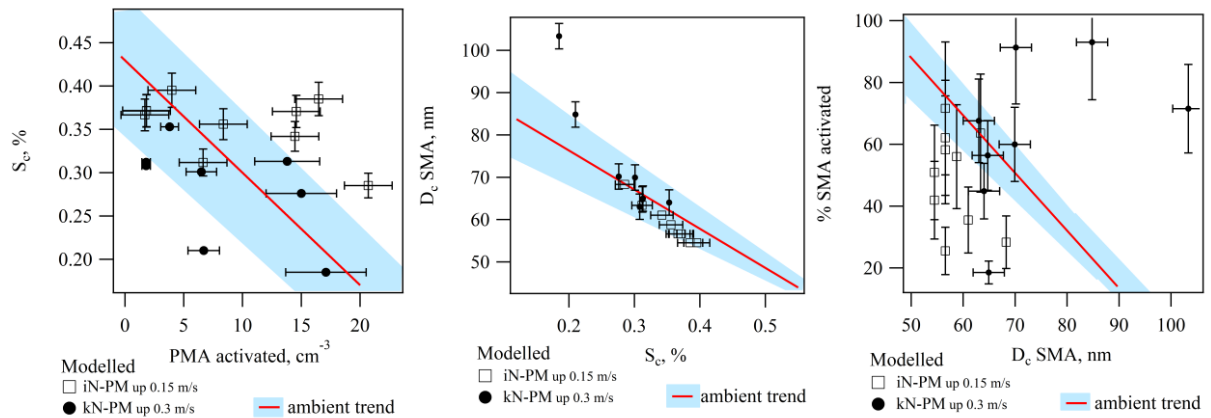


Figure 6.6. Calculated (or measured) and modelled values are shown as functions of different parameters with both iN-PM and κ N-PM model results. (Left) S_c and activated PMA (or sea-salt) relationship, (middle) SMA D_c and S_c , and (right) percent fraction of SMA activated and SMA D_c . In all plots the measured data and respective uncertainties are represented by the blue shaded region with associated fitted trend lines in red, while iN-PM are displayed as boxes and κ N-PM are closed circles. The error bars associated with each model are based on either the sensitivity or standard deviation of the model. The trends in the right two graphs are for trends using the inter-modal minimum (D_c) rather than the SMA D_c and are the same trend lines shown in the left-most graph panel in Figure 6.1. However, the blue shaded region corresponds to the measured SMA D_c .

6.5 Model sensitivity to environmental parameters and sea-salt number concentration

There is a clear trend in the ambient steady-state cases showing the suppressive effect of PMA activation on cloud peak supersaturation and the resultant reduction of SMA nuclei activation (Figure 6.1), which can be replicated by parcel models to some extent (Figure 6.6). With the use of the κ N-PM, the inter-modal minima analysis technique (developed from the Hoppel mechanism assumption) will be tested as a viable method for reconstructing MBL cloud supersaturation and processing. Moreover, using a full sea-salt spectrum and a monomodal SMA distribution, the extension of the suppression hypothesis (O'Dowd et al., 1999b) into the Aitken mode will be tested. Two cases are focused on: the average of the steady-state *mP* and *cAA* air mass aerosol populations (different from the merged cases in Chapter 5).

The main features of the average size distributions for the *mP* and *cAA* air masses are as follows: in the *mP* air mass, the minimum in the size distribution suggests a D_c of 71 nm with two accumulation mode peaks at 136 ± 5 nm and 190 ± 5 nm, in the *cAA* there are two accumulation mode peaks at 109 ± 5 nm and 174 ± 5 nm with the size distribution minima at 59 nm (Figure 6.7). In both cases the accumulation mode is

Results 3—sea-salt suppression of sulphate nuclei activation

made up of two SMA modes, where the modal diameter of the larger diameter accumulation mode is smaller in number concentration and consists of approximately 19 particles cm^{-3} for the *cAA* case, and 15 particles cm^{-3} for the *mP* case. For each case, chemical cloud processing is the only explanation for such a large modal diameter following arguments presented in O'Dowd et al. (2000b) and Chapter 5, where secondary vapour condensation is improbable with the low levels of OM present in either average case (Table 6.6). However, the higher D_c in the *mP* air can only be explained by a reduction in S_c . The reduction in S_c can be seen for each case on the CCN S_c - D_c curves in Figure 6.8, as the relevant S_c for each case corresponds to the inter-modal minimum point. The reduction in S_c could be explained by relatively lower vertical updrafts, by a larger fraction of activating hygroscopic particles such as sea-salt, or by a larger absolute concentration of activating particles, however the number of (absolute) activated particles was seen to be lower in *mP* cases (Table 6.1). Instead, the biological sources of SMA in the sub-Antarctic Ocean are proposed to produce a reservoir of sulphate CCN, possibly the cause of the persistent modal diameter of 43 nm in each air mass although probably with different sources, and that sea-salt particle number controls the fraction of these biogenic SMA particles which can activate into cloud droplets. To isolate sea-salt as the possible cause of the difference, updraft sensitivity is later tested for the average cases.

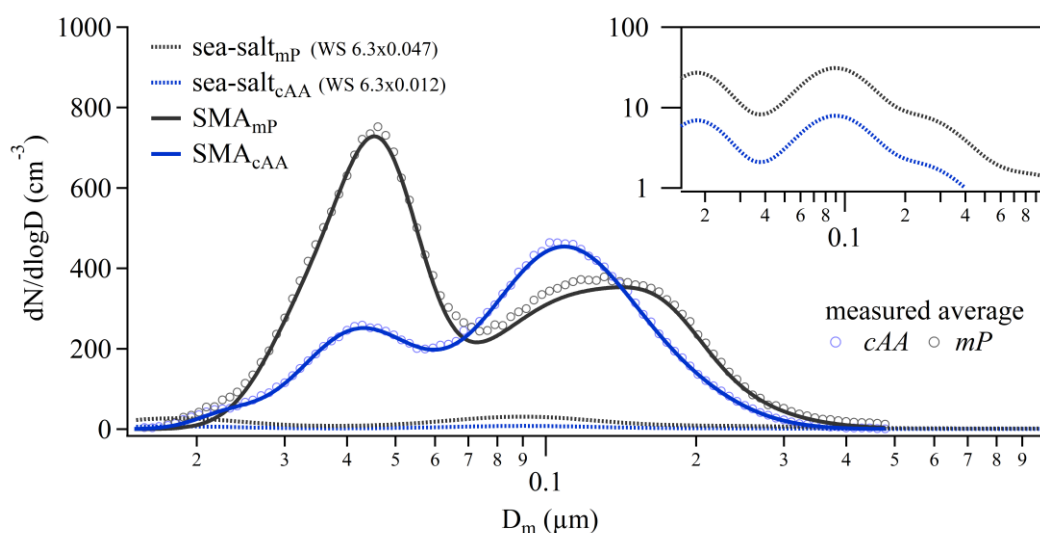


Figure 6.7. *cAA* averaged (blue) and *mP* averaged (black) size distributions for both cases. Measured average values are shown as circles, while calculated SMA are shown as solid lines, and sea-salt is shown as dashed lines. Sea-salt taken as PMA and derived from flux parametrisation in Ovadnevaite et al. (2014b) and scaled by mass while SMA is derived from the residuals (see Methods). In both cases, PMA consists of five modes and SMA consists of four modes, both shown as composites.

Results 3—sea-salt suppression of sulphate nuclei activation

The κN-PM was run for the size distribution inputs of the average cases. Using initial model inputs (Table 6.3), sea-salt modes, and an initiator nss-SO₄ mode, the parcel model was run resulting in simulated outputs of S_c , and profiles of particle radii, for both sea-salt and nss-SO₄ modes, respectively. From the particle growth along the vertical profile, particle activation could be determined. Subsequent particle critical radius (R_c) and CDNC were calculated. To establish results similar to the fitted ambient data which showed a second small amplitude accumulation mode in addition to the larger SMA accumulation mode, an internally mixed mode of nss-SO₄ and sea-salt was added to the average case inputs at particle concentrations of $\sim 10 \text{ cm}^{-3}$ at a mode peak of 185 nm ($\sigma_g = 1.16$). Notably, the reconstructed initiator modes for both the *mP* and *cAA* average cases were extremely similar in positioning and modal spread (but not in amplitude), further supporting the concept of a similar source of SMA. Due to their similarity (less than a 1 nm difference in modal positioning), the SMA mode initiators for each average case were adjusted to be the same position and spread for better comparison of the results.

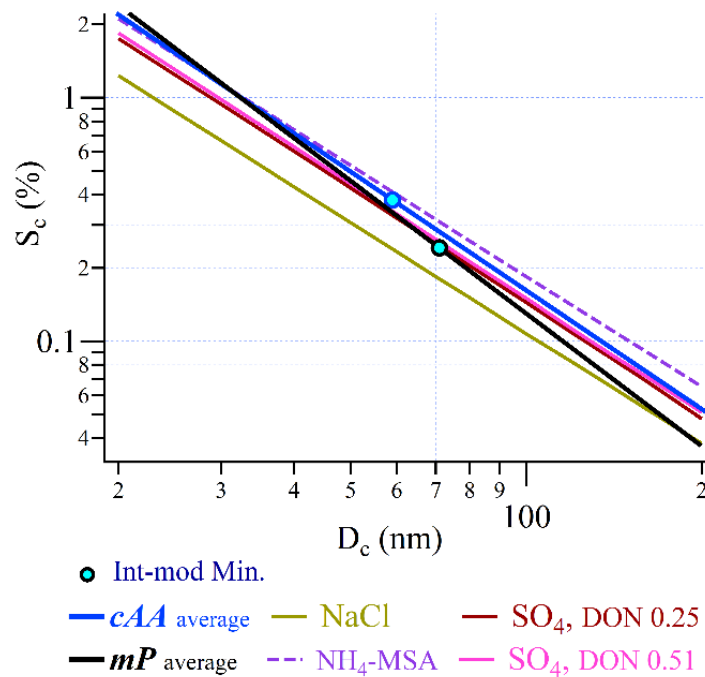


Figure 6.8. CCN activation (S_c - D_c) curves for the average cases of *mP* and *cAA* air masses. The *cAA* average case CCN curve is shown in blue, while the *mP* average case is shown in black. The inter-modal minimums of both cases are indicated by the bright blue marker along each respective curve. Theoretical curves for NaCl (proxy for sea-salt in olive brown) and partially neutralised SO₄ are indicated on the curve, where $\text{DON}_{\text{mol}} = 0.25$ (dark red curve) was determined for the *cAA* case and $\text{DON}_{\text{mol}} = 0.51$ (light pink curve) for the *mP* case. Theoretical activation of NH₄-MSA is also shown (dashed purple line). All theoretical curves are taken from the AIOMFAC (Zuend et al., 2011) model and calculated for a $T = 298.15\text{K}$, and $\sigma = 0.072 \text{ N m}^{-2}$.

Results 3—sea-salt suppression of sulphate nuclei activation

Table 6.6. Average chemical fractions from cases of *cAA* and *mP* air masses. Shown below are HR-ToF AMS measurements ($\mu\text{g m}^{-3}$) of organic mass (OM), nitrate (NO_3), non-sea-salt sulphate (nss- SO_4), ammonium (NH_4), sea-salt, methanesulphonic acid (MSA), and organic nitrogen (ON). Also shown below are total concentrations and biogenic concentrations (total without sea-salt), and averaged black carbon (BC) measurements from the SP2 (ng m^{-3}).

	<i>cAA average</i>			<i>mP average</i>		
OM	0.02	±	0.02	0.07	±	0.04
NO_3	0.01	±	0.00	0.01	±	0.00
nss- SO_4	0.37	±	0.09	0.4	±	0.3
NH_4	0.04	±	0.06	0.09	±	0.06
Sea-salt	0.03	±	0.04	0.3	±	0.2
MSA	0.08	±	0.03	0.12	±	0.08
ON	0.00	±	0.00	0.00	±	0.00
total	0.6	±	0.1	1.0	±	0.4
total biogenic	0.5	±	0.1	0.7	±	0.3
BC	0.2	±	0.2	0.1	±	0.2

The parcel model was tested for a range of ambient conditions to reproduce possible *mP* and *cAA* cloud conditions, which included changes in cloud base temperature, pressure and updraft velocity. Preliminary sensitivity testing suggested that the model was rather insensitive to changes in pressure associated with a cloud base height of 0.2-2 km. However, changes in temperature and updraft were quite significant to the determination of cloud peak supersaturation (Figure 6.9). Updraft sensitivity showed that a change in updraft of 0.1 m s^{-1} resulted in a change in supersaturation of 10-30 % with a corresponding change in CDNC of 15-100 %. High temperature sensitivity was found between reasonable temperatures (-15° - 0°C) of cloud base around Antarctica at time of observation, based on an average ambient surface temperature of $\sim 0^\circ\text{C}$. A change in temperature of 5° would result in a change in supersaturation of about 10 % and a corresponding change in CDNC of about 8 %. Due to the presence of both significant sensitivities, a different temperature was chosen for each case to effectively isolate an appropriate updraft for either. The initiation of the parcel model was set at a cloud base temperature of -5°C for *mP* and -10°C for *cAA*, as the latter should be the colder of the two air masses by nature (and as these temperature regimes should not be affected by mixed phase effects).

To isolate an appropriate updraft, relative closure between the model outputs and measured ambient aerosol was sought for the averaged air mass cases. Results of the model runs showed that, while using the appropriate number of SMA particles and reasonable temperature for each case respectively, the reasonable updraft for *mP*

Results 3—sea-salt suppression of sulphate nuclei activation

was found at $\sim 0.2 \text{ m s}^{-1}$ with an over-estimation of critical supersaturation by 15 % and under estimation of CDNC by 6 %. At 0.1 m s^{-1} updraft the critical supersaturation was under- estimated by 13 % while CDNC was under- estimated by 38 %. The *cAA* average case was found to have the best reproducibility at an updraft of 0.3 m s^{-1} with an over- estimation of critical supersaturation by 4 % and under estimation of CDNC by 6 %. At 0.2 m s^{-1} updraft the critical supersaturation was under- estimated by 12 % while CDNC was under- estimated by 20 %.

Reported updrafts from Snider et al. (2017) would imply that these updrafts (0.2 and 0.3 m s^{-1}) are on the lower end of the average vertical updraft of 0.4 m s^{-1} in the summer higher marine latitudes. However, increased updrafts result in a 55 % and 20 % difference in supersaturation and CDNC, respectively for the *mP* average case. This refers to an absolute 0.13 % increase in S_c and a difference of about 36 cm^{-3} in CDNC, which would be significant and may suggest that more water scavenging particles are present at larger sizes.

To test the sensitivity of the model outputs to changes of amplitude in the monomodal initiator, realistic SMA modes were fitted within uncertainty bounds of our cases (Figure 6.10) and the output was tested while varying updraft velocity (w). The particle number concentrations vary significantly ($141 - 658 \text{ cm}^{-3}$) between the *mP* cases, resulting in possible discrepancies of the defining variables such as the inter-modal minimum, S_c , and CDNC. While the *cAA* cases, conversely, had less particle number concentration variance ($230 - 309 \text{ cm}^{-3}$), different modal amplitudes were still tested for sensitivity analysis. The *cAA* case having less variance, also produces less variance in the model output with changed number. Decreasing the number of initial SMA increases the critical supersaturation but also decreases the CDNC, effectively worsening the closure. The *mP* case shows more variance in number but also shows the same sensitivity, that increasing the supersaturation by 0.04 % decreases the CDNC by ~ 100 particles at $w = 0.2 \text{ m s}^{-1}$.

Results 3—sea-salt suppression of sulphate nuclei activation

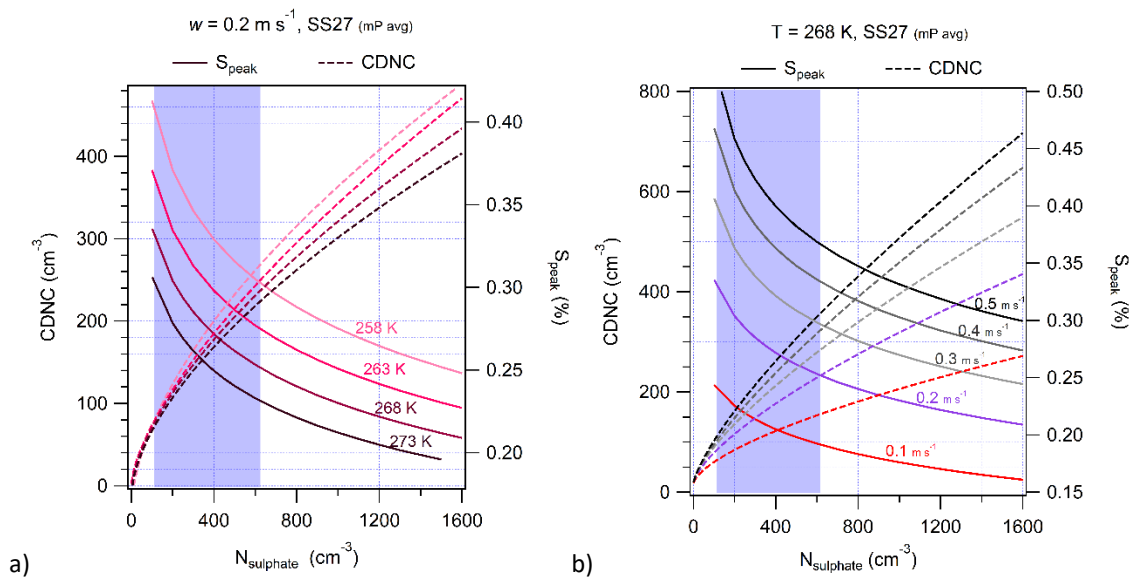


Figure 6.9. (a) Sensitivity analysis of the PN-PM to changes in cloud base temperature. (b) Sensitivity analysis of the PN-PM to changes in updraft velocity (w). On both graphs the left axis shows CDNC of sulphate in dashed lines while the right axis shows cloud peak supersaturation (%) in solid lines. The changes in colour (or shade) of the line refer to changes in temperature (from 258 -273 K) or w (from 0.1-0.5 m s^{-1}). The shaded region marks the range of N_{sulphate} measured in the eight steady-state cases.

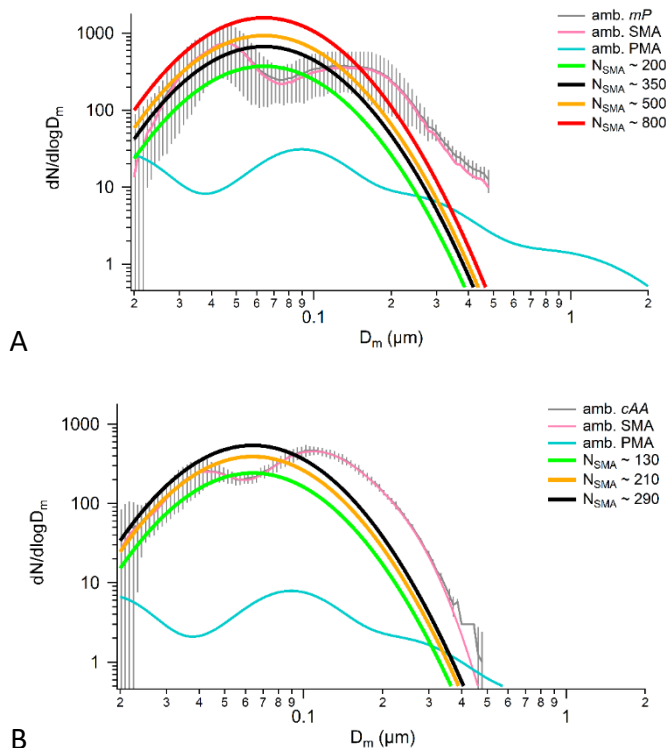


Figure 6.10. Different SMA initiator modes are shown for each air mass type average case to illustrate the range of possibilities from the error margin in the case averages. On each graph, the ambient data is represented with the vertical error bars, while the total SMA and PMA are represented by pink and blue distributions respectively. The actual SMA number for the initiator mode is indicated by the black line, with other possible modes with incorrect SMA number indicated by the other coloured lines. A) Shows the mP case average and B) shows the cAA case average.

Results 3—sea-salt suppression of sulphate nuclei activation

The positioning of the monomodal initiator, holding the spread and peak of the mode constant, is critical in representing cloud droplet activation because it determines what fraction of the mode fall above the critical diameter. Unsurprisingly, the model was highly sensitive to the positioning of the monomodal initiator (Figure 6.11). An input of $N_{\text{SO}_4} = 300 \text{ cm}^{-3}$ and a change of peak modal diameter of 20 nm would result in a 10 – 100 % increase in supersaturation and a 20 – 200 % change in CDNC. Of all the sensitivities, this is the only one which displays an inverse relationship between cloud peak supersaturation and CDNC. This is logical; the inverse relationship is due to the fraction of activating droplets controlling the maximum supersaturation (as sea-salt, updraft, and temperature are held fixed).

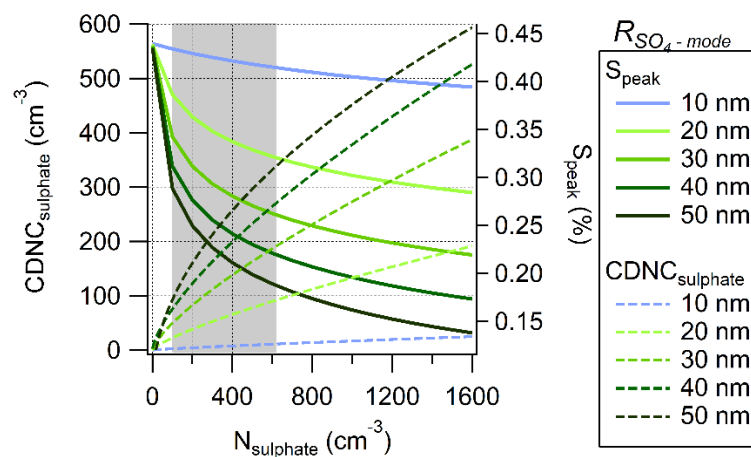


Figure 6.11. Sensitivity analysis of the κ N-PM to changes in SO_4 initiator modal positioning using peak radius ($R_{\text{SO}_4\text{-mode}}$). The left axis shows CDNC of sulphate in dashed lines while the right axis shows cloud peak supersaturation (%) in solid lines. The changes in colour (or shade) of the line refer to changes modal peak position (from a radius of 10 – 50 nm). The shaded region marks the range of N_{sulphate} measured in the eight steady-state cases.

Ambient features of the average cases were shown to be reproducible (within 20 % uncertainty) using the κ N-PM once environmental parameters were established. Overall, the parcel model showed sensitivity to cloud base temperature (Figure 6.9a), updraft velocity (Figure 6.9b), to the location and magnitude of the initial SMA monomodal input (Figure 6.11), and to sea-salt number concentration (Figure 6.12). Due to the method of reconstructing a monomodal initiator by anchoring the shape of the lognormal distribution to the smaller diameter side of the Aitken shoulder of the ambient aerosol, cAA monomodal inputs have overall higher σ_g and smaller amplitudes than the mP monomodal inputs (Table 6.5). To mitigate the complications of using different updrafts to compare the effects of sea-salt on ambient SMA, the model output when adjusting only the sea-salt distributions can be compared for the same SMA input and fixed updraft (using mP SMA distributions and 0.4 m s^{-1} and also

Results 3—sea-salt suppression of sulphate nuclei activation

0.2 m s⁻¹ w at -5°C). In this scenario, shown in Figure 6.12, we see a reduction in S_c , which is most significant for low values of n_{ss-SO_4} particles, and translates into a reduction of CDNC. At $w = 0.2$ m s⁻¹, for an input SMA particle concentration of 300 cm⁻³ the addition of 9 sea-salt particles (to 1 sea-salt particle) reduces the supersaturation by an absolute 0.006 % translating to a reduction in 4 cloud droplet particles cm⁻³ in. The addition of 39 sea-salt particles, rather than 9 particles, for the same scenario reduces the supersaturation by an absolute 0.025 % translating to a reduction in 13 cloud droplet particles cm⁻³. If we increase the updraft velocity for the same scenario to 0.4 m s⁻¹, the addition of 39 sea-salt particles also reduces the supersaturation by an absolute 0.025 % translating to an equal reduction in cloud droplet particles of 13 cm⁻³. However, the difference in absolute CDNC values between the higher and lower updrafts is 44 cm⁻³ (168 cm⁻³ from 124 cm⁻³) for the case of 40 sea-salt particles cm⁻³. The observed Southern Ocean, was calculated to have an SMA particle concentration as high as 611 cm⁻³. If we consider a scenario with a large amount of sea-salt (160 cm⁻³) compared with almost no sea-salt (<5 cm⁻³) then CDNC would be reduced by 31 % for $w = 0.2$ m s⁻¹ and reduced by 17 % for $w = 0.4$ m s⁻¹. However, if sea-salt particle concentration were to increase with a simultaneous decrease in updraft velocity (by only -0.2 m s⁻¹) then CDNC would be reduced by 50 % (Figure 6.12).

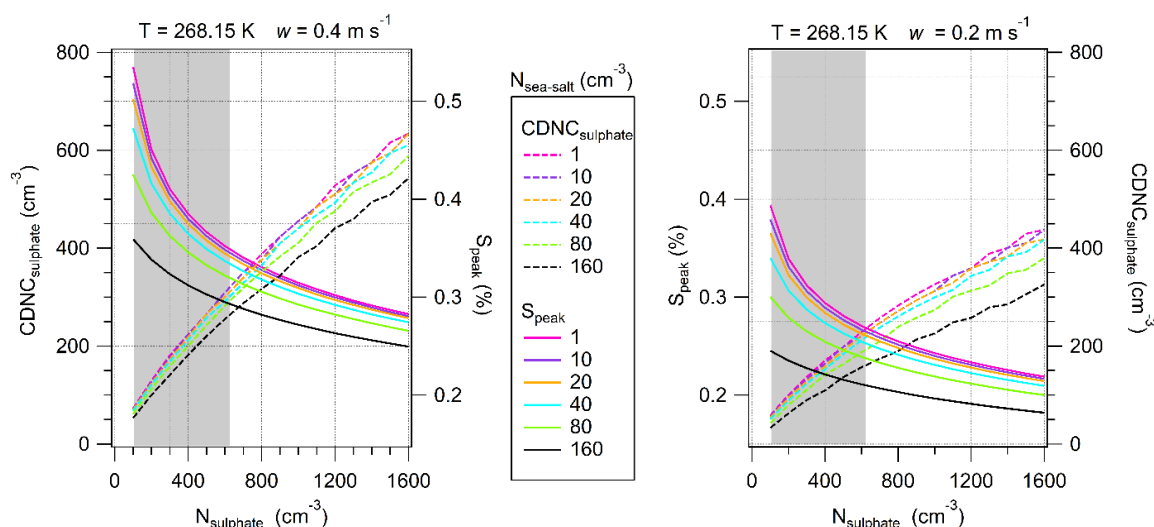


Figure 6.12. Sensitivity analysis of the κ N-PM to changes in sea-salt particle number concentration. For the graph on the left, the left axis shows CDNC of sulphate in dashed line while the right axis shows cloud peak supersaturation (%) in solid lines, while the graph on the right shows the right and left axis swapped. The changes in line colour refer to changes in sea-salt (SS) number concentration (from 1 to 160 sea-salt particle (SS) cm⁻³). The shaded region marks the range of $N_{sulphate}$ measured in the eight steady-state cases. On left, the graph shows values for $w = 0.4$ m s⁻¹, and on right the graph shows values for $w = 0.2$ m s⁻¹ both graphs are for -5°C.

6.6 Suppression analysis conclusions

Cloud peak supersaturation suppression and subsequent reductions in SMA CDNC is shown to be directly linked to the sea-salt aerosol number and size-distribution. The suppression influences cloud properties and, thus, the marine radiative budget through the lowering of CDNC. Trends in the ambient show that PMA particle activation effectively leads to a reduction in SMA particle activation. Using two parcel models, and an SMA reservoir approach to the model input, these trends are shown to be mirrored to a degree in the model output. Summer is typically correlated to a seasonal increase in CCN from biogenic sources, but sea-salt can compose a significant fraction of the CDNC when lower updrafts velocities are considered (see Section 5.3). Larger updrafts allow most of the small Aitken mode size distribution SMA particles to activate. This leads to aqueous phase processing and the internal mixtures of secondary and primary compounds.

This study also shows that supersaturation suppression is sensitive to a range of environmental conditions including updraft velocity, cloud base temperature, and the location of the initial lognormal distribution of SMA particle concentrations. Using a nominal SO_4 particle concentration of 300 cm^{-3} we can compare the sensitivities. Updraft sensitivity showed that an increase in w from 0.2 m s^{-1} to 0.4 m s^{-1} resulted in a change in S_c of $+0.1 \%$ and CDNC of $+48 \text{ cm}^{-3}$. Temperature sensitivity showed that a decrease in temperature from 273.15 K to 263.15 K resulted in a change in S_c of $+0.05 \%$ and CDNC of $+13 \text{ cm}^{-3}$. If we consider an SMA particle concentration of 600 cm^{-3} , then a combination of increased T ($+15^\circ\text{C}$), decreased updraft (-0.4 m s^{-1}) and increased sea-salt (from 1 to 160 particles cm^{-3}) would result in a 103 % reduction in CDNC. Modal positioning showed that a decrease in modal diameter from 60 to 40 nm (d_m) resulted in a relative decrease in S_c of 19 % and CDNC of 53 % (an absolute change of -59 cm^{-3}). This sensitivity implies that running each case (*cAA* and *mP*) using the same modal positioning is key to isolating any other single effect. If we ran the cases at different peak positions, then other sensitivities could not be properly isolated. The sensitivities in environmental input may be somewhat linked to the differences observed between the CDNC activation of the model output and the ambient cases, as all environmental conditions were held fixed. When using the average cases for the different air mass types and more case representative environmental conditions (*cAA* representing low sea-salt and *mP* representing higher sea-salt), better closure between activated and calculated CDNC is achieved.

If the presence of more condensing vapours or higher SO_2 concentrations leads to the growth of Aitken mode particles to larger sizes, then sea-salt particle concentration has a reduced supersaturation suppression effect. This is due to the increased supersaturation suppression effect that the number of overall sub-cloud

Results 3—sea-salt suppression of sulphate nuclei activation

particle concentration can have on supersaturation upon activation, as more particles will be above the critical diameter of activation. Higher updraft velocities lead to higher overall supersaturations which also reduces the suppression effect of sea-salt. Critical diameter and temperature have an inverse relationship as D_c slightly increases with decreasing temperature. However this is overpowered by the inverse relationship between temperature and cloud peak supersaturation seen in the temperature sensitivity model runs. As temperature decreases, cloud peak supersaturation increases for a fixed updraft, drastically reducing the critical diameter of activation (regardless of slight increases due to the initial drop in temperature). This implies that the competition effects of sea-salt seen in the Southern Ocean where it is cold and without high particle concentrations, may be further enhanced in warmer marine environments. This effect has also been seen in the warmer ambient North Atlantic, although with much higher concentrations of sea-salt particulates (O'Dowd et al., 1999). The effect of sea-salt on cloud activation of anthropogenic pollution may also be important, potentially even more so, as pollution is often more hydrophobic than biogenic SMA, while often existing at smaller particle sizes than sea-salt. The supersaturation suppression may have a notable effect, as particle concentration would be higher and the critical diameter of anthropogenic SMA would be significantly increased resulting in fewer activated particles, overall weakening the Twomey effect.

7. Conclusions

The aim of this research was to investigate marine aerosol influences on the chemical and physical nature of cloud condensation nuclei activation and thereby further our understanding of the complicated nature of aerosol-cloud interactions in the marine environment. To achieve this aim, aerosol measurements from remote marine regions (namely the Southern Ocean, but also to a lesser extent the North East Atlantic) were intensively studied, yielding numerous insights into the natural state of marine aerosol and the associated physico-chemical properties of marine cloud condensation nuclei (CCN).

Marine aerosol number-size distribution and chemical composition affect the fraction of particles which act to form marine low-level clouds which can be significantly altered by pollution. This work investigated black carbon (BC) data (as a tracer for air pollution) from the Southern Ocean to determine the extent to which anthropogenic pollution was detectable in the marine environment. The measurements of BC taken with an SP2 during the PEGASO cruise were compared to the SP2 data from the North East Atlantic (at Mace Head Atmospheric Research Station). It was shown that after the application of correct criteria, natural marine aerosol could then be separated from anthropogenically influenced marine aerosol for analysis.

The Southern Ocean was found to be pristine for 93 % of the observation period from the black carbon analysis, making it an ideal location to study the cloud nucleating properties of natural marine aerosol. Using a suite of *in-situ* instrumentation, a new method of analysing CCN data through a powerful multi-instrumental set-up was employed for the Southern Ocean aerosol analysis. In measuring the water uptake properties of the aerosol, this powerful setup elucidates many important properties of the CCN population through comparative analysis with modelled particle hygroscopicity, particularly the inferred composition of the nuclei as a function of size. This work quantified the relative importance of 'primary' wind-produced sea spray over secondary (gas-to-particle conversion) sulphate in forming marine clouds, revealing that for realistic marine boundary layer cloud supersaturation (e.g. < 0.45 %), primary CCN contributed 8–51 % for the marine air for surface-level wind speed < 16 m s⁻¹. At higher wind speeds, primary marine aerosol could even contribute up to 100 % of the activated CCN, for corresponding peak supersaturations as high as 0.32 %.

Importantly, the extended analysis of the Southern Ocean cases was able to show clear ambient trends for which an increase in primary cloud nucleating particles resulted in a significant reduction of the fraction of secondary nucleating particles. These ambient observations are further evidence of the link between sea-salt cloud

Conclusions

nucleated particles and supersaturation suppression, likely from the competitive activation of sea-salt particulates over secondary marine aerosol. Through 1-D parcel modelling of SMA and sea-salt (extended down to the Aitken mode), the Hoppel mechanism of cloud droplet activation (from the theory of well-mixed MBL droplet activation presented in Hoppel et al. (1986)) was found to accurately reproduce the ambient data and CDNC populations. The modelling study revealed the scope of sensitivities impacting the parcel model output at realistic marine boundary layer conditions, including input temperature, updraft, particulate distribution (modal amplitude, position, and width), and sea-salt particle concentration. Sea-salt particle concentration is especially important in marine environments with otherwise changing environmental conditions, as it impacts cloud peak supersaturation, and thereby marine CDNC. In remote oceanic regions, this marine CDNC significantly impacts the global albedo.

These findings are summarised in more detail in the next section (Section 7.1). The implications of these findings for the role of marine aerosols in cloud nucleation and other aerosol-cloud interactions will also be discussed (Section 7.2).

7.1 Summary of main results

Black carbon measurements in marine environments suggest the persistence of clean conditions

The study showed that the aerosol measurements that were taken during the PEGASO cruise were as free from pollution as possible for that region. Black carbon (BC) was frequently detected (93 % of the time) in the Southern Ocean region at a mass concentration $\leq 0.14 \text{ ng m}^{-3}$. At these low BC concentrations, marine aerosol may be considered pristine. No correlation between OM and BC existed at these levels, additionally implying that OM measured during pristine conditions were biogenic rather than anthropogenic in origin. The analysis of available SP2 measurements taken at Mace Head research station (MHD) showed that the background BC mass concentration (with a peak at 0.1 ng m^{-3}) for the North East Atlantic marine environment was about equal to the Southern Ocean. In the North East Atlantic 'clean' conditions persist when BC concentrations are $< 34 \text{ ng m}^{-3}$. When the concentration is $< 7 \text{ ng m}^{-3}$, the marine environment can be considered 'pristine'. The values reported here are valid for measurements from an SP2 instrument, other instrumentation such as the MAAP will have higher mass concentrations.

Conclusions

Summertime aerosol physico-chemical properties and links to cloud activation in the Southern Ocean

During the two-month research cruise, observations suggest that the sulphate-sea-salt system dominates in the Scotia Sea region, with little organic contributions to the marine aerosol. For this system, the main secondary marine aerosol (SMA) was a form of non-sea-salt sulphate (nss-SO₄). Depending on the availability of ammonium (NH₄), nss-SO₄ was in the form of bisulphate – sulfuric acid. The availability of NH₄ was not strictly linked to air mass type over all 12 steady-state cases, although the fraction was found to be larger overall in the merged marine air mass case. In addition to the nss-SO₄, methanesulphonic acid (MSA) was found in relatively high fractions (from 2 – 18 %). The highest fraction of OM (32 % non-inclusive of MSA) was measured concurrently with the lowest aerosol number concentrations, wind speeds > 10 m s⁻¹, and average BC mass concentration of 0.07 ng m⁻³.

Two main pristine air masses were observed during the cruise: maritime polar (*mP*) and continental AntArctic (*cAA*). Both the *mP* and *cAA* air masses were observed to have number-size distributions with a persistent Aitken mode centred on a d_m of 43 nm. The number contribution of particles to the Aitken or accumulation mode differed with air mass type. The *mP* air masses had ~4-fold larger Aitken mode number concentrations than the accumulation mode. Conversely, the *cAA* air masses showed ~2-fold the accumulation mode particles to Aitken. Overall, the *mP* cases had double the total number concentration of the *cAA*. However, when analysing the number-size distributions, using the inter-modal minima as an indicator for the in-cloud critical diameter of activation, it appears that the *cAA* case had double the amount of activated CCN concentrations as the *mP* despite having half the particle number concentration.

In *cAA* air, an estimated 75 % of the total measured particle concentration was activated into cloud droplets, while in *mP* air, an estimated 37 % was activated into droplets, for corresponding peak supersaturation ranges of 0.37-0.45 % and 0.19-0.31 %, respectively. In utilising Hoppel Theory to deduce cloud peak supersaturation from the inter-modal minimum (minimum between Aitken and accumulation mode), this study finds that cloud peak supersaturations above 0.45 % are not relevant. Therefore, when realistic marine boundary layer cloud supersaturations are considered, sea-salt CCN contributed 3-13 % of the activated nuclei in the *cAA* air and 9-51 % for the marine air for ship-level wind speed < 16 m s⁻¹. At higher wind speeds, primary marine aerosol can even contribute up to 100 % of the activated CCN, for corresponding peak supersaturations as high as 0.32 %.

Sea-salt suppression of sulphate nuclei activation

For the first time, the analysis of multiple marine ambient cases revealed a highly correlated inverse linear trend between activated sea spray particles (or PMA) and the percentage of activated sulphate particles (or SMA). In the Southern Ocean, while SMA contributed heavily to the particle number concentration, a difference between 25 cm^{-3} and 6 cm^{-3} particles of sea-salt caused a suppression of cloud peak supersaturation at low-average updrafts ($0.15 - 0.4 \text{ m s}^{-1}$). This leads to lower CDNC concentrations, due to an increase in particle critical radius over all chemical species. The effective CDNC and cloud peak supersaturation was found to be reproducible using a cloud (1-D) parcel model using only a dual chemical system of sulphate and sea-salt particles. A multi-modal distribution of sea-salt was used that ranged from the ultra-fine to coarse mode, which is important for particle concentrations between the Aitken-accumulation mode regime. The parcel model showed significant sensitivity to temperature, updraft velocity (w), and the position and shape of the initiator number-concentration modes. A change in cloud base temperature from 268.15 K to 273.15 K results in an absolute change in supersaturation of $\sim 0.05 \% S_c$. A change from 268.15 K to 283.15 K results in an absolute change in supersaturation of $\sim 0.1 \% S_c$ (at $N_{\text{SMA}} = 300 \text{ m}^{-3}$ and $w = 0.4 \text{ m s}^{-1}$). The w sensitivity showed an absolute difference of $+ 0.1 \% S_c$ between $w = 0.2$ and $w = 0.4 \text{ m s}^{-1}$ (at $N_{\text{SMA}} = 300 \text{ m}^{-3}$). A combination of sensitivities (T , w , and sea-salt) can act together favourably to produce as much as a 100 % enhancement (or reduction) in cloud droplet concentration. Depending on modal positioning of the SMA model input, this could be further increased to an enhancement (or reduction) of 150 %. The 1-D parcel models are sensitive to the water activity parametrisation (ion-based disassociation or κ -Köhler approximation) used, which can affect the resulting output of CDNC and S_c by as much as 40 %.

7.2 Discussion on Main Findings

This work sought to understand the components of marine aerosol and the extent to which those components affect the marine aerosol-cloud system. One objective of this work was to elucidate the nature of marine aerosol and the permeation of air pollution over remote oceans. This led to evaluating the extent to which anthropogenic aerosol is found in the marine environment, using black carbon (BC), a known tracer for human activity. BC was measured using one of the most sensitive BC instruments in wide use, a single particle soot photometer (SP2). Southern Ocean

Conclusions

and North East Atlantic air are rarely devoid of some trace of BC mass. Yet, the lowest prevailing BC mass concentration levels were nearly the same for either ocean (0.1 ng m^{-3}), which may be an indicator of the global marine background level.

Organic matter (OM) is both an indicator of human pollution (anthropogenic OM) and an important naturally occurring aerosol (biogenic OM) with interesting properties. It has been proposed (Shank et al., 2012) that most cases of so-called biogenic OM are actually correlated to BC and are thus not in fact biogenic but rather anthropogenic. The results presented in this dissertation would suggest an opposing conclusion, as it must be considered that the Southern Ocean and North East Atlantic are not the same marine system. The North East Atlantic experiences OM plumes with up to 10x the mass concentration of the observed OM in the Southern Ocean. For the Southern Ocean, the relatively clean conditions showed no such correlation between OM and BC, and O'Dowd et al. (2014) showed the same for the North East Atlantic. The importance of considering one's environment when cross comparing measurements in different ocean systems cannot be over-emphasized.

The original purpose of the Southern Ocean PEGASO campaign was to isolate the observed effects of biological activity on marine aerosol. Oceanic biological activity is linked to seasonal fluctuations in marine OM (both secondary and primary). However, measurements taken over the austral summer in the Southern Ocean revealed reduced mass concentrations of OM compared with observations of North Atlantic summer OM. Lab generated particles from sea-ice mixed with seawater from the Weddell Sea (a region of relatively high biological activity) were extremely hygroscopic, with high CCN activation efficiency. Yet, these hygroscopic CCN characteristics were not reflected in the ambient measurements of the Weddell Sea region (Appendix B.2). Overall the ambient aerosol was a relatively simple system in terms of mass domination, involving sulphate and sea-salt.

During the PEGASO cruise, number contributions of the Aitken and accumulation modes, respectively, differed between marine and continental air. These differences appeared to be caused by the activation of PMA particles resulting in a change to the fraction of activated SMA particles. In lower vertical updrafts, PMA (sea-salt) dominates the larger sized CCN, out-competing the smaller SMA CCN in water vapour scavenging. However, even in higher updrafts, a large concentration of sea-salt particles can cause significant supersaturation suppression, lessening the Twomey effect. Both the chemical properties of particles and their number-size distributions are important to determine the relative importance of secondary and primary aerosol to the actual cloud condensation nuclei (CCN) population. Gilgen et al. (2018) have recently reported that marine surface emissions from decreasing ice coverage in the Arctic may slow Arctic warming even with the loss of surface albedo from disappearing ice. This suggests an increasingly important role of marine emissions on

Conclusions

climate. The impact of marine emissions should be accurately estimated using its two largest constituents: PMA and SMA.

The Hoppel mechanism of cloud droplet activation and subsequent growth was used to perform an extended analysis on the Southern Ocean data. The Hoppel mechanism was reviewed for its feasibility in explaining the bimodality and apparent CCN from the ambient data, both as a function of physical particle activation and of subsequent growth by aqueous phase chemistry. The evidence suggested that the relative particle growth could be explained by model calculations of expected SO₄ addition (O'Dowd et al., 2000a) extrapolated for Southern Ocean conditions. Model simulations of two average cases for ambient measured air masses (*mP* and *cAA*) showed that good closure (within 15 % of S_c and 6 % of CDNC) could be achieved under reasonable environmental conditions, using only a reservoir mode of SMA, five sea-salt modes extending from the nucleation – coarse mode, and a small (< 20 particles cm⁻³) internally mixed (SMA + PMA) accumulation mode. The extension of the sea-salt distribution down into the Aitken mode was important for testing higher updraft velocities to accurately represent the number of nucleating PMA particles. These combined results confirm that the Hoppel mechanism of cloud droplet activation is a viable analytical approach for the Southern Ocean observations reported in this research. The extension of the Southern Ocean analysis yielded the first experimental evidence showing monotonically-decreasing cloud droplet concentrations with higher PMA activated fraction. These results are more extensive than those presented in O'Dowd et al. (1999b), showing the effects of sea-salt on nss-SO₄ at varying updrafts using one case study. These trends are enacted over multiple marine ambient cases and show sea spray activation effectively reducing secondary sulphate CDNC.

Modelled ambient aerosol activation show a variation of sensitivities to reasonably small changes in environmental conditions considering the range associated with the global marine boundary layer. The sensitivities can easily combine with sea spray number contribution for an absolute change in CDNC of ± 100 %. When considering that a 15-20 % change in cloud properties (e.g. cloud extent and albedo) would be sufficient to counteract the radiative perturbation awarded by a doubling of CO₂ (Slingo, 1990), a 100 % change in CDNC becomes very important to the susceptibility of the global cloud-radiation system. The initial monomodal distribution is important to the resultant activation of cloud droplets; a change in mode peak positioning can drastically change the degree to which number concentration becomes more important than sea-salt in supersaturation suppression. Furthermore, the temperature dependency found in the modelled output as well as the temperature dependency inherent to droplet activation calculation (Köhler Theory), implies that consideration of the sample aerosol temperature is important for accurate CCN activation comparisons as it can have large effects on droplet activation. Lab

Conclusions

generated calibrations keep temperature relatively stable at about 293 K, while ambient aerosol can be quite cold (or warm) and display different activation kinetics. This research involved only small temperature fluxes, as air samples equilibrated to the temperature-controlled lab environments prior to being measured.

North East Atlantic aerosol appears to be a more complicated than the Southern Ocean aerosol over the austral summer, although more long-term study is needed on Southern Ocean aerosol. The general increase in OM mass (when no correlations to BC are found) suggests that there are stronger biogenic emissions in the North East Atlantic than the Southern Ocean. In the Southern Ocean (Chapter 5), aerosol could be separated into its chemically constituent parts to derive number contribution because it was mostly comprised of sea-salt and nss-SO_4 . The same is not true of the observed periods in the North East Atlantic, and the analytical methods used for the majority of this research may need reconsideration to be applied to North East Atlantic aerosol.

CCN are important to measure directly as they bridge measurements of sub-cloud tropospheric conditions and remote sensing from either the bottom-up (ground based lidar or radar measurements) or top-down (Satellite retrievals). CCN describe the probabilistic activation of aerosol populations as a whole. This should not be overlooked as it is independent of external or internal mixing. Mono-dispersed CCN measurements and to some extent polydispersed CCN measurements also convey any hygroscopic transition of the aerosol population between size ranges if they exist. Otherwise activation would follow expected critical supersaturation by size of a chemically homogenous aerosol population.

The interpretation of CCN data can often lead to conflicting ideas about the relationship between CDNC (droplet concentration) and CCN (potential droplet nuclei dependent on supersaturation) measurements. The way an individual particle will behave in a cloud will not always be the same as the behaviour in a CCN chamber (CCNC). E.g. the monodispersed mode of the CCNC describes the (size-dependent) CCN activation by S_c (%), using the sum of the activation of individual particles at that size. However, for externally mixed particles, or particles with varying fractions of internal mixtures, the range of individual activation efficiencies are not captured but rather the dominant CCN activation efficiency for a given size. Poly-dispersed aerosol measurements are simpler as they count all particles which activate at a supersaturation, regardless of size. Particle competition effects should be considered as they change the number of particles which serve as CDNC in cloud where activation is more dynamic. To accommodate the fact that CCNC measurements better describe the average aerosol population properties, the analysis of steady-state aerosol is recommended rather than analysis of periods of changing environmental conditions. However, for short-time scale changes in a clean marine environment, polydispersed CCN concentrations are better suited for accurately

Conclusions

describing quickly changing CCN properties as the monodispersed set-up, having worse time resolution, contains more uncertainty during changing meteorological conditions.

7.3 Future work for elucidating marine cloud nucleating processes

Future studies could adapt the combined analytical methods (using S_c - D_c curves, the Hoppel Mechanism assumption, and microphysical 1-D parcel models) used in the Southern Ocean to the North East Atlantic air. To adapt and extend the analysis to the North East Atlantic, confirmation is needed that the parcel model water activity parameterisation (κ N-PM, see Section 6.3) is accurate enough to yield the correct absolute cloud droplet number and effective radius over the North East Atlantic. Additionally, 1-D parcel models are sensitive to the input position, shape, and hygroscopicity of the initiator modes, so further study is required to assess the proper inputs for different oceanic regions. The addition of a parametrisation for OM mass distribution is needed for input into the model. As it is suspected that the difference in hygroscopicity from secondary and primary OM is different (possibly even for different size regimes), different OM mass-size distribution and κ -values are needed for secondary and primary OM, respectively, to properly model the relative activation activity of the aerosol.

The ice nucleating ability of mixed-phase oceanic clouds as a function of the season could also be the focus of future work. Ice nucleation in clouds can significantly alter the radiative forcing of low-level marine cloud layers and can be initiated by small quantities of INP. Marine organics, which are seasonal in abundance and type, contribute most heavily to INP number concentrations in marine warm mixed phase-clouds. Yet, direct observations of the seasonal cycle of marine INP are limited. Whether or not marine INP are observed in seasons outside of high atmospheric OM summer months, warrants investigation. To this end, measurements have begun at MHD as a joint project between the Karlsruhe Institut für Technologie and the National University of Ireland Galway, partially funded by ACTRIS-II. The Long-term Ice Nucleating measurements At Mace head (LINAM) project commenced in November 2017 in partial design and operational set-up by the author of this dissertation (see Appendix B.3 for details on the experimental methods of INP filter measurements for the LINAM project). Another marine INP measurement long-term project which employs a different INP analysis technique has begun between the National University of Ireland Galway, the Institute of Atmospheric Sciences and Climate – National Research Council of Italy, and the Università di Bologna. Data from these two campaigns should be analysed with the aim of elucidating the seasonal INP

Conclusions

properties of the North Atlantic, and to isolate the major source(s) of INP active in seasonal mixed-phase clouds.

APPENDIX A

This appendix contains relevant CCNC data, both calibration and inter-comparison, used in this dissertation.

A.1 Calibration data for cloud condensation nuclei counters

Two continuous-flow streamwise thermal-gradient CCN chambers (CCN-100 instruments, *Droplet Measurement Technologies, Inc.*) were used over the course of the studies discussed within this dissertation. Each CCN chamber (CCNC) underwent calibrations with results distinct to that instrument. The older model, originally acquired in 2005 and nicknamed Phoenix (CCNC 0015), measured at MHD and is responsible for the datasets presented in Section 5.4. The newer model, owned by the *EPA* and nicknamed Pegasus (CCNC 086), was acquired in 2009. The Pegasus CCNC was used during the PEGASO campaign and is responsible for the datasets taken over the Southern Ocean. CCN data continually collected in ambient conditions must be adjusted for calibrated post-collection. The relevant calibrated column supersaturations and uncertainties used in this dissertation are presented in Table A1.

Table A1. CCNC set supersaturations, calibrated actual critical supersaturations (S_c), and uncertainties for each CCNC instrument and relevant sampling period (CCNC 0015, and 086).

CCNC 0015 BACCHUS			CCN 086 PEGASO		
S_c set	S_c actual	δ	S_c set	S_c actual	δ
0.1	0.19	0.01	0.10	0.08	0.02
0.25	0.44	0.03	0.25	0.29	0.02
0.35	0.56	0.04	0.35	0.47	0.02
0.5	0.76	0.06	0.50	0.82	0.04
0.75	1.11	0.09	0.75	1.48	0.05

A.2 Inter-comparison of two CCN chambers

Over several days in May 2017, the two CCNCs were run in parallel in poly-dispersed mode to assess the accuracy between the two separate instruments. After calibration, each instrument showed only two common supersaturation that fell between 0.01 %. The CCNC 086 was measuring a supersaturation of 0.31 % and 0.87

APPENDIX A

% and the CCNC 0015 was measuring at supersaturation of 0.3 % and 0.88 %, respectively. CCN concentrations of sampled ambient air at MHD over 22 days (May 8th- 30th) were compared (Figure A1). The sampling period included polluted periods in which CCN concentrations were more than 5,000 cm⁻³. Linear regression analysis of the 0.3 % supersaturation CCN concentrations revealed that the CCNC 086 was over counting in comparison with the CCNC 0015 by a factor of 1.2 plus an additional 16 particle offset. This may be partially accounted for by the +0.01 % supersaturation of the CCNC 086. Looking at longer periods in which the CCNCs were running, there is generally good comparison in time trends between the two instruments (Figure A2), with decreasing CCN concentrations for decreasing supersaturations. During clean periods when overall concentrations were on the order of 500 cm⁻³ or less, the CCNC 086 measures the same CCN concentration as the CCN 0015 at a supersaturation that is 0.1 % lower. This is apparent from the comparison at the same relative supersaturation (Figure A1). The period of high sea-salt concentration on May 14th at 07:00 (Figure A2) shows about a 62 % overall activation at supersaturations of ~ 0.7 % and above. However, the majority of the number concentration is centred on a mobility diameter < 30 nm. In these conditions this is normal activation. During this period there are about ~350 particles, of which a third activate at ~0.3 % supersaturation. There is approximately a +30-35 CCN concentration difference between the CCNC 086 and 0015 which is 28 % CCN concentration difference. During polluted periods, the CCNC 086 counts a higher CCN concentration than the CCNC 0015. This discrepancy is accounted for by the linear comparison mentioned earlier.

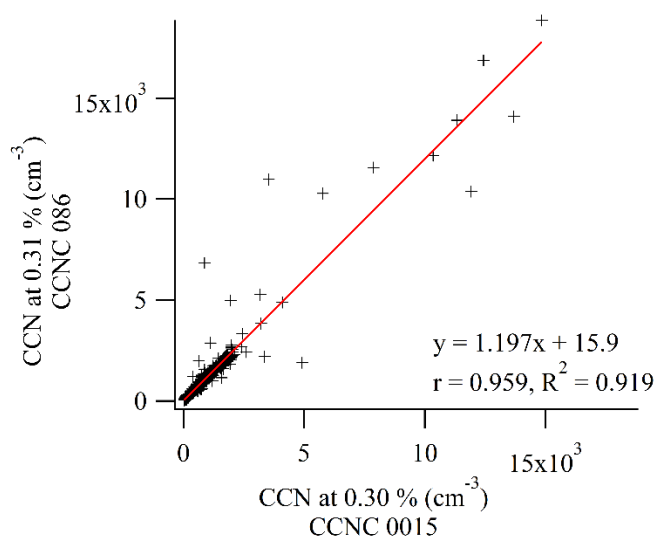


Figure A1. A comparison of the two CCNC instruments at ~ 0.3 % supersaturation over May 8th- 30th, 2017. CCN concentration measurements are indicated by black markers, while the red line is the linear fit to the data points, with results of the fit shown in the bottom right corner.

APPENDIX A

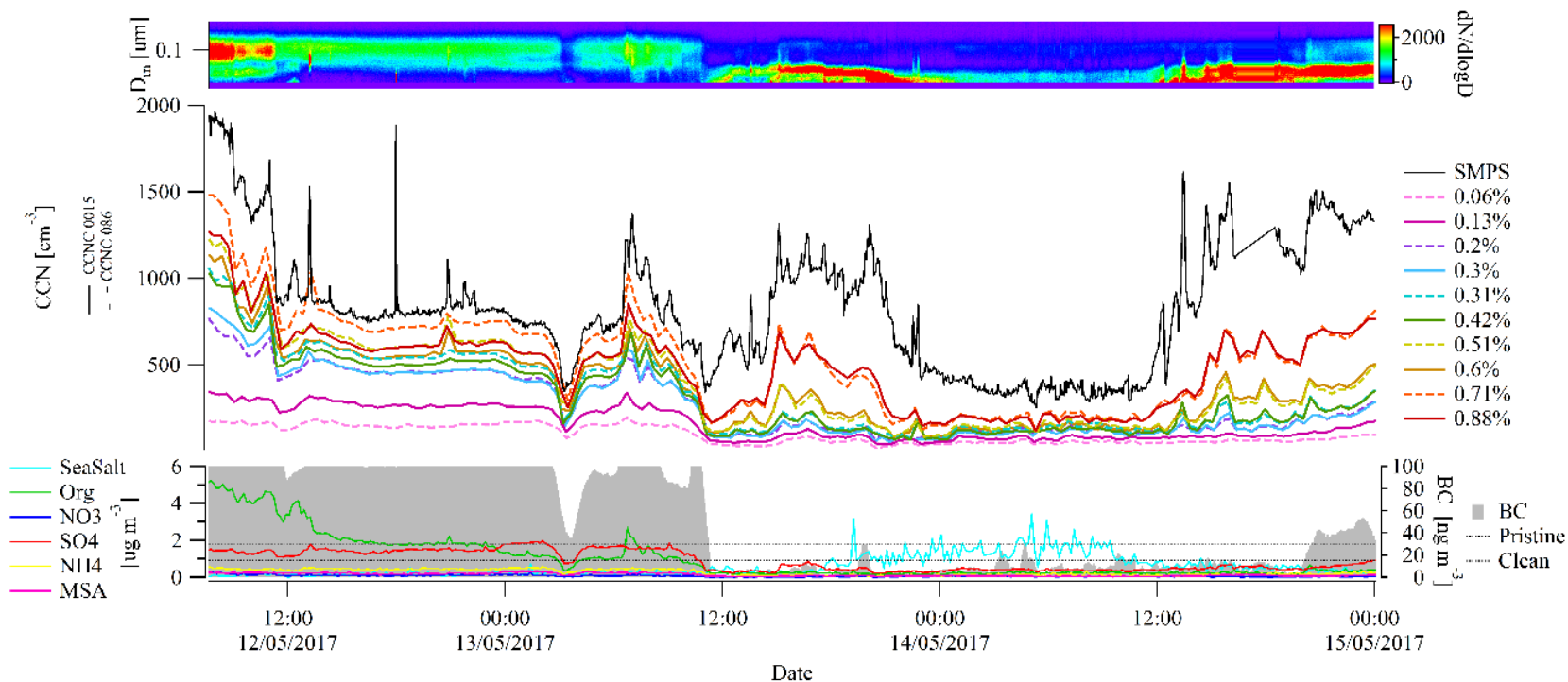


Figure A2. Time trends of parallel CCN measurements of polydispersity ambient air. The period shown is an excerpt (May 12th-15th) of the period used for B3 (May 8th- 30th). The top panel shows a concurrent time trends of SMPS data as a function of mobility diameter (vertical axis) and particle concentration (colour scale). The middle panel shows CCN number concentrations (cm^{-3}) of both the CCNC 0015 (solid lines) and the CCNC 086 (dashed lines) with their relative calibrated supersaturations (see Table A1 for uncertainties) indicated by the key on the right corresponding to the colour of each line. The bottom panel shown HR-ToF-AMS data (left vertical axis) of non-refractive mass concentrations and MAAP data (right vertical axis) of BC mass concentrations. Both clean and polluted air was sampled at MHD over this period, indicated roughly by the BC concentrations more than 15 ng m^{-3} .

APPENDIX B

B.1 AIOMFAC model

This appendix section contains supporting information used in this dissertation which was not the direct work of the Author.

The model predictions for the critical dry diameter and critical supersaturation of selected solutes in aqueous droplets were carried out by a combination of the Aerosol Inorganic-Organic Mixtures Functional groups Activity Coefficients (AIOMFAC) model (Zuend et al., 2008; Zuend et al., 2011) and application of the Köhler equation (Eq. 1), similar to the approach described in (Ovadnevaite et al., 2017). However, since the relatively simple systems considered in the present study did not contain mixtures of organic and inorganic components, nor exhibit liquid-liquid phase separation, consideration of an evolving surface tension was not necessary.

$$S = a_w \exp \left[\frac{4 \sigma M_w}{RT \rho_w D} \right] \quad (\text{B1})$$

Here, S is the equilibrium water vapour saturation ratio of a spherical aqueous solution droplet of diameter D and mole-fraction-based water activity a_w (both dependent on composition). $\exp[\dots]$ represents the exponential function with base e , σ is the effective liquid-air surface tension, M_w the molar mass of water, ρ_w the liquid-state density of water at temperature T , and R the ideal gas constant. The AIOMFAC model predicts the molar composition and activities of all components, including, a_w , as a function of input composition, thereby allowing the computation of water activities (i.e. bulk equilibrium RH) over a wide range of water contents. The molar solution composition can be converted into a droplet volume and sphere-equivalent diameter by using the molar masses and mass densities of the different mixture components. Additivity of volumes contributed by the individual components is assumed (assuming zero excess volume due to mixing). The density values used for the calculations are listed in Table B1. All calculations were performed assuming $T = 293.15$ K and a constant surface tension of $\sigma = 72.75$ mJ m⁻², the value of the surface tension of pure water at T (Vargaftik et al., 1983). Critical supersaturation values (S_c) were determined as the maximum values of S of the solute-specific Köhler curves computed with high numerical resolution in the high-water-activity range. The corresponding critical dry diameters, D_c , were calculated from the water-free composition. The predicted S_c vs. D_c values are listed in Table B2.

APPENDIX B

Table B1. Liquid- and solid-state densities of pure components at $T \approx 20$ °C (and ~ 105 Pa) used for the AIOMFAC-based calculations of critical CCN properties.

Chemical compound (physical state)	Density ρ (kg m ⁻³)
H ₂ O (liquid)	997
H ₂ SO ₄ (liquid)	1860 ^a
(NH ₄) ₂ SO ₄ (liquid)	1550 ^b
(NH ₄) ₂ SO ₄ (solid)	1770 ^b
NH ₄ HSO ₄ (liquid)	1730 ^b
NH ₄ HSO ₄ (solid)	1780 ^b
Methanesulfonic acid (MSA), (liquid)	1650 ^c
Sodium methanesulfonate (Na-MSA), (liquid)	2190 ^d
Ammonium methanesulfonate (NH ₄ -MSA), (liquid)	1440 ^e

^a Value obtained using the temperature-dependent parameterisation by Myhre et al. (1998).

^b Solid- (crystalline) and liquid-state values from Clegg and Wexler (2011).

^c Calculated based on apparent molar volume data of 7-molal aqueous solution by Teng and Lenzi (1975).

^d Calculated based on apparent molar volume data by Tamaki et al. (1983).

^e Determined using Eq. (1) of Kosova et al. (2017).

Methanesulfonic acid (MSA) contains a chemical structural group that was not available in prior versions of AIOMFAC. Therefore, to provide AIOMFAC predictions for mixtures containing MSA and its sodium (Na-MSA) or ammonium (NH₄-MSA) methanesulfonate salts, we introduce a new ionic subgroup, the methanesulfonate anion (CH₃SO₃⁻), to the list of ions considered by AIOMFAC. The relative van der Waals subgroup volume (R^H) and surface area parameters (Q^H) of the hydrated methanesulfonate anion were assumed to be equal to those of the hydrated sulphate ion; setting $R^H(\text{CH}_3\text{SO}_3^-) = 3.34$ and $Q^H(\text{CH}_3\text{SO}_3^-) = 3.96$ (Zuend et al., 2008). The adjustable AIOMFAC middle-range parameters, describing the interactions of CH₃SO₃⁻ anions with the cations H⁺, Na⁺ and NH₄⁺ in aqueous solutions, were determined by a weighted least-squares model-measurement optimization using the procedure described in Zuend et al. (2011) based on experimental data sets by Covington et al. (1973), Gregor et al. (1963), Liu and Laskin (2009), and Peng and Chan (2001). A graphical comparison of the model predictions and the experimental data is shown in Figure B1. The fitted model parameters are listed in Table B3. We note that available experimental data on mixtures containing methanesulfonates as well as organic compounds is scarce; therefore, this extension of the AIOMFAC model is a system-specific approach applicable to aqueous, organic-free systems of the considered ions only.

APPENDIX B

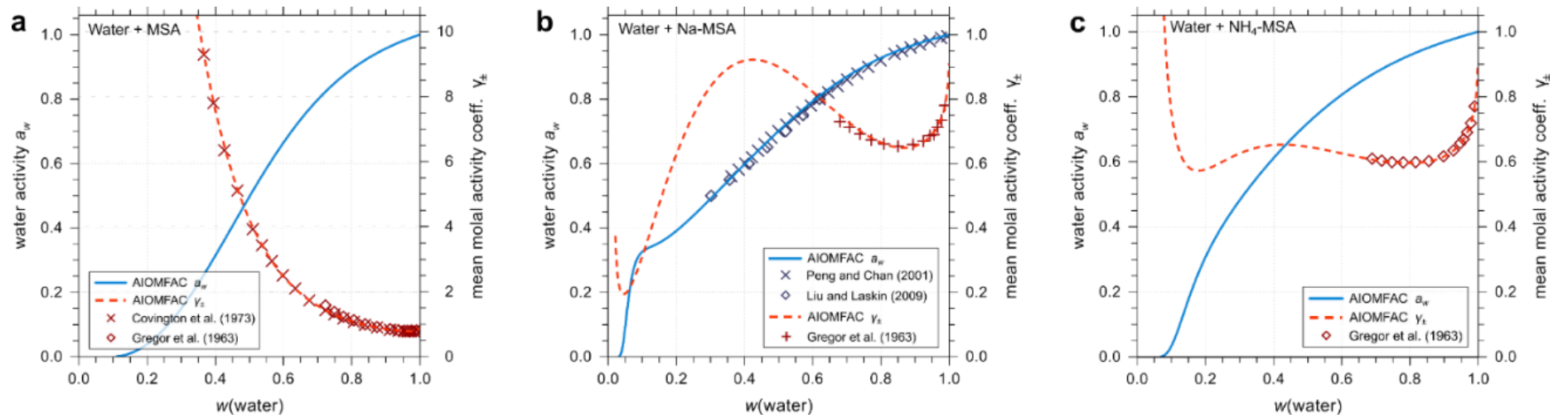


Figure B1. Comparison of experimental data and AIOMFAC predictions for water activity (left y-axis) and the mean molal ion activity coefficient (right y-axis) of the binary aqueous systems used to fit the model parameters at $T \approx 298$ K. The solutes are MSA (a), Na-MSA (b) and NH_4 -MSA (c).

APPENDIX B

Table B2. Critical supersaturation S_c (%) listed for a selection of corresponding critical dry diameters (D_c) from 20 to 200 nm predicted by the AIOMFAC model with Köhler theory. DON_{mol} indicates the degree of sulphate neutralization by ammonia (Eq. 1, main text) for solute mixtures containing ammonium sulphate and sulphuric acid at input; all data for $T = 293.15$ K and $\sigma = 72.75$ mJ m⁻².

Mixture		Dry diameter (nm)														
Solutes (at input)	DON_{mol}	20	25	30	35	40	45	50	60	70	80	100	120	140	160	200
H ₂ SO ₄	0.00	1.667	1.191	0.902	0.713	0.580	0.484	0.411	0.309	0.243	0.197	0.139	0.104	0.082	0.066	0.047
(NH ₄) ₂ SO ₄ , H ₂ SO ₄	0.10	1.708	1.218	0.922	0.727	0.592	0.493	0.419	0.315	0.248	0.201	0.142	0.106	0.083	0.068	0.048
(NH ₄) ₂ SO ₄ , H ₂ SO ₄	0.20	1.747	1.243	0.940	0.741	0.603	0.502	0.426	0.320	0.252	0.204	0.144	0.108	0.085	0.069	0.048
(NH ₄) ₂ SO ₄ , H ₂ SO ₄	0.30	1.782	1.267	0.956	0.754	0.612	0.510	0.433	0.325	0.255	0.207	0.146	0.110	0.086	0.070	0.049
(NH ₄) ₂ SO ₄ , H ₂ SO ₄	0.40	1.814	1.287	0.971	0.764	0.621	0.517	0.438	0.330	0.259	0.210	0.148	0.111	0.087	0.071	0.050
(NH ₄) ₂ SO ₄ , H ₂ SO ₄	0.50	1.841	1.304	0.983	0.773	0.628	0.522	0.443	0.333	0.262	0.212	0.150	0.112	0.088	0.072	0.051
(NH ₄) ₂ SO ₄ , H ₂ SO ₄	0.60	1.861	1.316	0.991	0.779	0.632	0.526	0.446	0.335	0.263	0.214	0.151	0.113	0.089	0.072	0.051
(NH ₄) ₂ SO ₄ , H ₂ SO ₄	0.70	1.876	1.325	0.996	0.783	0.635	0.528	0.448	0.337	0.265	0.215	0.152	0.114	0.090	0.073	0.052
(NH ₄) ₂ SO ₄ , H ₂ SO ₄	0.75	1.882	1.328	0.998	0.784	0.636	0.529	0.449	0.337	0.265	0.215	0.152	0.114	0.090	0.073	0.052
(NH ₄) ₂ SO ₄	1.00	1.905	1.340	1.005	0.788	0.639	0.532	0.451	0.339	0.267	0.217	0.154	0.116	0.091	0.074	0.053
NaCl	N/A	1.231	0.878	0.666	0.527	0.430	0.360	0.307	0.233	0.184	0.151	0.107	0.082	0.065	0.053	0.038
MSA	N/A	1.772	1.271	0.968	0.768	0.629	0.527	0.449	0.342	0.271	0.221	0.158	0.120	0.095	0.078	0.056
Na-MSA	N/A	1.738	1.240	0.941	0.745	0.609	0.510	0.435	0.330	0.261	0.213	0.152	0.116	0.092	0.075	0.053
NH ₄ -MSA	N/A	2.107	1.505	1.142	0.905	0.739	0.618	0.527	0.400	0.316	0.258	0.184	0.140	0.111	0.091	0.065

APPENDIX B

Table B3. Fitted binary cation—anion AIOMFAC middle-range interaction parameters (Zuend et al., 2008) for aqueous solutions of MSA, Na-MSA, and NH₄-MSA; determined for $T \approx 298.15$ K.

c	a	$b_{c,a}^{(1)}$ (kg mol ⁻¹)	$b_{c,a}^{(2)}$ (kg mol ⁻¹)	$b_{c,a}^{(3)}$ (kg ^{1/2} mol ^{-1/2})	$c_{c,a}^{(1)}$ (kg ² mol ⁻²)	$c_{c,a}^{(2)}$ (kg ^{1/2} mol ^{-1/2})
H ⁺	CH ₃ SO ₃ ⁻	4.67900×10^{-2}	4.56220×10^{-1}	2.40000×10^{-1}	-1.70295×10^{-1}	1.42818×10^{-1}
Na ⁺	CH ₃ SO ₃ ⁻	6.90732×10^{-3}	3.16640×10^{-1}	3.25673×10^{-1}	-4.38075×10^{-1}	2.10970×10^0
NH ₄ ⁺	CH ₃ SO ₃ ⁻	2.33752×10^{-2}	2.23470×10^{-2}	2.20000×10^{-1}	2.47270×10^{-2}	8.26574×10^{-1}

B.2 Bubble-Tank Antarctic ice experimentation

This section contains experimental data which is not essential to the main findings of this dissertation, but which support it as supplementary material. The contents of this section are all the direct work of the Author.

Bubble-Tank experiments were performed on-board the research cruise ship from ice samples collected in the Scotia Sea region, including the Weddell Sea. Three Tank Ice experiments were evaluated in terms of their CCN activation properties. The three Tank Ice experiments (separated as Tank Ice 1, 2 and 3) measured the aerosol generated in tank plunging jet conditions from collected Weddell Sea ice. The sea-ice was melted, and 35 L of collected seawater sampled at 4m depth by a conductivity, temperature and depth (CTD) instrument was added to account for natural conditions, such as the lack of sea-salt in ice. The first and second Tank Ice experiments were performed in a larger drum tank, while the second was performed in a smaller chamber tank (where only 2.51 L of collected CTD seawater was added). Both tanks generated aerosol using a plunging jet technique, and only sampled aerosol after flushing the tank with zero-air. The large Tank samples Tank Ice 1 sampled filtered (10µm pore) ice algae water for 1 hour and 42 minutes. The starting temperature of the water was 9.0°C and the ending temperature was 9.3°C, and the CCNC sample temperature read at ~18°C with the column T1 temperature at 20°C for the experiment. The Tank Ice 2 experiment used seawater filtered through a 20 µm pore nylon net to melt the ice and ran for 11 hours and 22 minutes. The starting temperature of the water was 7.4°C and the ending temperature was

APPENDIX B

11.4°C and the CCNC sample temperature read at ~16°C with the column T1 temperature at 18°C for the experiment. The Tank Ice 3 experiment sampled melted ice samples in CTD seawater from the larger tank for 3 hours and 37 minutes. The starting temperature of the water was 13.7°C and the ending temperature was 12.2°C and the CCNC sample temperature read at ~17-18°C with the column T1 temperature at 15-16°C for the experiment.

To explore the cloud droplet nucleating, or CCN activation, ability, we deployed an experimental set up (see Section 5.1.2) to enable us to produce CCN activation lines (i.e. plots of the critical supersaturation, S_c , versus the critical dry diameter, D_c) for both lab and environmental scenarios. In measuring the water uptake properties of the aerosol, this powerful setup elucidates many important properties of the CCN population through comparative analysis with the modelled particle hygroscopicity, particularly the inferred composition of the nuclei as a function of size. The three Bubble-Tank ice experiments resulted in increased CCN activation properties from that of ammonium sulphate and even sometimes NaCl, see Figure 5.1. CCN S_c - D_c curves showed that, for each tank experiment, CCN at size great than 70 nm were activating better than theoretical NaCl (calculated from the AIOMFAC model (Zuend et al., 2011)). Tank Ice 3 showed better activation at all measured supersaturations than NaCl. All three Tank Ice experiments showed similar logspace CCN-slopes, with the two filtered Tank Ice experiments (1 and 2) showing the best agreement in curvature. These curves reflected slight increases in activation potential towards larger sizes, as can be viewed in Figure B2 from the increasing deviations from NaCl at larger dry critical mobility diameters. Tank Ice 3 showed increased CCN activation from that of NaCl, with the largest increases at dry mobility sizes less than 40 nm or greater than 70 nm. The CCN size-dependent trend of Tank Ice 1 is expected of a sulphate-sea-salt mixture, which would tend to have higher concentrations of sulphate at smaller sizes, but less concentrations at larger, allowing for the more hygroscopic sea-salt particle to dominate activation. Tank Ice 2 represents a heavily sea-salt influenced activation trend, with higher activation at larger sizes ($d_m > 70$ nm). Organics can in some cases suppress activation or even aid it ((Ovadnevaite et al., 2011a), but tend to have the most effect when particles $10 < d_m < 50$ nm have an OM mass fraction in excess of ~ 55 % (Ovadnevaite et al., 2017). This may explain the increased activation of Tank Ice 3 at smaller sizes ($d_m < 40$ nm). However, the trend found in Tank Ice 3, and to a lesser extent Tank Ice 2, also reflects increased CCN activation at larger diameters, perhaps pointing to a different type of organic-sea-salt interaction which occurs for the Bubble-Tank generation, without filtering or even at large filter pore (20 μ m) sizes.

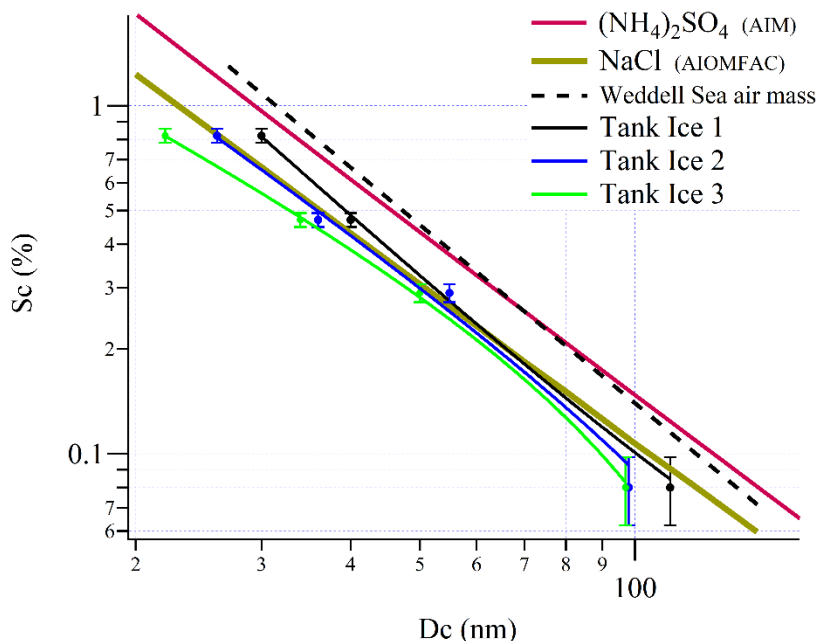


Figure B2. Tank ice experiments 1-3 shown as CCN critical activation curves, in dashed grey-tone lines. Theoretical ammonium sulphate (pink) and NaCl (olive brown) calculated at 293.15 K are shown. Also, a typical Weddell Sea air mass is shown in the black solid line.

The level of hygroscopicity measured in the tank experiments is rare as sea-salt (NaCl proxy) is generally thought of as the most CCN active soluble inorganic particle. The effects of temperature and shape correction (for the conversion between dry mobility and mass effective diameter) on the theoretical representation of NaCl were investigated (Figure B3). Due to the reduced initial temperatures of the experimentation, 10°C was looked at in contrast to the usual 25°C which standard κ -variables are reported at. The theoretical calculations were determined using κ -Köhler theory (Eq. 15 in Section 3.6.3) which is a robust method to describe this supersaturation regime (Riipinen et al., 2015). Following the reports of Rose et al. (2008), reduced initial CCNC column (or sample) temperatures lead to increased supersaturations which correspond to reductions in apparent CCN activity. These theoretical calculation assume particle diameters based on mass (or equivalent volume) which can be converted to mobility diameters when a shape correction for a particle's morphology is applied. Dry NaCl is predominantly cubic in shape, and therefore a correction factor (χ) of 1.08 was applied (Hinds, 1982). However, it should be noted that sometimes shape correction can lessen the agreement between certain models and measurements and should not be taken as absolutely necessary in all cases (Rose et al., 2008). As a cubic particle will have a larger electric mobility diameter than effective mass diameter, the CCN activation properties are further reduced by this correction. Neither temperature nor particle diameter correction was able to resolve the reason for 'greater-than-sea-salt'

hygroscopicity at larger sizes. The increased activation would then imply some droplet activation with an increase in one or both of the Köhler terms (i.e. an increase in surface tension suppression or increased water activity), although the cause has yet to be isolated.

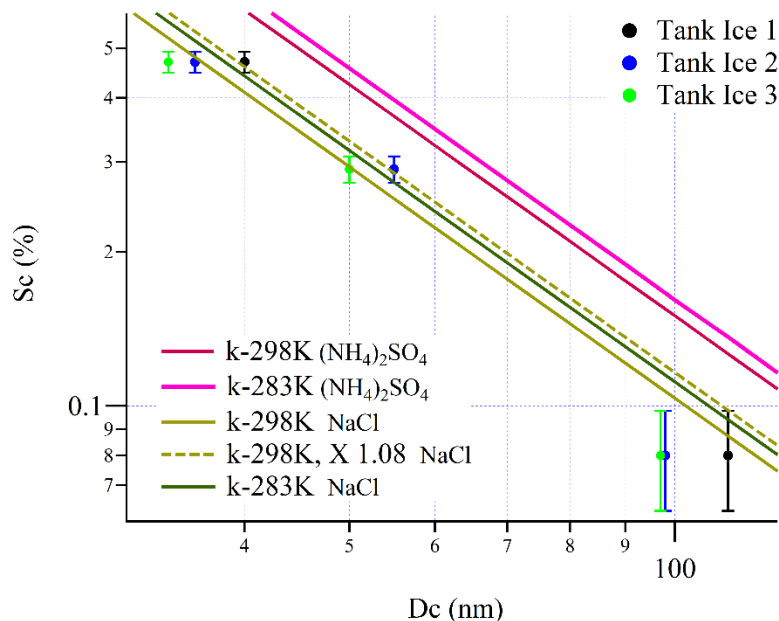


Figure B3. Theoretical CCN activation curves are shown along with Tank Ice experiment measurements. Ammonium sulphate ($(\text{NH}_4)_2\text{SO}_4$) calculated using κ -Köhler theory (Eq. 15 in Section 3.6.3) is shown in pink with the darker of the two calculated at 298.15 K and the lighter at 283 K. NaCl calculated in the same manner is shown with the solid olive brown line calculated for 298.15 K and the dark green line calculated at 283.15 K. The dashed olive brown line is calculated at 298.15 K, however a shape correction ($\chi = 1.08$) factor is applied for a cubic particle (Hinds, 1982).

To investigate the regional impact of melting ice-air interactions around the Weddell Sea in regards to this increase in CCN activation, ambient aerosols which traversed the sea-ice area before reaching the ship were analysed. The results of the Weddell Sea ambient aerosol analysis showed no regional propagation of the extremely hygroscopic aerosols found during the tank lab experiments (Figure B2), so they were therefore of little impact on the regional scale. The natural conclusion was, i) that some high activation potential particles were generated in the tanks experiments that were not being produced in nature, or ii) they were getting generated but not in a high enough quantity to have any effect on regional aerosol properties.

B.3 LINAM experimental technique

In terms of INP activation efficiency, marine organics are the most important deciding factor of INP number concentrations in warm mixed phase-clouds. Dust, transported (or re-suspended or settling cosmic dust), may even play a role in marine regions in colder temperatures. However, there is a dearth of information on what occurs in winter *versus* summer months in the marine environment, which leaves it hard to determine whether the marine organics showing good warm temperature INP activation ($< -15^{\circ}\text{C}$) are linked to marine productivity (which would show higher POC) or are more closely related to the dissolved organic carbon (DOC) which persists in the marine environment throughout the year. This could also be clarified by size segregation of the INP sampling, although that has yet to be tested for marine samples. McCluskey et al. (2018b), suggest that the most prominent INP from SSA (which may not be source specific) was heat stable but susceptible to peroxide digestion treatment resulting in a reduction in INP activation behaviour. This indicates that a large fraction of this INP type was some form of marine OM, not made up of proteins or other biological material that could be less INP active from a deformity of exposure to 95°C , which may likely be DOC. Simultaneously, a smaller fraction of marine INP were augmented in increased INP activation behaviour above -22°C , these particles were heat labile, and likely more like POC. However, these types were less frequent and even less active than the terrestrial OM types. Depending on the temperature of the mixed phase cloud, POC in small quantities could be significant enough to initiate the Wegener-Bergeron-Findeisen precipitation process.

To assess the ice nucleating ability of mixed-phase oceanic clouds as a function of the season, on-going INP filter measurements are being taken at MHD as a combined projection between the National University of Ireland Galway and the Karlsruhe Institute of Technology (KIT). The project, called Long-term Ice Nucleating measurements At Mace head (LINAM), is a year-long campaign that started in November 2017. INP samples are collected at MHD on $4.5\ \mu\text{m}$ pore width NucleporeTM track-etched polycarbonate membrane filters (Whatman). Analysis of the samples will be performed at KIT using INSEKT (a detailed methodology can be found in Schiebel (2017)). The NucleporeTM filters are pre-treated and cleaned in the same process described above following the description in CSU-IS procedure in the supplement of Hiranuma et al. (2015) at KIT and shipped in batch to MHD with two filters per sterile aluminium envelopes. Two samples are collected per week at MHD atmospheric research station at 10 m height, using PM₁₀ Lecklel head inlets (Sven Leckel, Berlin, Germany), with $\sim 1\text{m}$ of stainless steel 1" diameter tubing before reaching the NucleporeTM filter holders, which are custom manufactured by KIT. The pump draws $15\ \text{L}\ \text{min}^{-1}$ of sample through each filter membrane often starting with

APPENDIX B

a pressure of ~700 hPa, and dropping to ~300 hPa at the end of a week of sampling. Ambient pressure, start/end time/pressure are recorded for all the samples. Three sample types are collected at MH, clean sector, all sector, and polluted sector. Polluted sector are always run in parallel for ~24-72 hours depending on the loading conditions. Clean sector samples are run for a minimum of 3 days. All sector samples are run for ~7 days at a time. Samples re prepared and collected from the filter holders in a clean hood at MHD. Collected samples are frozen and shipped to Germany for analysis with the INSEKT instruments in batches with collected blanks. Error estimations can be calculated from parallel samples, while background levels can be resolved from blanks.

References

- Abdul-Razzak, H., and Ghan, S. J.: A parameterization of aerosol activation: 2. Multiple aerosol types, *Journal of Geophysical Research: Atmospheres*, 105, 6837-6844, 10.1029/1999JD901161, 2000.
- Adams, P. J., Seinfeld, J. H., and Koch, D. M.: Global concentrations of tropospheric sulfate, nitrate, and ammonium aerosol simulated in a general circulation model, *Journal of Geophysical Research: Atmospheres*, 104, 13791-13823, 10.1029/1999JD900083, 1999.
- Aitken, J.: XII.—On Dust, Fogs, and Clouds, *Transactions of the Royal Society of Edinburgh*, 30, 337-368, 10.1017/S0080456800029069, 1880.
- Aitken, J.: XIV.—On some Nuclei of Cloudy Condensation. Part III, *Proceedings of the Royal Society of Edinburgh*, 37, 215-245, 10.1017/S0370164600023592, 1918.
- Allan, J. D., Jimenez, J. L., Williams, P. I., Alfarra, M. R., Bower, K. N., Jayne, J. T., Coe, H., and Worsnop, D. R.: Quantitative sampling using an Aerodyne aerosol mass spectrometer 1. Techniques of data interpretation and error analysis, *Journal of Geophysical Research: Atmospheres*, 108, n/a-n/a, 10.1029/2002JD002358, 2003.
- Allan, J. D., Williams, P. I., Najera, J., Whitehead, J. D., Flynn, M. J., Taylor, J. W., Liu, D., Darbyshire, E., Carpenter, L. J., Chance, R., Andrews, S. J., Hackenberg, S. C., and McFiggans, G.: Iodine observed in new particle formation events in the Arctic atmosphere during ACCACIA, *Atmospheric Chemistry and Physics*, 15, 5599-5609, 10.5194/acp-15-5599-2015, 2015.
- Asa-Awuku, A., Sorooshian, A., Flagan, R. C., Seinfeld, J. H., and Nenes, A.: CCN properties of organic aerosol collected below and within marine stratocumulus clouds near Monterey, California, *Atmosphere*, 6, 1590-1607, 10.3390/atmos6111590, 2015.
- Atkinson, J. D. M., Benjamin J.; Woodhouse, Matthew T.; and Whale, T. F. B., Kelly J.; Carslaw, Kenneth S.; Dobbie, Steven; O'Sullivan, Daniel; Malkin, Tamsin L.: The importance of feldspar for ice nucleation by mineral dust in mixed-phase clouds, *Nature*, 498, 355-358, 10.1038/nature12278 <http://www.nature.com/nature/journal/v498/n7454/abs/nature12278.html#supplementary-information>, 2013.
- Ayers, G. P., and Gras, J. L.: Seasonal relationship between cloud condensation nuclei and aerosol methanesulphonate in marine air, *Nature*, 353, 834, 10.1038/353834a0, 1991.
- Ayers, G. P., and Cainey, J. M.: The CLAW hypothesis: a review of the major developments, *Environmental Chemistry*, 4, 366-374, 2007.
- Baker, A. R., and Croot, P. L.: Atmospheric and marine controls on aerosol iron solubility in seawater, *Marine Chemistry*, 120, 4-13, <https://doi.org/10.1016/j.marchem.2008.09.003>, 2010.
- Baker, A. R., Landing, W. M., Bucciarelli, E., Cheize, M., Fietz, S., Hayes, C. T., Kadko, D., Morton, P. L., Rogan, N., Sarthou, G., Shelley, R. U., Shi, Z., Shiller, A., and van Hulten, M. M. P.: Trace element and isotope deposition across the air-sea

References

- interface: progress and research needs, *Philosophical transactions. Series A, Mathematical, physical, and engineering sciences*, 374, 20160190, 10.1098/rsta.2016.0190, 2016.
- Barrie, L. A.: Arctic air pollution: An overview of current knowledge, *Atmospheric Environment* (1967), 20, 643-663, [https://doi.org/10.1016/0004-6981\(86\)90180-0](https://doi.org/10.1016/0004-6981(86)90180-0), 1986.
- Blanchard, D. C., and Woodcock, A. H.: Bubble Formation and Modification in the Sea and its Meteorological Significance, *Tellus*, 9, 145-158, 10.1111/j.2153-3490.1957.tb01867.x, 1957.
- Blanchard, D. C.: The electrification of the atmosphere by particles from bubbles in the sea, *Progress in Oceanography*, 1, 73-202, [https://doi.org/10.1016/0079-6611\(63\)90004-1](https://doi.org/10.1016/0079-6611(63)90004-1), 1963.
- Bowyer, P. A., Woolf, D. K., and Monahan, E. C.: Temperature dependence of the charge and aerosol production associated with a breaking wave in a whitecap simulation tank, *Journal of Geophysical Research: Oceans*, 95, 5313-5319, 10.1029/JC095iC04p05313, 1990.
- Broeke, M. R. v. d., Wal, R. S. W. v. d., and Wild, M.: Representation of Antarctic Katabatic Winds in a High-Resolution GCM and a Note on Their Climate Sensitivity, *Journal of Climate*, 10, 3111-3130, 10.1175/1520-0442(1997)010<3111:roakwi>2.0.co;2, 1997.
- Burkart, J., Hodshire Anna, L., Mungall Emma, L., Pierce Jeffrey, R., Collins Douglas, B., Ladino Luis, A., Lee Alex, K. Y., Irish, V., Wentzell Jeremy, J. B., Liggio, J., Papakyriakou, T., Murphy, J., and Abbatt, J.: Organic Condensation and Particle Growth to CCN Sizes in the Summertime Marine Arctic Is Driven by Materials More Semivolatile Than at Continental Sites, *Geophysical Research Letters*, 44, 10,725-710,734, 10.1002/2017GL075671, 2017.
- Burrows, S. M., Easter, R., Liu, X., Ma, P. L., Wang, H., Elliott, S. M., Singh, B., Zhang, K., and Rasch, P. J.: OCEANFILMS sea-spray organic aerosol emissions – Part 1: implementation and impacts on clouds, *Atmos. Chem. Phys. Discuss.*, 2018, 1-27, 10.5194/acp-2018-70, 2018.
- Cappa, C. D., Lack, D. A., Burkholder, J. B., and Ravishankara, A. R.: Bias in Filter-Based Aerosol Light Absorption Measurements Due to Organic Aerosol Loading: Evidence from Laboratory Measurements, *Aerosol Science and Technology*, 42, 1022-1032, 10.1080/02786820802389285, 2008.
- Cavalli, F., Facchini, M. C., Decesari, S., Mircea, M., Emblico, L., Fuzzi, S., Ceburnis, D., Yoon, Y. J., O'Dowd, C. D., Putaud, J. P., and Dell'Acqua, A.: Advances in characterization of size-resolved organic matter in marine aerosol over the North Atlantic, *Journal of Geophysical Research: Atmospheres*, 109, n/a-n/a, 10.1029/2004JD005137, 2004.
- Ceburnis, D., Garbaras, A., Szidat, S., Rinaldi, M., Fahrni, S., Perron, N., Wacker, L., Leinert, S., Remeikis, V., Facchini, M. C., Prevot, A. S. H., Jennings, S. G., Ramonet, M., and O'Dowd, C. D.: Quantification of the carbonaceous matter origin in submicron marine aerosol by ¹³C and ¹⁴C isotope analysis, *Atmos. Chem. Phys.*, 11, 8593-8606, 10.5194/acp-11-8593-2011, 2011.
- Ceburnis, D., Masalaite, A., Ovadnevaite, J., Garbaras, A., Remeikis, V., Maenhaut, W., Claeys, M., Sciare, J., Baisnée, D., and O'Dowd, C. D.: Stable isotopes measurements reveal dual carbon pools contributing to organic matter

References

- enrichment in marine aerosol, 6, 36675, 10.1038/srep36675
<https://www.nature.com/articles/srep36675#supplementary-information>,
2016.
- Charlson, R. J., Lovelock, J. E., Andreae, M. O., and Warren, S. G.: Oceanic phytoplankton, atmospheric sulphur, cloud albedo and climate, *Nature*, 326, 655-661, 1987.
- Chen, Q., Sherwen, T., Evans, M., and Alexander, B.: DMS oxidation and sulfur aerosol formation in the marine troposphere: a focus on reactive halogen and multiphase chemistry, *Atmos. Chem. Phys.*, 18, 13617-13637, 10.5194/acp-18-13617-2018, 2018.
- Choi, Y.-S., Lindzen, R. S., Ho, C.-H., and Jinwon, K.: Space observations of cold-cloud phase change, *Proceedings of the National Academy of Sciences of the United States of America*, 107, 11211-11216, 10.2307/20724047, 2010.
- Chylek, P., Jennings, S. G., and Pinnick, R.: AEROSOLS | Soot A2 - North, Gerald R, in: *Encyclopedia of Atmospheric Sciences (Second Edition)*, edited by: Pyle, J., and Zhang, F., Academic Press, Oxford, 86-91, 2015.
- Clarke, A. D., Varner, J. L., Eisele, F., Mauldin, R. L., Tanner, D., and Litchy, M.: Particle production in the remote marine atmosphere: Cloud outflow and subsidence during ACE 1, *Journal of Geophysical Research: Atmospheres*, 103, 16397-16409, 10.1029/97JD02987, 1998.
- Clarke, A. D., Owens, S. R., and Zhou, J.: An ultrafine sea-salt flux from breaking waves: Implications for cloud condensation nuclei in the remote marine atmosphere, *Journal of Geophysical Research: Atmospheres*, 111, n/a-n/a, 10.1029/2005JD006565, 2006.
- Clegg, S. L., Brimblecombe, P., and Wexler, A. S.: Thermodynamic Model of the System $H^+-NH_4^+-SO_4^{2-}-NO_3^- -H_2O$ at Tropospheric Temperatures, *The Journal of Physical Chemistry A*, 102, 2137-2154, 10.1021/jp973042r, 1998a.
- Clegg, S. L., Brimblecombe, P., and Wexler, A. S.: Thermodynamic Model of the System $H^+-NH_4^+-Na^+-SO_4^{2-}-NO_3^- -Cl^- -H_2O$ at 298.15 K, *The Journal of Physical Chemistry A*, 102, 2155-2171, 10.1021/jp973043j, 1998b.
- Clegg, S. L., and Wexler, A. S.: Densities and Apparent Molar Volumes of Atmospherically Important Electrolyte Solutions. 1. The Solutes H_2SO_4 , HNO_3 , HCl , Na_2SO_4 , $NaNO_3$, $NaCl$, $(NH_4)_2SO_4$, NH_4NO_3 , and NH_4Cl from 0 to 50 °C, Including Extrapolations to Very Low Temperature and to the Pure Liquid State, and $NaHSO_4$, $NaOH$, and NH_3 at 25 °C, *The Journal of Physical Chemistry A*, 115, 3393-3460, 10.1021/jp108992a, 2011.
- Collins, D. B., Bertram, T. H., Sultana, C. M., Lee, C., Axson, J. L., and Prather, K. A.: Phytoplankton blooms weakly influence the cloud forming ability of sea spray aerosol, *Geophysical Research Letters*, 43, 9975-9983, doi:10.1002/2016GL069922, 2016.
- Collins, D. R., Cocker, D. R., Flagan, R. C., and Seinfeld, J. H.: The Scanning DMA Transfer Function, *Aerosol Science and Technology*, 38, 833-850, 10.1080/027868290503082, 2004.
- Comer, B., Olmer, N., Mao, X., Roy, B., and Rutherford, D.: Black Carbon Emissions and Fuel Use in Global Shipping 2015, The International Council on Clean Transportation, 1225 I Street NW, Suite 900, Washington DC 20005 USA, 2017.

References

- Conant, W. C., VanReken, T. M., Rissman, T. A., Varutbangkul, V., Jonsson, H. H., Nenes, A., Jimenez, J. L., Delia, A. E., Bahreini, R., Roberts, G. C., Flagan, R. C., and Seinfeld, J. H.: Aerosol–cloud drop concentration closure in warm cumulus, *Journal of Geophysical Research: Atmospheres*, 109, n/a-n/a, 10.1029/2003JD004324, 2004.
- Covington, A. K., Robinson, R. A., and Thompson, R.: Osmotic and activity coefficients for aqueous methane sulfonic acid solutions at 25.deg, *J. Chem. Eng. Data*, 18, 422-423, 10.1021/jc60059a018, 1973.
- Cravigan, L. T., Ristovski, Z., Modini, R. L., Keywood, M. D., and Gras, J. L.: Observation of sea-salt fraction in sub-100 nm diameter particles at Cape Grim, *Journal of Geophysical Research: Atmospheres*, 120, 1848-1864, 10.1002/2014JD022601, 2015.
- Dadashazar, H., Braun, R. A., Crosbie, E., Chuang, P. Y., Woods, R. K., Jonsson, H. H., and Sorooshian, A.: Aerosol Characteristics in the Entrainment Interface Layer In Relation to the Marine Boundary Layer and Free Troposphere, *Atmos. Chem. Phys. Discuss.*, 2017, 1-23, 10.5194/acp-2017-913, 2017.
- Dall'Osto, M., Ovadnevaite, J., Paglione, M., Beddows, D. C. S., Ceburnis, D., Cree, C., Cortés, P., Zamanillo, M., Nunes, S. O., Pérez, G. L., Ortega-Retuerta, E., Emelianov, M., Vaqué, D., Marrasé, C., Estrada, M., Sala, M. M., Vidal, M., Fitzsimons, M. F., Beale, R., Airs, R., Rinaldi, M., Decesari, S., Cristina Facchini, M., Harrison, R. M., O'Dowd, C., and Simó, R.: Antarctic sea ice region as a source of biogenic organic nitrogen in aerosols, *Scientific Reports*, 7, 6047, 10.1038/s41598-017-06188-x, 2017.
- Dawson, K. W., Petters, M. D., Meskhidze, N., Petters, S. S., and Kreidenweis, S. M.: Hygroscopic growth and cloud droplet activation of xanthan gum as a proxy for marine hydrogels, *Journal of Geophysical Research: Atmospheres*, 121, 803-811,818, doi:10.1002/2016JD025143, 2016.
- DeCarlo, P. F., Slowik, J. G., Worsnop, D. R., Davidovits, P., and Jimenez, J. L.: Particle Morphology and Density Characterization by Combined Mobility and Aerodynamic Diameter Measurements. Part 1: Theory, *Aerosol Science and Technology*, 38, 1185-1205, 10.1080/027868290903907, 2004.
- DeCarlo, P. F., Kimmel, J. R., Trimborn, A., Northway, M. J., Jayne, J. T., Aiken, A. C., Gonin, M., Fuhrer, K., Horvath, T., Docherty, K. S., Worsnop, D. R., and Jimenez, J. L.: Field-Deployable, High-Resolution, Time-of-Flight Aerosol Mass Spectrometer, *Anal. Chem.*, 78, 8281-8289, 10.1021/ac061249n, 2006.
- DeMott, P. J., Hill, T. C. J., McCluskey, C. S., Prather, K. A., Collins, D. B., Sullivan, R. C., Ruppel, M. J., Mason, R. H., Irish, V. E., Lee, T., Hwang, C. Y., Rhee, T. S., Snider, J. R., McMeeking, G. R., Dhaniyala, S., Lewis, E. R., Wentzell, J. J. B., Abbatt, J., Lee, C., Sultana, C. M., Ault, A. P., Axson, J. L., Diaz Martinez, M., Venero, I., Santos-Figueroa, G., Stokes, M. D., Deane, G. B., Mayol-Bracero, O. L., Grassian, V. H., Bertram, T. H., Bertram, A. K., Moffett, B. F., and Franc, G. D.: Sea spray aerosol as a unique source of ice nucleating particles, *Proceedings of the National Academy of Sciences*, 113, 5797, 2016.
- Dinar, E., Taraniuk, I., Graber, E. R., Katsman, S., Moise, T., Anttila, T., Mentel, T. F., and Rudich, Y.: Cloud Condensation Nuclei properties of model and atmospheric HULIS, *Atmos. Chem. Phys.*, 6, 2465-2482, 10.5194/acp-6-2465-2006, 2006.

References

- Dorothy, K., and James, H.: Distant origins of Arctic black carbon: A Goddard Institute for Space Studies ModelE experiment, *Journal of Geophysical Research: Atmospheres*, 110, doi:10.1029/2004JD005296, 2005.
- Droplet-Measurement-Technologies: Cloud Condensation Nuclei (CCN) Counter: Manual for Single-Column CCNs, in, edited by: Droplet Measurement Technologies, I., DMT, 2545 Central Avenue, Boulder, CO 80301-5727 USA, 114, 2012.
- Duce, R. A., and Tindale, N. W.: Atmospheric transport of iron and its deposition in the ocean, *Limnology and Oceanography*, 36, 1715-1726, doi:10.4319/lo.1991.36.8.1715, 1991.
- Duce, R. A., LaRoche, J., Altieri, K., Arrigo, K. R., Baker, A. R., Capone, D. G., Cornell, S., Dentener, F., Galloway, J., Ganeshram, R. S., Geider, R. J., Jickells, T., Kuypers, M. M., Langlois, R., Liss, P. S., Liu, S. M., Middelburg, J. J., Moore, C. M., Nickovic, S., Oschlies, A., Pedersen, T., Prospero, J., Schlitzer, R., Seitzinger, S., Sorensen, L. L., Uematsu, M., Ulloa, O., Voss, M., Ward, B., and Zamora, L.: Impacts of Atmospheric Anthropogenic Nitrogen on the Open Ocean, *Science*, 320, 893-897, 10.1126/science.1150369, 2008.
- Dusek, U., Frank, G. P., Hildebrandt, L., Curtius, J., Schneider, J., Walter, S., Chand, D., Drewnick, F., Hings, S., Jung, D., Borrmann, S., and Andreae, M. O.: Size Matters More Than Chemistry for Cloud-Nucleating Ability of Aerosol Particles, *Science*, 312, 1375-1378, 10.1126/science.1125261, 2006.
- Cloud Physics Research - Light Scattering by Ice Crystals, access: August.
- Facchini, M. C., Rinaldi, M., Decesari, S., Carbone, C., Finessi, E., Mircea, M., Fuzzi, S., Ceburnis, D., Flanagan, R., Nilsson, E. D., de Leeuw, G., Martino, M., Woeltjen, J., and O'Dowd Colin, D.: Primary submicron marine aerosol dominated by insoluble organic colloids and aggregates, *Geophysical Research Letters*, 35, 10.1029/2008GL034210, 2008.
- Forestieri, S. D., Moore, K. A., Martinez Borrero, R., Wang, A., Stokes, M. D., and Cappa, C. D.: Temperature and Composition Dependence of Sea Spray Aerosol Production, *Geophysical Research Letters*, 0, 10.1029/2018GL078193, 2018.
- Fossum, K. N., Ovadnevaite, J., Ceburnis, D., Dall'Osto, M., Marullo, S., Bellacicco, M., Simó, R., Liu, D., Flynn, M., Zuend, A., and O'Dowd, C.: Summertime Primary and Secondary Contributions to Southern Ocean Cloud Condensation Nuclei, *Scientific Reports*, 8, 13844, 10.1038/s41598-018-32047-4, 2018.
- Fountoukis, C., Nenes, A., Meskhidze, N., Bahreini, R., Conant, W. C., Jonsson, H., Murphy, S., Sorooshian, A., Varutbangkul, V., Brechtel, F., Flagan, R. C., and Seinfeld, J. H.: Aerosol-cloud drop concentration closure for clouds sampled during the International Consortium for Atmospheric Research on Transport and Transformation 2004 campaign, *Journal of Geophysical Research: Atmospheres*, 112, n/a-n/a, 10.1029/2006JD007272, 2007.
- Fuchs, N. A.: On the stationary charge distribution on aerosol particles in a bipolar ionic atmosphere, *Pure and Applied Geophysics*, 185-186, <https://doi.org/10.1007/BF01993343>, 1963.
- Fuentes, E., Coe, H., Green, D., De Leeuw, G., and McFiggans, G.: On the impacts of phytoplankton-derived organic matter on the properties of the primary marine aerosol - Part 1: Source fluxes, *Atmospheric Chemistry and Physics*, 10, 9295-9317, 2010a.

References

- Fuentes, E., Coe, H., Green, D., de Leeuw, G., and McFiggans, G.: Laboratory-generated primary marine aerosol via bubble-bursting and atomization, *Atmos. Meas. Tech.*, 3, 141-162, 10.5194/amt-3-141-2010, 2010b.
- G. de Leeuw, Andreas, E. L., Anguelova, M. D., Fairall, C. W., Lewis, E. R., O'Dowd, C. D., Schulz, M., and Schwartz, S. E.: Production flux of sea spray aerosol, *Reviews of Geophysics*, 49, n/a-n/a, 10.1029/2010RG000349, 2011.
- Galindo, V., Levasseur, M., Scarratt, M., Mundy, C. J., Gosselin, M., Kiene, R. P., Gourdal, M., and Lizotte, M.: Under-ice microbial dimethylsulfoniopropionate metabolism during the melt period in the Canadian Arctic Archipelago, *Marine Ecology Progress Series*, 524, 39-53, 2015.
- Garrett, W. D.: Stabilization of air bubbles at the air-sea interface by surface-active material, *Deep Sea Research and Oceanographic Abstracts*, 14, 661-672, [https://doi.org/10.1016/S0011-7471\(67\)80004-4](https://doi.org/10.1016/S0011-7471(67)80004-4), 1967.
- Gaston, C., Cahill, J., Collins, D., Suski, K., Ge, J., Barkley, A., and Prather, K.: The Cloud Nucleating Properties and Mixing State of Marine Aerosols Sampled along the Southern California Coast, *Atmosphere*, 9, 52, 2018.
- Gavin Cornwell, Camille Marissa Sultana, Gregory P. Schill, Thomas Christopher James Hill, Richard E. Cochran, Paul J. DeMott, and Prather., K. A.: A11L-06: Resuspended dust as a novel source of marine ice nucleating particles, in: A11L Atmospheric Ice-Nucleating Particles and Ice-Cloud Formation: Field, Laboratory, and Modeling Studies I, AGU Fall Meeting, New Orleans, 2017.
- Geever, M., O'Dowd, C. D., van Ekeren, S., Flanagan, R., Nilsson, E. D., de Leeuw, G., and Rannik, Ü.: Submicron sea spray fluxes, *Geophysical Research Letters*, 32, 10.1029/2005GL023081, 2005.
- Gilgen, A., Huang, W. T. K., Ickes, L., Neubauer, D., and Lohmann, U.: How important are future marine and shipping aerosol emissions in a warming Arctic summer and autumn?, *Atmos. Chem. Phys.*, 18, 10521-10555, 10.5194/acp-18-10521-2018, 2018.
- Gogoi, M. M., Babu, S. S., Moorthy, K. K., Thakur, R. C., Chaubey, J. P., and Nair, V. S.: Aerosol black carbon over Svalbard regions of Arctic, *Polar Science*, 10, 60-70, <https://doi.org/10.1016/j.polar.2015.11.001>, 2016.
- Gong, S. L.: A parameterization of sea-salt aerosol source function for sub- and super-micron particles, *Global Biogeochemical Cycles*, 17, 10.1029/2003GB002079, 2003.
- Gregor, H. P., Rothenberg, M., and Fine, N.: MOLAL ACTIVITY COEFFICIENTS OF METHANE— AND ETHANESULFONIC ACIDS AND THEIR SALTS, *J. Phys. Chem.*, 67, 1110-1112, 10.1021/j100799a042, 1963.
- Grigas, T., Ovadnevaite, J., Ceburnis, D., Moran, E., McGovern, F. M., Jennings, S. G., and O'Dowd, C.: Sophisticated Clean Air Strategies Required to Mitigate Against Particulate Organic Pollution, *Scientific Reports*, 7, 44737, 10.1038/srep44737 <https://www.nature.com/articles/srep44737#supplementary-information>, 2017.
- Hallett, J., and Mossop, S. C.: Production of secondary ice particles during the riming process, *Nature*, 249, 26-28, 1974.
- Hamilton, D. S., Lee, L. A., Pringle, K. J., Reddington, C. L., Spracklen, D. V., and Carslaw, K. S.: Occurrence of pristine aerosol environments on a polluted planet, *Proceedings of the National Academy of Sciences*, 111, 18466, 2014.

References

- Hansell, D. A., and Carlson, C. A.: Marine Dissolved Organic Matter and the Carbon Cycle, *Oceanography*, 14, 2001.
- Hegg, D. A., Ferek, R. J., Hobbs, P. V., and Radke, L. F.: Dimethyl sulfide and cloud condensation nucleus correlations in the northeast Pacific Ocean, *Journal of Geophysical Research: Atmospheres*, 96, 13189-13191, 10.1029/91JD01309, 1991.
- Hinds, W. C.: *Aerosol Technology: Properties, Behavior, and Measurement of Airborne Particles*, John Wiley & Sons, New York, 424 pp., 1982.
- Hiranuma, N., Augustin-Bauditz, S., Bingemer, H., Budke, C., Curtius, J., Danielczok, A., Diehl, K., Dreischmeier, K., Ebert, M., Frank, F., Hoffmann, N., Kandler, K., Kiselev, A., Koop, T., Leisner, T., Möhler, O., Nillius, B., Peckhaus, A., Rose, D., Weinbruch, S., Wex, H., Boose, Y., DeMott, P. J., Hader, J. D., Hill, T. C. J., Kanji, Z. A., Kulkarni, G., Levin, E. J. T., McCluskey, C. S., Murakami, M., Murray, B. J., Niedermeier, D., Petters, M. D., O'Sullivan, D., Saito, A., Schill, G. P., Tajiri, T., Tolbert, M. A., Welti, A., Whale, T. F., Wright, T. P., and Yamashita, K.: A comprehensive laboratory study on the immersion freezing behavior of illite NX particles: a comparison of 17 ice nucleation measurement techniques, *Atmos. Chem. Phys.*, 15, 2489-2518, 10.5194/acp-15-2489-2015, 2015.
- Hoell, C., O'Dowd, C., Osborne, S., and Johnson, D.: Time-scale analysis of marine boundary layer aerosol evolution: Lagrangian case studies under clean and polluted cloudy conditions, *Tellus B: Chemical and Physical Meteorology*, 52, 423-438, 10.3402/tellusb.v52i2.16169, 2000.
- Hoppel, W. A., Frick, G. M., and Larson, R. E.: Effect of nonprecipitating clouds on the aerosol size distribution in the marine boundary layer, *Geophysical Research Letters*, 13, 125-128, 10.1029/GL013i002p00125, 1986.
- Hoppel, W. A., Frick, G. M., Fitzgerald, J. W., and Larson, R. E.: Marine boundary layer measurements of new particle formation and the effects nonprecipitating clouds have on aerosol size distribution, *Journal of Geophysical Research: Atmospheres*, 99, 14443-14459, 10.1029/94JD00797, 1994.
- Hoppel, W. A., Frick, G. M., and Fitzgerald, J. W.: Deducing droplet concentration and supersaturation in marine boundary layer clouds from surface aerosol measurements, *Journal of Geophysical Research: Atmospheres*, 101, 26553-26565, 10.1029/96JD02243, 1996.
- Hudson, J. G., Noble, S., and Jha, V.: Stratus cloud supersaturations, *Geophysical Research Letters*, 37, doi:10.1029/2010GL045197, 2010.
- Hudson, J. G., Noble, S., and Tabor, S.: Cloud supersaturations from CCN spectra Hoppel minima, *J. Geophys. Res. D Atmos.*, 120, 3436-3452, 10.1002/2014JD022669, 2015.
- Irwin, M., Good, N., Crosier, J., Choularton, T. W., and McFiggans, G.: Reconciliation of measurements of hygroscopic growth and critical supersaturation of aerosol particles in central Germany, *Atmos. Chem. Phys.*, 10, 11737-11752, 10.5194/acp-10-11737-2010, 2010.
- Jaeglé, L., Quinn, P. K., Bates, T. S., Alexander, B., and Lin, J. T.: Global distribution of sea salt aerosols: new constraints from in situ and remote sensing observations, *Atmos. Chem. Phys.*, 11, 3137-3157, 10.5194/acp-11-3137-2011, 2011.
- Jennings, S. G., Geever, M., McGovern, F. M., Francis, J., Spain, T. G., and Donaghy, T.: Microphysical and physico-chemical characterization of atmospheric marine

References

- and continental aerosol at mace head, *Atmospheric Environment*, 31, 2795-2808, [https://doi.org/10.1016/S1352-2310\(97\)00039-3](https://doi.org/10.1016/S1352-2310(97)00039-3), 1997.
- Jennings, S. G., Kleefeld, C., Colin D. O'Dowd, Junker, C., Spain, T. G., O'Brien, P., Roddy, A. F., and O'Connor, T. C.: Mace Head Atmospheric Research Station — characterization of aerosol radiative parameters, *Boreal Environment Research*, 8, 2003.
- Jickells, T., and Moore, C. M.: The Importance of Atmospheric Deposition for Ocean Productivity, *Annual Review of Ecology, Evolution, and Systematics*, 46, 481-501, [10.1146/annurev-ecolsys-112414-054118](https://doi.org/10.1146/annurev-ecolsys-112414-054118), 2015.
- Jimenez, J. L., Jayne, J. T., Shi, Q., Kolb, C. E., Worsnop, D. R., Yourshaw, I., Seinfeld, J. H., Flagan, R. C., Zhang, X., Smith, K. A., Morris, J. W., and Davidovits, P.: Ambient aerosol sampling using the Aerodyne Aerosol Mass Spectrometer, *Journal of Geophysical Research: Atmospheres*, 108, n/a-n/a, [10.1029/2001JD001213](https://doi.org/10.1029/2001JD001213), 2003.
- Kanji, Z. A., Welti, A., Chou, C., Stetzer, O., and Lohmann, U.: Laboratory studies of immersion and deposition mode ice nucleation of ozone aged mineral dust particles, *Atmos. Chem. Phys.*, 13, 9097-9118, [10.5194/acp-13-9097-2013](https://doi.org/10.5194/acp-13-9097-2013), 2013.
- Karp-Boss, L., Wheeler, P. A., Hales, B., and Covert, P.: Distributions and variability of particulate organic matter in a coastal upwelling system, *Journal of Geophysical Research: Oceans*, 109, doi:10.1029/2003JC002184, 2004.
- Karsten, U., Kück, K., Vogt, C., and Kirst, G. O.: Dimethylsulfoniopropionate Production in Phototrophic Organisms and its Physiological Functions as a Cryoprotectant, in: *Biological and Environmental Chemistry of DMSP and Related Sulfonium Compounds*, edited by: Kiene, R. P., Visscher, P. T., Keller, M. D., and Kirst, G. O., Springer, Boston, MA, 1996.
- Katoshevski, D., Nenes, A., and Seinfeld, J. H.: A Study of Processes that Govern the Maintenance of Aerosols in the Marine Boundary Layer, *J. Aerosol Sci.*, 30, 503-532, [https://doi.org/10.1016/S0021-8502\(98\)00740-X](https://doi.org/10.1016/S0021-8502(98)00740-X), 1999.
- Keene, W. C., Maring, H., Maben, J. R., Kieber, D. J., Pszenny, A. A. P., Dahl, E. E., Izaguirre, M. A., Davis, A. J., Long, M. S., Zhou, X., Smoydzin, L., and Sander, R.: Chemical and physical characteristics of nascent aerosols produced by bursting bubbles at a model air-sea interface, *Journal of Geophysical Research: Atmospheres*, 112, [10.1029/2007JD008464](https://doi.org/10.1029/2007JD008464), 2007.
- Keller, M. D.: Dimethyl Sulfide Production and Marine Phytoplankton: The Importance of Species Composition and Cell Size, *Biological Oceanography*, 6, 375-382, [10.1080/01965581.1988.10749540](https://doi.org/10.1080/01965581.1988.10749540), 1989.
- Kirpes, R. M., Bondy, A. L., Bonanno, D., Moffet, R. C., Wang, B., Laskin, A., Ault, A. P., and Pratt, K. A.: Secondary Sulfate is Internally Mixed with Sea Spray Aerosol and Organic Aerosol in the Winter-Spring Arctic, *Atmos. Chem. Phys. Discuss.*, 2017, 1-29, [10.5194/acp-2017-998](https://doi.org/10.5194/acp-2017-998), 2017.
- Klimont, Z., Kupiainen, K., Heyes, C., Purohit, P., Cofala, J., Rafaj, P., Borcken-Kleefeld, J., and Schöpp, W.: Global anthropogenic emissions of particulate matter including black carbon, *Atmos. Chem. Phys.*, 17, 8681-8723, [10.5194/acp-17-8681-2017](https://doi.org/10.5194/acp-17-8681-2017), 2017.
- Knutson, E. O., and Whitby, K. T.: Aerosol classification by electric mobility: apparatus, theory, and applications, *J. Aerosol Sci.*, 6, 443-451, [https://doi.org/10.1016/0021-8502\(75\)90060-9](https://doi.org/10.1016/0021-8502(75)90060-9), 1975.

References

- Köhler, H.: The nucleus in and the growth of hygroscopic droplets, *Transactions of the Faraday Society*, 32, 1152-1161, 10.1039/TF9363201152, 1936.
- Kondrashov, D., and Ghil, M.: Spatio-temporal filling of missing points in geophysical data sets, *Nonlin. Processes Geophys.*, 13, 151-159, 10.5194/npg-13-151-2006, 2006.
- Kosova, D. A., Navalayeu, T. I., Maksimov, A. I., Babkina, T. S., and Uspenskaya, I. A.: Experimental investigation of the solid – Liquid phase equilibria in the water – Ammonium methanesulfonate and in the water – Sodium methanesulfonate systems, *Fluid Phase Equilibria*, 443, 23-31, <https://doi.org/10.1016/j.fluid.2017.04.006>, 2017.
- Krüger, M. L., Mertes, S., Klimach, T., Cheng, Y. F., Su, H., Schneider, J., Andreae, M. O., Pöschl, U., and Rose, D.: Assessment of cloud supersaturation by size-resolved aerosol particle and cloud condensation nuclei (CCN) measurements, *Atmos. Meas. Tech.*, 7, 2615-2629, 10.5194/amt-7-2615-2014, 2014.
- Kulmala, M., Pirjola, L., and Mäkelä, J. M.: Stable sulphate clusters as a source of new atmospheric particles, *Nature*, 404, 66, 10.1038/35003550, 2000.
- Kyrö, E. M., Kerminen, V. M., Virkkula, A., Dal Maso, M., Parshintsev, J., Ruíz-Jimenez, J., Forsström, L., Manninen, H. E., Riekkola, M. L., Heinonen, P., and Kulmala, M.: Antarctic new particle formation from continental biogenic precursors, *Atmospheric Chemistry and Physics*, 13, 3527-3546, 10.5194/acp-13-3527-2013, 2013.
- Lamb, H. H.: *British Isles Weather Types and a Register of the Daily Sequence of Circulation Patterns 1861-1971*, Geophysical memoirs, edited by: Office, M., H.M. Stationery Office, 85 pp., 1972.
- Lance, S., Medina, J., Smith, J., and Nenes, A.: Mapping the Operation of the DMT Continuous Flow CCN Counter, *Aerosol Science & Technology*, 40, 242-254, 10.1080/02786820500543290, 2006.
- Latham, J., and Smith, M. H.: Effect on global warming of wind-dependent aerosol generation at the ocean surface, *Nature*, 347, 372-373, 1990.
- Leitch, W. R., Banic, C. M., Isaac, G. A., Couture, M. D., Liu, P. S. K., Gultepe, I., Li, S.-M., Kleinman, L., Daum, P. H., and MacPherson, J. I.: Physical and chemical observations in marine stratus during the 1993 North Atlantic Regional Experiment: Factors controlling cloud droplet number concentrations, *Journal of Geophysical Research: Atmospheres*, 101, 29123-29135, doi:10.1029/96JD01228, 1996.
- Leeuw, G., Neele, F. P., Hill, M., Smith, M. H., and Vignati, E.: Production of sea spray aerosol in the surf zone, *Journal of Geophysical Research: Atmospheres*, 105, 29397-29409, 10.1029/2000JD900549, 2000.
- Lewis, E. R., and Schwartz, S. E.: *Sea Salt Aerosol Production: Mechanisms, Methods, Measurements and Models-A Critical Review*, American Geophysical Union, 2004.
- Liss, P. S., Malin, G., and Turner, S. M.: Production of DMS by Marine Phytoplankton, in: *Dimethylsulphide: Oceans, Atmosphere and Climate (1992)*, edited by: Restelli, G., and Angeletti, G., Kluwer Academic Publishing, Dordrecht, NL, 1-14, 1993.

References

- Liss, P. S., Hatton, A. D., Malin, G., Nightingale, P. D., and Turner, S. M.: Marine sulphur emissions, *Philosophical Transactions of the Royal Society B: Biological Sciences*, 352, 159-169, 10.1098/rstb.1997.0011, 1997.
- Liu, Y., and Laskin, A.: Hygroscopic Properties of CH₃SO₃Na, CH₃SO₃NH₄, (CH₃SO₃)₂Mg, and (CH₃SO₃)₂Ca Particles Studied by micro-FTIR Spectroscopy, *J. Phys. Chem. A*, 113, 1531-1538, 10.1021/jp8079149, 2009.
- Lizotte, M., Levasseur, M., Michaud, S., Scarratt, M. G., Merzouk, A., Gosselin, M., Pommier, J., Rivkin, R. B., and Kiene, R. P.: Macroscale patterns of the biological cycling of dimethylsulfoniopropionate (DMSP) and dimethylsulfide (DMS) in the Northwest Atlantic, *Biogeochemistry*, 110, 183-200, 10.1007/s10533-011-9698-4, 2012.
- Lizotte, M., Levasseur, M., Law, C. S., Walker, C. F., Safi, K. A., Marriner, A., and Kiene, R. P.: Dimethylsulfoniopropionate (DMSP) and dimethyl sulfide (DMS) cycling across contrasting biological hotspots of the New Zealand subtropical front, *Ocean Sci.*, 13, 961-982, 10.5194/os-13-961-2017, 2017.
- Lohmann, U.: A glaciation indirect aerosol effect caused by soot aerosols, *Geophysical Research Letters*, 29, 11-11-11-14, 10.1029/2001GL014357, 2002.
- Lohmann, U., Ansmann, A., Facchini, C., Decesari, S., Kanakidou, M., Stier, P., Makkonen, R., Stevens, B., Kinne, S., Fiedler, S., Neubauer, D., and Carslaw, K.: D5.9; Community assessment of the importance of biogenic versus anthropogenic emissions for cloud formation and climate, in: BACCHUS Collaborative Project SEVENTH FRAMEWORK PROGRAMME (ENV.2013.6.1-2): Atmospheric processes, eco-systems and climate change, edited by: Burkert, M., Grant agreement no: 603445, ETHZ, 2018.
- Lovelock, J. E.: Gaia as seen through the atmosphere, *Atmospheric Environment* (1967), 6, 579-580, [https://doi.org/10.1016/0004-6981\(72\)90076-5](https://doi.org/10.1016/0004-6981(72)90076-5), 1972.
- Lovelock, J. E., and Watson, A. J.: The regulation of carbon dioxide and climate: Gaia or geochemistry, *Planetary and Space Science*, 30, 795-802, [https://doi.org/10.1016/0032-0633\(82\)90112-X](https://doi.org/10.1016/0032-0633(82)90112-X), 1982.
- Mårtensson, M. E., Nilsson, E. D., de Leeuw, G., Cohen, L. H., and Hansson, H. C.: Laboratory simulations and parameterization of the primary marine aerosol production, *Journal of Geophysical Research: Atmospheres*, 108, n/a-n/a, 10.1029/2002JD002263, 2003.
- Mårtensson, M. E., Tunved, P., Korhonen, H., and Nilsson, E. D.: The role of sea-salt emissions in controlling the marine Aitken and accumulation mode aerosol: a model study, *Tellus B*, 62, 259-279, 10.1111/j.1600-0889.2010.00465.x, 2010.
- Mason, R. H., Si, M., Chou, C., Irish, V. E., Dickie, R., Elizondo, P., Wong, R., Brintnell, M., Elsasser, M., Lassar, W. M., Pierce, K. M., Leitch, W. R., MacDonald, A. M., Platt, A., Toom-Sauntry, D., Sarda-Estève, R., Schiller, C. L., Suski, K. J., Hill, T. C. J., Abbatt, J. P. D., Huffman, J. A., DeMott, P. J., and Bertram, A. K.: Size-resolved measurements of ice-nucleating particles at six locations in North America and one in Europe, *Atmos. Chem. Phys.*, 16, 1637-1651, 10.5194/acp-16-1637-2016, 2016.
- McCluskey, C. S., Hill, T. C. J., Sultana, C. M., Laskina, O., Trueblood, J., Santander, M. V., Beall, C. M., Michaud, J. M., Kreidenweis, S. M., Prather, K. A., Grassian, V., and DeMott, P. J.: A mesocosm double feature: Insights into the chemical make-

References

- up of marine ice nucleating particles, *Journal of the Atmospheric Sciences*, null, 10.1175/jas-d-17-0155.1, 2018a.
- McCluskey, C. S., Ovadnevaite, J., Rinaldi, M., Atkinson, J., Belosi, F., Ceburnis, D., Marullo, S., Hill Thomas, C. J., Lohmann, U., Kanji Zamin, A., O'Dowd, C., Kreidenweis Sonia, M., and DeMott Paul, J.: Marine and Terrestrial Organic Ice-Nucleating Particles in Pristine Marine to Continentally Influenced Northeast Atlantic Air Masses, *Journal of Geophysical Research: Atmospheres*, 123, 6196-6212, 10.1029/2017JD028033, 2018b.
- McCoy, D. T., Burrows, S. M., Wood, R., Grosvenor, D. P., Elliott, S. M., Ma, P.-L., Rasch, P. J., and Hartmann, D. L.: Natural aerosols explain seasonal and spatial patterns of Southern Ocean cloud albedo, *Science Advances*, 1, 10.1126/sciadv.1500157, 2015.
- McFiggans, G., Artaxo, P., Baltensperger, U., Coe, H., Facchini, M. C., Feingold, G., Fuzzi, S., Gysel, M., Laaksonen, A., Lohmann, U., Mentel, T. F., Murphy, D. M., O'Dowd, C. D., Snider, J. R., and Weingartner, E.: The effect of physical and chemical aerosol properties on warm cloud droplet activation, *Atmos. Chem. Phys.*, 6, 2593-2649, 10.5194/acp-6-2593-2006, 2006.
- McMeeking, G. R., Hamburger, T., Liu, D., Flynn, M., Morgan, W. T., Northway, M., Highwood, E. J., Krejci, R., Allan, J. D., Minikin, A., and Coe, H.: Black carbon measurements in the boundary layer over western and northern Europe, *Atmos. Chem. Phys.*, 10, 9393-9414, 10.5194/acp-10-9393-2010, 2010.
- Middlebrook, A. M., Bahreini, R., Jimenez, J. L., and Canagaratna, M. R.: Evaluation of Composition-Dependent Collection Efficiencies for the Aerodyne Aerosol Mass Spectrometer using Field Data, *Aerosol Science and Technology*, 46, 258-271, 10.1080/02786826.2011.620041, 2012.
- Modini, R. L., Frossard, A. A., Ahlm, L., Russell, L. M., Corrigan, C. E., Roberts, G. C., Hawkins, L. N., Schroder, J. C., Bertram, A. K., Zhao, R., Lee, A. K. Y., Abbatt, J. P. D., Lin, J., Nenes, A., Wang, Z., Wonaschütz, A., Sorooshian, A., Noone, K. J., Jonsson, H., Seinfeld, J. H., Toom-Sauntry, D., Macdonald, A. M., and Leitch, W. R.: Primary marine aerosol-cloud interactions off the coast of California, *J. Geophys. Res. D Atmos.*, 10.1002/2014JD022963, 2015.
- Monahan, E. C.: Sea spray as a function of low elevation wind speed, *Journal of Geophysical Research*, 73, 1127-1137, 10.1029/JB073i004p01127, 1968.
- Monahan, E. C., Spiel, D. E., and Davidson, K. L.: A Model of Marine Aerosol Generation Via Whitecaps and Wave Disruption, in: *Oceanographic Sciences Library*, Springer Netherlands, 167-174, 1986.
- Mulcahy, J. P., O'Dowd, C. D., Jennings, S. G., and Ceburnis, D.: Significant enhancement of aerosol optical depth in marine air under high wind conditions, *Geophysical Research Letters*, 35, n/a-n/a, 10.1029/2008GL034303, 2008.
- Murphy, D. M., Anderson, J. R., Quinn, P. K., McInnes, L. M., Brechtel, F. J., Kreidenweis, S. M., Middlebrook, A. M., Posfai, M., Thomson, D. S., and Buseck, P. R.: Influence of sea-salt on aerosol radiative properties in the Southern Ocean marine boundary layer, *Nature*, 392, 62-65, 1998.
- Murray, B. J., O'Sullivan, D., Atkinson, J. D., and Webb, M. E.: Ice nucleation by particles immersed in supercooled cloud droplets, *Chemical Society Reviews*, 41, 6519-6554, 10.1039/C2CS35200A, 2012.

References

- Myhre, C. E., Nielsen, C. J., and Saastad, O. W.: Density and surface tension of aqueous H₂SO₄ at low temperature, *Journal of Chemical & Engineering Data*, 43, 617-622, 1998.
- NASA: MODIS Atmosphere Level-3 Global Products (08_M3), in: Collection 6.1, edited by: MOD08_M3.A2015001.061.2017319074723.hdf, Goddard Space Flight Center, Greenbelt, Maryland, USA, https://modis-images.gsfc.nasa.gov/MOD08_M3/_BROWSE_FIXEDSCALE/2015_01/C061/LL/browse_main_m7.php, 2017.
- NASA: Worldview 2.4.0, in: Earth Science Data and Information System (ESDIS) Project Goddard Space Flight Center, Maryland, USA, <https://worldview.earthdata.nasa.gov/>, 2018.
- Nenes, A., Ghan, S., Abdul-Razzak, H., Chuang, P. Y., and Seinfeld, J. H.: Kinetic limitations on cloud droplet formation and impact on cloud albedo, *Tellus B*, 53, 133-149, doi:10.1034/j.1600-0889.2001.d01-12.x, 2001.
- Nenes, A., Charlson, R. J., Facchini, M. C., Kulmala, M., Laaksonen, A., and Seinfeld, J. H.: Can chemical effects on cloud droplet number rival the first indirect effect?, *Geophysical Research Letters*, 29, 29-21, 2002.
- Nightingale, P. D., and Liss, P. S.: Gases in Seawater, in: *Treatise on Geochemistry*, edited by: Elderfield, H., Elsevier, 49-81, 2003.
- Nilsson, E. D., Rannik, Ü., Swietlicki, E., Leck, C., Aalto, P. P., Zhou, J., and Norman, M.: Turbulent aerosol fluxes over the Arctic Ocean: 2. Wind-driven sources from the sea, *Journal of Geophysical Research: Atmospheres*, 106, 32139-32154, 10.1029/2000JD900747, 2001.
- Norris, S. J., Brooks, I. M., de Leeuw, G., Smith, M. H., Moerman, M., and Lingard, J. J. N.: Eddy covariance measurements of sea spray particles over the Atlantic Ocean, *Atmos. Chem. Phys.*, 8, 555-563, 10.5194/acp-8-555-2008, 2008.
- Norris, S. J., Brooks, I. M., Hill, M. K., Brooks, B. J., Smith, M. H., and Sproson, D. A. J.: Eddy covariance measurements of the sea spray aerosol flux over the open ocean, *Journal of Geophysical Research: Atmospheres*, 117, 10.1029/2011JD016549, 2012.
- O'Dowd, C., Ceburnis, D., Ovadnevaite, J., Vaishya, A., Rinaldi, M., and Facchini, M. C.: Do anthropogenic, continental or coastal aerosol sources impact on a marine aerosol signature at Mace Head?, *Atmos. Chem. Phys.*, 14, 10687-10704, 10.5194/acp-14-10687-2014, 2014.
- O'Dowd, C. D., and Smith, M. H.: Physicochemical properties of aerosols over the northeast Atlantic: Evidence for wind-speed-related submicron sea-salt aerosol production, *Journal of Geophysical Research: Atmospheres*, 98, 1137-1149, 10.1029/92JD02302, 1993.
- O'Dowd, C. D., Smith, M. H., and Jennings, S. G.: Submicron particle, radon, and soot carbon characteristics over the northeast Atlantic, *Journal of Geophysical Research: Atmospheres*, 98, 1123-1135, doi:10.1029/92JD02387, 1993.
- O'Dowd, C. D., Lowe, J. A., Smith, M. H., Davison, B., Hewitt, C. N., and Harrison, R. M.: Biogenic sulphur emissions and inferred non-sea-salt-sulphate cloud condensation nuclei in and around Antarctica, *Journal of Geophysical Research: Atmospheres*, 102, 12839-12854, 10.1029/96JD02749, 1997a.

References

- O'Dowd, C. D., Smith, M. H., Consterdine, I. E., and Lowe, J. A.: Marine aerosol, sea-salt, and the marine sulphur cycle: a short review, *Atmospheric Environment*, 31, 73-80, [https://doi.org/10.1016/S1352-2310\(96\)00106-9](https://doi.org/10.1016/S1352-2310(96)00106-9), 1997b.
- O'Dowd, C. D., Lowe, J. A., and Smith, M. H.: Coupling sea-salt and sulphate interactions and its impact on cloud droplet concentration predictions, *Geophysical Research Letters*, 26, 1311-1314, 1999a.
- O'Dowd, C. D., Lowe, J. A., Smith, M. H., and Kaye, A. D.: The relative importance of non-sea-salt sulphate and sea-salt aerosol to the marine cloud condensation nuclei population: An improved multi-component aerosol-cloud droplet parametrization, *Quarterly Journal of the Royal Meteorological Society*, 125, 1295-1313, [10.1002/qj.1999.49712555610](https://doi.org/10.1002/qj.1999.49712555610), 1999b.
- O'Dowd, C. D., Lowe, J. A., Clegg, N., Smith, M. H., and Clegg, S. L.: Modeling heterogeneous sulphate production in maritime stratiform clouds, *Journal of Geophysical Research: Atmospheres*, 105, 7143-7160, [doi:10.1029/1999JD900915](https://doi.org/10.1029/1999JD900915), 2000a.
- O'Dowd, C. D., Lowe, J. A., and Smith, M. H.: The effect of clouds on aerosol growth in the rural atmosphere, *Atmospheric Research*, 54, 201-221, [https://doi.org/10.1016/S0169-8095\(00\)00046-6](https://doi.org/10.1016/S0169-8095(00)00046-6), 2000b.
- O'Dowd, C. D., Hämeri, K., Mäkelä, J. M., Pirjola, L., Kulmala, M., Jennings, S. G., Berresheim, H., Hansson, H.-C., de Leeuw, G., Kunz, G. J., Allen, A. G., Hewitt, C. N., Jackson, A., Viisanen, Y., and Hoffmann, T.: A dedicated study of New Particle Formation and Fate in the Coastal Environment (PARFORCE): Overview of objectives and achievements, *Journal of Geophysical Research: Atmospheres*, 107, PAR 1-1-PAR 1-16, [10.1029/2001JD000555](https://doi.org/10.1029/2001JD000555), 2002a.
- O'Dowd, C. D., Jimenez, J. L., Bahreini, R., Flagan, R. C., Seinfeld, J. H., Hämeri, K., Pirjola, L., Kulmala, M., Jennings, S. G., and Hoffmann, T.: Marine aerosol formation from biogenic iodine emissions, *Nature*, 417, 632-636, 2002b.
- O'Dowd, C. D., Facchini, M. C., Cavalli, F., Ceburnis, D., Mircea, M., Decesari, S., Fuzzi, S., Yoon, Y. J., and Putaud, J.-P.: Biogenically driven organic contribution to marine aerosol, *Nature*, 431, 676-680, http://www.nature.com/nature/journal/v431/n7009/supinfo/nature02959_S1.html, 2004.
- O'Dowd, C. D., and de Leeuw, G.: Marine aerosol production: a review of the current knowledge, *Philosophical Transactions of the Royal Society A: Mathematical, Physical and Engineering Sciences*, 365, 1753, 2007.
- O'Dowd, C. D., Lowe, J. A., and Smith, M. H.: Observations and modelling of aerosol growth in marine stratocumulus—case study, *Atmospheric Environment*, 33, 3053-3062, [https://doi.org/10.1016/S1352-2310\(98\)00213-1](https://doi.org/10.1016/S1352-2310(98)00213-1), 1999.
- O'Dowd, C. D., Ceburnis, D., Ovadnevaite, J., Bialek, J., Stengel, D. B., Zacharias, M., Nitschke, U., Connan, S., Rinaldi, M., Fuzzi, S., Decesari, S., Cristina Facchini, M., Marullo, S., Santoleri, R., Dell'Anno, A., Corinaldesi, C., Tangherlini, M., and Danovaro, R.: Connecting marine productivity to sea-spray via nanoscale biological processes: Phytoplankton Dance or Death Disco?, *Scientific Reports*, 5, 14883, [10.1038/srep14883](https://doi.org/10.1038/srep14883), 2015.
- Ovadnevaite, J., Ceburnis, D., Martucci, G., Bialek, J., Monahan, C., Rinaldi, M., Facchini, M. C., Berresheim, H., Worsnop, D. R., and O'Dowd, C.: Primary marine

References

- organic aerosol: A dichotomy of low hygroscopicity and high CCN activity, *Geophysical Research Letters*, 38, L21806, 10.1029/2011GL048869, 2011a.
- Ovadnevaite, J., O'Dowd, C., Dall'Osto, M., Ceburnis, D., Worsnop, D. R., and Berresheim, H.: Detecting high contributions of primary organic matter to marine aerosol: A case study, *Geophysical Research Letters*, 38, n/a-n/a, 10.1029/2010GL046083, 2011b.
- Ovadnevaite, J., Ceburnis, D., Canagaratna, M., Berresheim, H., Bialek, J., Martucci, G., Worsnop, D. R., and O'Dowd, C.: On the effect of wind speed on submicron sea salt mass concentrations and source fluxes, *Journal of Geophysical Research: Atmospheres*, 117, n/a-n/a, 10.1029/2011JD017379, 2012.
- Ovadnevaite, J., Ceburnis, D., Leinert, S., Dall'Osto, M., Canagaratna, M., O'Doherty, S., Berresheim, H., and O'Dowd, C.: Submicron NE Atlantic marine aerosol chemical composition and abundance: Seasonal trends and air mass categorization, *Journal of Geophysical Research: Atmospheres*, 119, 11,850-811,863, 10.1002/2013JD021330, 2014a.
- Ovadnevaite, J., Manders, A., de Leeuw, G., Ceburnis, D., Monahan, C., Partanen, A. I., Korhonen, H., and O'Dowd, C. D.: A sea spray aerosol flux parameterization encapsulating wave state, *Atmos. Chem. Phys.*, 14, 1837-1852, 10.5194/acp-14-1837-2014, 2014b.
- Ovadnevaite, J., Zuend, A., Laaksonen, A., Sanchez, K. J., Roberts, G., Ceburnis, D., Decesari, S., Rinaldi, M., Hodas, N., Facchini, M. C., Seinfeld, J. H., and O'Dowd, C.: Surface tension prevails over solute effect in organic-influenced cloud droplet activation, *Nature*, 546, 637-641, 10.1038/nature22806 <http://www.nature.com/nature/journal/v546/n7660/abs/nature22806.html#supplementary-information>, 2017.
- Peng, C., and Chan, C. K.: The water cycles of water-soluble organic salts of atmospheric importance, *Atmos. Environ.*, 35, 1183-1192, [https://doi.org/10.1016/S1352-2310\(00\)00426-X](https://doi.org/10.1016/S1352-2310(00)00426-X), 2001.
- Petelski, T., and Piskozub, J.: Vertical coarse aerosol fluxes in the atmospheric surface layer over the North Polar Waters of the Atlantic, *Journal of Geophysical Research: Oceans*, 111, 10.1029/2005JC003295, 2006.
- Petters, M. D., Prenni, A. J., Kreidenweis, S. M., DeMott, P. J., Matsunaga, A., Lim, Y. B., and Ziemann, P. J.: Chemical aging and the hydrophobic-to-hydrophilic conversion of carbonaceous aerosol, *Geophysical Research Letters*, 33, 10.1029/2006GL027249, 2006.
- Petters, M. D., and Kreidenweis, S. M.: A single parameter representation of hygroscopic growth and cloud condensation nucleus activity, *Atmospheric Chemistry and Physics*, 7, 1961-1971, 2007.
- Petters, M. D., Prenni, A. J., Kreidenweis, S. M., and DeMott, P. J.: On Measuring the Critical Diameter of Cloud Condensation Nuclei Using Mobility Selected Aerosol, *Aerosol Science and Technology*, 41, 907-913, 10.1080/02786820701557214, 2007.
- Petzold, A., and Schönlinner, M.: Multi-angle absorption photometry—a new method for the measurement of aerosol light absorption and atmospheric black carbon, *J. Aerosol Sci.*, 35, 421-441, <https://doi.org/10.1016/j.jaerosci.2003.09.005>, 2004.

References

- Pierce, J. R., and Adams, P. J.: Global evaluation of CCN formation by direct emission of sea salt and growth of ultrafine sea salt, *Journal of Geophysical Research: Atmospheres*, 111, 10.1029/2005JD006186, 2006.
- Pitzer, K. S.: *Activity Coefficients in Electrolyte Solutions*, CRC Press, Taylor & Francis Group, Boca Raton, FL, 1991.
- Prather, K. A., Bertram, T. H., Grassian, V. H., Deane, G. B., Stokes, M. D., DeMott, P. J., Aluwihare, L. I., Palenik, B. P., Azam, F., Seinfeld, J. H., Moffet, R. C., Molina, M. J., Cappa, C. D., Geiger, F. M., Roberts, G. C., Russell, L. M., Ault, A. P., Baltrusaitis, J., Collins, D. B., Corrigan, C. E., Cuadra-Rodriguez, L. A., Ebben, C. J., Forestieri, S. D., Guasco, T. L., Hersey, S. P., Kim, M. J., Lambert, W. F., Modini, R. L., Mui, W., Pedler, B. E., Ruppel, M. J., Ryder, O. S., Schoepp, N. G., Sullivan, R. C., and Zhao, D.: Bringing the ocean into the laboratory to probe the chemical complexity of sea spray aerosol, *Proceedings of the National Academy of Sciences of the United States of America*, 110, 7550-7555, 10.1073/pnas.1300262110, 2013.
- Preißler, J., Martucci, G., Saponaro, G., Ovadnevaite, J., Vaishya, A., Kolmonen, P., Ceburnis, D., Sogacheva, L., Leeuw, G., and O'Dowd, C.: Six years of surface remote sensing of stratiform warm clouds in marine and continental air over Mace Head, Ireland, *Journal of Geophysical Research: Atmospheres*, 121, 14,538-514,557, 10.1002/2016JD025360, 2016.
- Pruppacher, H. R., and Klett, J. D.: *Microphysics of Clouds and Precipitation*, in, 1978.
- Pruppacher, H. R. K., James D.: *Microphysics of Clouds and Precipitation*, Kluwer Academic Publishers, Dordrecht, The Netherlands, 714 pp., 1997.
- Quinn, P. K., Coffman, D. J., Kapustin, V. N., Bates, T. S., and Covert, D. S.: Aerosol optical properties in the marine boundary layer during the First Aerosol Characterization Experiment (ACE 1) and the underlying chemical and physical aerosol properties, *Journal of Geophysical Research: Atmospheres*, 103, 16547-16563, 10.1029/97JD02345, 1998.
- Quinn, P. K., Bates, T. S., Miller, T. L., Coffman, D. J., Johnson, J. E., Harris, J. M., Ogren, J. A., Forbes, G., Anderson, T. L., Covert, D. S., and Rood, M. J.: Surface submicron aerosol chemical composition: What fraction is not sulfate?, *Journal of Geophysical Research: Atmospheres*, 105, 6785-6805, 10.1029/1999JD901034, 2000.
- Quinn, P. K., Bates, T. S., Schulz, K. S., Coffman, D. J., Frossard, A. A., Russell, L. M., Keene, W. C., and Kieber, D. J.: Contribution of sea surface carbon pool to organic matter enrichment in sea spray aerosol, *Nature Geosci*, 7, 228-232, 10.1038/ngeo2092
<http://www.nature.com/ngeo/journal/v7/n3/abs/ngeo2092.html#supplementary-information>, 2014.
- Quinn, P. K., Coffman, D. J., Johnson, J. E., Upchurch, L. M., and Bates, T. S.: Small fraction of marine cloud condensation nuclei made up of sea spray aerosol, *Nature Geosci*, 10, 674-679, 10.1038/ngeo3003
<http://www.nature.com/ngeo/journal/v10/n9/abs/ngeo3003.html#supplementary-information>, 2017.
- Raatikainen, T., Brus, D., Hyvärinen, A. P., Svensson, J., Asmi, E., and Lihavainen, H.: Black carbon concentrations and mixing state in the Finnish Arctic, *Atmos. Chem. Phys.*, 15, 10057-10070, 10.5194/acp-15-10057-2015, 2015.

References

- Ramanathan, V., Chung, C., Kim, D., Bettge, T., Buja, L., Kiehl, J. T., Washington, W. M., Fu, Q., Sikka, D. R., and Wild, M.: Atmospheric Brown Clouds: Impacts on South Asian Climate and Hydrological Cycle, *Proceedings of the National Academy of Sciences of the United States of America*, 102, 5326-5333, 10.2307/3375048, 2005.
- Ramanathan, V., and Carmichael, G.: Global and regional climate changes due to black carbon, *Nature Geoscience*, 1, 221, 10.1038/ngeo156, 2008.
- Reid, J. S., Jonsson, H. H., Smith, M. H., and Smirnov, A.: Evolution of the vertical profile and flux of large sea-salt particles in a coastal zone, *Journal of Geophysical Research: Atmospheres*, 106, 12039-12053, 10.1029/2000JD900848, 2001.
- Riipinen, I., Rastak, N., and Pandis, S. N.: Connecting the solubility and CCN activation of complex organic aerosols: a theoretical study using solubility distributions, *Atmos. Chem. Phys.*, 15, 6305-6322, 10.5194/acp-15-6305-2015, 2015.
- Rinaldi, M., Facchini, M. C., Decesari, S., Carbone, C., Finessi, E., Mircea, M., Fuzzi, S., Ceburnis, D., Ehn, M., Kulmala, M., de Leeuw, G., and O'Dowd, C. D.: On the representativeness of coastal aerosol studies to open ocean studies: Mace Head – a case study, *Atmos. Chem. Phys.*, 9, 9635-9646, 10.5194/acp-9-9635-2009, 2009.
- Rinaldi, M., Decesari, S., Finessi, E., Giulianelli, L., Carbone, C., Fuzzi, S., #39, Dowd, C. D., Ceburnis, D., and Facchini, M. C.: Primary and Secondary Organic Marine Aerosol and Oceanic Biological Activity: Recent Results and New Perspectives for Future Studies, *Advances in Meteorology*, 2010, 10.1155/2010/310682, 2010.
- Rinaldi, M., Fuzzi, S., Decesari, S., Marullo, S., Santoleri, R., Provenzale, A., von Hardenberg, J., Ceburnis, D., Vaishya, A., O'Dowd, C. D., and Facchini, M. C.: Is chlorophyll-a the best surrogate for organic matter enrichment in submicron primary marine aerosol?, *Journal of Geophysical Research: Atmospheres*, 118, 4964-4973, 10.1002/jgrd.50417, 2013.
- Roberts, G., Mauger, G., Hadley, O., and Ramanathan, V.: North American and Asian aerosols over the eastern Pacific Ocean and their role in regulating cloud condensation nuclei, *Journal of Geophysical Research: Atmospheres*, 111, doi:10.1029/2005JD006661, 2006.
- Roberts, G. C., and Nenes, A.: A Continuous-Flow Streamwise Thermal-Gradient CCN Chamber for Atmospheric Measurements, *Aerosol Science & Technology*, 39, 206-221, 2005.
- Real-time Environmental Applications and Display sYstem (READY) Website <http://www.ready.noaa.gov/index.php>, 2016.
- Rose, D., Gunthe, S. S., Mikhailov, E., Frank, G. P., Dusek, U., Andreae, M. O., and Pöschl, U.: Calibration and measurement uncertainties of a continuous-flow cloud condensation nuclei counter (DMT-CCNC): CCN activation of ammonium sulfate and sodium chloride aerosol particles in theory and experiment, *Atmospheric Chemistry and Physics*, 8, 1153-1179, 2008.
- Rothenberg, D., and Wang, C.: Metamodeling of Droplet Activation for Global Climate Models, *Journal of the Atmospheric Sciences*, 73, 1255-1272, 10.1175/JAS-D-15-0223.1, 2015.
- Salter, M. E., Nilsson, E. D., Butcher, A., and Bilde, M.: On the seawater temperature dependence of the sea spray aerosol generated by a continuous plunging jet,

References

- Journal of Geophysical Research: Atmospheres, 119, 9052-9072, 10.1002/2013JD021376, 2014.
- Salter, M. E., Zieger, P., Acosta Navarro, J. C., Grythe, H., Kirkevåg, A., Rosati, B., Riipinen, I., and Nilsson, E. D.: An empirically derived inorganic sea spray source function incorporating sea surface temperature, *Atmos. Chem. Phys.*, 15, 11047-11066, 10.5194/acp-15-11047-2015, 2015.
- Sanchez, K. J., Roberts, G. C., Calmer, R., Nicoll, K., Hashimshoni, E., Rosenfeld, D., Ovadnevaite, J., Preissler, J., Ceburnis, D., O'Dowd, C., and Russell, L. M.: Top-down and bottom-up aerosol–cloud closure: towards understanding sources of uncertainty in deriving cloud shortwave radiative flux, *Atmos. Chem. Phys.*, 17, 9797-9814, 10.5194/acp-17-9797-2017, 2017.
- Sanchez, K. J., Chen, C.-L., Russell, L. M., Betha, R., Liu, J., Price, D. J., Massoli, P., Ziemba, L. D., Crosbie, E. C., Moore, R. H., Müller, M., Schiller, S. A., Wisthaler, A., Lee, A. K. Y., Quinn, P. K., Bates, T. S., Porter, J., Bell, T. G., Saltzman, E. S., Vaillancourt, R. D., and Behrenfeld, M. J.: Substantial Seasonal Contribution of Observed Biogenic Sulfate Particles to Cloud Condensation Nuclei, *Scientific Reports*, 8, 3235, 10.1038/s41598-018-21590-9, 2018.
- Schiebel, T.: Ice Nucleation Activity of Soil Dust Aerosols, Karlsruhe Institut für Technologie (KIT), 2017.
- Schwier, A. N., Rose, C., Asmi, E., Ebling, A. M., Landing, W. M., Marro, S., Pedrotti, M. L., Sallon, A., Iuculano, F., Agustí, S., Tsiola, A., Pitta, P., Louis, J., Guieu, C., Gazeau, F., and Sellegri, K.: Primary marine aerosol emissions from the Mediterranean Sea during pre-bloom and oligotrophic conditions: correlations to seawater chlorophyll *a* from a mesocosm study, *Atmos. Chem. Phys.*, 15, 7961-7976, 10.5194/acp-15-7961-2015, 2015.
- Schwier, A. N., Sellegri, K., Mas, S., Charrière, B., Pey, J., Rose, C., Temime-Roussel, B., Jaffrezo, J. L., Parin, D., Picard, D., Ribeiro, M., Roberts, G., Sempéré, R., Marchand, N., and D'Anna, B.: Primary marine aerosol physical flux and chemical composition during a nutrient enrichment experiment in mesocosms in the Mediterranean Sea, *Atmos. Chem. Phys.*, 17, 14645-14660, 10.5194/acp-17-14645-2017, 2017.
- Seinfeld, J.: Atmospheric science: Black carbon and brown clouds, *Nature Geosci*, 1, 15-16, 2008.
- Seinfeld, J. H., and Pandis, S. N.: *Atmospheric Chemistry and Physics from air pollution to climate change*, John Wiley and Sons, Incorporated, New York, 1998.
- Sellegri, K., O'Dowd, C. D., Yoon, Y. J., Jennings, S. G., and de Leeuw, G.: Surfactants and submicron sea spray generation, *Journal of Geophysical Research: Atmospheres*, 111, n/a-n/a, 10.1029/2005JD006658, 2006.
- Sellegri, K., Pey, J., Rose, C., Culot, A., DeWitt, H. L., Mas, S., Schwier, A. N., Temime-Roussel, B., Charriere, B., Saiz-Lopez, A., Mahajan, A. S., Parin, D., Kukui, A., Sempere, R., D'Anna, B., and Marchand, N.: Evidence of atmospheric nanoparticle formation from emissions of marine microorganisms, *Geophysical Research Letters*, 43, 6596-6603, 10.1002/2016GL069389, 2016.
- Shank, L. M., Howell, S., Clarke, A. D., Freitag, S., Brekhovskikh, V., Kapustin, V., McNaughton, C., Campos, T., and Wood, R.: Organic matter and non-refractory aerosol over the remote Southeast Pacific: oceanic and combustion sources, *Atmos. Chem. Phys.*, 12, 557-576, 10.5194/acp-12-557-2012, 2012.

References

- Slingo, A.: Sensitivity of the Earth's radiation budget to changes in low clouds, *Nature*, 343, 49, 10.1038/343049a0, 1990.
- Slowik, J. G., Cross, E. S., Han, J.-H., Davidovits, P., Onasch, T. B., Jayne, J. T., Williams, L. R., Canagaratna, M. R., Worsnop, D. R., Chakrabarty, R. K., Moosmüller, H., Arnott, W. P., Schwarz, J. P., Gao, R.-S., Fahey, D. W., Kok, G. L., and Petzold, A.: An Inter-Comparison of Instruments Measuring Black Carbon Content of Soot Particles, *Aerosol Science and Technology*, 41, 295-314, 10.1080/02786820701197078, 2007.
- Smith, M. H., Park, P. M., and Consterdine, I. E.: Marine aerosol concentrations and estimated fluxes over the sea, *Quarterly Journal of the Royal Meteorological Society*, 119, 809-824, 10.1002/qj.49711951211, 1993.
- Smith, R. L., and Konferenzen, D.: *The Physical Processes of Coastal Ocean Upwelling Systems*, *Upwelling in the Ocean: modern processes and ancient records*, Berlin, 1995.
- Snider, J. R., Guibert, S., Brenguier, J.-L., and Putaud, J.-P.: Aerosol activation in marine stratocumulus clouds: 2. Köhler and parcel theory closure studies, *Journal of Geophysical Research: Atmospheres*, 108, doi:10.1029/2002JD002692, 2003.
- Snider, J. R., Leon, D., and Wang, Z.: Droplet Concentration and Spectral Broadening in Southeast Pacific Stratocumulus Clouds, *Journal of the Atmospheric Sciences*, 74, 719-749, 10.1175/jas-d-16-0043.1, 2017.
- Sorooshian, A., Prabhakar, G., Jonsson, H., Woods, R. K., Flagan, R. C., and Seinfeld, J. H.: On the presence of giant particles downwind of ships in the marine boundary layer, *Geophysical Research Letters*, 42, 2024-2030, 10.1002/2015GL063179, 2015.
- Stein, A. F., Draxler, R. R., Rolph, G. D., Stunder, B. J. B., Cohen, M. D., and Ngan, F.: NOAA's HYSPLIT Atmospheric Transport and Dispersion Modeling System, *Bulletin of the American Meteorological Society*, 96, 2059-2077, 10.1175/bams-d-14-00110.1, 2015.
- Stephens, M., Turner, N., and Sandberg, J.: Particle identification by laser-induced incandescence in a solid-state laser cavity, *Appl. Opt.*, 42, 3726-3736, 10.1364/AO.42.003726, 2003.
- Stocker, T. F., D. Qin, G.-K. Plattner, M. Tignor, S.K. Allen, J. Boschung, A. Nauels, Y. Xia, V. Bex and P.M. Midgley (eds.): IPCC, 2013: *Climate Change 2013: The Physical Science Basis.*, Cambridge, United Kingdom and New York, NY, USA, 2013.
- Sun, J., Ariya, P. A., Leighton, H. G., and Yau, M. K.: Mystery of ice multiplication in warm-based precipitating shallow cumulus clouds, *Geophysical Research Letters*, 37, L10802, 10.1029/2010GL042440, 2010.
- Sun, Z., and Shine, K. P.: Studies of the radiative properties of ice and mixed-phase clouds, *Quarterly Journal of the Royal Meteorological Society*, 120, 111-137, 10.1002/qj.49712051508, 1994.
- Suski, K. J., Bell, D. M., Hiranuma, N., Möhler, O., Imre, D., and Zelenyuk, A.: Activation of Intact Bacteria and Bacterial Fragments Mixed with Agar as Cloud Droplets and Ice Crystals in Cloud Chamber Experiments, *Atmos. Chem. Phys. Discuss.*, 2018, 1-30, 10.5194/acp-2018-594, 2018.

References

- Svenningsson, B., Rissler, J., Swietlicki, E., Mircea, M., Bilde, M., Facchini, M. C., Decesari, S., Fuzzi, S., Zhou, J., Mønster, J., and Rosenørn, T.: Hygroscopic growth and critical supersaturations for mixed aerosol particles of inorganic and organic compounds of atmospheric relevance, *Atmos. Chem. Phys.*, 6, 1937-1952, 10.5194/acp-6-1937-2006, 2006.
- Sweeney, J. C.: The Changing Synoptic Origins of Irish Precipitation, *Transactions of the Institute of British Geographers*, 10, 467-480, 10.2307/621892, 1985.
- Tamaki, K., Ohara, Y., Inabe, M., Mori, T., and Numata, F.: The Physicochemical Properties of Aqueous Solutions of Sodium Alkanesulfonates. Apparent Molar Volumes, Viscosity B Coefficients, Heats of Solution, and Surface Tensions, *Bull. Chem. Soc. Jpn.*, 56, 1930-1934, 10.1246/bcsj.56.1930, 1983.
- Tang, I. N., and Munkelwitz, H. R.: Water activities, densities, and refractive indices of aqueous sulfates and sodium nitrate droplets of atmospheric importance, *Journal of Geophysical Research: Atmospheres*, 99, 18801-18808, 10.1029/94JD01345, 1994.
- Teng, T. T., and Lenzi, F.: Methanesulfonic and Trichloroacetic Acids: Densities of Aqueous Solutions at 20, 25, and 35 °C, *J. Chem. Eng. Data*, 20, 432-434, 10.1021/je60067a700, 1975.
- TSI: Fundamentals of Condensation Particle Counters (CPC) and Scanning Mobility Particle Sizer™ (SMPS™) Spectrometers; Application note CPC-003 (US), in, <http://www.tsi.com/>, 2014.
- Twomey, S.: The nuclei of natural cloud formation part II: The supersaturation in natural clouds and the variation of cloud droplet concentration, *Geofisica pura e applicata*, 43, 243-249, 10.1007/BF01993560, 1959.
- Twomey, S., and Wojciechowski, T. A.: Observations of geographical variation of cloud nuclei, *Journal of the Atmospheric Sciences*, 26, 684-688, 1969.
- Twomey, S.: Pollution and the planetary albedo, *Atmospheric Environment (1967)*, 8, 1251-1256, [http://dx.doi.org/10.1016/0004-6981\(74\)90004-3](http://dx.doi.org/10.1016/0004-6981(74)90004-3), 1974.
- Tyree, C. A., Hellion, V. M., Alexandrova, O. A., and Allen, J. O.: Foam droplets generated from natural and artificial seawaters, *Journal of Geophysical Research: Atmospheres*, 112, 10.1029/2006JD007729, 2007.
- Vaishya, A., Jennings, S. G., and O'Dowd, C.: Wind-driven influences on aerosol light scattering in north-east Atlantic air, *Geophysical Research Letters*, 39, doi:10.1029/2011GL050556, 2012.
- Vallina, S. M., and Simó, R.: Strong Relationship Between DMS and the Solar Radiation Dose over the Global Surface Ocean, *Science*, 315, 506-508, 10.1126/science.1133680, 2007.
- Vargaftik, N. B., Volkov, B. N., and Voljak, L. D.: International Tables of the Surface Tension of Water, *Journal of Physical and Chemical Reference Data*, 12, 817-820, 10.1063/1.555688, 1983.
- Wagner, R., Kaufmann, J., Möhler, O., Saathoff, H., Schnaiter, M., Ullrich, R., and Leisner, T.: Heterogeneous Ice Nucleation Ability of NaCl and Sea Salt Aerosol Particles at Cirrus Temperatures, *Journal of Geophysical Research: Atmospheres*, 123, 2841-2860, 10.1002/2017JD027864, 2018.
- Wang, Z., Cheng, Y., Ma, N., Mikhailov, E., Pöschl, U., and Su, H.: Dependence of the hygroscopicity parameter κ on particle size, humidity and solute concentration:

References

- implications for laboratory experiments, field measurements and model studies, *Atmos. Chem. Phys. Discuss.*, 2017, 1-33, 10.5194/acp-2017-253, 2017.
- WaveMetrics: The Igor Pro Manual, in, edited by: Inc., W., Lake Oswego, OR, USA, 2015.
- Weller, R., Minikin, A., Petzold, A., Wagenbach, D., and König-Langlo, G.: Characterization of long-term and seasonal variations of black carbon (BC) concentrations at Neumayer, Antarctica, *Atmos. Chem. Phys.*, 13, 1579-1590, 10.5194/acp-13-1579-2013, 2013.
- Wexler, A., S., and Clegg, S., L.: Atmospheric aerosol models for systems including the ions H⁺, NH₄⁺, Na⁺, SO₄²⁻, NO₃⁻, Cl⁻, Br⁻, and H₂O, *Journal of Geophysical Research: Atmospheres*, 107, ACH 14-11-ACH 14-14, 10.1029/2001JD000451, 2002.
- Wiedensohler, A.: An approximation of the bipolar charge distribution for particles in the submicron size range, *J. Aerosol Sci.*, 19, 387-389, [https://doi.org/10.1016/0021-8502\(88\)90278-9](https://doi.org/10.1016/0021-8502(88)90278-9), 1988.
- Wilson, T. W., Ladino, L. A., Alpert, P. A., Breckels, M. N., Brooks, I. M., Browse, J., Burrows, S. M., Carslaw, K. S., Huffman, J. A., Judd, C., Kalthau, W. P., Mason, R. H., McFiggans, G., Miller, L. A., Najera, J. J., Polishchuk, E., Rae, S., Schiller, C. L., Si, M., Temprado, J. V., Whale, T. F., Wong, J. P. S., Wurl, O., Yakobi-Hancock, J. D., Abbatt, J. P. D., Aller, J. Y., Bertram, A. K., Knopf, D. A., and Murray, B. J.: A marine biogenic source of atmospheric ice-nucleating particles, *Nature*, 525, 234-238, 10.1038/nature14986, 2015.
- Wise, M. E., Baustian, K. J., Koop, T., Freedman, M. A., Jensen, E. J., and Tolbert, M. A.: Depositional ice nucleation onto crystalline hydrated NaCl particles: a new mechanism for ice formation in the troposphere, *Atmos. Chem. Phys.*, 12, 1121-1134, 10.5194/acp-12-1121-2012, 2012.
- Wolff, E. W., and Cachier, H.: Concentrations and seasonal cycle of black carbon in aerosol at a coastal Antarctic station, *Journal of Geophysical Research: Atmospheres*, 103, 11033-11041, doi:10.1029/97JD01363, 1998.
- Woodcock, A. H., Kientzler, C. F., Arons, A. B., and Blanchard, D. C.: Giant Condensation Nuclei from Bursting Bubbles, *Nature*, 172, 1144-1145, 1953.
- Woolf, D. K.: Bubbles and their role in gas exchange, in: *The Sea Surface and Global Change*, edited by: Liss, P. S., and Duce, R. A., Cambridge University Press, Cambridge, 173-206, 1997.
- Woolf, D. K.: Bubbles, in: *Encyclopedia of Ocean Sciences (Second Edition)*, Elsevier B.V., 2001.
- Zábori, J., Matisāns, M., Krejci, R., Nilsson, E. D., and Ström, J.: Artificial primary marine aerosol production: a laboratory study with varying water temperature, salinity, and succinic acid concentration, *Atmos. Chem. Phys.*, 12, 10709-10724, 10.5194/acp-12-10709-2012, 2012.
- Zemmelink, H. J., Houghton, L., Dacey, J. W. H., Worby, A. P., and Liss, P. S.: Emission of dimethylsulfide from Weddell Sea leads, *Geophysical Research Letters*, 32, 10.1029/2005GL024242, 2005.
- Zemmelink, H. J., Dacey, J. W. H., Houghton, L., Hints, E. J., and Liss, P. S.: Dimethylsulfide emissions over the multi-year ice of the western Weddell Sea, *Geophysical Research Letters*, 35, 10.1029/2007GL031847, 2008.

References

- Zeng, X., Tao, W.-K., Zhang, M., Hou, A. Y., Xie, S., Lang, S., Li, X., Starr, D. O. C., Li, X., and Simpson, J.: An Indirect Effect of Ice Nuclei on Atmospheric Radiation, *Journal of the Atmospheric Sciences*, 66, 41-61, 10.1175/2008jas2778.1, 2009.
- Zuend, A., Marcolli, C., Luo, B. P., and Peter, T.: A thermodynamic model of mixed organic-inorganic aerosols to predict activity coefficients, *Atmos. Chem. Phys.*, 8, 4559-4593, 10.5194/acp-8-4559-2008, 2008.
- Zuend, A., Marcolli, C., Booth, A. M., Lienhard, D. M., Soonsin, V., Krieger, U. K., Topping, D. O., McFiggans, G., Peter, T., and Seinfeld, J. H.: New and extended parameterization of the thermodynamic model AIOMFAC: calculation of activity coefficients for organic-inorganic mixtures containing carboxyl, hydroxyl, carbonyl, ether, ester, alkenyl, alkyl, and aromatic functional groups, *Atmos. Chem. Phys.*, 11, 9155-9206, 10.5194/acp-11-9155-2011, 2011.

Table of Abbreviations and Symbols

AOD	aerosol optical depth
<i>cAA</i>	<i>continental Antarctic</i>
<i>cP</i>	<i>continental Polar</i>
BC	(refractory) black carbon
CCN	cloud condensation nuclei
CCNC	cloud condensation nuclei counter
CDNC	cloud droplet number concentration
<i>D</i>	wet droplet diameter
<i>D_c</i>	critical diameter
<i>D_d</i>	dry diameter
<i>d_{ev}</i>	equivalent volume dry diameter
<i>d_m</i>	dry mobility diameter
<i>d_{va}</i>	vacuum aerodynamic diameter
DOC	dissolved organic carbon
DON _{mol}	(molar) degree of neutralisation
DMS	dimethyl sulphide , (CH ₃) ₂ S
DMSP	dimethylsulfoniopropionate , (CH ₃) ₂ S ⁺ CH ₂ CH ₂ COO ⁻
FT	free troposphere
GF, <i>gf</i>	growth factor
INP	ice nucleating particles
MBL	marine boundary layer
MHD	Mace Head Atmospheric Research Station
<i>mA</i>	<i>maritime Arctic</i>
<i>mP</i>	<i>maritime Polar</i>
MSA	methanesulphonic acid , CH ₃ SO ₃ H
<i>mT</i>	<i>maritime Tropical</i>
M_w	molecular weight of pure water = 18.015 g mol ⁻¹
<i>N_{CN}</i>	total aerosol concentration
<i>N_{CCN}</i>	CCN concentration
<i>N_{CCN}/N_{CN}</i>	activated fraction of particles at a relative supersaturation
NPF	new particle formation

Table of Abbreviations and Symbols

n_x	molar amounts of species x
OM	organic matter
OM _{ss}	organic matter mass-fraction enrichment in sea spray
P	vapour pressure
POM, POC	particulate organic matter, carbon
PMA	primary marine aerosol
P_s	equilibrium partial pressure of a flat surface
P^0	saturated vapour pressure
Q_a	sample flow
Q_{sh}	sheath flow
r	radius (of the droplet)
R	ideal gas constant
s, s_c	saturation ratio, critical saturation ratio
S, S_c, S_{peak}	supersaturation, critical supersaturation, cloud peak supersaturation (%)
SMA	secondary marine aerosol
SSA	sea spray aerosol
T	temperature
V_m	molar volume
w	updraft velocity (m s^{-1})
WD	wind direction
WIOM, WIOC	water insoluble organic matter, carbon
WSOM, WSOC	water soluble organic matter, carbon
κ	hygroscopicity parameter
ρ_{ss}	density of sea-salt = 2.165 g cm^{-3}
ρ_w	density of pure water = 1.0 g cm^{-3}
σ	surface tension
σ_g	geometric spread of lognormal mode
X	shape correction factor
X_{AMS}	HR-ToF AMS associated shape factor = 0.8

List of Figures

FIGURE 2.1. THE GENERAL BREAKDOWN OF AEROSOL PARTICLE TYPE BY SIZE RANGES AND NOMENCLATURE. THIS GRAPH IS ADAPTED FROM A SIMILAR GRAPH IN HINDS (1982).	4
FIGURE 2.2. MODELLED WIND DISPERSAL OF VAST QUANTITIES OF DUST (RED), SEA-SALT (BLUE), SULPHATE (WHITE) AND BLACK AND ORGANIC CARBON (GREEN) AROUND THE WORLD. REPRODUCED FROM NASA (HTTP://GALLAGHER-PHOTO.COM/2013/09/12/A-PORTRAIT-GLOBAL-AEROSOLS-NASA/).....	6
FIGURE 2.3. RADIATIVE FORCING BREAKDOWN OF THE EARTH (IN 2011 RELATIVE TO 1750) REPRODUCED FROM STOCKER (2013). BEST ESTIMATES ARE SHOWN IN BLACK DIAMONDS WITH UNCERTAINTY INTERVALS AND LEVEL OF CONFIDENCE ON THE RIGHT (VH-VERY HIGH, H-HIGH, M-MEDIUM, L-LOW, AND VL-VERY LOW).....	9
FIGURE 2.4. CCN (A) AND INP (B) REPRESENTATIONS OF ACTIVATION EFFICIENCY BY CHEMICAL COMPOSITION. GRAPH A) IS REPRODUCED FROM PETERS AND KREIDENWEIS (2007) AND SHOWS S_c-D_b DATA FOR PURE COMPOUNDS, ORGANIC MIXTURES AND ORGANIC-INORGANIC MIXTURES. DATA FOR (A) ARE TAKEN FROM SVENNINGSSON ET AL. (2006), DINAR ET AL. (2006), AND PETERS ET AL. (2006). THE 3:7 ORGANIC:INORGANIC MIXTURE IS THE "POLLUTED" MIXTURE FROM SVENNINGSSON ET AL. (2006). DASHED LINES INDICATE BEST-FIT K VALUES FOR EACH PARTICLE TYPE, AS SHOWN IN THE LEGEND. SHADED AREA INDICATES REPORTED RANGE OF VALUES FOR AMMONIUM SULPHATE (TABLE 1 IN PETERS AND KREIDENWEIS (2007)). KAPPA VALUES WERE COMPUTED FOR $\Sigma_{s/A}=0.072 \text{ JM}^{-2}$ AND $T=298.15 \text{ K}$. GRAPH B) IS REPRODUCED FROM ATKINSON AND WHALE (2013) SHOWING THE NUCLEATION SITE DENSITY FOR K-FELDSPAR AND NATURAL DUSTS. DATA FOR (B) IS FROM PICOLITRE EXPERIMENTS EXTENDED TO HIGHER TEMPERATURES BY USE OF MICROLITRE-SIZED DROPLETS, WITH A FIT PROVIDED ($\ln(NS)=-1.038T+275.26$, VALID BETWEEN 248 AND 268 K). EXPERIMENTAL K-FELDSPAR CONCENTRATIONS IN WEIGHT PERCENT ARE PROVIDED IN THE KEY. TEMPERATURE UNCERTAINTIES FOR MICROLITRE EXPERIMENTS (NOT SHOWN) WERE ESTIMATED AT $\pm 0.4\text{K}$ AND UNCERTAINTY IN NS (NOT SHOWN) IS ESTIMATED AT $\pm 25\%$. SEVERAL NATURAL DUST SAMPLES (N12 AND C09) ARE COMPARED. THE MINERALOGICAL COMPOSITIONS OF THE DUSTS USED IN THOSE SAMPLES ARE UNKNOWN, BUT FELDSPAR MASS CONTENT IN NATURAL SOILS TYPICALLY VARIES BETWEEN 1% AND 25%. HENCE, NS VALUES ARE SCALED ASSUMING K-FELDSPAR IS PRESENT AT BETWEEN 1% AND 25% OF THE NATURAL DUST PARTICLES' SURFACE.	12
FIGURE 2.5. HOPPEL THEORY OVERVIEW OF THE FORMATION OF A BIMODAL SIZE-DISTRIBUTION FROM AN INITIAL DISTRIBUTION AFTER BEING EXPOSED TO NON-PRECIPITATING CLOUD(S) (BOTH FULL DISTRIBUTIONS ARE SHOWN IN BLACK AS A FUNCTION OF MOBILITY DIAMETER IN LOG-SCALE).	13
FIGURE 2.6. REPRODUCED FROM OVADNEVAITE ET AL. (2014B), THE GRAPH SHOWS A COMPARISON OF THE SEA SPRAY AEROSOL SOURCE FUNCTION DERIVED IN OVADNEVAITE ET AL. (2014B) (OSSA-SSSF) WITH OTHER SSSF (MÅRTENSSON ET AL., 2003; LEWIS AND SCHWARTZ, 2004; CLARKE ET AL., 2006; MONAHAN ET AL., 1986; SMITH ET AL., 1993; NILSSON ET AL., 2001; GONG, 2003; LEEUW ET AL., 2000; REID ET AL., 2001; GEEVER ET AL., 2005; TYREE ET AL., 2007; NORRIS ET AL., 2008; NORRIS ET AL., 2012; PETELSKI AND PISKOZUB, 2006; KEENE ET AL., 2007), EVALUATED FOR WIND SPEED $U_{10} = 8 \text{ M s}^{-1}$ (OR $U_{22} = 8 \text{ M s}^{-1}$ FOR GEEVER ET AL. (2005)).	17
FIGURE 2.7. CHEMICAL SIZE BREAKDOWN AND CHLOROPHYLL-A MAPS IN WINTER (A) AND SUMMER (B), REPRODUCED FROM O'DOWD ET AL. (2004). ORGANIC MATTER AT THE SEA-SURFACE. SEAWIFS-DERIVED SEASONAL AVERAGE (5-YEAR) SEA-SURFACE CHLOROPHYLL CONCENTRATIONS IN WINTER (A) AND SPRING (B), ILLUSTRATING LOW BIOLOGICAL ACTIVITY IN NORTH ATLANTIC WATERS DURING WINTER AND HIGH ACTIVITY IN SPRING (COURTESY OF SEAWIFS PROJECT, NASA/GODDARD SPACE FLIGHT CENTER AND ORBIMAGE). THE LOCATION OF MACE HEAD IS SHOWN IN A. MARINE AIR MASSES ARRIVE AT MACE HEAD AFTER AT LEAST 96 H TRANSIT OVER THE OCEAN FROM THE ARCTIC AND NORTHWEST ATLANTIC. CHEMICAL COMPOSITION OF MARINE AEROSOLS. SHOWN ARE AVERAGE SIZE-SEGREGATED CHEMICAL COMPOSITIONS AND ABSOLUTE MASS CONCENTRATIONS FOR NORTH ATLANTIC MARINE AEROSOLS SAMPLED WITH A BERNER IMPACTOR, FOR LOW BIOLOGICAL ACTIVITY (A) AND HIGH BIOLOGICAL ACTIVITY (B) PERIODS. THE CONCENTRATIONS OF WSOC, WIOC AND BC ARE REPORTED AS MASS OF ORGANIC MATTER (SEE CAVALLI ET AL. (2004) FOR A FULL DISCUSSION).	18
FIGURE 2.8. THIS GRAPH SHOWS EXTERNAL AND INTERNAL MIXTURE TYPES OF LAB GENERATED MARINE PARTICLES BY SIZE AND MASS FRACTION, REPRODUCED FROM PRATHER ET AL. (2013). (A) SIZE-RESOLVED CHEMICAL MIXING STATE	

List of Figures

FOR R1 (SEE PRATHER ET AL. (2013) FIG. 2). INTEGRATION OF TWO SINGLE PARTICLE ANALYSIS METHODS [TEM WITH ENERGY-DISPERSIVE X-RAY (EDX) ANALYSIS < 562 NM AND ATOFMS > 562 NM] SHOWS THE EXISTENCE OF FOUR MAJOR PARTICLE TYPES. (B) STXM CHEMICAL SPATIAL MAPS OF THE TWO MOST DOMINANT SUBMICROMETRE PARTICLE TYPES (TYPES 2 AND 4) HIGHLIGHT THE DIFFERENCES IN THE INORGANIC-TO-ORGANIC RATIOS (LEFT), ABUNDANCE OF CHLORIDE (CENTRE), AND CARBOXYLATES (RIGHT).	21
FIGURE 2.9. ICE CRYSTAL MORPHOLOGY AS A FUNCTION OF ICE SUPERSATURATION AND AMBIENT TEMPERATURE, REPRODUCED FROM THE UNIVERSITY OF MANCHESTER, CENTRE FOR ATMOSPHERIC SCIENCE, WEBSITE (EMERSIC).	27
FIGURE 3.1. SAMPLING LOCATIONS OVERLAID ON A PARTIAL WORLD MAP. THE PEGASO CRUISE PATH IS MARKED WITH THE RED LINE, AND MHD IS MARKED ON THE MAP WITH A PINK CIRCLE. BOTH SITES ARE SHOWN IN HIGHER RESOLUTION ON THE RIGHT SIDE OF THE GRAPH.	31
FIGURE 3.2. COUNTING EFFICIENCY CURVE OF 3772 TSI CPC, REPRODUCED FROM THE <i>FUNDAMENTALS OF CONDENSATION PARTICLE COUNTERS (CPC) AND SCANNING MOBILITY PARTICLE SIZER™ (SMPS™) SPECTROMETERS</i> LITERATURE PROVIDED BY TSI ON THEIR WEBSITE HTTP://WWW.TSI.COM/UPLOADEDFILES/_SITE_ROOT/PRODUCTS/LITERATURE/APPLICATION_NOTES/REVIEW_ON_CPC_AND_SMPS_CPC-003-US-WEB.PDF?ID=32305 (TSI, 2014).	33
FIGURE 3.3. SCHEMATIC OF AEROSOL FLOW THROUGH A DMA, REPRODUCED FROM THE <i>FUNDAMENTALS OF CONDENSATION PARTICLE COUNTERS (CPC) AND SCANNING MOBILITY PARTICLE SIZER™ (SMPS™) SPECTROMETERS</i> LITERATURE PROVIDED BY TSI ON THEIR WEBSITE HTTP://WWW.TSI.COM/UPLOADEDFILES/_SITE_ROOT/PRODUCTS/LITERATURE/APPLICATION_NOTES/REVIEW_ON_CPC_AND_SMPS_CPC-003-US-WEB.PDF?ID=32305 (TSI, 2014).	35
Figure 3.4. A diagram of airflow through the CCNC instrument adapted from Roberts and Nenes (2005) and the basic theory of column centreline supersaturation adapted from the DMT Inc. Cloud Condensation Nuclei (CCN) Counter Manual for Single-Column CCNs; DOC-0086 Revision I-2.....	38
FIGURE 3.5. CCNC CALIBRATION INSTRUMENT SET-UP.....	40
FIGURE 3.6. ACTIVATION CURVES FOR DIFFERENT CCN OPERATING CONDITIONS REPRODUCED FROM (ROBERTS AND NENES, 2005). AEROSOL AT A PARTICULAR DRY DIAMETER IS CONSIDERED ACTIVATED WHEN THE RATIO OF CCN (I.E., DROPLETS GREATER THAN 1 μM) TO TOTAL AEROSOL IS GREATER THAN 0.5. THE SHOULDERS RESULT FROM MULTIPLE CHARGE PARTICLES FROM THE DMA CLASSIFICATION.	40
FIGURE 3.7. TYPICAL CCNC INSTRUMENT COLUMN SUPERSATURATION DRIFT SHOWN AS CALIBRATION SLOPES FROM ONE CCNC INSTRUMENT AS A FUNCTION OF CRITICAL SUPERSATURATION (S_c) AND EQUIVALENT VOLUME DIAMETER (D_c (EQ)) DERIVED FROM D_M	43
FIGURE 4.1. OVERLAIN AIR MASS BACK TRAJECTORIES (AMBT) ON CRUISE REGION. EACH TRAJECTORY SHOWS THE RELATIVE AIR MASS PATH (WHITE-BLACK LINES) 72 HOURS PRIOR TO CROSSING THE SHIP'S PATH (RED) AT 100 M ABOVE SEA LEVEL (ASL). THE HEIGHT OF THE TRAJECTORY RELATIVE TO SEA LEVEL IS SHOWN IN GREYSCALE, AND FOR THE MOST PART REFLECTS THAT MOST OF THE TRAJECTORIES STAYED WELL BELOW 500 M ASL.	54
FIGURE 4.2. THE SHIP'S CRUISE PATH IS SHOWN ON A LATITUDE-LONGITUDE MAP, WITH CONTINENTAL BORDERS SHOWN IN GREEN. THE BC CONCENTRATION IS SHOWN IN A LINEAR GREYSCALE, WHERE WHITE REPRESENTS A BC MASS CONCENTRATION OF 0 NG M ⁻³ AND BLACK REPRESENTS +17 NG M ⁻³ . IT SHOULD BE NOTED THAT BC WAS SOMETIMES MEASURED IN EXCESS OF 1000 NG M ⁻³ , HOWEVER THE SCALE IS USED TO DEMONSTRATE THE FREQUENCY AND LOCATION FOR WHICH THE MEASUREMENTS WERE LESS THAN 1 NG M ⁻³ . THE RED DOTTED LINE INDICATES PARTS OF THE CRUISE IN WHICH NO AMBIENT DATA WAS AVAILABLE, OR FOR WHICH AMBIENT DATA WAS EXPOSED TO THE RESEARCH VESSEL'S OWN SHIP EXHAUST PLUMES AND DELETED FOR ANALYSIS.	55
FIGURE 4.3. FREQUENCY DISTRIBUTION PLOT OF AD DATASET FROM THE SP2 INSTRUMENT. NORMALISED FREQUENCY OF OCCURRENCE (%) ARE SHOWN AGAINST BC MASS CONCENTRATIONS FOR BINS EQUALLY SPACED IN LOGSPACE. FITTED LOGNORMAL MODES ARE SHOWN. TOP OF THE GRAPH SHOWS THE LOGNORMAL MODE POSITION WITH GEOMETRIC STANDARD DEVIATION (σ_g) UNDERNEATH.	57
FIGURE 4.4. COMPARISON BETWEEN THE OM (μG M ⁻³) CONCENTRATION AND OM:BC (NG M ⁻³ /NG M ⁻³) RATIOS OF SOUTHERN OCEAN (LEFT PANELS) WHICH WERE TAKEN AS CLEAN LEVELS FOR BC < 5 NG M ⁻³ (BLACK CIRCLES) AND PRISTINE FOR BC < 0.4 NG M ⁻³ (RED CIRCLES), AND MH FROM O'DOWD ET AL. (2014) REPRODUCED (RIGHT PANELS). SOUTHERN OCEAN DATA POINTS ARE SHOWN IN OPEN BLACK CIRCLES. CROSSES REPRESENT THE O'DOWD ET AL. (2014) DATA, WHERE THE RED CROSSES DENOTE BC < 15 NG M ⁻³ . THE MH DATA SHOWS EQUIVALENT BC	

List of Figures

(EBC) FROM AN MAAP, SO LIKELY BC CONCENTRATIONS ARE BIASED HIGH AS COMPARED WITH THE SOUTHERN OCEAN SP2 DATA.	60
FIGURE 4.5. AIR MASS BACK TRAJECTORIES SHOWN FOR APRIL 2–20 AT 12-HOUR INTERVALS (RED LINES). EACH TRAJECTORY IS PROJECTED 72 HOURS FROM 15 M ABOVE SEA LEVEL FROM MACE HEAD RESEARCH STATION (MHD). TOP RIGHT OF THE GRAPH SHOWS DETAILED OVERLAY OF THE MHD GEOGRAPHIC LOCATION RELATIVE TO OTHER IRISH CITIES.	61
FIGURE 4.6. PERCENTAGE OF TOTAL BC MASS LOADING (CONCENTRATION) BY WIND DIRECTION (0°–360°) FOR THE MONTH OF APRIL 2015 AT MACE HEAD ATMOSPHERIC RESEARCH STATION (MHD). TOTAL BLACK CARBON MASS CONCENTRATION MEASURED OVER THE ENTIRE MEASUREMENT PERIOD IS SHOWN AT THE BOTTOM. THE PERCENT OF THE TOTAL BC MASS LOADING MEASURED (RADIAL LINES IN %) BY EACH 10° WD INCREMENT IS SHOWN IN BLUE AS A FUNCTION OF WD. THE MHD “CLEAN SECTOR” IS CONSIDERED BETWEEN 190–300°, WHICH IS INDICATED IN THICKER BLACK LINES.	62
FIGURE 4.7. TIME SERIES OF MHD BC DATA AND WIND DIRECTION (WD) DATA FOR APRIL 2–20, 2015 DURING THE MHD CAMPAIGN. ON TOP, BC DATA FROM THE SP2 (BLACK—HOURLY AVERAGED, GREY—1-MINUTE RESOLUTION) AND MAAP (RED—HOURLY AVERAGED, PINK—1-MINUTE RESOLUTION) ARE SHOWN. THE GREEN LINE STRAIGHT ACROSS INDICATES 7 NG M ⁻³ . ON THE BOTTOM, WD DATA IS SHOWN IN DEGREES (°), WITH THE BLUE SHADED AREA DENOTING CLEAN SECTOR WD.	63
FIGURE 4.8. FREQUENCY DISTRIBUTION PLOT OF MHD BC MASS CONCENTRATION MEASUREMENTS FROM THE SP2 INSTRUMENT. THE GRAPH SHOWS BC MASS CONCENTRATIONS FOR BINS LOGNORMALLY SPACED (DLOGBC ≈ 0.06 NG M ⁻³ IN DEPTH). LOGNORMAL MODES ARE SHOWN SEPARATE FROM THE COMBINE FREQUENCY DISTRIBUTION WITH THE LOGNORMAL MODE POSITION AND GEOMETRIC STANDARD DEVIATION (Σ _g) SHOWN AT TOP.	65
FIGURE 4.9. COMPARISON BETWEEN THE FITTED FREQUENCY DISTRIBUTIONS OF THREE SETS OF BC DATA. THE DISTRIBUTION FOR ANTARCTICA IS REPRESENTED IN RED. THE MHD DATA IS REPRESENTED BY TWO DISTRIBUTIONS OF THE SP2 DATA, FILTERED FOR CLEAN WD (GREEN) AND UNFILTERED (BLACK). THE ACTUAL FREQUENCY DISTRIBUTION DATA WHICH WAS FITTED IS SHOWN IN LIGHTER SHADES OF THE AFOREMENTIONED COLOURS. FITTED DISTRIBUTIONS FOR ANTARCTICA AND MHD CLEAN WD DATA ARE SHOWN WITH PEAK MODES.	65
FIGURE 4.10. COMPARISON OF THE SP2 AND MAAP MEASUREMENTS RUNNING SIMULTANEOUSLY AT MACE HEAD FOR THE MONTH OF APRIL 2015. GREEN POINTS ARE FOR AVERAGED HOUR RESOLUTION DATA. A 1:1 FIT LINE IS SHOWN IN BACK DASHES. RED LINE IS A LEAST SQUARE FIT LINEAR REGRESSION FOR DATA ON THE RANGE OF MAAP BC CONCENTRATIONS OF 150–1371 NG M ⁻³ , WHERE THE BLACK LINE IS THE SAME BUT FOR CONCENTRATIONS BELOW 150 NG M ⁻³ , AND THE BLUE LINE FOR CONCENTRATIONS OF 0–30 NG M ⁻³ . COMPARISON IS NOT LINEAR OVER ALL CONCENTRATIONS, SO THIS IS USED TO DERIVE RELATIVE BC CONCENTRATION OVER DIFFERENT REGIMES. IF MAAP CONCENTRATION IS 15 NG M ⁻³ , THEN SP2 CONCENTRATION ~ 7 NG M ⁻³ , AND WHERE THE MAAP CONCENTRATION WOULD READ 50 NG M ⁻³ , THE SP2 WOULD READ ~ 34 NG M ⁻³	68
FIGURE 4.11. A) BLACK CARBON CONCENTRATIONS ARE SHOWN WITH STATISTICAL GROUPING BY BOX PLOT (LEFT AXIS) AND BY FREQUENCY OF OCCURRENCE (RIGHT AXIS) FOR WD CLEAN DATA. B) BLACK CARBON MASS CONCENTRATIONS ARE SHOWN WITH STATISTICAL GROUPING BY BOX PLOT (LEFT AXIS) AND THE PERCENT CONTRIBUTION TO TOTAL BC MASS MEASURED (RIGHT AXIS) FOR ALL MHD SP2 DATA. BOTH PLOTS ARE AS A FUNCTION OF BC SECTOR CLASSIFICATION (SEE TABLE 6.2) DEFINED IN GRIGAS ET AL. (2017) AND ADAPTED TO SP2 CONCENTRATIONS.	69
FIGURE 5.1. AEROSOL CHEMICAL AND PHYSICAL CHARACTERIZATION, EACH PRESENTED PERIOD LISTED IN CHRONOLOGICAL ORDER BY AIR MASS. EACH PERIOD HAS 5 COLUMNS, DESCRIPTOR, A, B, C, AND D. THE DESCRIPTOR LISTS PERIOD NUMBER FOLLOWED BY ANY AIR MASS MODIFICATION THEN THE STEADY-STATE DURATION OF THE PERIOD. [A] CHL-A SATELLITE DAILY RETRIEVALS WITH OVERLAID AIR MASS BACK-TRAJECTORIES EXTRACTED FROM HYSPLIT (ROLPH, 2016; STEIN ET AL., 2015). IN DOTTED RED, PEGASO CRUISE SHIP PATH. IN BLUE, 120 HR BACK TRAJECTORY ENDING 100M AGL DIRECTLY ABOVE THE SHIP LOCATION. THERE ARE THREE TRAJECTORIES, REPRESENTING THE AIR MASS ORIGIN AT THE START, MIDDLE, AND END OF THE PERIOD. CHL-A SATELLITE RETRIEVALS ARE AT 0.1° X 0.1° RESOLUTION, WHERE THE DARKEST GREEN REPRESENTS CLOSE TO 0 MG M ⁻³ , AND NEARLY WHITE REPRESENTS 3 MG M ⁻³ AVERAGE CHL-A IN THAT PIXEL. CHL-A SCALE ON THE TOP LEFT AND THE AVERAGE CHL-A CONCENTRATION DURING THE PERIOD UNDER THE TRAJECTORIES ON THE TOP RIGHT CORNER. [B] PARTICLE NUMBER (BLACK) AND VOLUME (BLUE) SIZE DISTRIBUTIONS: NUMBER DISTRIBUTION VARIANCE DURING THE PERIOD IS SHOWN IN GREY. ON TOP ARE THE TOTAL AVERAGE NUMBER OF PARTICLES [CM ⁻³] (N), AND TOTAL AVERAGE PARTICULATE VOLUME [μM ³ CM ⁻³] (V). [C] PIE CHART OF CHEMICAL MASS FRACTIONS (OM:	

List of Figures

- ORGANIC MATTER, SS: SEA-SALT, ON: ORGANIC NITROGEN). ON TOP, SUBMICRON PARTICLE MASS [$\mu\text{g m}^{-3}$] FOLLOWED BY BLACK CARBON MASS [ng m^{-3}] (BC). ON BOTTOM, DEGREE OF NEUTRALIZATION (DON) WHERE 1 MEANS THAT ALL SULPHATE AND NITRATE EXIST AS AMMONIUM SULPHATE AND AMMONIUM NITRATE (ADAMS ET AL., 1999). [D] CCN ACTIVATION EFFICIENCY CURVES. GRAPH SHOWS CRITICAL SUPERSATURATION AGAINST CRITICAL DRY DIAMETER; THE SLOPE DERIVED FROM THE MEASUREMENTS DURING THE PERIOD IS SHOWN IN BLACK (SUPERSATURATION UNCERTAINTY PRESENTED BY VERTICAL ERROR BARS), AND THE PREDICTED SLOPES OF PARTIALLY NEUTRALIZED (BASED ON DON) SULPHURIC ACID FROM THE AIOMFAC MODEL SHOWN IN RED WHILE THE NaCl LINE SHOWN IN OLIVE BROWN PREDICTED BY AP3 MODEL (ROSE ET AL., 2008). THE INTER-MODAL MINIMUM POINT, EXTRACTED FROM THE LOG-NORMAL FIT OF NUMBER-SIZE-DISTRIBUTIONS, SHOWN IN BLUE WITH $\pm 5\%$ SIZE ERROR. AT TOP, THE NUMBER OF PARTICLES LARGER THAN THE INTER-MODAL MINIMUM..... 78
- FIGURE 5.2. MAP OF SOUTHERN OCEAN REGION, SHIP COURSE MARKED IN RED. MOVEMENT OF AIR MASSES FROM THREE PRINCIPAL SOURCE REGIONS SHOWN IN BLUE ARROWS; CONTINENTAL ANTARCTIC (CAA), MARITIME POLAR (MP) FROM THE WEST, AND MARITIME TROPICAL (MT) OR MODIFIED-MT, BOTH FROM NORTH AND NORTHWEST OF -60° LATITUDE. APPROXIMATE SUMMER REGIONS OF PACK ICE (GREEN STRIPED) AND LASTING SHEET ICE (BLACK STRIPED) IN THE WEDDELL SEA ARE SHOWN..... 80
- FIGURE 5.3. PHYSICAL AND CHEMICAL PROPERTIES OF CAA (WEDDELL SEA INFLUENCED) AIR MASSES (A) AND MP AIR MASSES (B). ALL DATA FROM EACH STEADY-STATE CASE ARE LUMPED TOGETHER INTO AN AIR MASS AVERAGE. BOTTOM LEFT: MEDIAN NUMBER-SIZE DISTRIBUTION (BLACK) AND VOLUMETRIC SIZE DISTRIBUTION (BLUE), WITH D_p THE SMPS-DERIVED DRY PARTICLE DIAMETER. SHADED GREY AREA REPRESENTS 25TH-75TH PERCENTILE RANGE WITH THE TOTAL PARTICLE NUMBER AND CORRESPONDING VOLUME CONCENTRATIONS NOTED AT THE TOP. BOTTOM RIGHT: ON TOP, THE RATIO OF CCN TO ALL PARTICLES GREATER THAN 20 NM, ON BOTTOM, THE TOTAL NUMBER OF CCN FOR VARYING SUPERSATURATION. SHADED RANGE OF SUPERSATURATIONS REPRESENT TYPICAL VALUES FOR MARINE STRATOCUMULUS CLOUDS. TOP LEFT: CCN ACTIVATION EFFICIENCY AS A FUNCTION OF CRITICAL SUPERSATURATION AND PARTICLE DIAMETER, ON TOP, THE INTER-MODAL MINIMA POINT INDICATED IN BLUE, WITH 10% SMPS SIZING ERROR (THE BLUE SHADED REGION CORRESPONDS TO THE SPREAD OF S_c VALUES CONSIDERING SMPS SIZING ERRORS) AND THE TOTAL NUMBER CONCENTRATION OF PARTICLES AT SIZES GREATER THAN THE INTER-MODAL MINIMA. IN BLACK, FITTED CCN ACTIVATION CURVE OBTAINED FROM THE MEASUREMENTS WITH CORRESPONDING ERROR BARS. THE RED LINE REPRESENTS PARTIALLY NEUTRALIZED SULPHATE ACCORDING TO THE DON INDICATED (USING MIXTURE OF $\text{H}_2\text{SO}_4 + (\text{NH}_4)_2\text{SO}_4$), THE OLIVE BROWN LINE REPRESENTS NaCl, AND THE PURPLE DASHED LINE REPRESENTS AMMONIA-NEUTRALISED MSA (I.E. NH_4 -MSA SALT) WHERE ALL LINES ARE BASED ON PREDICTIONS BY THE AIOMFAC MODEL. TOP RIGHT: PIE CHART OF CHEMICAL MASS FRACTIONS, WITH THE TOTAL MASS CONCENTRATION, AVERAGE BLACK CARBON CONCENTRATION, AND DON_{MOL} NOTED ON TOP. THE SMALLER PIE CHART IS THE BREAKDOWN OF THE NON-SEA-SALT AEROSOL SPECIES..... 82
- FIGURE 5.4. CCN ACTIVATION EFFICIENCY AS A FUNCTION OF CRITICAL SUPERSATURATION AND DIAMETER. TWO MERGED CASES, CAA AND MP, SHOWN IN BLACK AND BLUE RESPECTIVELY. AIOMFAC MODEL-PREDICTED VALUES OF NaCl IN OLIVE BROWN, SULPHATE VARYING DEGREE OF NEUTRALIZATION IN PINK COVERING THE DON_{MOL} RANGE FROM H_2SO_4 TO $(\text{NH}_4)_2\text{SO}_4$ (DARK PINK), AND AMMONIA-NEUTRALISED MSA (I.E. NH_4 -MSA SALT) IN DASHED PURPLE..... 83
- FIGURE 5.5. SATELLITE IMAGES TAKEN FROM NASA WORLDVIEW (NASA, 2018) ([HTTPS://WORLDVIEW.EARTHDATA.NASA.GOV/](https://worldview.earthdata.nasa.gov/)) FOR FOUR SEPARATE DAYS IN JANUARY 2015; (i) JAN 1ST, (ii) JAN 7TH, (iii) JAN 16TH, AND (iv) JAN 31ST. IMAGES SHOW DAILY RESOLUTION OF THE CLOUDINESS IN THE REGION AND ARE REPRESENTATIVE OF THE CLOUD COVER OCCURRING FOR THE EXTENT OF THE PEGASO CRUISE. EACH IMAGE IS AT ~ 5 KM RESOLUTION AND SHOWS A COMPOSITE OF EACH DAY AT LATITUDES FROM -80 TO -45 DEGREES AND LONGITUDES FROM -103 TO -35 DEGREES. 84
- FIGURE 5.6. SATELLITE MONTHLY MEAN COMPOSITES OF LIQUID CLOUD OPTICAL THICKNESS (TOP) AND THE MONTHLY STANDARD DEVIATION (BOTTOM) GLOBALLY. IMAGES TAKEN OF JANUARY 2015 FROM MODIS L3 MONTHLY COLLECTION 6.1, [[HTTPS://MODIS-ATMOS.GSFC.NASA.GOV/IMAGES/L3-MONTHLY-BROWSE](https://modis-atmos.gsfc.nasa.gov/images/l3-monthly-browse/)](NASA, 2017)... 85
- FIGURE 5.7. ON TOP, THE RATIO OF CCN TO ALL PARTICLES GREATER THAN 20 NM, LISTED BY AIR MASS SOURCE REGION. ON BOTTOM, THE TOTAL NUMBER OF CCN FOR VARYING SUPERSATURATION SHADED RANGE OF SUPERSATURATIONS REPRESENT TYPICAL VALUES FOR MARINE STRATOCUMULUS CLOUDS..... 89
- FIGURE 5.8. FREQUENCY DISTRIBUTIONS OF WIND (GREY) AND GUST (BLUE-GREY) MEASUREMENTS TAKEN ON THE RESEARCH SHIP DURING AMBIENT SAMPLING PERIODS USED IN THIS ANALYSIS. 90

List of Figures

- FIGURE 5.9. SEA-SALT EVENT ANALYSIS SHOWN FOR SMPS, HR-TOF AMS, AND CCNC DATA SHOWN. THE LEFT PANEL SHOWING NUMBER (N) AND VOLUME (V) SIZE DISTRIBUTIONS OF EVENT 1 -4 (E1-4), BLACK AND GREY SOLID AND DASHED LINES REPRESENT THE NUMBER-SIZE DISTRIBUTIONS WHILE THE COLOURED SOLID LINES REPRESENT THE VOLUME DISTRIBUTIONS. THE MIDDLE PANEL SHOWS AMS CHEMICAL FRACTIONS OF ALL FOUR EVENTS WITH TOTAL MASS CONCENTRATION AT THE BOTTOM OF EACH PIE-CHART, RESPECTIVELY. THE RIGHT PANEL SHOWS CCN ACTIVATION EFFICIENCY CURVES OF SEA-SALT EVENTS WITH CRITICAL SUPERSATURATION PLOTTED AGAINST CRITICAL DRY DIAMETER; THE SLOPES DERIVED FROM THE MEASUREMENTS DURING THE PERIODS ARE SHOWN. THE AIOMFAC MODEL PREDICTED NaCl LINE, IN OLIVE BROWN, AND THE SULPHURIC ACID TO NEUTRALIZED SULPHATE ($H_2SO_4 - (NH_4)_2SO_4$) RANGE ARE SHOWN.91
- FIGURE 5.10. AIR MASS BACK TRAJECTORIES FROM HYSPLIT CALCULATED FOR 120 HRS AT A STARTING HEIGHT OF 50 M AMSL ARE SHOWN FOR THE SUMMER PERIODS A (IN PINK) AND B (IN BLUE). EACH PERIOD SHOWS A NEW TRAJECTORY EVERY 6 HOUR.94
- FIGURE 5.11. NUMBER-SIZE DISTRIBUTION DATA AND CHEMICAL MASS FRACTIONS FOR THE SUMMER NORTH EAST ATLANTIC CASES SAMPLED AT MACE HEAD RESEARCH STATION IN 2015 AND 2017. THE LEFT COLUMN SHOWS THE MEDIAN SMPS DATA FOR EACH CASE IN DOTTED LINES, WITH THE FITTED DATA SHOWN IN A THICK SOLID LINE. SHADED AREAS BETWEEN THE LIGHTER LINES REPRESENT THE 75TH-25TH PERCENTILES, WITH TOTAL MEAN NUMBER CONCENTRATION WRITTEN AT THE TOP. THE RIGHT COLUMN SHOWS THE HR-TOF-AMS NON-REFRACTORY CHEMICAL DATA AND MAAP BC MASS CONCENTRATIONS AS PIE CHARTS OF THE MASS FRACTIONS. THE ABSOLUTE MASS CONCENTRATIONS AND DON_{MOL} ARE WRITTEN AT THE BOTTOM, WITH A COLOUR KEY ON THE RIGHTMOST OF THE FIGURE.95
- FIGURE 5.12. CCN ACTIVATION CURVES FOR MHD SUMMER MARINE DATA. INDIVIDUAL DATA POINTS ARE PLOTTED AS MARKERS WITH ERROR BARS REPRESENTING THE UNCERTAINTIES IN THE SUPERSATURATIONS. THE BLACK LINE IS THE FITTED SLOPE OF THE PLOTTED DATA. THE PREDICTED SLOPES OF AMMONIUM SULPHATE (AS) FROM THE AP3 MODEL (ROSE ET AL., 2008) AND NaCl FROM THE AIOMFAC MODEL (ZUEND ET AL., 2008) ARE SHOWN IN RED AND OLIVE BROWN, RESPECTIVELY.96
- FIGURE 5.13. A COMPARISON OF CCN S_c - D_c CURVES BETWEEN SOUTHERN OCEAN (S.O.) AND NORTH EAST ATLANTIC (N.E.A.) SUBMICROMETRE SUMMER CCN POPULATIONS. CCN S_c - D_c CURVES OF THE OVERALL TREND THE NORTH EAST ATLANTIC MARINE SUMMER CASE STUDY (SOLID BLACK LINE) AND THE MP MERGED SUMMER SOUTHERN OCEAN CASE (DOT-DASHED BLACK LINE) ARE SHOWN. THEORETICAL CURVES (ALL FOR 298.15 K, AND A CONSTANT SURFACE TENSION OF 0.072 N m^{-1}) OF AMMONIUM SULPHATE (AS) (MAROON LINE) FROM THE AP3 MODEL (ROSE ET AL., 2008), NaCl (OLIVE BROWN LINE) AND NH_4 -MSA (DASHED PURPLE LINE) CALCULATED FROM THE AIOMFAC MODEL (ZUEND ET AL., 2011; ZUEND ET AL., 2008), AND A THEORETICAL LINE FOR A $k \sim 0.1$ (GREEN LINE) CALCULATED FROM K-KÖHLER THEORY (PETTERS AND KREIDENWEIS, 2007).97
- FIGURE 6.1. LINEAR REPRESENTATION OF THE LINK BETWEEN THE CRITICAL SUPERSATURATION (S_c , %) AND NUMBER OF PMA WHICH ACTIVATE INTO CLOUD DROPLETS (PMA ACTIVATED) (LEFT); CRITICAL DIAMETERS (D_c) AND S_c (MIDDLE); AND THE FRACTION OF SMA WHICH THEN ACTIVATE INTO CLOUD DROPLETS (FRACTION SMA ACTIVATED) AND D_c (RIGHT). THE THREE LINEAR REPRESENTATION GIVE PEARSON'S R-VALUES AT THE TOP OF THE GRAPH (ALL ARE SIGNIFICANT FOR $p < 0.01$) AND SHOW EACH MP AND CAA CASES AS OPEN CIRCLES, WITH THE BLUE CLOSED CIRCLES SHOWING THE RESULTS OF THE AVERAGE CASE EXAMPLES.102
- FIGURE 6.2. MODIS RETRIEVALS OF THE PEGASO CRUISE REGION FROM DECEMBER – FEBRUARY 2015.105
- FIGURE 6.3. (LEFT) INTER-COMPARISON OF MODEL RESULTS OF CLOUD PEAK SUPERSATURATION (S_c , %) AND CLOUD DROPLET NUMBER CONCENTRATION ($CDNC \text{ cm}^{-3}$) FOR THREE PARCEL MODEL TYPES IS SHOWN. THE IN-PM, kA-PM, AND kN-PM ARE COMPARED AT 0.1 m s^{-1} AND 0.3 m s^{-1} UPDRAFT AND VARYING SO_4 NUMBER CONCENTRATIONS (N_{SO_4}). (RIGHT) INTER-COMPARISON OF TWO MODEL TYPES, THE IN-PM AND kA-PM, AT 0.07 m s^{-1} AND 0.3 m s^{-1} AND VARYING SO_4 NUMBER CONCENTRATIONS (N_{SO_4}). THE DIFFERENT UPDRAFTS ARE REPRESENTED BY DIFFERENT COLOURS AND THE DIFFERENT MODELS ARE REPRESENTED BY DIFFERING LINE FORMAT. THE GREY SHADED AREA MARKS MEASURED AMBIENT N_{SO_4} , $CDNC$, AND S_c VALUES.108
- FIGURE 6.4. ACTIVATION SPECTRUM OF AN ADIABATIC LIFTING PARCEL IN A 1-D MODEL (PYRCEL), USING 20 BIN SECTIONS, WITH STARTING TEMPERATURE OF 268.15 K, AT 0.3 m s^{-1} VERTICAL VELOCITY. (A) (LEFT) THE TEMPERATURE AND SUPERSATURATION VERTICAL PROFILES. (RIGHT) DROPLET RADIUS AS A FUNCTION OF PARCEL HEIGHT. THE ACTIVATION OF DROPLETS CAN BE SEEN IN PARTICLES WHICH ARE AT LARGER DIAMETERS AT MAXIMUM HEIGHT. THREE REGIMES ARE HIGHLIGHTED BY COLOUR CODED HORIZONTAL LINES, WITH BLACK (i) REFERRING TO THE TIME AT CLOUD BASE BEFORE DROPLET ACTIVATION, RED (ii) AT DROPLET ACTIVATION, AND BLUE (ii) AT CLOUD

List of Figures

TOP AFTER DROPLET ACTIVATION, RESPECTIVELY. (B) THE RELATIVE WET DROPLET DIAMETER (D) FOR THE THREE REGIMES ARE SHOWN AS A FUNCTION OF SMA NUMBER CONCENTRATION (N_{SMA}).	111
FIGURE 6.5. CDNC RELATIONSHIP BETWEEN CALCULATED (MEASURED) AND MODELLED FROM AMBIENT SOUTHERN OCEAN CASES. THE IN-PM IS SHOWN AS SQUARE MARKERS, AND THE KN-PM ARE SHOWN AS CLOSED CIRCLES WITH AVERAGES OF EACH AIR MASS (MP AND CAA) CASE SHOWN IN OPEN CIRCLES. A 1:1 LINE IS SHOWN IN RED, WITH THE FITTED RELATIONSHIP BETWEEN MEASURES AND MODELLED OF EACH MODEL ALSO SHOWN. THE LINEAR RELATIONSHIP OF THE PN-PM IS SHOWN AS A SOLID LINE WHILE THE KN-PM IS SHOWN AS A DASHED LINE.	112
FIGURE 6.6. CALCULATED (OR MEASURED) AND MODELLED VALUES ARE SHOWN AS FUNCTIONS OF DIFFERENT PARAMETERS WITH BOTH IN-PM AND KN-PM MODEL RESULTS. (LEFT) S_c AND ACTIVATED PMA (OR SEA-SALT) RELATIONSHIP, (MIDDLE) SMA D_c AND S_c , AND (RIGHT) PERCENT FRACTION OF SMA ACTIVATED AND SMA D_c . IN ALL PLOTS THE MEASURED DATA AND RESPECTIVE UNCERTAINTIES ARE REPRESENTED BY THE BLUE SHADED REGION WITH ASSOCIATED FITTED TREND LINES IN RED, WHILE IN-PM ARE DISPLAYED AS BOXES AND KN-PM ARE CLOSED CIRCLES. THE ERROR BARS ASSOCIATED WITH EACH MODEL ARE BASED ON EITHER THE SENSITIVITY OR STANDARD DEVIATION OF THE MODEL. THE TRENDS IN THE RIGHT TWO GRAPHS ARE FOR TRENDS USING THE INTER-MODAL MINIMUM (D_c) RATHER THAN THE SMA D_c AND ARE THE SAME TREND LINES SHOWN IN THE LEFT-MOST GRAPH PANEL IN FIGURE 6.1. HOWEVER, THE BLUE SHADED REGION CORRESPONDS TO THE MEASURED SMA D_c	113
FIGURE 6.7. CAA AVERAGED (BLUE) AND MP AVERAGED (BLACK) SIZE DISTRIBUTIONS FOR BOTH CASES. MEASURED AVERAGE VALUES ARE SHOWN AS CIRCLES, WHILE CALCULATED SMA ARE SHOWN AS SOLID LINES, AND SEA-SALT IS SHOWN AS DASHED LINES. SEA-SALT TAKEN AS PMA AND DERIVED FROM FLUX PARAMETRISATION IN OVADNEVAITE ET AL. (2014B) AND SCALED BY MASS WHILE SMA IS DERIVED FROM THE RESIDUALS (SEE METHODS). IN BOTH CASES, PMA CONSISTS OF FIVE MODES AND SMA CONSISTS OF FOUR MODES, BOTH SHOWN AS COMPOSITES.	114
FIGURE 6.8. CCN ACTIVATION (S_c - D_c) CURVES FOR THE AVERAGE CASES OF MP AND CAA AIR MASSES.	115
FIGURE 6.9. (A) SENSITIVITY ANALYSIS OF THE PN-PM TO CHANGES IN CLOUD BASE TEMPERATURE. (B) SENSITIVITY ANALYSIS OF THE PN-PM TO CHANGES IN UPDRAFT VELOCITY (w). ON BOTH GRAPHS THE LEFT AXIS SHOWS CDNC OF SULPHATE IN DASHED LINES WHILE THE RIGHT AXIS SHOWS CLOUD PEAK SUPERSATURATION (%) IN SOLID LINES. THE CHANGES IN COLOUR (OR SHADE) OF THE LINE REFER TO CHANGES IN TEMPERATURE (FROM 258 -273 K) OR w (FROM 0.1-0.5 $m s^{-1}$). THE SHADED REGION MARKS THE RANGE OF $N_{SULPHATE}$ MEASURED IN THE EIGHT STEADY-STATE CASES.	118
FIGURE 6.10. DIFFERENT SMA INITIATOR MODES ARE SHOWN FOR EACH AIR MASS TYPE AVERAGE CASE TO ILLUSTRATE THE RANGE OF POSSIBILITIES FROM THE ERROR MARGIN IN THE CASE AVERAGES.	118
FIGURE 6.11. SENSITIVITY ANALYSIS OF THE KN-PM TO CHANGES IN SO_4 INITIATOR MODAL POSITIONING USING PEAK RADIUS ($R_{SO4-MODE}$). THE LEFT AXIS SHOWS CDNC OF SULPHATE IN DASHED LINES WHILE THE RIGHT AXIS SHOWS CLOUD PEAK SUPERSATURATION (%) IN SOLID LINES. THE CHANGES IN COLOUR (OR SHADE) OF THE LINE REFER TO CHANGES MODAL PEAK POSITION (FROM A RADIUS OF 10 – 50 nm). THE SHADED REGION MARKS THE RANGE OF $N_{SULPHATE}$ MEASURED IN THE EIGHT STEADY-STATE CASES.	119
FIGURE 6.12. SENSITIVITY ANALYSIS OF THE KN-PM TO CHANGES IN SEA-SALT PARTICLE NUMBER CONCENTRATION. FOR THE GRAPH ON THE LEFT, THE LEFT AXIS SHOWS CDNC OF SULPHATE IN DASHED LINE WHILE THE RIGHT AXIS SHOWS CLOUD PEAK SUPERSATURATION (%) IN SOLID LINES, WHILE THE GRAPH ON THE RIGHT SHOWS THE RIGHT AND LEFT AXIS SWAPPED. THE CHANGES IN LINE COLOUR REFER TO CHANGES IN SEA-SALT (SS) NUMBER CONCENTRATION (FROM 1 TO 160 SEA-SALT PARTICLE (SS) cm^{-3}). THE SHADED REGION MARKS THE RANGE OF $N_{SULPHATE}$ MEASURED IN THE EIGHT STEADY-STATE CASES. ON LEFT, THE GRAPH SHOWS VALUES FOR $w = 0.4 m s^{-1}$, AND ON RIGHT THE GRAPH SHOWS VALUES FOR $w = 0.2 m s^{-1}$ BOTH GRAPHS ARE FOR $-5^\circ C$	120
FIGURE A1. A COMPARISON OF THE TWO CCNC INSTRUMENTS AT $\sim 0.3\%$ SUPERSATURATION OVER MAY 8 TH - 30 TH , 2017. CCN CONCENTRATION MEASUREMENTS ARE INDICATED BY BLACK MARKERS, WHILE THE RED LINE IS THE LINEAR FIT TO THE DATA POINTS, WITH RESULTS OF THE FIT SHOWN IN THE BOTTOM RIGHT CORNER.	133
FIGURE A2. TIME TRENDS OF PARALLEL CCN MEASUREMENTS OF POLYDISPERSITY AMBIENT AIR.	134
FIGURE B1. COMPARISON OF EXPERIMENTAL DATA AND AIOMFAC PREDICTIONS FOR WATER ACTIVITY (LEFT Y-AXIS) AND THE MEAN MOLAL ION ACTIVITY COEFFICIENT (RIGHT Y-AXIS) OF THE BINARY AQUEOUS SYSTEMS USED TO FIT THE MODEL PARAMETERS AT $T \approx 298 K$. THE SOLUTES ARE MSA (A), NA-MSA (B) AND NH4-MSA (C).	137
FIGURE B2. TANK ICE EXPERIMENTS 1-3 SHOWN AS CCN CRITICAL ACTIVATION CURVES, IN DASHED GREY-TONE LINES. THEORETICAL AMMONIUM SULPHATE (PINK) AND NA ₂ CO ₃ (OLIVE BROWN) CALCULATED AT 293.15 K ARE SHOWN. ALSO, A TYPICAL WEDDELL SEA AIR MASS IS SHOWN IN THE BLACK SOLID LINE.	141

List of Tables

FIGURE B3. THEORETICAL CCN ACTIVATION CURVES ARE SHOWN ALONG WITH TANK ICE EXPERIMENT MEASUREMENTS. AMMONIUM SULPHATE ((NH₄)₂SO₄) CALCULATED USING K-KÖHLER THEORY (EQ. 15 IN SECTION 3.6.3) IS SHOWN IN PINK WITH THE DARKER OF THE TWO CALCULATED AT 298.15 K AND THE LIGHTER AT 283 K. NaCl CALCULATED IN THE SAME MANNER IS SHOWN WITH THE SOLID OLIVE BROWN LINE CALCULATED FOR 298.15 K AND THE DARK GREEN LINE CALCULATED AT 283.15 K. THE DASHED OLIVE BROWN LINE IS CALCULATED AT 298.15 K, HOWEVER A SHAPE CORRECTION ($x = 1.08$) FACTOR IS APPLIED FOR A CUBIC PARTICLE (HINDS, 1982).142

List of Tables

TABLE 4.1. PARAMETERS FROM THE LOGNORMAL MODE FITTINGS OF THE FREQUENCY DISTRIBUTION BY PEAK (PK). MODE POSITIONS (C_0) AND Σ_G ARE IN TERMS OF THE BC MASS CONCENTRATION IN NG M^{-3} , WHILE THE AMPLITUDE OF THE MODE (AMP) IS IN % OCCURRENCE AND IS NOT THE HEIGHT OF THE MODE BUT RATHER THE AMPLITUDE AS DESCRIBED IN HINDS (1982). THE BC CONCENTRATION FOR WHICH 95 % OF THE MODE IS ACCOUNTED FOR ($C_{95\%}$, SEE METHODS) IS IN NG M^{-3}	59
TABLE 4.2. THE CLASSIFICATION OF AIR MASSES ARRIVING AT MHD FROM BC MASS CONCENTRATION DATA. THE CLASSIFICATIONS WERE DERIVED BY GRIGAS ET AL. (2017) BASED UPON FIVE YEARS OF MAAP DATA FROM MHD. USING SP2 AND MAAP COMPARISONS THE EQUIVALENT MASS CONCENTRATIONS AS MEASURED BY AN SP2 INSTRUMENT ARE REPORTED.	68
TABLE 5.1. LOG-NORMAL PARAMETER FITS FOR NUMBER AND VOLUME SIZE DISTRIBUTIONS. PARTICLE SIZE, MODAL SPREAD (Δ), AND HYGROSCOPICITY PARAMETER (κ) FOR FITTED NUMBER—SIZE DISTRIBUTION PEAKS SHOWN ON LEFT. FITTED PARTICLE VOLUME AND SPREAD PEAKS SHOWN ON RIGHT. DASHED LINES REPRESENT THE LACK OF MORE PEAKS IN THE VOLUMETRIC DISTRIBUTIONS. MISSING κ -VALUES INDICATE THAT LOGNORMALLY FITTED PEAK DIAMETERS WERE OUTSIDE OF SIZES RESOLVED BY CCNC.	79
TABLE 5.2. LOG-NORMAL FIT PARAMETERS FOR NUMBER AND VOLUME SIZE DISTRIBUTIONS. PARTICLE DRY DIAMETER (PEAK DIAMETER, NM), SPREAD (Δ), κ , AND EQUIVALENT κ -VALUE FOR PURE AMMONIUM SULPHATE AT THAT PARTICLE SIZE ($AS_{EQ, \kappa}$) FOR FITTED NUMBER PEAKS SHOWN ON LEFT. PARTICLE VOLUME-SIZE DISTRIBUTION (PEAK DIAMETER, NM) AND SPREAD (Δ) OF THE FITTED PEAKS SHOWN ON RIGHT. EMPTY SPACES INDICATE THAT CORRESPONDING PEAKS HAVE AN AMPLITUDE TOO SMALL TO BE FITTED RELIABLY. ALL κ COMPUTED ASSUMING A CONSTANT SURFACE TENSION OF 0.072 N M^{-1}	86
TABLE 5.3. INTER-MODAL MINIMA POINTS AND CORRESPONDING PARAMETERS LISTED ACCORDING TO THEIR OCCURRENCE: INTER-MODAL DIAMETER, NUMBER OF PARTICLES AT THE INTER-MODAL DIAMETER, CRITICAL SUPERSATURATION CORRESPONDING TO INTER-MODAL MINIMUM AND NUMBER OF PARTICLES ABOVE INTER-MODAL MINIMUM DIAMETER.	87
TABLE 5.4. VALUES USED FOR PMA NUMBER CONTRIBUTION CALCULATION. INTER-MODAL MINIMUM (D_c) VALUES GAVE CORRESPONDING CLOUD PEAK SUPERSATURATION (S_{PEAK}) BASED ON AMBIENT S_c - D_c CURVES. THE SAME CURVES RESOLVED THE CRITICAL DIAMETERS OF SMA (D_{SMA}) AND PMA (D_{PMA}) WHICH WERE USED IN CONJUNCTION WITH NUMBER-SIZE DISTRIBUTION DATA TO FIND THE NUMBER OF ACTIVATED SMA AND PMA PARTICLES AND FIND THE PERCENT CONTRIBUTION OF PMA (% PMA) TO THE CLOUD DROPLET NUMBER. THE NUMBER CONCENTRATION OF PMA AND SMA HAS AN ASSOCIATED $\pm 5 \text{ CM}^{-3}$	90
TABLE 6.1.	103
TABLE 6.2. SEA-SALT MODAL PARAMETERS USED FOR SCALING FOR SEA-SALT INITIATOR FOR PARCEL MODELS. THE MODES ARE BASED ON A 6.3 M S^{-1} WIND SPEED PARAMETRISATION IN OVADNEVAITE ET AL. (2014B). PEAK LOCATION (x_0), PEAK GEOMETRIC SPREAD (Σ_G), AND PEAK AMPLITUDE (A) ARE SHOWN.	107
TABLE 6.3. THE IN-PM INPUT VARIABLES AND EXAMPLE OF INPUT USED FOR COMPARISON TO KN-PM. THE PARAMETERS WERE SLIGHTLY CHANGED WHEN COMPARING TO THE KA-PM.	107
TABLE 6.4. SMA MONOMODAL INPUT PARAMETERS OF THE CASE USED TO COMPARE THE CLOUD PARCEL MODELS.....	107

List of Tables

TABLE 6.5. SMA MONOMODAL INPUT PARAMETERS OF THE PEGASO AMBIENT CASES FOR THE CLOUD PARCEL MODELS.	112
TABLE 6.6. AVERAGE CHEMICAL FRACTIONS FROM CASES OF <i>CAA</i> AND <i>MP</i> AIR MASSES. SHOWN BELOW ARE HR-TOF AMS MEASUREMENTS ($\mu\text{g m}^{-3}$) OF ORGANIC MASS (OM), NITRATE (NO_3), NON-SEA-SALT SULPHATE (NSS- SO_4), AMMONIUM (NH_4), SEA-SALT, METHANESULPHONIC ACID (MSA), AND ORGANIC NITROGEN (ON). ALSO SHOWN BELOW ARE TOTAL CONCENTRATIONS AND BIOGENIC CONCENTRATIONS (TOTAL WITHOUT SEA-SALT), AND AVERAGED BLACK CARBON (BC) MEASUREMENTS FROM THE SP2 (ng m^{-3}).	116
TABLE A1. CCNC SET SUPERSATURATIONS, CALIBRATED ACTUAL CRITICAL SUPERSATURATIONS (S_c), AND UNCERTAINTIES FOR EACH CCNC INSTRUMENT AND RELEVANT SAMPLING PERIOD (CCNC 0015, AND 086).	132
TABLE B1. LIQUID- AND SOLID-STATE DENSITIES OF PURE COMPONENTS AT $T \approx 20^\circ\text{C}$ (AND $\sim 105\text{ Pa}$) USED FOR THE AIOMFAC-BASED CALCULATIONS OF CRITICAL CCN PROPERTIES.	136
TABLE B2. CRITICAL SUPERSATURATION S_c (%) LISTED FOR A SELECTION OF CORRESPONDING CRITICAL DRY DIAMETERS (D_c) FROM 20 TO 200 NM PREDICTED BY THE AIOMFAC MODEL WITH KÖHLER THEORY. DONMOL INDICATES THE DEGREE OF SULPHATE NEUTRALIZATION BY AMMONIA (EQ. 1, MAIN TEXT) FOR SOLUTE MIXTURES CONTAINING AMMONIUM SULPHATE AND SULPHURIC ACID AT INPUT; ALL DATA FOR $T = 293.15\text{ K}$ AND $\varepsilon = 72.75\text{ MJ m}^{-2}$. .	138
TABLE B3. FITTED BINARY CATION—ANION AIOMFAC MIDDLE-RANGE INTERACTION PARAMETERS (ZUEND ET AL., 2008) FOR AQUEOUS SOLUTIONS OF MSA, NA-MSA, AND NH_4 -MSA; DETERMINED FOR $T \approx 298.15\text{ K}$	139

Dissemination of Research

Publications

Fossum, K.N., Ovadnevaite, J., Ceburnis, D., Dall'Osto, M., Marullo, S., Bellacicco, M., Simo, R., Liu, D., Flynn, M., Zuend, A., and O'Dowd, C. Summertime primary and secondary contributions to Southern Ocean cloud condensation nuclei. *Scientific Reports*, (2018).

Publications In progress

Fossum, K.N., Ovadnevaite, J., Ceburnis, D., Preißler, J., D., Snider, J., and O'Dowd, C. Marine CCN trends of competitive droplet activation between primary and secondary marine aerosol; measured and modelled. To be submitted to *Scientific Reports*, 2019.

Fossum, K.N., J., Ceburnis, Liu, D., Flynn, M., and O'Dowd, C. Black Carbon measurements in two hemispheres, new criteria for degrees of anthropogenic influence. To be submitted to *Scientific Reports*, 2019.

Fossum, K.N., Preißler, J., and O'Dowd, C. Comparison of ground-based measurements of cloud droplet properties and parcel model estimations droplet properties using size resolved cloud condensation nuclei data from Mace Head Research Station. To be submitted 2019.

Conference presentations

Fossum, K.N., Ovadnevaite, J., Ceburnis, D., Dall'Osto, M., Marullo, S., Bellacicco, M., Simo, R., Liu, D., Flynn, M., Zuend, A., and O'Dowd, C. Summertime Primary and Secondary Contributions to Southern Ocean Cloud Condensation Nuclei. BACCHUS Final Meeting, Zurich, Switzerland. 2018 (*Oral presentation*).

Fossum, K.N., Ovadnevaite, J., Ceburnis, D., Preißler, J., O'Dowd, C. *Marine CCN activation: A battle between primary and secondary sources?* American Geophysical Union, Fall Meeting, 2017 (*Poster*).

Fossum, K.N. Clouds; where do they come from, where do they go? Soapbox Science, Galway, 2017. (*Oral presentation*).

Fossum, K.N., Ovadnevaite, J., Ceburnis, Dall'Osto, M., Marullo, S., Bellacicco, M., Simo, Zuend, A., and O'Dowd, C. *Aerosol Physico-chemical and CCN Properties in and around Antarctica during the Austral Summer*. International Conference on Nucleation and Atmospheric Aerosols, Helsinki, Finland, 2017 (*Poster*).

Fossum, K.N., Ovadnevaite, J., Ceburnis, Dall'Osto, M., Simo, Zuend, A., and O'Dowd, C. *Cloud Condensation Nuclei (CCN) Potential in Antarctic Marine Aerosols*. European Aerosol Conference, Tours, France, 2016 (*Poster*).

Dissemination of Research

Fossum, K.N., Ovadnevaite, J., Ceburnis, Dall'Osto, M., Simo, Zuend, A., and O'Dowd, C. *Cloud Condensation Nuclei (CCN) in Antarctic Marine Aerosols Released from Melting Ice*. Institute of Physics, Spring Meeting, Belfast, Ireland, 2016 (*Poster*).